NASA CONTRACTOR REPORT 166360

NASA-CR-166360
19820020436

Pioneer 10/11 Data Analysis of the Trapped Radiation Experiment

Walker Fillius

University of California at San Diego

CONTRACT NAS2–6552
January 1982

NASA

NASA CONTRACTOR REPORT 166360

Pioneer 10/11 Data Analysis of the Trapped Radiation Experiment

Walker Fillius

Center for Astrophysics and Space Science
University of California
San Diego, California

Prepared for
Ames Research Center
under Contract NAS2-6552

National Aeronautics and
Space Administration

Ames Research Center
Moffett Field, California 94035

CONTENTS

PART ONE, DISCUSSION

1.1 INTRODUCTION AND BACKGROUND

1.2 DATA ANALYSIS OPERATIONS

1.2.1 Data Analysis Procedures

1.2.2 Processing Summary

1.2.3 NSSDC Deposits

1.3 LIST OF PUBLICATIONS

PART TWO, PUBLICATIONS

2.1 JUPITER ENCOUNTER

2.2 SATURN ENCOUNTER

2.3 INTERPLANETARY

1.1 INTRODUCTION AND BACKGROUND

Contract NAS2-6552 was undertaken by the National Aeronautics and Space Administration (NASA) and the University of California, San Diego (UCSD) to accomplish the reduction, analysis, dissemination, and publication of data from the UCSD Trapped Radiation Experiment on the NASA Pioneer 10 and 11 spacecraft. The instrumentation for this experiment was built for NASA by UCSD under Contract NAS2-5602. Identical instrument packages were carried aboard the Pioneer 10 and Pioneer 11 spacecraft to make the first exploration of the outer solar system beyond the orbit of Mars, and, in particular, of the neighborhoods of Jupiter and Saturn.

The UCSD instrumentation was designed to delineate the principal features of the Jovian Van Allen radiation belts with minimum ambiguity as to interpretation of the data. More specifically, the instrument design objectives were to distinguish trapped protons and electrons, to measure absolute intensities within known energy ranges, to obtain several points on energy spectra for these particles, to gain information on angular distributions and spatial extent, and to probe the total corpuscular energy flux. Although the design was carried out with just Jupiter in mind, the intrument was very suitable for the exploration of Saturn's magnetosphere, and it has also proven to be a unique and valuable cosmic ray detector system.

Figure 1 shows the interplanetary trajectories of the Pioneer 10 and 11 spacecraft. Pioneer 10 was launched on March 3, 1972 and encountered Jupiter in December, 1973. It acquired enough additional energy from its gravitational interaction with Jupiter to put it on a trajectory destined to

PIONEER 10 AND 11 HELIOCENTRIC TRAJECTORIES

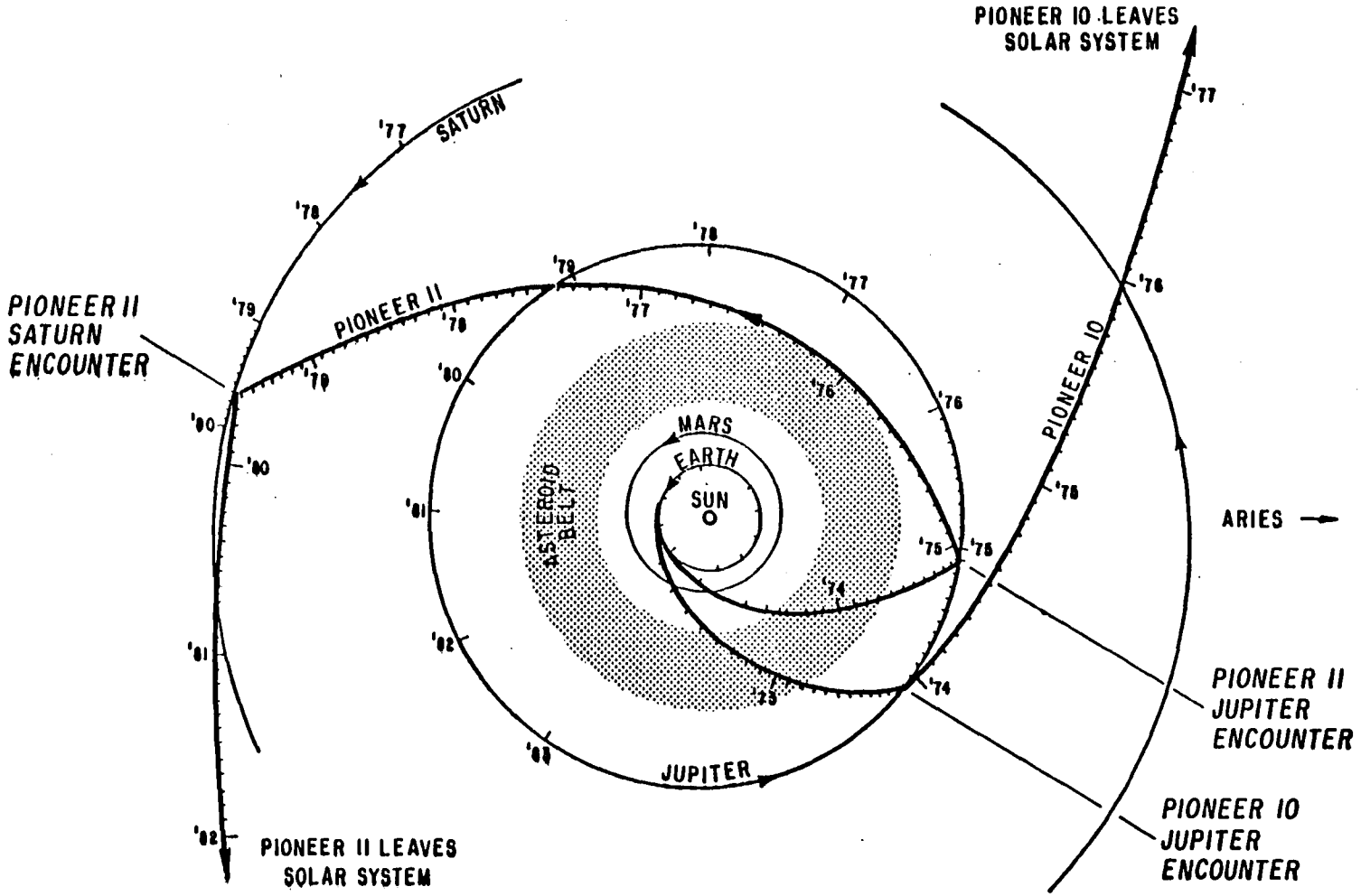

Figure 1

escape from the solar system. Pioneer 11 was launched on April 6, 1973 and encountered Jupiter in December, 1974. Following the successful encounter of Pioneer 10, the Pioneer 11 encounter was retargeted so that Pioneer 11 would make a first-ever encounter with Saturn. This encounter took place in September, 1979, and the Pioneer 11 spacecraft is now on a heliospheric escape trajectory carrying it in the direction opposite from Pioneer 10. At the time of this writing (December, 1981) Pioneer 10 is 26 AU from the sun and Pioneer 11 is 11 AU from the sun. Both spacecraft continue to function and transmit excellent data.

The UCSD experiment exceeded its objectives. Trapped radiation measurements were made in the magnetospheres of earth, Jupiter, and Saturn, and cosmic radiation measurements were made and are still being made in interplanetary space. The data have been reduced and written on magnetic tape in both complete formats and in condensed formats for scientific analysis. Key tapes have been copied and deposited in the National Space Science Data Center archive for use by other scientists. Section II of this report is a compilation of articles which describe results and analyses from this experiment to date.

1.2 DATA ANALYSIS OPERATIONS

1.2.1 Data Analysis Procedures The flow chart in Figure 2 shows the procedures we have used routinely on the Pioneer data. Starting with the Experimenter Data Record (EDR) and Trajectory (TRAJ) tapes, we generate Summary (SUM) and, sometimes, Binary Reduction (BRT) tapes in which the data are

Figure 2

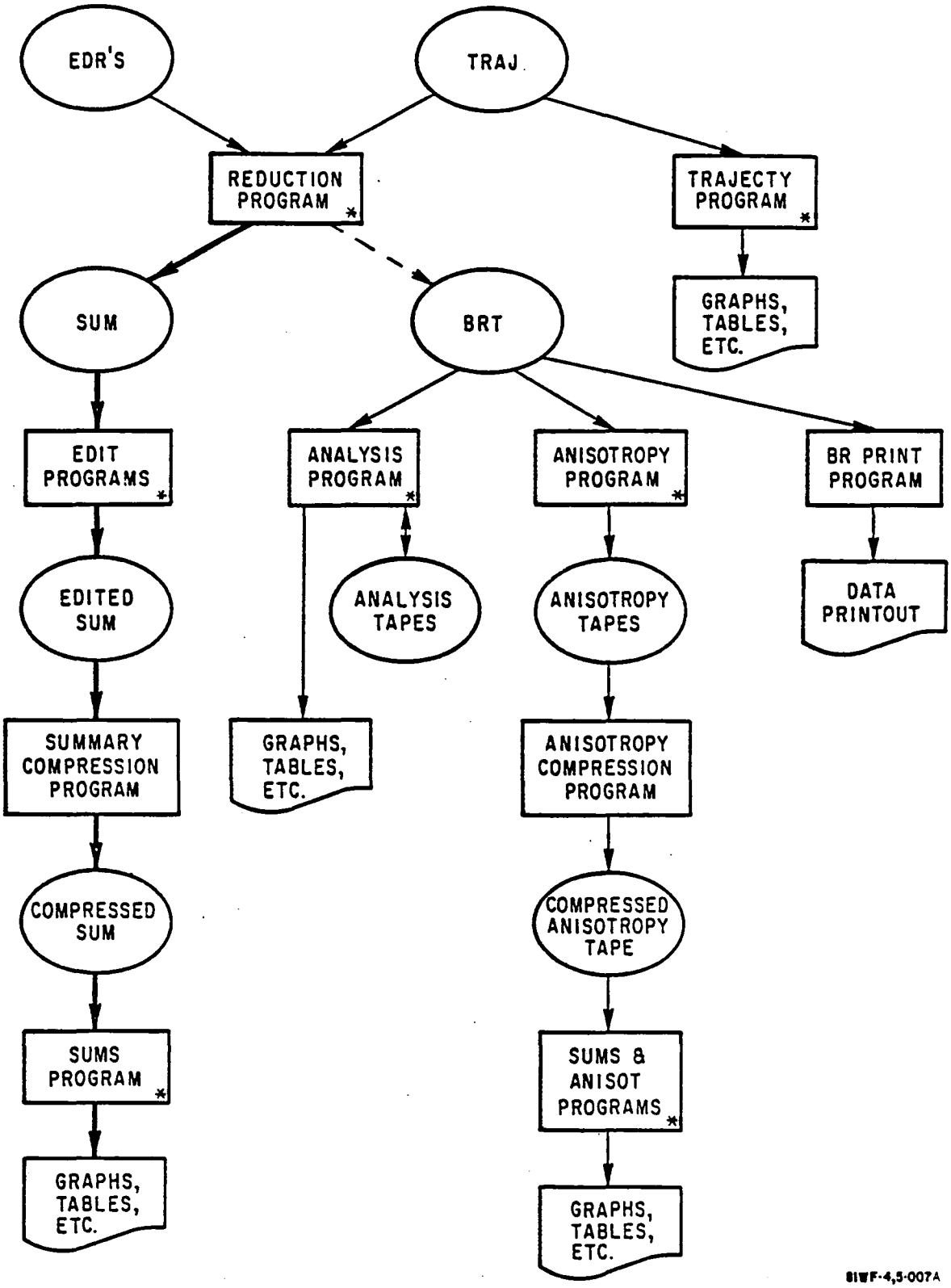
EDR'S
TRAJ.
REDUCTION PROGRAM *
TRAJECTY PROGRAM *
GRAPHS, TABLES, ETC.
SUM
BRT
EDIT PROGRAMS *
ANALYSIS PROGRAM *
ANISOTROPY PROGRAM *
BR PRINT PROGRAM
EDITED SUM
ANALYSIS TAPES
ANISOTROPY TAPES
DATA PRINTOUT
SUMMARY COMPRESSION PROGRAM
GRAPHS, TABLES, ETC.
ANISOTROPY COMPRESSION PROGRAM
COMPRESSED SUM
COMPRESSED ANISOTROPY TAPE
SUMS PROGRAM *
SUMS & ANISOT PROGRAMS *
GRAPHS, TABLES, ETC.
GRAPHS, TABLES, ETC.
BWF-4,5-007A

decoded and tagged with the spacecraft position so as to be ready for analysis. The BRT's contain every individual reading, whereas the SUM's contain averages accumulated over some interval. Following the left-hand column in Figure 2, the Edit Program deletes bad data from a SUM tape, producing a new tape in the same format. The Summary Compression Program also produces a new tape in the same format, except that the averages are combined to extend over a longer interval. The bulk of our interplanetary data deposited in the National Space Science Data Center (NSSDC) is on Compressed Summary Tapes.

BRT's were generated for all planetary encounters and also for much of the interplanetary mission. The analysis program analyzes and fits angular distributions on a short time scale. It produces Analysis Tapes which contain the most concise description of the data for the close encounters. The planetary encounters are represented at the NSSDC with Analysis Tapes, BRT's, and Summary Tapes.

The anisotropy column was used to extract directional information on interplanetary cosmic rays from the Cerenkov counter channels or our instrument.

The format of the Compressed Anisotropy Tapes is given in Table 1. The formats of the other tapes are documented in the "Data Package for the UCSD Trapped Radiation Detector," which has been deposited with the National Space Science Data Center.

Revised 7/13/78

COMPRESSED ANISOTROPY TAPES

Datum Sequence #	Name of Datum	Bits per Datum	Place in Record
1	Time of earliest reading in record (cole milliseconds)	48	1 - 48
2	Time of latest reading in record (cole milliseconds)	48	49 - 96
3	Roll period (milliseconds)	32	97 - 128
4	Attitude colatitude (microradians)	32	129 - 160
5	Attitude longitude (microradians)	32	161 - 192
Sequence #'s 6 - 25 apply to 1.5 sec accumulations on channel C1			
6	Number of readings $N_0 = \sum_i 1$	24	193 - 216
7	Number of counts $A_0 = \sum_i C_i$ *	24	217 - 240
8	Encoded Fourier coef: * $A_1 = 10^6 * \left(\sum_i C_i(1 + \cos\theta_i) / \sum_i C_i\right)$	24	241 - 264
9	Encoded Fourier coef: † $B_1 = 10^6 * \left(\sum_i C_i(1 + \sin\theta_i) / \sum_i C_i\right)$	24	265 - 288
10	Number of readings in sector 1(337.5°-22.5°) $n_1 = \sum_i i_1$	24	289 - 312
11	Number of counts in sector 1 $a_1 = \sum_i C_{1i}$	24	313 - 336
12 - 13	Same as 10 & 11 for sector 2 (22.5° - 67.5° ecliptic nadir angle)	24 * 2	337 - 384
14 - 25	Sameas 10 & 11 for sectors 3 - 8	24 * 12	385 - 672
26 - 45	Same as 6 - 25 for 1.5 sec accumulations on channel C2	24 * 20	673 - 1152
46 - 65	Same as 6 - 25 for 1.5 sec accumulations on channel C3	24 * 20	1153 - 1632
66 - 85	Same as 6 - 25 for 3.0 sec accumulations on channel C1	24 * 20	1163 - 2112
86 - 105	Same as 6 - 25 for 3.0 sec accumulations on channel C2	24 * 20	2113 - 2592
106 - 125	Same as 6 - 25 for 3.0 sec accumulations on channel C3	24 * 20	2593 - 3072
126 - 145	Same as 6 - 25 for 6.0 sec accumulations on channel C1	24 * 20	3073 - 3552
146 - 165	Same as 6 - 25 for 6.0 sec accumulations on channel C2	24 * 20	3553 - 4032
166 - 185	Same as 6 - 25 for 6.0 sec accumulations on channel C3	24 * 20	4033 - 4512
186 - 199	Blank padding to round out record **	672	4513 - 5184

Table 1 Format of Compressed Anisotropy Tapes

† Decoded Fourier coefficients can be recovered with the following equations:

$C(\theta) = a_0 + a_1 \cos\theta + b_1 \sin\theta + \ldots\ldots$

$a_0 = \sum_i C_i / \sum_i i = A_0/N_0$, $N_0 = \sum_i i$, $A_0 = \sum_i C_i$

$a_1 = \frac{2}{N_0} \sum_i C_i \cos\theta_i = 2(A_1 * 10^{-6} - 1) * A_0 / N_0$, $A_1 = 10^6 * \left(1 + \frac{\sum C_i \cos\theta_i}{\sum C_i}\right)$

$b_1 = \frac{2}{N_0} \sum_i C_i \sin\theta_i = 2(B_1 * 10^{-6} - 1) * A_0 / N_0$, $B_1 = 10^6 * \left(1 + \frac{\sum C_i \sin\theta_i}{\sum C_i}\right)$

θ = Ecliptic nadir angle (angle between look direction and ecliptic nadir)

** Note that $48 = 2^4 * 3$, $36 = 2^2 * 3^2$, $32 = 2^5$. Least common denominator of 48, 36, 32 = $2^5 * 3^2 = 288$ bits.

*** Packed 2 Logical Records (LR) per Physical Record (PR).
One LR = 108 * 48 bits. One PR = 216 * 48 bits

1.2.2 Processing Summary

Data processing at UCSD was originally performed on a CDC3600 owned and operated by the UCSD Computer Center. This machine was taken out of service in July, 1980. In 1977 our space physics group acquired its own DEC 11/70, and in 1980, a larger 11/780 VAX. All new programs written since that time have been executed on our own computers. Furthermore, in 1979 we undertook an explicit effort to convert our essential programs from the CDC3600 to our DEC equipment, and the major programs have been converted. Those shown with an asterisk on Figure 2 were brought into service on our equipment. Because of the historical precedence of the CDC machine, all of the data tapes are written with the 48 bit words peculiar to that machine.

From launch through December 31, 1981, Pioneer 10 has logged 3591 days in space, and Pioneer 11, 3192 days. The Reduction Program has processed 2567 Pioneer 10 EDR's through December 30, 1981, and 2328 Pioneer 11 EDR's through December 31, 1981. One more Pioneer 11 EDR and two Pioneer 10 EDR's have been received and await processing, and one day's data have not yet been received to complete 1981. For all of these data Summary Tapes were produced, with 1/2 hour time intervals for interplanetary data, and with 108 second intervals for encounter data. Interplanetary data to mid-1977 have been edited and compressed into 24 hour intervals. These Compressed Summary Tapes are deposited in the NSSDC. Editing is in progress for the remaining interplanetary data, and compression will take place as soom as successful test runs are completed with the 11/70 version of the Summary Compression Program. If the Pioneer 10 and 11 mission is contin-

ued and funds are available for data reduction, data will be deposited in the NSSDC annually.

1.2.3 NSSDC Deposits

The following data tapes have been deposited in the National Space Science Data Center (NSSDC).

Pioneer 10 Jupiter Encounter

Six 108 second Summary Tapes

M44900	11/26 - 29/73
M44901	11/30-12/3/73
M44902	12/4 - 7/73
M44903	12/8 - 11/73
M44904	12/12 - 15/73
M44905	12/16 - 19/73

Pioneer 11 Jupiter Encounter

One Binary Reduction Tape (BRT)

Four 108-second Summary Tapes

M53744	BRT	12/3/74 hours 0-14
M54790	SUM	11/26 - 29/74
M54791	SUM	11/30-12/3/74
M54792	SUM	12/4 - 7/74
M54793	SUM	12/8 - 9/74

Pioneer 11 Saturn Encounter

Ten BRT's

M53580-1	8/31/79
M53582-3	9/1/79
M53584-5	9/2/79
M53586-7	9/3/79
M53588-9	9/4/79

Pioneer 10 Interplanetary

Three 24-hour Summary Tapes

M45905X	3/3/72 - 12/3/73
M45906X	12/4/73 - 6/29/76
M45910X	7/1/76 - 5/30/77

Pioneer 11 Interplanetary

Two 24-hour Summary Tapes

M55905X	4/16/73 - 12/2/74
M55906X	12/3/74 - 5/31/77

1.3 LIST OF PUBLICATIONS

Axford, W. I., W. Fillius, L. J. Gleeson, W.-H. Ip, and A. Mogro-Campero, "Measurements of Cosmic Ray Anisotropies From Pioneers 10 and 11," Proceedings 14th ICRC, Munich, pp 1519-1524, 1975.

Axford, W. I., W. Fillius, L. J. Gleeson, and W.-H. Ip, "Cosmic-Ray Gradients from Pioneer-10 and Pioneer-11," Astrophysical Journal, 210, 603-613, Dec. 1, 1976.

Fillius, R. W., and C. E. McIlwain, "Radiation Belts of Jupiter," Science, 183, 314, January 25, 1974.

Fillius, R. W., and C. E. McIlwain, "Measurements of the Jovian Radiation Belts," J. Geophys. Res., 79, 3589-3599, September 1, 1974.

Fillius, R. W., C. E. McIlwain, and A. Mogro-Campero, "Radiation Belts of Jupiter: A Second Look," Science, 188, 465-467, 2 May, 1975.

Fillius, W., "The Trapped Radiation Belts of Jupiter," in Jupiter, T. Gehrels, ed., Univ. Arizona Press, Tucson, 896-927, 1976.

Fillius, W., C. McIlwain, A. Mogro-Campero, and G. Steinberg, "Evidence That Pitch Angle Scattering is an Important Loss Mechanism for Energetic Electrons in the Inner Radiation Belt of Jupiter," Geophys. Res. Lett., 3, 33-36, January, 1976.

Fillius, W., W.-H. Ip, and P. Knickerbocker, "Interplanetary Electrons: What is the Strength of the Jupiter Source?" Proceedings of the 15th International Cosmic Ray Conference, Plovdiv, Bulgaria, 1977, Vol. 11, pp 334-339.

Fillius, W., and P. Knickerbocker, "The Phase of the Ten-Hour Modulation in the Jovian Magnetosphere (Pioneers 10 and 11)," J. Geophys. Res., 84, 5763-5772, Oct. 1, 1979.

Fillius, W., W.-H. Ip, and C. E. McIlwain, "Trapped Radiation Belts of Saturn: First Look," Science, 207, 425-431, 25 January, 1980.

Fillius, W., and C. McIlwain, "Very Energetic Protons in Saturn's Radiation Belt," J. Geophys. Res., 85, 5803-5811, Nov. 1, 1980.

Fillius, W., M. F. Thomsen, J. A. Van Allen, W.-H. Ip, M. Acuna, and N. F. Ness, "Trapped Radiation Absorption at the Ring of Jupiter," submitted to Icarus, March, 1981.

Ip, W.-H., W. Fillius, A. Mogro-Campero, L. J. Gleeson, and W. I. Axford, "Quiet Time Interplanetary Cosmic Ray Anisotropies Observed From Pioneer 10 and 11," J. Geophys. Res., 83, 1633-1640, April 1, 1978.

McIlwain, C. E., and R. W. Fillius, "Differential Spectra and Phase Space Densities of Trapped Electrons at Jupiter," J. Geophys. Res., 80, 1341-1345, April, 1975.

Mogro-Campero, A., R. W. Fillius, and C. E. McIlwain, "Electrons and Protons in Jupiter's Radiation Belts," Space Research XV, 521-528, Akademie-Verlag, Berlin, 1975.

Mogro-Campero, A., "Absorption of Radiation Belt Particles by the Inner Satellites of Jupiter," in Jupiter, T. Gehrels, ed., Univ. Arizona Press, Tucson, 1190-1214, 1976.

Mogro-Campero, A., and W. Fillius, "The Absorption of Trapped Particles by the Inner Satellites of Jupiter and the Radial Diffusion Coefficient of Particle Transport," J. Geophys. Res., 81, 1289-1295, March, 1976.

Smith, E. J., R. W. Fillius, and J. H. Wolfe, "Compression of Jupiter's Magnetosphere by the Solar Wind," J. Geophys. Res., 83, 4733-4742, Oct. 1, 1978.

Smith, Z. K., M. Dryer, R. W. Fillius, E. J. Smith, and J. H. Wolfe, "Compression of Jupiter's Magnetosphere by the Solar Wind: Re-examination Via MHD Simulation of Evolving Corotating Interaction Regions," J. G. R., 86, 6773-6780, August 1, 1981.

PART TWO

PUBLICATIONS

JUPITER ENCOUNTER

Radiation Belts of Jupiter

Abstract. Pioneer 10 counted relativistic electrons throughout the magnetosphere of Jupiter, with the greatest fluxes being inside 20 Jupiter radii. The peak flux of electrons with energy greater than 50 million electron volts was 1.3 × 10⁷ per square centimeter per second at the innermost penetration of the radiation belts.

Charged particle instruments aboard the National Aeronautics and Space Administration's Pioneer 10 spacecraft made the first in situ measurements ever of the Van Allen radiation belts of Jupiter during a 2-week passage through Jupiter's magnetosphere in early December 1973. Jupiter is the only planet besides the earth known to have a radiation belt, and the new measurements show that many features of it are in unexpected contrast to those at the earth. The onboard trapped radiation detector of the University of California, San Diego (UCSD), identified electrons with energies from 100 kev to 50 Mev and protons with energies greater than 70 Mev and measured fluxes, energy spectra, and angular distributions through the flyby.

Two different trapping regions emerge from the data. The outer region has been dubbed the magnetodisk and extends from about 20 Jupiter radii (R_J) outward. Energetic electrons are concentrated in a disk close to the tilted magnetic equator and wobble up and down past the spacecraft at the planetary rotation rate, modulating the observed flux. In addition, the electrons exhibit rapid time variations and erratic directionality with little radial dependence in flux or energy. The intensities are abruptly lower outside the magnetopause, but a trickle of relativistic electrons extend outside the bow shock (*1*, *2*) to 120 R_J. These and other particles in the magnetodisk are most easily interpreted as particles escaping outward, either torn out of the inner region by violent plasma storms or accelerated in the magnetodisk by electric potentials such as those associated with the rapid planetary rotation. This region is aptly compared with the earth's magnetic tail.

Inside 20 R_J the radiation belts assume a more ordered character, whose most dramatic feature is a steep radial intensity gradient [$\exp(-R/1.2\,R_J)$ for electrons with energy greater than 50 Mev] giving an increase in intensity of three or four orders of magnitude in all detectors. The electron energy spectrum also becomes harder closer in, the relativistic component increasing most dramatically, and the nonrelativistic component peaking and actually decreasing below 10 R_J. Just outside the magnetic shell of Europa, fluxes of electrons were $j = 3 \times 10^7$ cm^{-2} sec^{-1} ster^{-1} with energy above 0.1 Mev, and $J_0 = 1.2 \times 10^4$ cm^{-2} sec^{-1} with energy above 40 Mev. At 3.2 R_J the flux of electrons above 50 Mev was 1.3×10^7 cm^{-2} sec^{-1}, but electrons between 0.1 and 2 Mev were less than 2×10^7 cm^{-2} sec^{-1} ster^{-1}.

The spatial distribution of omnidirectional electrons with energy greater than 50 Mev is shown in Fig. 1. The counter is a small solid state detector buried in a thick omnidirectional shield. The effective area rises from 4×10^{-3} cm² at 27 Mev to 4×10^{-2} cm² above 70 Mev. Because the efficiency varies with energy, so does the conversion from count rate to flux. The fluxes in Fig. 1 were obtained by multiplying count rate by 30 cm^{-2}, but the characteristic electron energy, and thus the flux conversion factor, varies somewhat because of the hardening electron spectrum. The spacecraft trajectory, projected onto the magnetic meridian plane, is shown by the dashed line. The location where the count rate equals each contour value is marked by a circle, and each circle is reflected by symmetry through the equator. Whereas a poor magnetic field model would result in misalignment of primary and reflected circles, the present model is seen to be satisfactory out to 10 R_J.

Figure 2 shows count rates in the inner region for four data channels. Channels C2 and M1 represent rela-

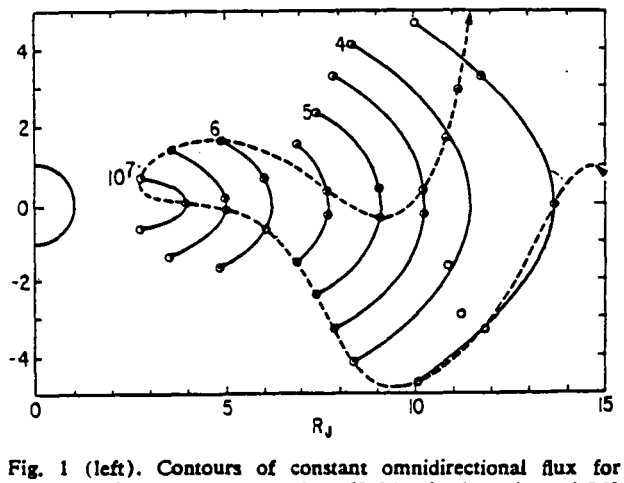

Fig. 1 (left). Contours of constant omnidirectional flux for electrons with energy greater than 50 Mev in data channel M1 (electrons per square centimeter per second). The figure represents a magnetic meridian plane according to the preliminary magnetic field model of Smith *et al.* (*2*).

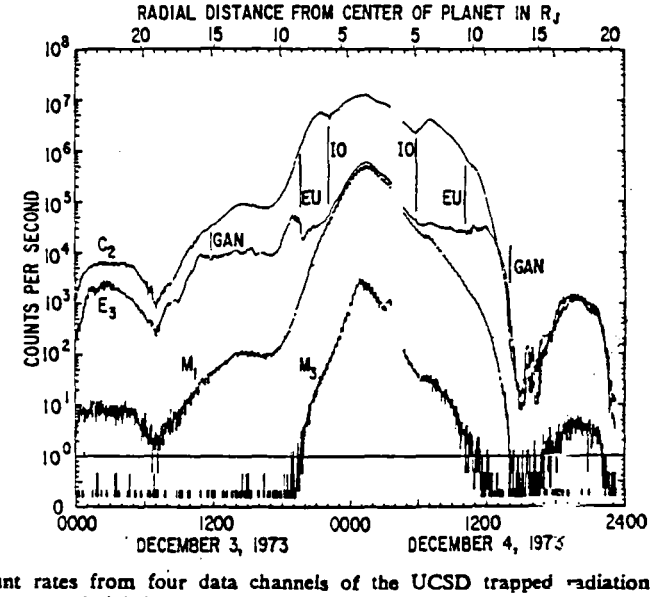

Fig. 2 (right). Count rates from four data channels of the UCSD trapped radiation detector. Channels C2 and M1 count relativistic electrons, E3 counts relativistic and nonrelativistic electrons, and M3 counts protons with a background of electrons. Abbreviations: *Gan*, Ganymede; *Eu*, Europa.

tivistic electrons with energy > 20 Mev and > 50 Mev. Channel E3 is the rate from a solid state detector identical to M1 except that a bent aperture in the shield permits direct access of particles that scatter by 45°. Thus E3 is susceptible to the same penetrating electrons that trigger M1 plus nonpenetrating electrons that scatter through the aperture and trigger the 0.4-Mev discriminator. Comparing E3 with C2 and M1 demonstrates the hardening of the electron spectrum toward periapsis, and differencing E3 with M1 demonstrates the loss of the nonpenetrating component below 10 R_J.

Several of the Galilean satellites are immersed in the radiation belts, and there is clear evidence that at least two of them, Io and Europa, influence the trapped particle fluxes. Marks are shown on Fig. 2 where the spacecraft crossed the dipole model magnetic shells containing Io, Europa, and Ganymede. There are prominent dips in the 20-Mev electrons at the Io shell and small fluctuations in the 0.4-Mev electrons. On the other hand, at Europa there are prominent variations in the 0.4-Mev electrons and only small effects in the 20-Mev electrons. An effect at Ganymede is questionable.

Channel M3 is a high energy discriminator on the omnidirectionally shielded solid state detector. Set high enough to have low ($< 2 \times 10^{-3}$) efficiency for electrons, this discriminator is efficient for protons between 70 and 150 Mev. The M3 response seen in Fig. 2 is caused partly by single electrons at low efficiency, partly by double coincidence of electrons, and partly by protons. When the appropriate linear and quadratic terms in M1 that represent electron background are subtracted from M3, one is left with two proton peaks, one at 0100, one at 0300, with a relative minimum between them. The second peak is clearly visible in the figure. These peaks are at the inbound and outbound crossings of the $L = 3.6$ shell, and the maximum proton intensity is $J_0 = 2.5 \times 10^4$ cm^{-2} sec^{-1}. These peaks represent the only proton fluxes visible to our counters during the flyby.

Particle identification features in the instrument design were successful in separating electrons from protons, and we name the particle species with confidence. Specifically, one of our detectors was a Cerenkov counter sensitive only to particles with velocity greater than 0.75c (for example, C2 in Fig. 2). There is evidence against significant proton fluxes above this energy (450 Mev) and so the counts are known to be electrons. Comparisons between the Cerenkov counter and channel M1 are in agreement, and because M3 found so few protons, M1 counted essentially all electrons.

Flux values and energy ranges are preliminary as we have not yet made proper integrations of the particle spectra over the detector responses. Therefore these numbers should be given an uncertainty of about 50 percent.

More serious data misinterpretation could arise from spacecraft charging. The expected average photoelectron flux is similar to the measured fluxes of energetic electrons inside 10 R_J. This means that, unless there is an unmeasured cold plasma component, the spacecraft may need to assume a large negative potential in order to maintain zero net current (*3*). Until it can be shown that Pioneer 10 was not driven to megavolt potentials, the present measurements cannot be safely assumed to correspond to the ambient Jovian particle fluxes. The relative absence of 0.1- to 2-Mev electrons is not firm evidence for spacecraft charging, as this would be expected for a relativistic Maxwellian distribution with a temperature over 5 Mev.

In conclusion, we note that the presence of very energetic electrons in the magnetodisk cannot be easily explained in terms of solar wind injection and convective acceleration. As an alternative, we would like to point out that interactions with the nonrotating solar wind may cause a differential rotation between the planet and the outer magnetodisk which in turn can lead to large electric fields parallel to the magnetic field lines. The expected sign and magnitude of these electric fields is such that photoelectrons in the Jovian atmosphere could be accelerated outward to very high energies. Presumably the angular distributions measured by the various detectors on Pioneer 10 will provide clues to the true nature of the injection and acceleration processes.

R. WALKER FILLIUS
CARL E. MCILWAIN
University of California, San Diego, La Jolla 92037

References and Notes

1. J. H. Wolfe, H. R. Collard, J. D. Mihalov, D. S. Intriligator, *Science* 183, 303 (1974).
2. E. J. Smith, L. Davis, Jr., D. E. Jones, D. S. Colburn, P. J. Coleman, P. Dyal, C. P. Sonett, *ibid.*, p. 305.
3. S. E. DeForest, *J. Geophys. Res.* 77, 651 (1972).
4. We thank G. E. Peters, E. W. Strain, and G. W. Schmidt of the University of California, San Diego, for their help in developing the instrumentation and the data reduction programs, and we thank C. F. Hall and D. Porter of the NASA/Ames Research Center for their support. This work was supported by NASA contracts NAS 2-5602 and NAS 2-6552, and by NASA grant NGL 05-005-007.

21 December 1973

VOL. 79, NO. 25 JOURNAL OF GEOPHYSICAL RESEARCH SEPTEMBER 1, 1974

Measurements of the Jovian Radiation Belts

R. W. FILLIUS AND C. E. MCILWAIN

Physics Department, University of California at San Diego, La Jolla, California 92037

The University of California at San Diego trapped radiation detector measured proton and electron fluxes, angular distributions, and energy spectra throughout the Pioneer 10 flyby of Jupiter last December. Here the instrumentation and calibrations are described, and good values for particle fluxes in the inner and outer regions are presented. The major features of the Jovian radiation belts are described, with preliminary discussions of their meanings.

The existence of Van Allen radiation belts at Jupiter has been known for almost as long as the existence of Van Allen radiation belts at earth [*Van Allen*, 1958; *Drake and Hvatum*, 1959]. However, whereas rockets, satellites, and spacecraft have had access to the earth's radiation belts for the last 15 years, it was only last December that a spacecraft, Pioneer 10, first probed the immediate vicinity of Jupiter [*Hall*, 1974]. On board this spacecraft were several instruments designed to make direct measurements of the Van Allen belts. Preliminary notes on experiments were written 2 weeks after encounter and appeared together in the January 25, 1974, issue of *Science* [*Van Allen et al.*, 1974; *Simpson et al.*, 1974; *Trainor et al.*, 1974; *Fillius and McIlwain*, 1974]. The present paper gives a more thorough account of results from one of these experiments, the University of California at San Diego (UCSD) trapped radiation detector.

INSTRUMENTATION

Constraints and objectives. It is obvious that one hyperbolic cut through Jupiter's magnetosphere cannot bring us the same level of knowledge that we enjoy of the earth's environment. Also, the instruments on Pioneer 10 cannot approach the sophistication of those flown today in the neighborhood of earth. The constraints on weight, power, and telemetry forced too much simplification on our design, and the range of environmental unknowns was too wide. We committed our instrument to obtain just the basic features of the radiation belts with minimum ambiguity as to interpretation of the data. Specifically, our instrument design objectives were to distinguish trapped protons and electrons, to measure absolute intensities within known energy ranges, to obtain several points on energy spectra for these particles, to gain information on angular distributions and spatial extent, and to probe the total corpuscular energy flux.

Sensors. The UCSD trapped radiation detector on Pioneer 10 includes five different sensors. Three are operated in a pulse-counting mode, and two are read out through an electrometer. We report here data from the pulse sensors because a malfunction that occurred earlier in the flight makes the electrometer readings difficult to interpret. The three sensors that operated in the pulse mode are detector C (a Cerenkov counter sensitive to particles with $\beta > 0.75$), detector E (a solid state detector that can be reached by soft electrons that scatter through a crooked aperture), and detector M (an identical solid state detector that can be reached only by particles that penetrate 1 cm of inert shielding). Table 1 lists the principal characteristics of these sensors and their data channels.

Electronics and rate limitations. Connected to each sensor is a preamplifier, a delay line pulse shaper, and one or two voltage amplifiers. After this the signals go to a linear gate that commutates one of the three to a shared amplifier string. The amplifiers drive three integral pulse height discriminators that are set to the ratios 1:2.12:4.5, and the outputs of the discriminators go to a commutator that gates one of them to a 23-bit accumulator. A particular channel is determined by the linear gate, which chooses the sensor, and by the commutator, which selects the pulse height discriminator: e.g., E3, M1, etc.

At high counting rates, two characteristic times associated with the electronics become important: the width of the analog pulse and the dead time of the discriminator. The pulse width determines the probability that two pulses, each of which is too small to trigger the discriminator separately, will add in height and produce a spurious event. The pulse width is set to 90 ns by the delay line pulse shaper, and the two-pulse resolving time is less than this value because the leading and trailing edges are rounded by the finite frequency response of the circuitry. The discriminator dead time limits the maximum rate of the counters and determines the relationship between the true input rate and the observed counting rate near the limit. The observed rate approaches 1.5 MHz asymptotically (Figure 1). By using an empirical formula, one can obtain true rates accurately up to 10 MHz and approximately beyond that. Both the discriminator dead time and the analog pulse width were made as short as they could be made within the power limitations of the spacecraft.

Commutator. During encounter with Jupiter the accumulation time was 1.5 s per reading, and the commutator took seven or eight consecutive readings from each directional sensor (C and E) so as to sample for approximately one roll period. (The actual roll period was 12.62 s.) Detector M, which was not designed for directionality, was sampled at isolated times. The period for the commutator to cycle through all the channels was 108 s.

Particle selectivity. Particle identification is accomplished by sensor design with detectors C and E and by pulse height discrimination with detector M. Detectors M and E are identical surface barrier detectors 1 mm thick by 3 mm in diameter. Detector M is buried inside heavy shielding with a minimum thickness of 1 cm. When detector M is gated on, the lowest discriminator is at the energy left by a minimum-ionizing particle (Table 1); thus channel M1 counts any particle that can get through the omnidirectional shielding. Channel M3, the highest discriminator, requires a highly ionizing particle. Therefore it rejects electrons while it counts protons that range in energy from the shielding cutoff at 80 MeV up to several hundred MeV, where the specific ionization falls below threshold. Channel M2, which is at half the height of M3, has

TABLE 1. Characteristics of the UCSD Pioneer 10 Trapped Radiation Detector at Jupiter Encounter in December 1973

Channel	Discrimination Level	Particle Sensitivity	Geometric Factor
		Cerenkov Counter C	
C1	31 photoelectrons	>6-MeV electrons	11.5 cm^2 sr
C2	65 photoelectrons	>9-MeV electrons	4.5 cm^2 sr
C3	135 photoelectrons	>13-MeV electrons	0.5 cm^2 sr
		Electron Scatter Counter E	
E1	0.089 MeV	>0.16-MeV electrons	1.3×10^{-2} cm^2 sr
E2	0.19 MeV	>0.255-MeV electrons	1.04×10^{-2} cm^2 sr
E3	0.40 MeV	>0.460-MeV electrons	5.7×10^{-3} cm^2 sr
		Minimum Ionizing Particle Counter M	
M1	0.40 MeV	>35-MeV electrons	0.038 cm^2
M2	0.85 MeV	Background	
M3	1.77 MeV	>80-MeV protons	

been useful in estimating the rate at which twofold coincidences of smaller pulses pile up to M3 and also in monitoring the small ($\sim 10^{-3}$) efficiency of M3 for single electrons.

Detector E is surrounded by similar shielding except that a crooked aperture in the shield permits low-energy electrons to scatter in to the detector (Figure 2). The aperture was carefully designed so that protons, which travel in straight paths because of their high momentum, cannot reach the detector except by penetrating as much shielding as surrounds detector M. Because of the electrons' propensity to scatter, this design is efficient for electrons and provides a high ratio of electron to proton response. During encounter, the proton contribution to the E detector count rates was negligible.

The Cerenkov counter uses a water-methanol radiator with an index of refraction equal to 1.33, so that Cerenkov light is generated by particles whose velocity is greater than 1/1.33 times the speed of light. The liquid is enclosed in a fused silica bottle 14 mm in diameter and 5½ cm long, and the pulse height discriminators require a path length of more than 1 cm for a particle to emit enough light to be counted. This range requirement and the housing thickness raise the threshold energy for electrons to 6 MeV. The discrimination levels are also high enough that the response is not spoiled by other light sources, such as scintillation and unwanted Cerenkov emission in the phototube. As protons below 485 MeV do not have the necessary velocity to emit Cerenkov light, the detector is insensitive to them. This selectivity was sufficient during encounter to assure that detector C counted electrons only.

Directionality. The directional acceptance lobes of the Cerenkov counter are determined by the geometric cross section of the radiator, the path length required by the pulse height discriminators, the forward emission cone of the Cerenkov light, and the selective collection efficiency of the optics. One end of the radiator is coupled directly to the photomultiplier face plate, and internal reflection in the radiator aids the collection of light emitted toward the phototube. Light that is emitted away from the phototube or does not meet the internal reflection condition is absorbed by blackened surfaces on the housing or the front end of the radiator. The resulting response is unidirectional, with a fore to aft efficiency ratio of 100:1. For 23-MeV electrons the acceptance lobes have a full width at half maximum of 120° for channel C1, 90° for channel C2, and 65° for channel C3. These lobes become narrower for higher energies and broader for lower energies.

The angular response of detector E is determined by the shielding. It is nearly conical, with a full width of 55°, and is the same for all channels.

All directional sensors are mounted to face perpendicular to the spin axis, and their look directions sweep around the spacecraft equatorial plane once per revolution. During each reading the spacecraft rotated through 43°, so that the net angular resolution is the convolution of the detector's angular response with the sweep angle.

Energy response. Figure 3 shows the experimentally determined responses of detectors C and M for monoenergetic electrons. Given any spectrum of particles, one can integrate it over these delta function responses to get the spectral response of the detectors. In practice, of course, we are not given the

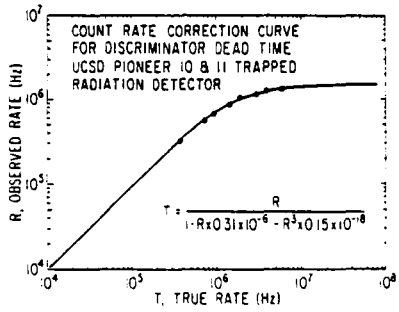

Fig. 1. Relationship between true and observed counting rates.

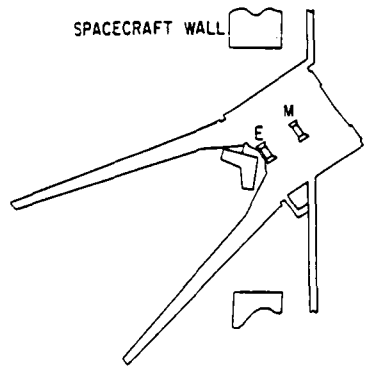

Fig. 2. Cross section of the aperture and shielding for detectors E and M. The spacecraft spin axis is perpendicular to the page.

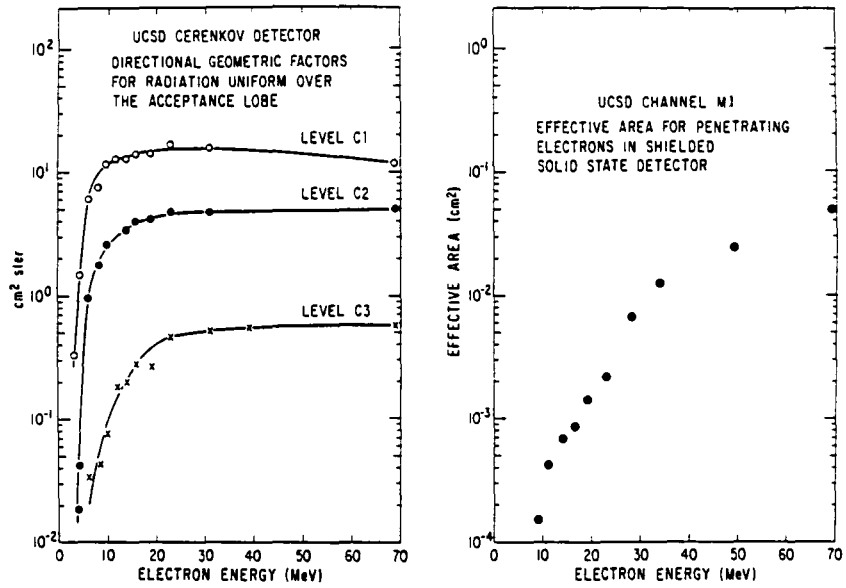

Fig. 3. Experimentally determined responses of detectors C and M for monoenergetic electrons.

particle spectrum, but we do have the spectral response as a count rate. The particle spectrum is the solution of an integral equation

$$R = \int_{4\pi} \int_0^\infty A_{eff}(E, \Omega) f(E)\, dE\, d\Omega$$

where

R spectral response;
$f(E)$ particle spectrum;
$A_{eff}(E, \Omega)$ delta function response.

As we cannot solve this integral equation in a general way, what we do is to assume a spectral form, perform the integration, and determine a coefficient that relates the integral to the flux above a threshold energy. Figure 4 shows the results of such an integration when the energy spectrum is assumed to be a power law, and Figure 5 shows the same results for detector E. What has been plotted is the ratio of the spectral response to the incident number flux above any named threshold energy. This presentation is copied from a method of Van Allen's that he calls a 'bow tie diagram.' The virtue of the diagram is that if a family of lines intersects at or near a point (the knot of the bow tie), this point marks a useful conversion constant between spectral response and particle flux, whose generality extends to spectra within the family. If one has a detector whose response is an ideal step function at some threshold energy, the knot of its bow tie will shrink at that energy to a point that is valid for all spectra.

The geometric factors in Table 1 were obtained by this technique with the assumption of power law spectra. These conversion constants are valid for a wide range of spectra but not for all. In the Jovian radiation belts some spectra were encountered that need special treatment.

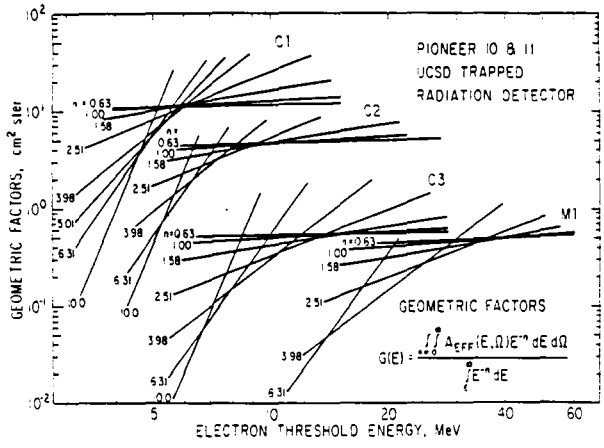

Fig. 4. Bow tie diagrams for the response of detectors C and M to a power law spectrum of electrons. The geometric factor is a conversion coefficient between detector response and particle flux above some threshold energy.

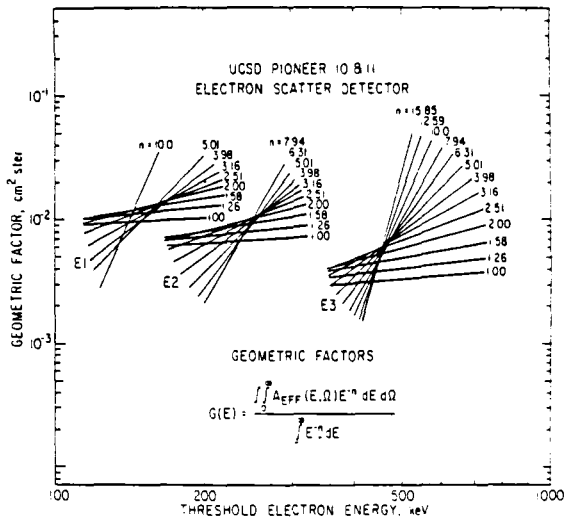

Fig. 5. Bow tie diagrams for the response of detector E to a power law spectrum of electrons. The geometric factor is a conversion coefficient between detector response and particle flux above some threshold energy.

TABLE 2. Design Factors Affecting the Measurement of Nonrelativistic Electron Fluxes With the UCSD Trapped Radiation Detector on Pioneer 10 and 11

Factor	Soft Electrons	Hard Electrons	Ratio of Hard to Soft Electrons
Solid angle	0.72 sr	4π sr	17.5:1
Effective detective area			
E1	1.8 mm^2	8.5 mm^2	4.7:1
E2	1.45 mm^2	6.8 mm^2	4.7:1
E3	0.8 mm^2	3.8 mm^2	4.7:1
Combined solid angle * area			
E1	1.3 mm^2 sr	105. mm^2 sr	85:1
E2	1.04 mm^2 sr	85. mm^2 sr	85:1
E3	0.57 mm^2 sr	48. mm^2 sr	85:1
Energy threshold			
E1	0.16 MeV	35 MeV	1:220
E2	0.255 MeV	35 MeV	1:137
E3	0.46 MeV	35 MeV	1:76
Ratio of corrected count rate to observed count rate at peak			
E1	1.63:1		
E2	1.48:1		
E3	1.22:1		
M1	1.15:1		

Penetrating particle background. Measurement of soft electron fluxes with detector E is straightforward only if the number of low-energy electrons coming through the aperture is much greater than the number of high-energy particles coming through the omnidirectional shield. This condition was not fulfilled inside 6 R_J at encounter, although the foreground to background ratio was deliberately optimized by the design. We review the design now in order to demonstrate that improvement on our results will require a major effort on some new spacecraft. The design factors discussed here are summarized in Table 2.

The first problem is that the high-energy particles come from all directions, whereas the low-energy electrons must come through the entrance aperture. The disadvantage factor is the ratio of solid angles available to the two classes of particles. We minimized this factor by opening the aperture as far as possible without sacrificing directionality. The solid angle for the foreground is 0.72 sr, and that for the background is 4π sr, giving a disadvantage of 17.5:1.

The next problem is that for low-energy electrons the scatter requirement reduces the effective area of the detector below the real area. The scatter efficiency is 25% for channel E1, 20% for E2, and 11% for E3. These values are high when one considers that the baffles allow no rectilinear paths to the detector. Comparing the effective areas for soft and hard electrons, one has a 4.7:1 disadvantage in all three channels.

Combining the number for solid angle and geometric factor, one computes a net disadvantage of 85:1. This ratio is caused by geometric considerations alone and cannot be improved upon substantially.

To offset this disadvantage, one relies on having a much larger flux of low-energy electrons than of high-energy electrons. The critical design factor is the ratio of the energy thresholds. When the omnidirectional threshold is at 35 MeV, these ratios are 1:220, 137, and 76 for channels E1, E2, and E3, respectively. Although these ratios could be improved by adding shielding, one obtains diminishing returns and drastic increases in weight beyond the amount used here. In our design the break-even point in the foreground and background rates occurs for an integral spectrum of about E^{-1}.

As is shown in Table 1, the discrimination level for channel M1 is at the same particle energy as that for channel E3. Thus

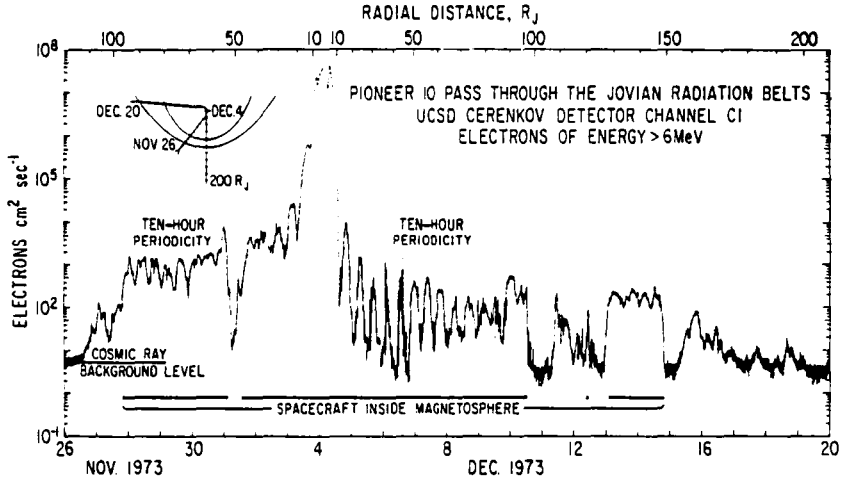

Fig. 6. Profile of Jupiter's radiation belts from channel C1, November 26 to December 20. The position of the spacecraft inside or outside the magnetosphere is taken from *Wolfe et al.* [1974*b*].

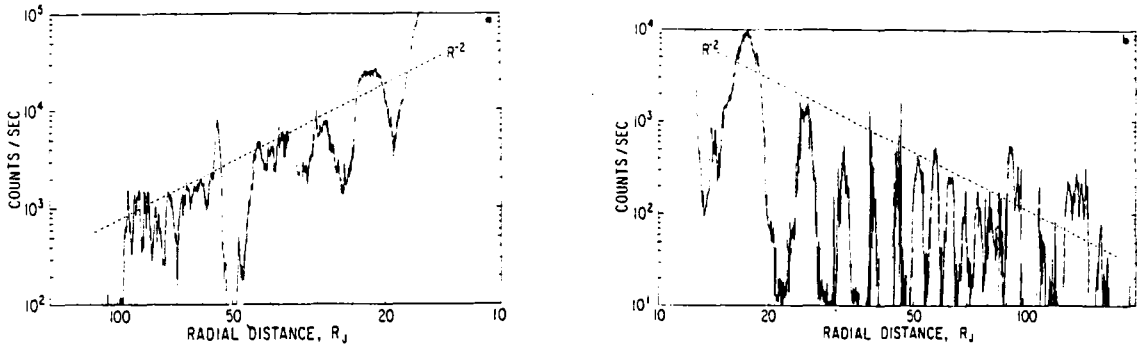

Fig. 7. Radial dependence of relativistic electrons in the magnetodisk. (*a*) Electrons of >6 MeV (channel C1), inbound pass. (*b*) Electrons of <6 MeV (channel C1), outbound pass.

M1 serves as a background monitor for E3, and by calibrating the sensitivities of E2 and E1 to penetrating particles, one can use it with these lower channels as well. Subtracting the omnidirectional background of course extends the usefulness of the electron scatter detector to harder spectra. In performing this subtraction with the UCSD encounter data we have no difficulty with counting statistics or with dead-time corrections (Table 2 lists the maximum correction factors). The primary uncertainty is caused by the inexact duplication of shielding between detectors. Near periapsis the M1 count rate was 80% of the E3 rate, and there is good evidence that a substantial part of the difference is caused by more shielding at M1, leaving less than 10% that might be attributed to low-energy electrons. The integral power law to cause this little difference is $E^{-1/2}$.

Clearly, our instrument is being pushed to its limits. After this much subtraction the uncertainties in the low-energy fluxes are quite high. What we have tried to show here is that this problem was foreseen, and improvement will be hard to come by.

Radiation damage. The photomultiplier tube in the Cerenkov detector experienced a gain loss of about 15%, presumably caused by radiation damage, and this loss caused the detector C count rates after periapsis to be less than they were before periapsis. Fluxes and count rates quoted in this paper are not corrected for this difference, but a typical correction would be a factor of 2.

Outer Region, or Magnetodisk

Magnetodisk. It is quite natural to divide the Jovian magnetosphere into two regions. These regions can be distinguished easily in a time profile of the entire magnetosphere (Figure 6). The most striking feature is the monumental spike inside 20 R_J that rises 3 orders of magnitude above the rest of the data. This is the inner region, or core, to be discussed separately below.

Many features of the outer region are visible in Figure 6. There is not a strong radial variation, but the 10-hour periodicity is attributable to a strong latitude dependence. The magnetopause crossings identified by *Wolfe et al.* [1974*b*] fall on sharp boundaries for energetic electrons, but the shock crossings have little effect. On both the inbound and the outbound legs the magnetopause was encountered more than once. Upon comparing different energy channels, one finds a hardening of the electron energy spectrum at the peaks of the 10-hour cycle and no velocity dispersion in the abrupt fine structure.

The radial variation follows roughly a $1/R^2$ envelope for relativistic electrons (Figure 7) and a steeper $1/R^4$ envelope for 260- to 460-keV electrons (Figure 8). Lack of dispersion seems to be a consistent characteristic of the sharp features. The 10-hour modulation is explained by the concentration of particles near a tilted magnetic equator that wobbles up and down as the planet rotates. The sharpness of this concentration is evidence that the field lines are stretched out at the equator, forming a flat disk more or less symmetrical around the planet [*Van Allen*, 1974]. Evidence that this magnetodisk is filled with a high-beta plasma has been given by *Wolfe et al.* [1974*a*] and *Smith et al.* [1974*a*].

Corotation: microscopic features. The 10-hour periodicity suggests a corotating pattern in the particle distribution. To investigate this pattern, we have plotted count rates versus system III longitude (cf. *Mead* [1974] for explanation of longitude systems at Jupiter) for 17 planetary rotations on the inbound leg (Figure 9, left) and 15 rotations on the outbound leg (Figure 9, right).

On a microscopic scale, features generally do not persist from one rotation to the next. This observation seems to support the hypothesis that the acceleration is local and the features appear and disappear in time like bubbles in a boiling cauldron of unstable plasma.

However, there are exceptions. A striking example occurs on rotations *e* and *f* outbound (Figure 9, right) near 20° longitude. These dropouts are preceded by spikes and have a depth of 2 orders of magnitude. Since they are the biggest such events in all 32 rotations, they are probably the same feature persisting from one rotation to the next. It is noteworthy that there is no dispersion between 0.16 and 13 MeV on the edges of the impulses.

There is also a suggestive correspondence between features on outbound passes *l* and *m* from 0° to 270° longitude. The likeness is not sharp, but the features look as if they were imbedded in an elastic medium and would match up if the left edge of pass *l* were stretched 45° or so. Using the freedom to stretch the medium and studying the graphs intently, one can find many more correspondences (some of them surely imaginary). These correspondences suggest that the accelerator is sometimes persistent and extensive in space, perhaps on a time scale of hours and a spatial scale of 5 or 10 R_J, and tends to follow the planetary rotation.

Corotation: the fundamental periodicity. The 10-hour modulation in Figure 6 shows up in Figure 9 as the fundamental wave of 360° period. This finding is explained by the position of the tilted Jovimagnetic equator as it wobbles up and

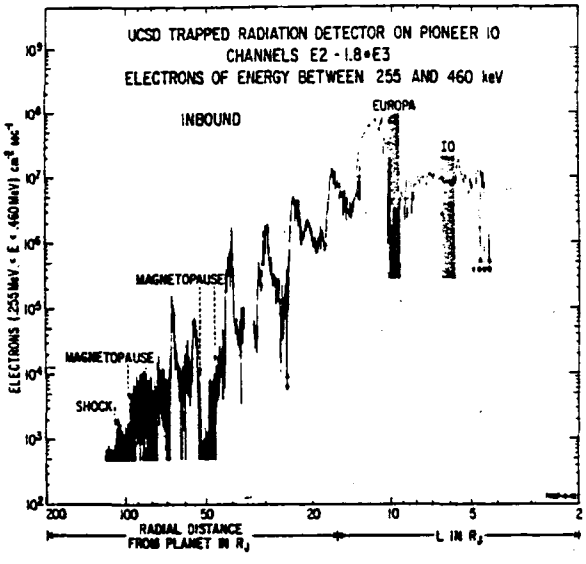

Fig. 8a. Inbound pass.

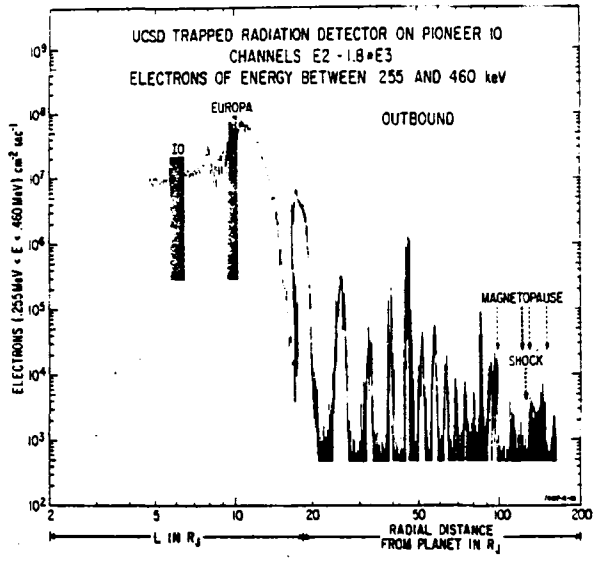

Fig. 8b. Outbound pass.

Fig. 8. Radial dependence of nonrelativistic electrons in the magnetosphere.

down at the planetary rotation rate toward and away from the spacecraft. On some rotations it appears that the spacecraft crosses the equator, producing a second harmonic in the modulation pattern. The swaybacked peaks prominent in inbound passes E, F, and G are easily interpreted as equator crossings, the dip near 120° being an excursion into the opposite hemisphere.

However, it is easily seen that the position of the equator is not constant. Evidently, space and/or time dependent external currents warp the magnetic equator. To pursue this, we sought to identify the magnetic phase of each rotation cycle. The most easily marked feature in Figure 9 is the minimum where the spacecraft reaches its highest latitude. This minimum is in the southern hemisphere inbound and in the northern hemisphere outbound. We placed the identification letters in Figure 9 at the longitude of the minimum after doing our best to match the 360° cycles of neighboring curves. This is a subjective fit and arbitrary in many cases. Then we plotted the positions of these minimums in radial polar coordinates (Figure 10).

Comparison with the internal dipole field deduced by *Smith et al.* [1974*a*] reveals that inside 20 R_J the equator is found where it was expected, but further out one finds deviations of a suggestive nature. On the outbound pass there is a clear tendency for the minimums to lag their expected positions, and, the planetary rotation being counterclockwise, the lag is in the 'garden hose' direction. The amount of lag is moderate out to 70 R_J but then jumps by 90°. On the inbound pass there is a different trend with conflicting interpretations. Beyond 50 R_J there is a phase lead of 90° (or a lag of 270°); inside 25 R_J there is no phase shift, and the transition from one to the other is ambiguous.

Confusing the transition is a dropout of energetic particle fluxes visible in Figure 6 on December 1. Several interpretations of the phase crossover are possible. One is that the phase lead decreased of its own accord after pass K and the dropout in pass L is not related but happened to arrive at such a time as to screen the transition. A contrasting interpretation is that the dropout is an inner dynamic feature of the magnetosphere, marking the boundary between regions of one phase and those of the other. A third interpretation is that the dropout was externally applied and disturbed the magnetosphere enough for the phase to reset.

Dropout of December 1. The dropout of December 1 corresponded to the expected arrival of a high-velocity plasma stream in the solar wind and returned the plasma at the spacecraft to flow conditions characteristic of the magnetosheath [*Wolfe et al.*, 1974*a*]. These observations led to the conclusion that the solar wind compressed the magnetosphere, pushing the magnetopause in past the spacecraft. Supporting this hypothesis are the observation that the last cycle of relativistic electron fluxes before the dropout was unexpectedly high (Figure 7*a*) and the fact that the particle fluxes returned to magnetosheath levels during the dropout. Other suggestions have been made that the magnetodisk was deflected up or down and that it tore off completely, centrifugal forces whirling it away into interplanetary space. These hypotheses all leave one with the distasteful coincidence that just when one is expecting (through hindsight) some change to straighten out the phase of the warped equator, a solar-induced event occurs that has the required outcome. Therefore until contrary proof is shown, one should also entertain the possibility that there is a cause-effect relationship between the dropout and the rectification of the equatorial warp.

Directional flux. For the most part the energetic electron fluxes in the outer magnetosphere are isotropic. However, this is not always the case. Figure 11 shows a field-aligned particle distribution that lasted several hours. The parallel to perpendicular ratio is an impressive 5:1 without deconvolution of the instrumental resolution.

One way to produce a stream of particles parallel to the magnetic field is by accelerating particles near the foot of the line of force in the ionosphere. No matter what pitch angle they started out with, they will be moving parallel near the equator because of the first adiabatic invariant. However, there is another possibility that seems likely in the dynamic inflated magnetosphere of Jupiter. If a current sheet or ring current increases with time, it will lower the value of $|B|$ on a line of force, distending the field. A particle distribution that started out isotropic at that position will be squeezed into two

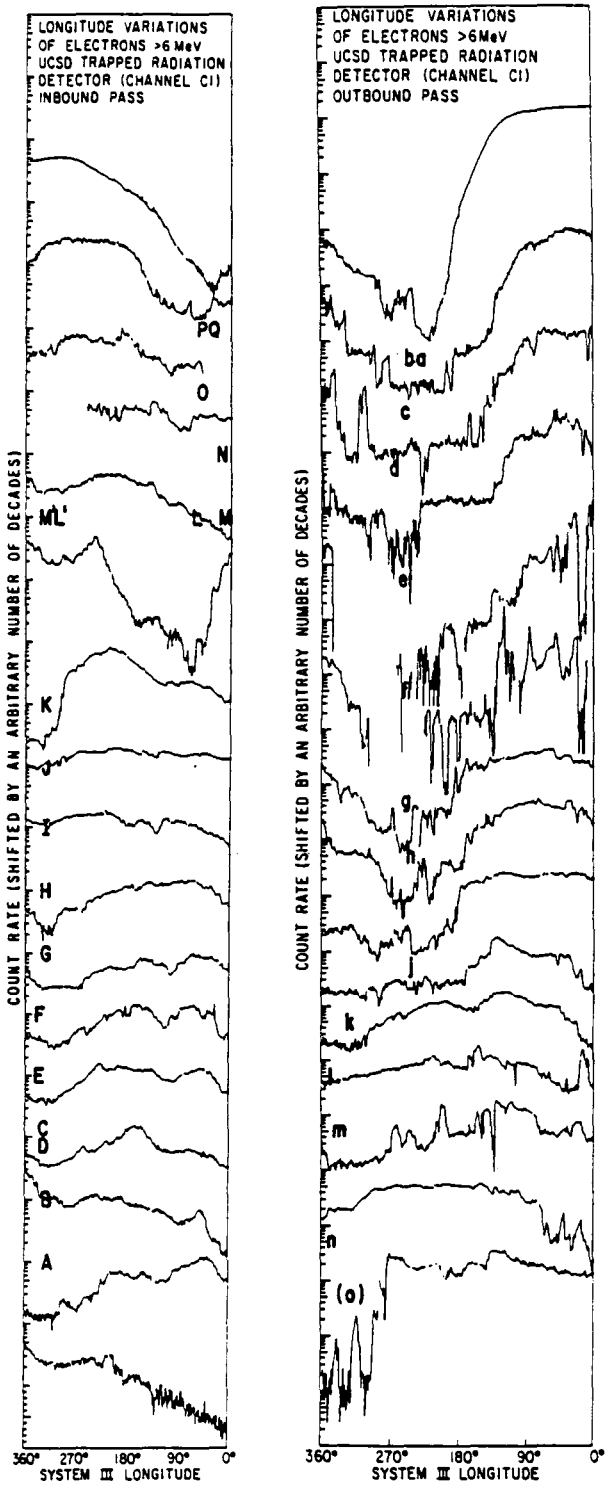

Fig. 9. Longitude variations of relativistic electrons. System III longitude is plotted from right to left, since it is a left-handed system, and so time progresses from right to left on each curve. The curves are in alphabetical order from one rotation to the next. (Left) Inbound pass: the alphabetical label for each rotation is placed at the ordinate corresponding to 10^3 counts s^{-1}. (Right) Outbound pass: the alphabetical label for each rotation is at 50 counts s^{-1}. The abscissa of the label indicates the system III longitude of the minimum selected by matching to the 360° cycles of the neighboring curves.

cones parallel to the field with no locally mirroring particles. Comparison with other detectors and with the magnetic field data may explain this particle distribution.

Stable Core of High-Intensity Radiation

Summary. Inside 20 R_J the radiation belts take on a different character. The scale increases (Figure 6), and the impulsive dynamism of the outer region gives way to a more stable diffusive equilibrium. The angular distributions tend to peak near 90°, although the amplitude of modulation is rarely as great as 30%. Comparing high- and low-latitude crossings of the same L shell gives pitch angle distributions that range from $\sin^4 \alpha$ near periapsis to no dependence farther out. The characteristic energy of the electron energy spectra increases inward, and the intensities of high-energy electrons rise dramatically; for example, electrons of energy >35 MeV have an e-folding length of 1.1 R_J. The nonrelativistic electron flux reaches a peak near 10 R_J but decreases closer in, much of the decrease clearly being caused by Europa. The satellites Io and Europa interact strongly with the trapped radiation, both moons acting as absorbers of high-energy radiation and Io apparently acting as a source of low-energy electrons. The only proton-sensitive channel in the UCSD package (M3 for protons of energy >80 MeV) responded only inside 9 R_J, where it detected a shell of protons peaked at L = 3.7 with lower intensities inward of the peak.

Nonrelativistic electrons. We have already discussed the design of detector E and the background problem from penetrating particles. In this section we present electron fluxes that result from performing careful but still tentative background subtractions.

One approach was seen in Figure 8. Using detector E alone, one can form a differential energy slice by subtracting the flux above one threshold from the flux above a lower threshold. Because the geometric factor of channel E2 is 1.8 times that for channel E3, for these channels this amounts to the difference between E2 and 1.8 • E3, normalized to the E2 geometric factor. The difference was computed once per commutation cycle by using average values for the count rates. The data inside 4 R_J were deleted from Figure 8 because the difference went negative, with E2 ≈ 1.7 • E3.

Although this approach is straightforward, it is imperfect in that the geometric factors were obtained for nonpenetrating particle spectra of a particular form. Near periapsis this spectral form is known to be invalid, and channel M1 gives us evidence that most of the counts are from penetrating particles.

To subtract penetrating particles, we turn to channel M1. However, before proceeding we must introduce some additional information that is important for determining the exact amount of subtraction needed. The responses of E and M to penetrating particles differ significantly from isotropy, producing directionally modulated counting rates. Out where the spectrum is soft the phase of the modulation for detector M is in quadrature with that for detector E. That is, detector E is peaked when the look direction is perpendicular to the line of force, as one expects for the pancake-shaped distribution characteristic of trapped particles; but detector M is peaked when the look direction is parallel to the line of force. It is inferred that the penetrating particle response is highest for particles going sideways (Figure 2), and this finding is attributed to a thin spot in the shielding plus higher efficiency because sideways particles have a longer path length in the detector.

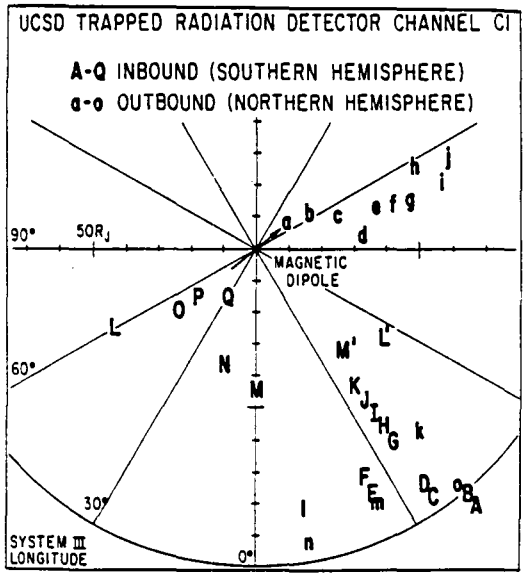

Fig. 10. Position of the high-latitude minimums of the relativistic electron flux ($E > 6$ MeV). The arrow marks the tilt direction of the internal dipole field. With no external currents the minimums should line up with the arrow.

Near periapsis, however, the modulation on all three E channels shifts so as to be in phase with M and peaked when one is looking along the line of force. This shift confirms the evidence from the average M1 rate that detector E is swamped by penetrating particles. Modulation in this phase is a signature of penetrating radiation and a useful criterion for determining the amount of subtraction needed to recover soft electron fluxes.

Such a criterion is necessary because the shielding around detectors E and M is not perfectly matched, and as can be seen from Figure 2, detector M gets more protection from the spacecraft. Thus it is not surprising that the naive difference, E3 − M1, exhibits modulation in the phase of penetrating radiation; i.e., it does not remove all of the background. The minimum subtraction that yields a difference peaked perpendicular to the line of force is E3 − 1.12 • M1. Each term of this expression and the difference itself are exhibited in Figure 12, and subtractions for all three E channels are shown in Figure 13. (Times given are spacecraft time, about 45 min earlier than ground-received times.)

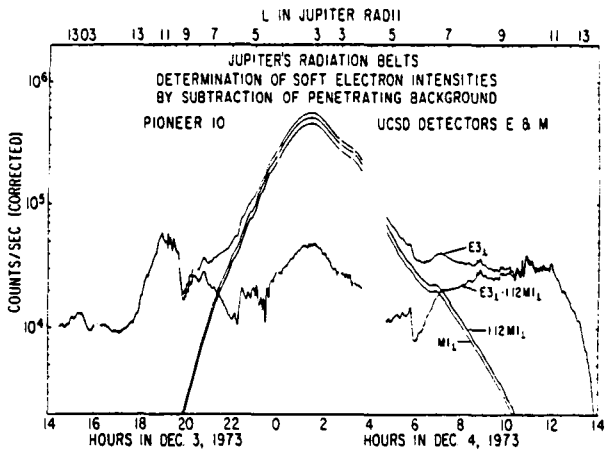

Fig. 12. Minimum background subtraction that yields a difference that is peaked perpendicular to the field direction. Symbol ⊥ indicates that each rate is evaluated in looking perpendicular to the local field.

These subtraction coefficients were obtained empirically by using the directionality test plus the condition that $E1' > E2' > E3' > 0$, where $E1'$ denotes the corrected count rates from channel E1, $E2'$ denotes those from E2, etc. We have laboratory calibrations of the efficiencies of these channels to penetrating radiation, and the empirical coefficients fall within the uncertainties of our laboratory data. However, the reasonability criteria from the flight are more stringent than the laboratory calibrations.

The differences are such a small fraction of the original rates that uncertainties in the soft particle intensities are quite high. However, most of the features appear in Figure 13 that were in Figure 8, and this leaves no doubt of their reality. Several features of interest are as follows:

1. The soft electrons go through a maximum at 11 R_J and are not so intense at periapsis.
2. The intensities decrease at the orbits of Europa and Io.
3. There is a spike of soft electrons at the innermost edge of the Io band.
4. At 8 R_J outbound, there is a 'teat' in which the electrons mostly have energy below 460 keV.

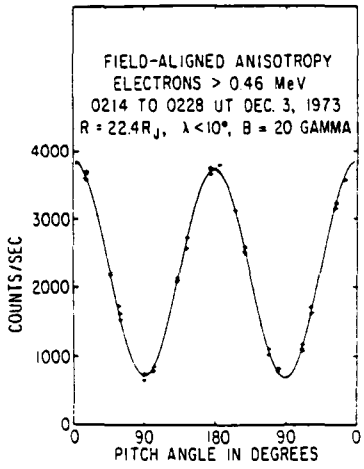

Fig. 11. Occurrence of a field-aligned particle flux.

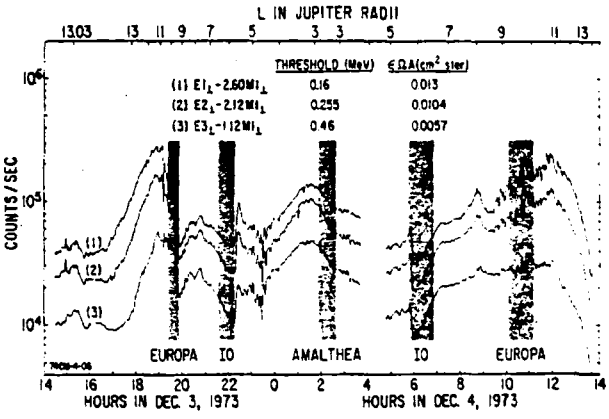

Fig. 13. Detector E rates after a tentative background subtraction. The shaded bands indicate times when the spacecraft is on L shells traversed by the inner moons of Jupiter.

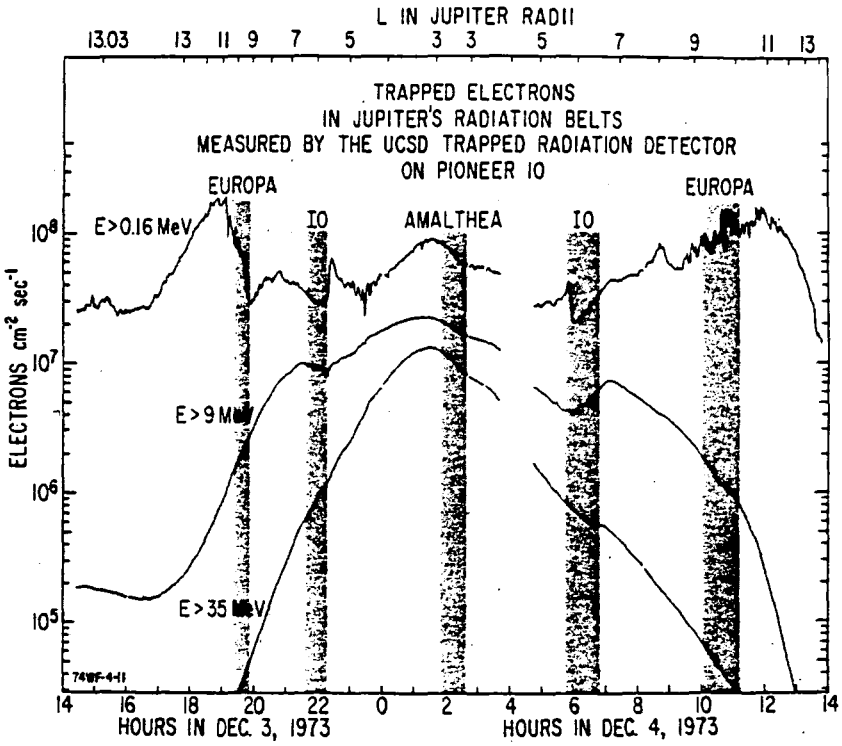

Fig. 14. Electron fluxes measured by detectors E, C, and M. The directional fluxes from detectors C and E were converted to omnidirectional fluxes by multiplying the peak flux by 8.5 sr. The shaded bands indicate times when the spacecraft is on L shells traversed by the inner moons of Jupiter. Throughout this paper we refer to time at the spacecraft, which is approximately 45 min earlier than ground-received time.

5. There are large-scale fluctuations outbound in the band of Europa.

6. There is a broad secondary peak at periapsis.

Figure 13 confirms our expectation that the radiation belts come about by inward diffusion of particles from an external source. The first cause for the dearth of soft electrons is the loss that takes place at Europa and Io. Lack of replenishment would imply that the moons cut the inner region off from the source of these particles. For the most part this appears to be true.

However, there is evidence for an internal particle source. The spikes just inside the Io band seem too sharp to have undergone much diffusion. Furthermore, the angular distribution in these spikes is dissimilar to that in its surroundings, being more concentrated perpendicular to the magnetic field. These properties could result from local acceleration. Indeed, acceleration of electrons in this energy range at Io was suggested by *Gurnett* [1972], but we note with caution that Gurnett's model produces pitch angles parallel to the field line [*Hubbard et al.*, 1974].

The teat at 8 R_J outbound has some of the characteristics of local acceleration, but it is much more equivocal. A better quantitative understanding of the diffusion process may enable us to trace this feature to the source.

The fluctuations outbound in the band of Europa are real, but their origin is a matter for speculation. They give evidence for dynamic processes acting on a certain scale, and if these are the determining processes for the radiation belts as a whole, they may help to establish the relationship between the microscopic and the macroscopic viewpoints.

The secondary peak at periapsis may be artifactual or real. It replicates the M1 profile with suspicious fidelity. However, if the difference is forced to zero here, it misbehaves elsewhere. We believe that a more precise estimate of differential low-energy fluxes can be effected by subtracting two terms, one from detector M and one from a higher channel of detector E. The question may be resolved when this subtraction is done.

Electron spectrum. Figure 14 displays electron intensities spanning the energy range of our instrument. The channels shown are E1′, C2, and M1, but the other channels on detectors E and C are similar to the ones given. Fluxes measured by the directional detectors E and C were converted to omnidirectional fluxes by multiplying the peak flux $j_\perp$ by 8.5 sr.

Besides the features at low energies that we have discussed already we note the satellite absorption effects at higher energies and the different shapes of the profiles. The >9-MeV channel is scarcely affected by Europa but takes large losses at Io. On the other hand, the >35-MeV electrons seem to diffuse by both satellites with little or no absorption.

The energy spectrum undergoes many variations throughout the figure, but the central feature is the hardening of the spectrum toward periapsis. When an integral power law approximation is used, the spectrum runs from E^{-3} outside Europa to $E^{-0.4}$ or less at periapsis. However, this spectral form does not adequately represent the data. We are still looking for an adequate form, but we present a better approximation in a later section of this paper.

Satellite interactions. Interactions of energetic electrons with Jupiter's moons show up clearly in Figures 8, 13, and 14. We reiterate the main observations here:

1. Europa strongly absorbs electrons in the energy range from 0.16 to about 1 MeV.

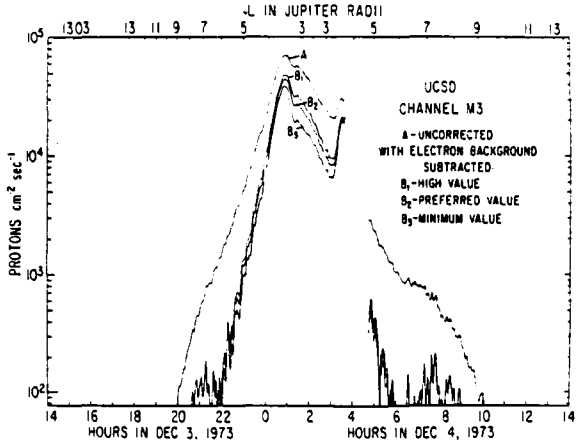

Fig. 15. Protons of energy >80 MeV counted in channel M3.

2. Europa exerts little or no absorption on electrons of energy >9 and >35 MeV.

3. Io strongly absorbs electrons near 9 MeV in energy.

4. Io also absorbs lower-energy electrons, of energy down to 0.16 MeV, but the fluxes and energies are too uncertain for a quantitative evaluation.

5. Electrons in the >35-MeV channel experience little or no absorption at Io.

6. Injection of electrons takes place in the vicinity of Io, resulting in a spike of particles in the energy range 0.16–1 MeV with a pancake angular distribution just inside Io's orbit.

The importance of the moons' immersion in the radiation belts has long been foreseen and discussed. The sweeping of energetic particles in particular was covered recently by *Mead and Hess* [1973] and *Hess et al.* [1974]. Although the data bear out some of their predictions, there seem to be additional complexities and, not surprisingly, poor quantitative agreement between predictions and observations.

We leave a thorough treatment of the data to a later paper, but we list below some of the features that we think will enter into the accounting:

1. The relative latitude of spacecraft and moon; i.e., does the spacecraft pass the moon's orbit at higher latitude or equatorward of the moon?

2. The effect of the moon on the angular distribution of trapped particles.

3. The particle drift frequency in a coordinate frame corotating with Jupiter.

4. The orbital frequency of the moon in a coordinate frame corotating with Jupiter.

5. The relative longitude of spacecraft and moon at the time that the spacecraft crosses the moon's path.

With respect to items 3 and 4 above, we note that at the orbit of Io, the drift velocity of 35-MeV electrons in a corotating frame of reference keeps pace with the orbital corotational velocity of Io. Thus the moon never catches up with the particles, and no sweeping is accomplished.

Proton observations by channel M3. In the entire 3 weeks inside the Jovian magnetosphere the only time Pioneer 10 encountered protons of energy >80 MeV was in the ½ day centered on periapsis. Channel M3 made unequivocal identification of protons, but there was enough electron contamination in the channel to create uncertainty in the absolute flux.

Trace A in Figure 15 shows the profile of channel M3 converted to particle flux but uncorrected for electron background. Note the two peaks, both of which occur at L = 3.7. Channel M1, counting electrons, has only one peak centered on L = 3 inbound.

Figure 16 shows the M3 rate plotted versus the M2 rate. The proton contribution to the M2 rate is less than 5%. The twin peaks of channel M3 and the single peak in channel M2 can be seen, and if any doubt remains, the double-valued nature of this plot proves that there are two independent functions.

The electron background in channel M3 can be evaluated as the sum of two terms in M2: a linear term representing their relative efficiencies for single electrons and a quadratic term representing the chance that two M2 pulses will occur simultaneously so as to look like a single pulse of twice the height. The linear term is plotted in Figure 16 as line B, and the quadratic term as line A. Line B is the maximum linear term that will not force the corrected M3 rate negative, and this term was adopted. There is some uncertainty in the coefficient for the quadratic term. The correct value is certainly between 10 and 90 ns, and the value of 45 ns is our best estimate. Lines B_1, B_2, and B_3 in Figure 15 show channel M3 after subtracting the adopted linear term and quadratic terms using the extreme and the most probable coefficients named above. Subtraction of the electron background does little to change the character of the proton distribution. The peaks at L = 3.7 only become more distinct, and there clearly are protons in the valley between the peaks.

The reason for this remarkable proton behavior is not understood. The peaks are so sharp that a discontinuity in the diffusion rate or a nearby source or loss term seems needed. The spacecraft might enter the band of L shells traversed by Amalthea, but if the innermost moon is sweeping up protons, it is strange that it does not have the same effect on electrons. (All magnetic field calculations in this paper use the preliminary D_1 model of *Smith et al.* [1974*a*]. According to this model the spacecraft trajectory overlaps the Amalthea L shells below L = 2.95. However, a new model labeled D_2 is presented in this issue [*Smith et al.*, 1974*b*], and with this model the overlap disappears [*Mead*, 1974].) We look forward to the electron counter of Pioneer 11 to find out what the protons do closer in.

Differential energy spectra and phase space densities. Since the phase space density of electrons is needed for certain types

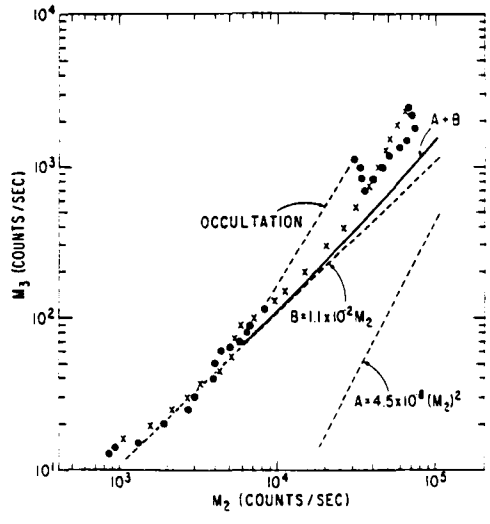

Fig. 16. Evaluation of the electron background in the proton channel

TABLE 3. Parameters for Constructing Differential Spectra From the UCSD Data

L, R_J	K, el cm^{-2} s^{-1} sr^{-1} MeV^{-1}	H, MeV	γ
25	4.0×10^5	1.3	4.39
20	6.2×10^6	0.9	4.30
15	6.0×10^6	2.1	4.85
12	7.6×10^7	1.9	5.00
11	6.2×10^7	2.7	5.35
10	9.4×10^6	7.8	6.8
9	1.65×10^6	75.	25.1
8	2.20×10^6	60.	18.7
7	1.55×10^6	150.	33
6	9.4×10^5	45.	9.0
5.56	4.1×10^6	7.0	3.58
5	1.26×10^6	15	3.89
4	1.72×10^6	7.4	2.44
3.5	4.7×10^6	2.6	1.93
3*	1.19×10^7	1.1	1.74
3†	1.88×10^6	4.4	1.89

*E1 - 2.60M1 was used (as was done in Figure 13).
†Six percent more background was subtracted (reduces net by a factor of 2).

of theoretical work, an attempt has been made to obtain differential spectra. After trying a number of functional forms the function $jdE = K(1 + pc/H)^{-\gamma}dE$ was chosen, where j is the directional number flux per unit energy, p is the electron momentum, c is the velocity of light, and K, H, and γ are the fitting parameters.

The phase space density is then $\tau d^3p = jp^{-2}d^3p = Kp^{-2}(1 + pc/H)^{-\gamma}d^3p$. It is convenient for computation to put this in terms of the first invariant, $\mu = p^2/(2m_0B)$, where B is the mirror point magnetic field:

$$\tau d^3p = \frac{K}{2m_0B\mu}\left[1 + (2m_0c^2B\mu)^{1/2}/H\right]^{-\gamma} d^3p$$

The total number density of electrons with momentums greater than p is easily computed:

$$n(>p) = \frac{4\pi KH}{(\gamma - 1)c}(1. + pc/H)^{1-\gamma}$$

A preliminary set of fits to the data on the inbound part of the traversal is given in Table 3. Values of the parameters H and γ have been determined by comparing the observed ratios E1/C2 and C2/M1 with the ratios obtained by integration over the measured efficiencies versus energy. Channels E1, C2, and M1 were chosen because (1) they are relatively free from saturation, drift, and background problems and (2) they cover the full energy range available with the UCSD instruments. The E1 rates were corrected for penetrating particles as was previously described, and the C2 rates have been multiplied by a factor varying between 1.0 and 1.3 to compensate for photomultiplier gain losses. Effects due to deviations from isotropy were ignored in this first attempt. No normalization for latitude variation is included. These fits will undoubtedly be supplanted as the data analysis is further refined but should provide useful interim estimates over the energy range of 0.2–60 MeV. It must be kept in mind, however, that these three-parameter differential fits were derived from three integral measurements made by instruments that are at times near their performance limits.

Evaluations of the phase space density at constant μ inside $L = 12$ reveal a monotonic decrease toward smaller L values with the exception of the narrow region associated with the apparent injection by Io ($L \simeq 5.6$, $\mu \simeq 10$ MeV/G). The fits are thus compatible with the notion of electron injection in the outer region and radial diffusion inward. In addition to the losses associated with the satellites Europa and Io the fits seem to require an additional mechanism to cause losses of a factor of 4 or more between $L = 5$ and $L = 3$.

Acknowledgments. We thank G. E. Peters, E. W. Strein, and G. W. Schmidt of the University of California at San Diego for their help in developing the instrumentation and the data reduction programs, and we thank C. F. Hall, D. Porter, and the staff of the NASA Ames Research Center for their cooperation. We are indebted to Irving Goldman of the Salk Institute, La Jolla, California, for assistance with the calibration shown in Figure 1. We also thank Antonio Mogro-Campero of the University of California at San Diego for comments and discussions. This work was supported by NASA contracts NAS 2-5602 and NAS 2-6552 and by NASA grant NGL 05-005-007.

REFERENCES

Drake, F. D., and S. Hvatum, Non-thermal microwave radiation from Jupiter, *Astron. J., 64*, 329, 1959.

Fillius, R. W., and C. E. McIlwain, Radiation belts of Jupiter, *Science, 183*, 314, 1974.

Gurnett, D. A., Sheath effects and related charged-particle acceleration by Jupiter's satellite Io, *Astrophys. J., 175*, 525, 1972.

Hall, C. F., Pioneer 10, *Science, 183*, 301, 1974.

Hess, W. N., T. J. Birmingham, and G. D. Mead, Absorption of trapped particles by Jupiter's moons, *J. Geophys. Res., 79*, 2877, 1974.

Hubbard, R. F., S. D. Shawhan, and G. Joyce, Io as an emitter of 100-keV electrons, *J. Geophys. Res., 79*, 920, 1974.

Mead, G. D., Magnetic coordinates for the Pioneer 10 Jupiter encounter, *J. Geophys. Res., 79*, this issue, 1974.

Mead, G. D., and W. N. Hess, Jupiter's radiation belts and the sweeping effect of its satellites, *J. Geophys. Res., 78*, 2793, 1973.

Simpson, J. A., D. Hamilton, G. Lentz, R. B. McKibben, A. Mogro-Campero, M. Perkins, K. R. Pyle, and A. J. Tuzzolino, Protons and electrons in Jupiter's magnetic field: Results from the University of Chicago experiment on Pioneer 10, *Science, 183*, 306, 1974.

Smith, E. J., L. Davis, Jr., D. E. Jones, D. S. Colburn, P. J. Coleman, Jr., P. Dyal, and C. P. Sonett, Magnetic field of Jupiter and its interaction with the solar wind, *Science, 183*, 305, 1974*a*.

Smith, E. J., L. Davis, Jr., D. E. Jones, P. J. Coleman, Jr., D. S. Colburn, P. Dyal, C. P. Sonett, and A. M. A. Frandsen, The planetary magnetic field and magnetosphere of Jupiter, *J. Geophys. Res., 79*, this issue, 1974*b*.

Trainor, J. H., B. J. Teegarden, D. E. Stillwell, and F. B. McDonald, Energetic particle population in the Jovian magnetosphere: A preliminary note, *Science, 183*, 311, 1974.

Van Allen, J. A., Observations of high intensity radiation by satellites 1958 Alpha and 1958 Gamma, paper presented at Joint Meeting, Nat. Acad. of Sci. and Amer. Phys. Soc., Washington, D. C., May 1, 1958.

Van Allen, J. A., D. N. Baker, B. A. Randall, M. F. Thomsen, D. D. Sentman, and H. R. Flindt, Energetic electrons in the magnetosphere of Jupiter, *Science, 183*, 309, 1974.

Wolfe, J. H., H. R. Collard, J. D. Mihalov, and D. S. Intriligator, Preliminary Pioneer 10 encounter results from the Ames Research Center plasma analyzer experiment, *Science, 183*, 303, 1974*a*.

Wolfe, J. H., J. D. Mihalov, H. R. Collard, D. D. McKibbin, L. A. Frank, and D. S. Intriligator, Pioneer 10 observations of the solar wind interaction with Jupiter, *J. Geophys. Res., 79*, this issue, 1974*b*.

(Received May 24, 1974;
accepted June 21, 1974.)

Radiation Belts of Jupiter: A Second Look

Abstract. *The outbound leg of the Pioneer 11 Jupiter flyby explored a region farther from the equator than that traversed by Pioneer 10, and the new data require modification or augmentation of the magnetodisk model based on the Pioneer 10 flyby. The inner moons of Jupiter are sinks of energetic particles and sometimes sources. A large spike of particles was found near Io. Multiple peaks occurred in the particle fluxes near closest approach to the planet; this structure may be accounted for by a complex magnetic field configuration. The decrease in proton flux observed near minimum altitude on the Pioneer 10 flyby appears attributable to particle absorption by Amalthea.*

Pioneer 11 traversed Jupiter's magnetosphere almost exactly 1 year after its predecessor, Pioneer 10 (*1*). The outbound trajectory was farther from the equator than previous passes, and high particle fluxes encountered here challenge the original magnetodisk model of the outer radiation belts.

Figure 1a illustrates the observations. The large peak spans the closest approach to the planet at 0523 on 3 December with the inbound leg to the left and the outbound leg to the right. The low latitude data inbound exhibit modulation at the Jovian rotation rate with intensity maxima near the expected position of the magnetic equator. Crossings of the current sheet, identified by the magnetometer experiment (*2*), were found to be in coincidence with some of the maxima. These observations are similar to those from Pioneer 10 and are consistent with the magnetodisk model. The outbound pattern is deceptively similar to that near the equator, with strong modulation at the planetary rotation frequency and comparable intensities. However, there were no current sheet crossings (*2*), and the maxima were higher even than recorded inbound. Such high intensities were not already reduced by one or two orders of magnitude only 10° from the equator, we had expected very little radiation at higher latitudes.

It may be that the configuration is altered by a local time difference. If so, however, the change must take place across only 45° in rotation from midmorning to noon. Alternatively, if the high outbound fluxes are caused by a real time change, it would have to be synchronized coincidentally with closest planetary approach, and no such changes were recorded at other times when the spacecraft was in the magnetosphere. If these possibilities are ruled out, it is still not clear that the magnetodisk model must be abandoned, for this model and the higher latitude phenomena may exist side by side. If this is the case, the Pioneer 11 data imply a latitude profile that initially decreases from a maximum at the equator, goes through a minimum, and then increases to a greater maximum at higher latitudes before dropping off again. The physical processes responsible for this latitude stratification and the interaction between these radiation zones are open questions. However this problem is resolved, it is clear that the new measurements at high latitude provide indispensable information regarding the dynamics and configuration of the vast Jovian magnetosphere.

It is natural to investigate the phase of the modulation for clues regarding the magnetospheric model and internal physical processes. The data in Fig. 1b have been filtered to display frequencies near the planetary rotation cycle, and we have included tic marks synchronized to Jupiter's rotation. The tics on the lower border occur at intervals of one Jovian day (9 hours, 55 minutes, 29.37 seconds); the marks on the bottom line indicate when the spacecraft is aligned and antialigned with visualized in the original magnetodisk model.

According to the original model, the energetic radiation is contained in a disklike volume defined by nearly radial lines of force stretched outward by a current sheet at the equator. The tilt of the internal planetary field imparts an up-and-down motion to the current sheet at the planetary rotation frequency, and the modulation of the trapped radiation is caused by this up-and-down motion in conjunction with a very sharp vertical gradient of the trapped radiation. Because the intensity was

Table 1. Zenocentric and magnetic coordinates for particle features in Fig. 3; L, magnetic shell parameter.

Feature in Fig. 3	Zenocentric coordinates			Magnetic cordinates		
				Model D_1*		Model O_3†
	R (R_J)	Latitude (deg)	Longitude III (deg)	L	Magnetic latitude	L
N1	1.76	− 38.6	315	2.79	− 36.2	2.48
X1	1.62	− 24.3	342	2.15	− 27.0	1.72
N2	1.60	− 18.0	352	1.99	− 22.7	1.61
X2	1.63	1.0	18.0	1.77	− 8.3	1.61
N3	1.75	13.2	35.1	1.84	2.0	1.79
X3	1.82	18.5	43.3	1.92	6.8	1.93
N4	2.13	31.8	68.7	2.47	20.5	2.56

* See (*8*). † See (*7*).

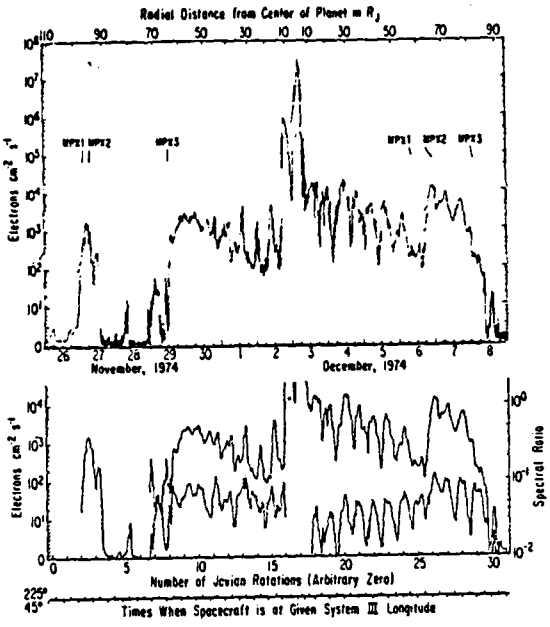

Fig. 1. (a) The flux of electrons of energy > 5 Mev recorded by the UCSD trapped radiation detector along the Pioneer 11 trajectory through the Jovian radiation belts. The labels MPX-1, MPX-2, and MPX-3 mark the times when the spacecraft entered or left the magnetosphere (*10*). (b) Running averages (1 hour) of flux and a spectral ratio for electrons of energy near 5 Mev. The middle trace is identical to the top trace except for the 1-hour filter. The bottom trace is the ratio of two channels with energy thresholds above and below 5 Mev. Higher ratios indicate harder spectra.

the internal magnetic dipole. These would be the times of highest and lowest latitudes in a coordinate system fixed to a wobbly magnetodisk that was rigid and unwarped. Phase shifts between this and the diurnal clock are caused by the angular swing of the spacecraft around the planet. For an unwarped wobbly magnetodisk the closest approach to the equator would be at 225° inbound, would change phase when the spacecraft crosses the equator, and would be at 45° outbound. The phase change is the difference between this model and one in which the maxima occur at a single longitude in both hemispheres.

None of these timing marks predict the maxima with any precision. A phase change seems called for to describe the intensity modulation; however, the ratio is in phase with the intensity after closest approach although it is not in phase for several cycles before.

Differences in phase between a model and the observed peaks can be explained in terms of spiraling of field lines caused by the angular momentum lag of an outward moving plasma, or warping of field lines from viscous interactions with the solar wind, or other mechanisms. Although these differences contain important information, unfortunately they allow different models enough freedom to be brought into agreement with the data.

A comparison of Fig. 1a with Fig. 1b emphasizes the abruptness of the fluctuations. Without filtering, the data are very spiky and suggest large temporal changes. The prevalent angular distribution is isotropic. In these respects the Pioneer 11 data are similar to the Pioneer 10 data.

The Pioneer 11 data confirm the major findings of Pioneer 10 in the high-intensity inner magnetosphere. Figure 2 shows five channels of the University of California at San Diego (UCSD) instrument plotted versus time. If these data were plotted versus

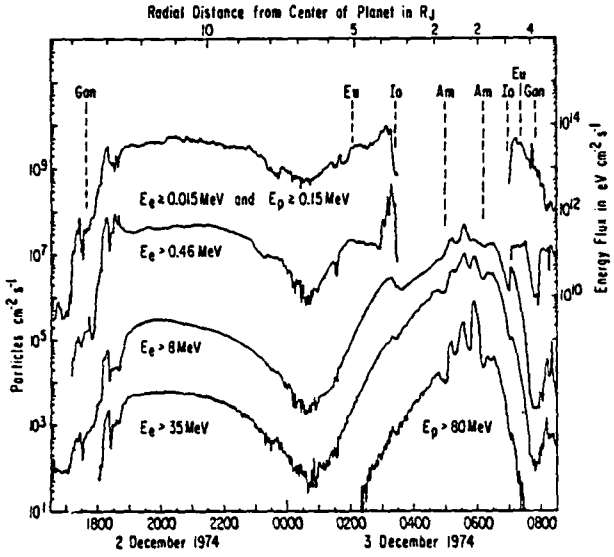

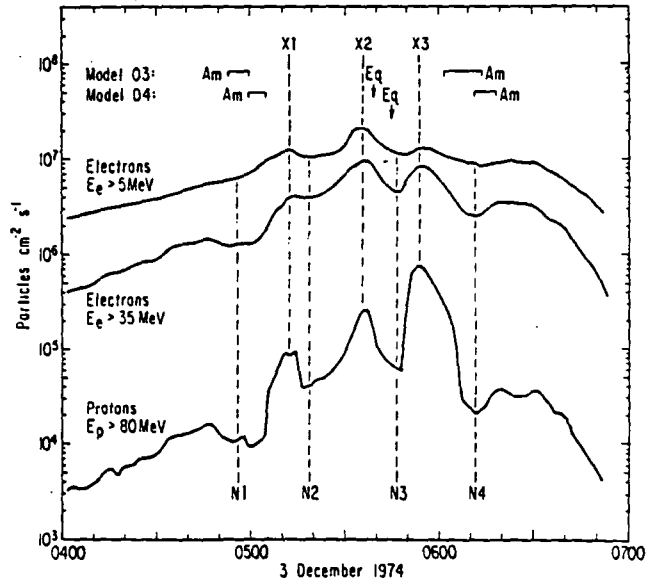

Fig. 2 (left). Integral fluxes of protons and electrons of kinetic energies greater than the values indicated. The uppermost trace shows the combined energy flux for electrons and protons above the threshold and below ~0.1 Mev (electrons) and several Mev (protons). The right scale refers to the uppermost trace only; all other profiles should be measured with the left scale. The average positions of the orbits of the inner Jovian satellites are indicated by dashed lines as calculated with the use of the D_4 magnetic field model (*5*). Particle fluxes corresponding to the two top profiles are not shown near closest approach to the planet because they are too low to be distinguished from the energetic particle background. Fig. 3 (right). Electron and proton fluxes measured near the closest approach of Pioneer 11 to Jupiter (1.6 R_J from the center of the planet at 0523). The multiple peak structure may be accounted for by a higher-order spherical harmonic expansion of the magnetic field.

magnetic coordinates, the broad peak on 2 December and the minimum at 0100 on 3 December would emerge as spatial effects associated with magnetic latitude. As with Pioneer 10, the largest numbers of high-energy particles are found nearest the planet and there is a cavity of low-energy particles inside the moons Europa and Io. With the Pioneer 10 data we demonstrated that these features are consistent with inward radial diffusion (*3*), and we derived diffusion coefficients from the loss rate at the moons (*4*).

The peak fluxes of electrons experienced by the Pioneer 11 spacecraft were comparable to those experienced by the Pioneer 10 spacecraft. Since Pioneer 11 approached the planet more than 1 Jupiter radii (R_J) closer than Pioneer 10, this comparison shows that the radial gradient levels off.

The Pioneer 11 electron fluxes at high latitude are significantly higher than those which would be extrapolated from the Pioneer 10 latitude dependence near the equator. This may be another manifestation of the same phenomenon discussed above for the outer magnetosphere. The Pioneer 10 and Pioneer 11 magnetic coordinates crossed each other in the inner region only between 10 and 13 R_J. At three crossover points the ratios of electron fluxes were near unity for energies from 0.2 to > 35 Mev, and we believe that the radiation belts are stable over the time period of a year.

On 3 December Pioneer 11 had a near encounter with the magnetic flux tube containing Io. Between 0300 and 0330 the spacecraft passed within probably 6000 km of the flux tube. [This distance is based on the D_2 magnetic field model (*5*) and will differ for other models.] The flux of electrons of energy $E > 0.46$ Mev jumped suddenly by an order of magnitude to the highest level encountered by either spacecraft (see Fig. 2). Just past the magnetic coordinate of Io these particles disappeared below the minimum we can accurately extract from the high-energy background. Particle acceleration on this flux tube had been predicted (*6*) because of Io's remarkable control over the decametric radio noise from Jupiter. In the context of these models, a conservative estimate for the power in the particles near Io is $\sim 10^{13}$ watts, and this can easily supply the 10^8 watts of radio power observed.

During its closest approach to the planet, Pioneer 11 passed through multiple peaks in the trapped particle fluxes at all energies. This region is shown in detail in Fig. 3. Three maxima and four minima are indicative of the time profile, and position coordinates for these features are given in Table 1. Minima N1 and N4 may reasonably be attributed to particle absorption by Amalthea. However, since there are no more moons nearby, the other features require another explanation.

It might be that the field is convoluted in such a way that the trajectory passed through the same features more than once; or it might be that asymmetries in the field cause certain particle drift surfaces to dip into the planetary atmosphere where the particles would be absorbed. Such effects would not be predicted by a dipole representation of the field, but higher-order terms in the magnetic field expansion are likely to become important at these close distances. One might then expect a magnetic field model which contains higher-order terms to be necessary to organize the particle data. It is not assured that the field mapping by Pioneer 10 and Pioneer 11 covered a sufficient range to determine all the possibly complex radial, longitudinal, and latitudinal irregularities near the planet. However, we do have the opportunity to compare a preliminary octopole model with what is probably the best dipole representation possible (*7*, *8*). Magnetic coordinates from these models are listed in Table 1, and times when the spacecraft crossed the magnetic equator and when it passed through the range of particle drift shells traversed by Amalthea are marked for each model in Fig. 3. As we expect minima at Amalthea and maxima on or near the equator, it is clear that a better correspondence is obtained with the octopole model. Further work is required to explain the multiple peaks, but it is encouraging that the first attempt at a higher-order field expansion brings about this much improvement. We believe that further work in this direction will be fruitful.

With regard to the absorption of particles by Amalthea, it may be recalled that for Pioneer 10 there was a decrease in the proton flux near its closest approach, but the reason for this behavior was not determined. The peaks observed for Pioneer 10 correspond closely to the relative maxima outside minima N1 and N4 in Fig. 3, and those minima can be identified with the decrease in the Pioneer 10 mission. The Pioneer 11 flux recovered inside this position and climbed by a factor of ~ 15 higher than the maximum of Pioneer 10. It is now safe to conclude that, of the possibilities discussed for Pioneer 10, the absorption effect of Amalthea is dominant.

Since absorption losses depend upon the radial diffusion velocity of the particles, we can estimate the diffusion coefficient from the observed decrease in the particle fluxes across the region of Amalthea. We deduce the following preliminary values of the diffusion coefficient D: for protons of ~ 100 Mev, $D \sim 3 \times 10^{-9}$ sec^{-1} and for electrons of ~ 90 Mev, $D \sim 2 \times 10^{-9}$ sec^{-1}. These values are $\sim 1/20$ of the value we derived for 14-Mev electrons at the orbit of Io based on Pioneer 10 data. However, spatial and energy dependences of the diffusion coefficient are expected (*9*).

In conclusion, we note that the integrated radiation dose received by Pioneer 11 was considerably smaller than that received by Pioneer 10, and there was no permanent radiation damage to the UCSD instrument.

R. WALKER FILLIUS
CARL E. MCILWAIN
ANTONIO MOGRO-CAMPERO
Physics Department, University of California, San Diego, La Jolla 92037

References and Notes

1. Preliminary reports by Pioneer 10 experimenters appeared in *Science* 183, 301–324 (1974); more extensive articles were published in *J. Geophys. Res.* 79, 3489–3694 (1974).
2. E. J. Smith, personal communication.
3. C. E. McIlwain and R. W. Fillius, *J. Geophys. Res.*, in press.
4. A. Mogro-Campero and R. W. Fillius, *EOS Trans. Assoc. Geophys. Union* 56, 1172 (1974); in preparation. Diffusion coefficients for protons and electrons were also derived by J. A. Simpson, D. C. Hamilton, R. B. McKibben, A. Mogro-Campero, K. R. Pyle, and A. J. Tuzzolino [*J. Geophys. Res.* 79, 3522 (1974)].
5. E. J. Smith, L. Davis, Jr., D. E. Jones, P. J. Coleman, Jr., D. S. Colburn, P. Dyal, C. P. Sonett, A. M. A. Frandsen, *J. Geophys. Res.* 79, 3501 (1974).
6. P. Goldreich and D. Lynden-Bell, *Astrophys. J.* 156, 55 (1969); D. Shawhan, D. A. Gurnett, R. F. Hubbard, G. Joyce, *Science* 182, 1348 (1973).
7. M. H. Acuna and N. F. Ness, personal communication. The spherical harmonic analysis model of Smith *et al.* (*8*) was not available before the deadline for this report.
8. E. J. Smith, L. Davis, Jr., D. E. Jones, P. J. Coleman, Jr., D. S. Colburn, P. Dyal, C. P. Sonett, *Science* 188, 451 (1975).
9. A. Mogro-Campero, R. W. Fillius, C. E. McIlwain, in *Space Research XV*, in press.
10. J. D. Mihalov, H. R. Collard, D. D. McKibben, J. H. Wolfe, *Science* 188, 448 (1975).
11. We thank the staffs of the Pioneer Project Office and the Deep Space Network for another well-organized and highly successful encounter with Jupiter. We also thank the programming staff at UCSD, and J. Peters in particular, for their help. This work was supported by NASA contract NAS2-6552.

14 March 1975

REVISED VERSION
January 1976

THE TRAPPED RADIATION BELTS OF JUPITER

Walker Fillius

Abstract

We review the data and initial analyses from the University of California, San Diego instruments on Pioneers 10 and 11. The Pioneer measurements are the first ever made in the Jovian magnetosphere, and, as they are still too fresh and too copious to be interpreted completely, we encounter unanswered and new problems in our discussion. Energetic electrons of Jovian origin are found in interplanetary space. Although we now know that the Jovian magnetosphere is larger than had been expected and is inflated by distributed currents, there is uncertainty regarding its configuration and the dynamics of energetic electrons contained in the outer region. The five innermost moons of Jupiter orbit within the radiation belts and affect the intensities and angular distributions of the radiation by both absorbing and injecting particles. In the inner region radial and pitch angle diffusion are dominant processes as at Earth. Near the Pioneer 11 periapsis there were multiple peaks in the proton and electron intensities that have not been explained. We also present the Pioneer 10 and Pioneer 11 flyby trajectories in several coordinate systems useful for studying the behavior of the trapped radiation.

I. INTRODUCTION

The two Pioneer flyby's have initiated direct studies of the trapped radiation belts of Jupiter. These in situ measurements supplant the meagre inferences which were the best that could be drawn from remote observations. The new knowledge is an important step toward generalizing our understanding of radiation belts. Before Pioneer 10 one had only one observable example from which to infer the properties of radiation belts as a class. More cases exist and the class is important, not only from its intrinsic interest per se, but also because of its bearing on astrophysics and plasma physics. Reciprocally, there is no doubt that a more generalized understanding of other radiation belts will have application to the original case at Earth.

The only remote indication of the presence and properties of energetic particles surrounding a planet or astronomical object is their radio emission. The Earth and Jupiter are both sources of radio waves, as are many astronomical objects. However, the mechanisms for generating all of the waves are not well known, and even if they were, they would enable one to deduce only a limited amount of information. One of the exercises prompted by the Pioneer data is to relate local particle fluxes to remote radio emissions. Examining these relationships should improve the inferences one derives about other objects.

By far the best and most reliable information we have on the Jovian radiation belts is that collected by Pioneers 10 and 11.

This paper is a review of preliminary results from the University of California, San Diego Trapped Radiation Detector package. This is one of several charged particle instruments on board, and some of our findings overlap those of other experiment teams. We will refer to their work when we feel it augments ours, but for a complete view of their findings, the reader is referred to the companion pieces in this volume [Van Allen, 1976; Simpson and McKibben, 1976; McDonald and Trainor, 1976]. The Pioneer data are too recent, too copious, and too undigested to allow a definitive review at this time. Our paper will not look backward, then, but forward, and as we present some of the major features of the Jovian radiation belts, we will emphasize the questions which they pose to our understanding.

II. THE UCSD INSTRUMENT AND THE FLYBY TRAJECTORY

Tables I and II summarize the capabilities of the University of California (UCSD) Trapped Radiation Detectors during the Pioneer 10 and Pioneer 11 flybys. The instrument package contains five sensors of three different kinds, consumes 2.9 watts, and weighs 3.9 lbs. The instrumental characteristics are described in more detail by Fillius and McIlwain [1974b].

The encounter trajectories have been described by Hall [1974; 1975] and Mead [1974]. We complete this section by showing the flyby trajectories in coordinate systems helpful for studies of the radiation belts (Figures 1-5). In Figure 1 the trajectories are projected onto Jupiter's equatorial plane to show the local time coverage, which is predominantly in the morning quadrant. The coverage in magnetic latitude is shown in Figure 2. The plane of this figure is defined to contain Jupiter's internal dipole moment vector and the spacecraft (or moon). Thus the magnetic equator always intersects this plane in a horizontal line through the origin, and magnetic latitude appears in the usual way. Because the dipole is tilted by 10.6° with respect to the spin axis, a fixed observer would see the magnetic meridian plane wobble back and forth with the planetary rotation period. This wobble is what causes the spacecraft and lunar loci to oscillate in latitude. The fixed observer would also see the meridian plane swing as if hinged on the dipole vector and follow the spacecraft (or moon) in local time. It is because of this swing that the spacecraft appears not to go around the planet. The dipole magnetic field line through Io is shown for illustration.

The gyrocenter of a trapped particle travels along a magnetic field line, bouncing back and forth between mirror points. It is hard to trace this motion in Figure 2 because of the varying curvature of the field lines. Therefore Figure 3 shows the trajectories in magnetic dipole coordinates, where lines of force are straight. The vertical axis is related to latitude by $B/_{BEQ} = \sqrt{4-3\cos^2\lambda}\,/\cos^6\lambda$ where λ is the magnetic latitude. The shaded areas represent L shells where sweeping of trapped radiation can be accomplished by the moons (see Section V (a).)

In addition to bouncing in latitude, particles also drift in longitude. Longitude drift is driven by electric fields and by the gradient and curvature of the magnetic field. In the idealized case, where there are no electric fields parallel to the magnetic field, electric field drift causes particles to circle the planet at just the planetary rotation frequency. In this case we refer to the magnetosphere as "corotating," and, by viewing the particles' longitudinal motion in a coordinate system fixed to the planet, we can forget about this component of the drift. Figures 4 and 5 show the paths of the Pioneer spacecraft and the five innermost moons in such a system. Magnetic field drift will still occur, and particles of different signs will go in the directions shown. Although the moons have prograde orbits as seen from Earth, they move in the retrograde sense in this coordinate system. In this figure one can visualize the periodic motion of the moons through the trapped radiation, and determine the longitudinal relationship between moon and spacecraft when the spacecraft crossed a moon's L shell.

The dipole magnetic field representations shown here are quantitatively accurate only inside about 10 R_J. However, we have extended the figures beyond this limit of validity in order to give a qualitative picture of the region farther out.

III. INTERPLANETARY ELECTRONS OF JOVIAN ORIGIN

6

Perhaps the first novelty with which Jupiter greeted the incoming Pioneer spacecraft was bursts of energetic electrons of Jovian origin. Figure 6 shows a time profile of Jovian electrons recorded by the UCSD Cerenkov detector on Pioneer 10 between April, 1973 and encounter with Jupiter in December of that year. Since the counter, which responds to particles with velocity greater than 3/4 the speed of light, counts both cosmic ray nucleons and relativistic electrons, two channels were used to separate components by solving two simultaneous linear equations. The data are one-day averages, and the apparent negative counting rates are merely the result of systematic and statistical errors in the separation procedure. This profile resembles those shown by Chenette et al [1974] and by Teegarden et al [1974]. Note that electron bursts appear as far away from Jupiter as 1 AU. Reanalysis of data taken at Earth orbit by earlier Imp satellites revealed that Jovian electrons are detectable as far away as 4 AU [Teegarden et al, 1974].

Figure 7 shows a series of bursts recorded by the Cerenkov counter just before Pioneer 10 reached the Jovian magnetosphere. The anisotropy dials show that the flux tends to be higher when the detector faces west in solar-ecliptic coordinates. This is the direction in which the magnetic field spiral leads away from the sun, and the electrons are flowing inward from Jupiter. One of the most significant features of these bursts is that peaks tend to reoccur at ten hour intervals. Ten hours is the rotation period of Jupiter, and this periodicity is a dramatic signature of the electrons' origin. (More precisely the rotation period of Jupiter is 9 hours, 55 minutes, 29.711 seconds according to the System III (1965.0) convention. In our discussions we round it off to ten hours.)

The mode of escape of these particles and its implications for the stability and structure of the Jovian magnetosphere are questions open to investigation. So are the characteristics of their radial and longitudinal propagation, and particularly how they retain their cohesion and periodicity. Studies of their directionality, energy spectra, and frequency spectra should shed light on these questions.

Any new ideas generated by this study on Jovian particle propagation in the heliosphere will have a direct effect on the models of propagation of solar and galactic cosmic rays. One of the advantages of using Jovian electrons as test particles in the heliosphere is that Pioneers 10 and 11 have directly sampled the regions of their origin (the Jovian magnetosphere), whereas in the case of solar cosmic rays we do not have in situ measurements of these particles at their origin, and in the case of galactic cosmic rays we have not yet sampled their fluxes in interstellar space.

IV. THE CONFIGURATION OF THE MAGNETOSPHERE

Energetic particles are trapped within the magnetosphere. Figure 8 (Pioneer 10) and Figure 9 (Pioneer 11) show the entire radiation belts in profile. One easily distinguishes the inner magnetosphere, $R \leq 20\ R_J$, and the magnetopause crossings, where there are abrupt steps between interplanetary and trapped flux levels. There are at least three magnetopause crossings on each inbound and outbound pass. The position of the magnetopause is evidently variable, moving inward and outward rapidly in response to changes in the solar wind. This and other evidence have been cited [Mihalov et al, 1975; Wolfe et al, 1974] to picture the magnetosphere as a blunt, spongy region.

Large scale fluctuations with a ten hour period dominate the trapped electron fluxes outside $20\ R_J$. The first explanation of this periodicity held that the radiation belts were confined to a thin disc near the magnetic equator. The modulation was attributed to wobbling of the disc at the planetary rotation rate. [Fillius and McIlwain, 1974a; Simpson et al, 1974a; Trainor et al, 1974a; Van Allen et al, 1974]. This explanation was compelling until the outbound half of the Pioneer 11 encounter. Whereas all previous data were acquired in and near the disc at low latitudes, the Pioneer 11 outbound leg was at a latitude well outside the disc. Thus it was a surprise to see the ten hour periodicity continue as before, with intensity peaks higher even than during the inbound leg.

There is not a consensus of opinion as to why this pass does not follow the predictions of the original model. Van Allen et al [1975] concluded

that the disc is blunted in the subsolar direction (the outbound direction of Pioneer 11). Fillius et al [1975a] suggested that, if local time was not the cause, the latitude profile might be bifurcated, with peaks at the equator and at high latitude, too. Such a profile is a possible configuration of the analytical model magnetosphere since published by Barish and Smith [1975]. Simpson et al [1975] argued that, although there may be some modulation due to a disc-like structure of the radiation belts, the primary cause of the ten-hour periodicity is time-dependent. That is, the maxima and minima occur as determined by time, and they appear nearly simultaneously throughout the sunward side of the radiation belts irregardless of latitude.

Much attention has been given to the phase of the variations. The bottom half of Figure 9 includes tic marks placed at the phase expected in the disc model and the time model. The reader may see for himself that neither model makes a good fit. Qualifications may be added to either model. However, it seems that the preliminary appraisal of the data is inconclusive.

More thorough studies can be expected to shed light on the configuration of the magnetosphere. In addition to the phase of the particle peaks, the magnetometer data are certainly important. The magnetic field is discussed by Smith et al at this symposium [1976]. Combined studies of the magnetic field and particle distributions are being undertaken.

Yet more information is contained in the particle angular distributions. One significant result is the east-west anisotropy

of the low energy protons which indicates that these particles corotate with the planet. [Trainor et al, 1974a; Van Allen et al, 1975]. Near the inner magnetosphere both spacecraft encountered intense field-aligned fluxes of highly energetic particles. Figure 10 shows an example that persisted for several hours, although evidently of high significance, these events are ambiguous of interpretation [Fillius and McIlwain, 1974b].

Present studies are in an undigested state. This region differs from the Earth's radiation belts both in the larger dimensions and in the influence of the rapid rotation of the planet. Basic theoretical understanding is lacking for such features as the effect of a distributed ring current, the possibility of non-corotation or slippage of the magnetic field, and particle convection and acceleration in the possibly turbulent field. Clarification of these features can be expected to improve our understanding of such diverse subjects as pulsars and laboratory plasmas as well.

V. INTERACTIONS BETWEEN THE TRAPPED RADIATION BELTS AND JUPITER'S MOONS

A unique feature at Jupiter is the presence of moons within the radiation belts. Besides being useful probes of trapped particle behavior, they generate extraordinary particle and electrodynamic effects which give them intrinsic interest. Before the Pioneer mission, the Io-controlled decametric emission had already broadcast evidence that these moons could have remarkable electrodynamic effects. The recent observation of sodium emission lines from a halo surrounding Io, [Brown and Yung, 1976] and the discovery by Pioneer 10 of a partial torus of hydrogen emission in Io's orbit, [Judge et al, 1976] heighten the interest. The energetic particle detectors on Pioneer 10 and Pioneer 11 add to the list of moon-associated features the absorption of energetic trapped radiation and the injection or acceleration of energetic particles. These will be the best observations until 1979 when the Mariner spacecraft to Jupiter will make a near encounter with Io and take a much closer look.

(a) Absorption of Trapped Radiation

All particle experiments on Pioneer 10 and 11 observed absorption at the three innermost moons, Amalthea, Io and Europa. Figures 11 and 12 illustrate the absorption features in several channels of the UCSD instrument. The flux or counting rate is plotted vs time, and the labels indicate the times when the spacecraft crossed the particle drift shells occupied by each moon. Absorption at Ganymede is hard to be sure of because the spacecrafts' latitude excursions caused rapid changes near this L shell, and there seem to be other variations which should be accounted for before a definite association can be made.

Mogro-Campero and Fillius [1975] and Mogro-Campero [1976] constructed a statistical model for the rate of absorption of trapped particles at a moon, and then, exploiting this effect as a probe of trapped particle dynamics, derived diffusion coefficients for the particles' radial motion in the Jovian magnetosphere. Ignoring complications from the moons' variations in magnetic latitude, it is an easy model to deal with. The key simplification is a statistical approximation to the probability of a particle's being absorbed by a moon. Noting that diffusive excursions in the particles' motion tends to redistribute the particles randomly, they assumed that complete randomization is achieved throughout a sweeping region of width ΔL in less time than the recurrence period, P, of the moon in a frame of reference rotating at the particles' drift rate. If ΔL is greater than the moon's diameter, d, the probability per unit time of a particle's being met by the moon and absorbed is given by $d/(P\Delta L)$. Thus the rate of change of the particle density, τ, is given by

$$\frac{d\tau}{dt} = -\tau d/(P\Delta L) \qquad (1)$$

Particles diffusing inward are absorbed at this rate for as long as they remain inside the sweeping region. This time is ΔL divided by the diffusion velocity, Dn, where D is the diffusion coefficient and n is the average slope $\frac{\partial}{\partial L}(\ell n\, \tau)$. The fraction of particles that diffuse through the region without being absorbed is given by integrating equation (1) from $t = 0$ to $t = \Delta L/(Dn)$. Note that the arbitrary

width ΔL cancels out of the result:

$$\tau/\tau_o = \exp(-d/PDn) \qquad (2)$$

With observations of τ/τ_o equation (2) can be inverted to solve for D:

$$D = -d/\left(Pn\ \ell n(\tau/\tau_o)\right) \qquad (3)$$

The statistical assumption may not be accurate for all types and energies of particles. However, the more the particles' positions are randomized, the better the assumption will be. Randomization will be enhanced by instabilities in the moons' wakes such as discussed by R. A. Smith [1976] and by Huba and Wu at this conference. Particles with substantial drift rates ($E \geq 1$ Mev) will approach the moon at different longitudes each time around, and this introduces another dimension of variability. Because the detectors have wide energy ranges, their responses cover a spectrum of different conditions, which may be appropriately represented by a statistical ensemble.

Furthermore, the statistical assumption can be checked for self-consistency. We calculate the rms displacement of a set of particles in a time P, following the derivation given in Reif [1965]:

$$< \Delta L^2 > = 4DP \qquad (4)$$

Using a moon's period for P, we can obtain from equation (4) $\sqrt{<\Delta L^2>}$, or the width of the region over which the particles' positions are effectively randomized. For most values of D obtained by Mogro-Campero and Fillius, $\sqrt{<\Delta L^2>} \gg d$, as required by the statistical approach.

Deterministic models have been used by others to derive values for the diffusion coefficient [Simpson et al, 1974b; Thomsen and Goertz, 1975]. Their values have not differed substantially from the results of the statistical model, but with suitable refinement the deterministic approach may offer the ability to look further into the interaction between the moons and particles and to account for some of the detail in the trapped radiation observations.

(b) Effect On Angular Distributions

The angular distribution of the trapped radiation is also affected by the moons. As predicted by Mead and Hess [1973] the probability of absorption depends upon a particle's equatorial pitch angle. This is simply a geometrical effect depending upon whether the particle's bounce motion carries it across the moon's orbital path. The vertigo diagrams (Figures 4 & 5) demonstrate how the moons' magnetic latitude varies with planetary longitude, and illustrate the zones where a particle which mirrors close to the equator can slip under a moon's orbital path and escape absorption.

The UCSD Trapped Radiation Detector observed changes in the pitch angle distributions which are consistent with this model of selective absorption. Traces 2 and 3 in Figure 13 show how the pancake shaped angular distribution of 9 Mev electrons sharpens as the particles diffuse past Io. Evidently particles with small equatorial pitch angles are absorbed preferentially. A more complete interpretation of Figure 13 includes pitch angle diffusion to reduce the sharpness of the angular distribution inside Io. This interpretation is discussed at more length by Fillius et al [1976]. As exploited in that paper, the moon serves again as a probe of trapped particle behavior. Further insights may be expected from analysis of these absorption features.

(c) Injection of Energetic Radiation

Besides being a sink of particles, Io is also a source. Injection of particles is predicted by a sheath model for Io's interaction with the magnetosphere [Shawhan, 1976]. During the

Pioneer 10 flyby local peaks were detected near the magnetic L shell of Io. Fillius and McIlwain [1974b] suggested that these were caused by a local source of particles, and McIlwain and Fillius [1975] demonstrated that the phase space density went through a local maximum here, proving the existence of a source. The peaks appear in Figure 14 just inside the inner edge of Io's sweeping region. They occurred only for channels E1, E2, and E3 for electron energies $E_e > 150$, 250, and 460 kev. The C and M detectors ($E_e > 6$ Mev and 35 Mev) did not record such a feature.

As shown in Figures 4a and b, Pioneer 10 crossed the L shell of Io 2 hours (inbound) and 5 1/2 hours (outbound) after Io had passed the same longitude. Thus it was never near the instantaneous flux tube occupied by Io. Pioneer 11, on its inbound pass, was fortunate to come very close to the Io flux tube (see Figure 5a). The exact miss distance depends upon the magnetic field model because there was a large latitude difference between spacecraft and satellite, and differences in magnetic declination are critical to the connection. The miss distance could be quoted as the actual distance from the spacecraft to the nearest point on the surface of the flux tube, but it is more useful to project the satellite and spacecraft positions to the magnetic equator along lines of force and measure the miss distance in the equatorial plane. Projected in this manner the miss distance from the center of Io was ~ 13,000 km (7 R_{Io}) in D4 coordinates, and ~ 7000 km (4 R_{Io}) in the D2 system (The D2 and D4 magnetic models are defined by E. J. Smith et al [1976].)

As Pioneer 11 passed the Io flux tube, all channels of detector E jumped to the highest counting rates recorded in either flyby. This

peak can be seen in Figure 12, and in more detail in Figure 15. Neither of the higher energy channels recorded such a spike, and so the particle energies were below several Mev. Certainly a local source is needed to explain such an impulsive event.

Figure 15 also shows the relative coordinates of the spacecraft and Io as projected to the equator using the D2 system. It is similar for D4. Pioneer 11 apparently passed to the west of the flux tube, and the electron spike ended abruptly just as the spacecraft crossed the Io L shell. As corotating magnetospheric plasma goes from west to east faster than Io's orbital motion, the trajectory is on the upstream side of the moon in this projection. The reader should be cautious with this statement, because it could look different with a more complex magnetic field model. Also Io itself could cause local disturbances which perturb the field. However, if the D2 projection is correct, particles upstream of Io should cause no more surprise than the other phenomena associated with this remarkable satellite.

One of the virtues of the sheath acceleration model is that it makes specific predictions that can be tested. The electron power content, energy spectra, angular distributions, and spatial extent are all important quantities to be determined. This information will be better known after more sophisticated analyses have been performed on the data, but, in the preliminary inspection, there are differences

between predictions and observations. The most significant of these are (1) that the pitch angle distribution is peaked perpendicular to the field line rather than parallel, (2) that there seem to be electrons with energies exceeding the maximum available sheath potential, and (3) that the peak found by Pioneer 11 was outside the Io sweeping region whereas those found by Pioneer 10 were inside. Although this is disappointing, the sheath model does achieve a major success in predicting an electron source of about the right energy, and it seems more likely that the sheath model needs to be embellished than that it should be dropped.

VI. THE BEHAVIOR OF ELECTRONS IN THE INNER JOVIAN MAGNETOSPHERE

The inner radiation belts of Jupiter consist of stably trapped particles in a dipole-like magnetic field, and the methods of radiation belt theory developed for Earth are applicable with minor modifications. The Pioneer 10 flyby demonstrated that, as in the case of Earth, the inner Jovian radiation belt is populated by particles which have diffused inward toward the planet, [McIlwain and Fillius, 1975]. The value of the radial diffusion coefficient has been estimated from a study of the absorption of these particles by the satellites (Section V). Evidence for pitch angle diffusion has been found in the angular distributions and in an analysis of the radial profile of the trapped electron density. [Fillius et al, 1976]

These effects are easiest to see after the data have been converted to density, τ, in phase space, which we express in units of $(ev\ -s)^{-3}$. We relate τ to the radiation intensity by $\tau = 900\ j/(pc)^2$ where pc is the particle momentum times the velocity of light expressed jointly in Mev, and j is the flux of particles $cm^{-2}s^{-1}ster^{-1}Mev^{-1}$. As a consequence of Liouville's Theorem, the phase space density should be constant along a dynamical trajectory. It follows that in the absence of sources or sinks τ should be constant everywhere, and it also follows that in time-stationary circumstances a local maximum is a sure manifestation of a source. Trajectories that intersect an absorbing surface, such as the planet or a moon, become vacated forward of the point of intersection. The image of the absorber is projected forward as a cluster of vacant trajectories -- a forbidden cone in velocity space. Although Liouville's Theorem

assures us that the cones always retain their identities, the orbits of trapped particles are so complex that forbidden and allowed cones become microscopically intermingled in a very complicated way. No realizable detector can resolve the individual allowed and forbidden cones; all that can be measured is a macroscopic average. A sink, local or not, dilutes the volume of phase space that is occupied at full density with an inextricable volume that is vacant, and a detector senses this dilution as a reduction in the apparent phase space density. A theoretical basis for dealing with this mixture has been worked out [Birmingham et al, 1967; Birmingham et al, 1974] and a diffusion-like equation is obtained for the ensemble-averaged phase space density. It is this, the macroscopic, or ensemble-averaged phase space density, that we refer to in this paper as τ.

Figure 16 shows near-equatorial profiles of τ vs L for electrons over a range of values of the first adiabatic invariant. These are from the Pioneer 10 inbound pass, and the method used to obtain τ from the data is described in McIlwain and Fillius [1975]. It is immediately apparent that the major source is on the left, there is a sink on the right, and the net diffusive flow is toward the planet. At low energies, a subsidiary maximum occurs just inside the orbit of Io at L = 5.9. This corresponds to the peak seen in Figure 14, but since it appears in the phase space density, Liouville's Theorem proves that it is caused by a local source.

If Figure 16 is a solution of the radial transport equation, one can demonstrate that losses must take place throughout the region

$3 \leq L \leq 10$. Lumping sources and sinks into one term, S, the radial equation is

$$\frac{\partial \tau}{\partial t} = L^2 \frac{\partial}{\partial L}\left(\frac{D}{L^2}\frac{\partial \tau}{\partial L}\right) + S \qquad (5)$$

where D is the radial diffusion coefficient. Inside 10 R_J, most profiles in Figure 16 can be described by a power law with slope of 4. Thus we will write as a solution of equation (5), $\tau(L) = \tau_1 L^{n_\tau}$ with $n_\tau \cong 4$. Mogro-Campero [1976] has represented the diffusion coefficient as a power law in L, $D(L) = D_1 L^{n_D}$, with $n_D \cong 4$. Anticipating that it is a sink, we treat the source/sink term as an exponential in time, and write $S = \frac{d\tau}{dt} = \frac{d}{dt}\left(\tau_o\, e^{\frac{-t}{T}}\right) = -\frac{\tau}{T}$. Finally, assuming that Figure 16 represents a steady state solution, $\frac{\partial \tau}{\partial t} = 0$. Substituting these representations into equation (5) and differentiating, we get

$$\frac{1}{T} = \frac{D(L)}{L^2}\,(n_D + n_\tau - 3)\, n_\tau \qquad (6)$$

Note that a lack of distributed losses would correspond to $T = \infty$, and in that case the equation would balance only if $n_D + n_\tau - 3 = 0$. As it stands, the equation will not balance without distributed losses, and their lifetime is given by

$$T \cong \frac{1}{20}\frac{L^2}{D(L)} \qquad (7)$$

At L = 5, T is about a year.

The identity of the loss mechanism has been discussed by Fillius et al [1976] and they conclude that the particles are lost from the equator by pitch angle diffusion into the planetary loss cone. The particle trajectories are thus vacated in the atmosphere, which is accessed along the line of force after pitch angle scattering takes place at the equator.

VII. MULTIPLE PEAKS NEAR PIONEER 11 PERIAPSIS

Data from Pioneer 11 exhibit multiple peaks in the particle flux profiles near the closest approach to the planet. These are shown in Figure 17 and their positions are listed in Table III. Note that the same features appear in both electron and proton profiles. Two of the minima, N1 and N4, are reasonably attributed to sweeping by Amalthea. There is some imprecision in matching L values, but this is presumably caused by uncertainties in the present magnetic field models. The remaining minima (and the maxima which complement them) are unexplained.

The reason for this multiple structure is a mystery, and it is one of the new and challenging problems of the Jovian radiation belts. Hypotheses that are specific to only one particle species cannot account for the fact that protons and electrons both exhibit the same features. Thus latitude-dependent synchrotron radiation losses, or regions of critical wave-particle interactions, seem to be incomplete explanations. A critic may speculate that our proton detector is really responding to electrons. He is referred to our earlier paper [Fillius and McIlwain, 1974b] for an account of the particle identification and background elimination procedures, but he will probably derive greater satisfaction from the fact that the University of Chicago fission detector independently recorded similar proton features [Simpson et al, 1975]. We regard the experimental evidence as convincing.

It remains, then, to explain the unexpected features with a mechanism that operates on both protons and electrons. The simplest

is absorption by a solid body. Indeed, we have attributed minima N1 and N4 to the sweeping effects of Amalthea. If the magnetic field is so distorted that the particle drift shells become rippled, the spacecraft could have passed through these features again. Alternatively, in a distorted field some of the drift shells might dip down to the planet's surface and be emptied. Detailed calculations of particle drift shells will be necessary to test these hypotheses. Furthermore the results of the calculations will only be as good as the magnetic field models, and the magnetometer experimenters have cautioned us against extrapolating to the planet's surface. However, it may still be possible to test these ideas.

A more radical hypothesis was raised by Acuña and Ness [1976]. They suggested that, if the drift shells were not sufficiently complex, the possibility should be considered of another, hitherto undetected, moon inside the orbit of Amalthea. It would not have to be a single mass, for a ring of smaller particles could do the job as well. Indeed, since minima N2 and N3 are inside the Roche limit, a particle ring is more likely. What with the similarities between Jupiter and Saturn, there seems to be no a priori reason against a dust ring near Jupiter, too. However, there are obvious questions which need to be investigated. Why has there been no optical detection of such a ring? What would be the gravitational effect on the other satellites and on the Pioneer spacecraft? Would one expect the Pioneer Meteoroid Detectors to detect the ring when they passed near it? This exciting hypothesis has obvious problems, and it will take some time to sort out all of the possibilities and ramifications.

Acknowledgement

We thank Drs. Carl McIlwain, Tony Mogro-Campero, and Wing-Huen Ip for their collaboration on the work reviewed here. This research was supported by NASA contracts NAS 2-5602, NAS 2-6552, and NASA Grant NASA-NGL 05-005-007.

References

Acûna, M. H.; and Ness, N. F. 1976. The complex main magnetic field of Jupiter. J. Geophys. Res. (in press).

Barish, Franklin D.; and Smith, Robert A. 1975. An analytical model of the Jovian magnetosphere. Geophys. Res. Letters 2, 269-272.

Birmingham, T. J.; Northrup, T. G.; and Fälthammar, C. G. 1967. Charged particle diffusion by violation of the third adiabatic invariant. Phys. Fluids 10, 2389-2398.

Birmingham, T.; Hess, W.; Northrup, T.; Baxter, R.; and Lojko, M. 1974. The electron diffusion coefficient in Jupiter's magnetosphere. J. Geophys. Res. 79, 87-97.

Brown, R. A., and Y. L. Yung, Io, Its Atmosphere and Optical Emissions, Proceedings of the Jupiter Colloquium held at Tucson, Arizona, May 1974, U of A Press.

Chenette, D. L.; Conlon, T. F.; and Simpson, J. A. 1974. Bursts of relativistic electrons from Jupiter observed in interplanetary space with the time variation of the planetary rotation period. J. Geophys. Res. 79, 3551-3558.

Fillius, R. W.; and McIlwain, C. E. 1974a. Radiation belts of Jupiter. Science 183, 314-315.

Fillius, R. W.; and McIlwain, C. E. 1974b. Measurements of the Jovian radiation belts. J. Geophys. Res. 79, 3589-3599.

Fillius, R. W.; McIlwain, C. E.; and Mogro-Campero, A. 1975a. Radiation belts of Jupiter: a second look. Science 188, 465-467.

Fillius, W.; McIlwain, C.; Mogro-Campero, A.; and Steinberg, G. 1976. Evidence that pitch angle scattering is an important loss mechanism for energetic electrons in the inner radiation belt of Jupiter. Geophys. Res. Letters, in press.

Hall, C. F. 1974. Pioneer 10. Science 183, 301-302.

Hall, C. F. 1975. Pioneer 10 and 11. Science 188, 445-446.

Judge, D. L., R. W. Carlson, F. M. Wu, U. G. Hartmann, "Pioneer 10 and 11 Ultraviolet Photometer Observations of the Jovian Satellites," Proceedings of the Jupiter Colloquium held at Tucson, Arizona, May 1974, U of A Press.

McDonald, F. B.; and Trainor, J. H. 1976. Observations of energetic Jovian electrons and protons. Proceedings of the Jupiter colloquium held at Tucson, Arizona May, 1975. University of Arizona Press.

McIlwain, C. E.; and Fillius, R. W. 1975 Differential spectra and phase space densities of trapped electrons at Jupiter. J. Geophys. Res. 80, 1341-1345.

Mead, G. D.; and Hess, W. N. 1973. Jupiter's radiation belts and the sweeping effect of its satellites. J. Geophys. Res. 78, 2793-2811.

Mead, Gilbert D. 1974. Magnetic coordinates for the Pioneer 10 Jupiter encounter. J. Geophys. Res. 79, 3514-3521.

Mihalov, J. D.; Collard, H. R.; McKibbin, D. D.; Wolfe, J. H.; and Intriligator, D. S. 1975. Pioneer 11 encounter : preliminary results from the Ames research center plasma analyzer experiment. Science 188, 448-451.

Mogro-Campero, A. 1976. Absorption of radiation belt particles by the inner satellites of Jupiter. Proceedings of the Jupiter colloquium held at Tucson, Arizona, University of Arizona Press.

Mogro-Campero, A.; and Fillius, W. 1975. The absorption of trapped particles by the inner satellites of Jupiter and the radial diffusion coefficient of particle transport. J. Geophys. Res. in press.

Reif, F. 1965. Fundamentals of statistical and thermal physics. McGraw-Hill, Inc. New York, pp 486-488.

Shawhan, S. D. 1976. Io sheath-accelerated electrons and ions. Proceedings of the Jupiter colloquium held at Tucson, Arizona May 1975, University of Arizona Press.

Simpson, J. A.; Hamilton, D.; Lentz, G.; McKibbin, R. B.; Mogro-Campero, A.; Perkins, M.; Pyle, K. R.; Tuzzolino, A. J.; and O'Gallagher, J. J. 1974a. Protons and electrons in Jupiter's magnetic field: results from the University of Chicago experiment on Pioneer 10. Science 183, 306-309.

Simpson, J. A.; Hamilton, D. C.; McKibben, R. B.; Mogro-Campero, A; Pyle, K. R.; and Tuzzolino, A. J. 1974b. The protons and electrons trapped in the Jovian dipole magnetic field region and their interaction with Io. J. Geophys. Res. 79, 3522-3544.

Simpson, J. A.; Hamilton, D. C.; Lentz, G. A.; McKibben, R. B.; Perkins, M.; Pyle, K. R.; Tuzzolino, A. J.; and O'Gallagher, J. J.; Jupiter revisited: first results from the University of Chicago charged particle experiment on Pioneer 11. Science 188, 455-458.

Simpson, J. A.; and McKibben, R. B. 1976. Dynamics of the Jovian magnetosphere and energetic particle radiation. Proceedings of the Jupiter colloquium held at Tucson, Arizona May 1975, University of Arizona Press.

Smith, Edward J.; Davis, Leverett Jr.; and Jones, Douglas E. 1976. Jupiter's magnetic field and magnetosphere. Proceedings of the Jupiter colloquium held at Tucson, Arizona May 1975, University of Arizona Press.

Smith, Robert A. 1976. Models of Jovian Decametric Radiation, Proceedings of the Jupiter colloquium held at Tucson, Arizona May 1975, University of Arizona Press.

Teegarden, B. J.; McDonald, F. B; Trainor, J. H.; Webber, W. R.; and Roelof, E. C. 1974. Interplanetary mev electrons of Jovian origin. J. Geophys. Res. 79, 3615-3622.

Trainor, J. H.; Teegarden, B. J.; Stilwell, D. E.; McDonald, F. B.; Roelof, E. C.; and Webber, W. R. 1974a. Energetic particle population in the Jovian magnstosphere: a preliminary note. Science 183, 311-313.

Trainor, J. H.; McDonald, F. B.; Teegarden, B. J.; Webber, W. R.; and Roelof, E. C. 1974b. Energetic particles in the Jovian magnetosphere. J. Geophys. Res. 79, 3600-3613.

Thomsen, M. F.; and Goertz, C. K. 1975. Satellite sweep-up effects at Jupiter. Trans Am. Geophys. Union 56, 428-9.

Van Allen, J. A.; Baker, D. N.; Randall, B. A.; Thomsen, M. F.; Sentman, D. D.; Flindt, H. R. 1974. Energetic Electrons in the magnetosphere of Jupiter. Science 183, 309-311.

Van Allen, J. A.; Randall, B. A.; Baker, D. N.; Goertz; Sentman, D. D.; Thomsen, M. F.; and Flindt, H. R. 1975. Pioneer 11 observations of energetic particles in the Jovian magnetosphere. Science 188, 459-462.

Van Allen, James A. 1976. High energy particles in the Jovian magnetosphere. Proceedings of the Jupiter colloquium held at Tucson, Arizona May 1974, University of Arizona Press.

Wolfe, J. H.; Mihalov, J. D.; Collard, H. R.; McKibbin, D. D.; Frank, L. A.; and Intriligator, D. S. 1974. Pioneer 10 observations of the solar wind interaction with Jupiter. J. Geophys. Res. 79, 3489-3500.

TABLE I

CHARACTERISTICS OF THE UNIVERSITY OF CALIFORNIA, SAN DIEGO
PIONEER 10 TRAPPED RADIATION DETECTOR
AT JUPITER ENCOUNTER, DECEMBER 1973

Designation	Channels	Discrimination Levels		Particle Sensitivity	Geometric Factor
C	C1	31 photoelectrons	>	6 Mev electrons	11.5cm^{2}ster
	C2	65 photoelectrons	>	9 Mev electrons	4.5cm^{2}ster
Cerenkov Counter	C3	135 photoelectrons	>	13 Mev electrons	0.5cm^{2}ster
E	E1	.089 Mev	>	.16 Mev electrons	1.3 x10^{-2}cm^{2}ster
	E2	.19 Mev	>	.255Mev electrons	1.04x10^{-2}cm^{2}ster
Electron Scatter Counter	E3	.40 Mev	>	.460Mev electrons	5.7 x10^{-3}cm^{2}ster
M	M1	.40 Mev	>	35 Mev electrons	.038cm^2
Minimum Ionizing	M2	.85 Mev		background	
Particle Counter	M3	1.77 Mev	>	80 Mev protons	

22 March 74

74WF-4-15

TABLE II

PRELIMINARY CHARACTERISTICS OF THE UNIVERSITY OF CALIFORNIA, SAN DIEGO
PIONEER 11 TRAPPED RADIATION DETECTOR
AT JUPITER ENCOUNTER, DECEMBER 1974

Designation	Channels	Discrimination Levels	Particle Sensitivity	Geometric Factor
C	C1	31 photoelectrons	$\geq$ 5 Mev electrons	$\sim$ 13.5 cm^2ster
	C2	65 photoelectrons	$\geq$ 8 Mev electrons	$\sim$ 5.9 cm^2ster
Cerenkov Counter	C3	135 photoelectrons	$\geq$ 12 Mev electrons	$\sim$ 1.0 cm^2ster
	CDC	10^{-13} - 10^{-5} Amp	$\geq$ 1 Mev electrons	$\sim$ 35 cm^2ster
E	E1	.089 Mev	> .16 Mev electrons	1.3 x 10^{-2} cm^2ster
	E2	.19 Mev	> .255 Mev electrons	1.04 x 10^{-2} cm^2ster
Electron Scatter Counter	E3	.40 Mev	> .460 Mev electrons	5.7 x 10^{-3} cm^2ster
M	M1	.40 Mev	> 35 Mev electrons	.038 cm^2
Minimum Ionizing	M2	.85 Mev	background	
Particle Counter	M3	1.77 Mev	> 80 Mev protons	
SP Scintillator	SPDC	10^{-14} - 10^{-5} Amp	> 150 kev protons	7.4×10^{-23} amp $ev^{-1} cm^2$ sec str(p)
			> 10 kev electrons	7.4×10^{-23} amp $ev^{-1} cm^2$ sec str(e)
SE Scintillator	SEDC	10^{-14} - 10^{-5} Amp	> 150 kev protons	$2. \times 10^{-24}$ amp $ev^{-1} cm^2$ sec str(p)
			> 10 kev electrons	1.4×10^{-23} amp $ev^{-1} cm^2$ sec str(e)

68

TABLE III

Zenocentric Coordinates for
Particle Features in Figure 17

Feature in Figure 17	Time	Zenocentric Coordinates		
		$R(R_J)$	Latitude (degrees)	Longitude III (degrees)
N1	0455	1.78	- 39.5	312
X1	0512	1.62	- 24.6	342
N2	0518	1.60	- 18.2	351
X2	0538	1.66	3.9	22
N3	0546	1.74	12.0	33
X3	0553	1.82	18.3	43
N4	0611	2.11	31.0	67

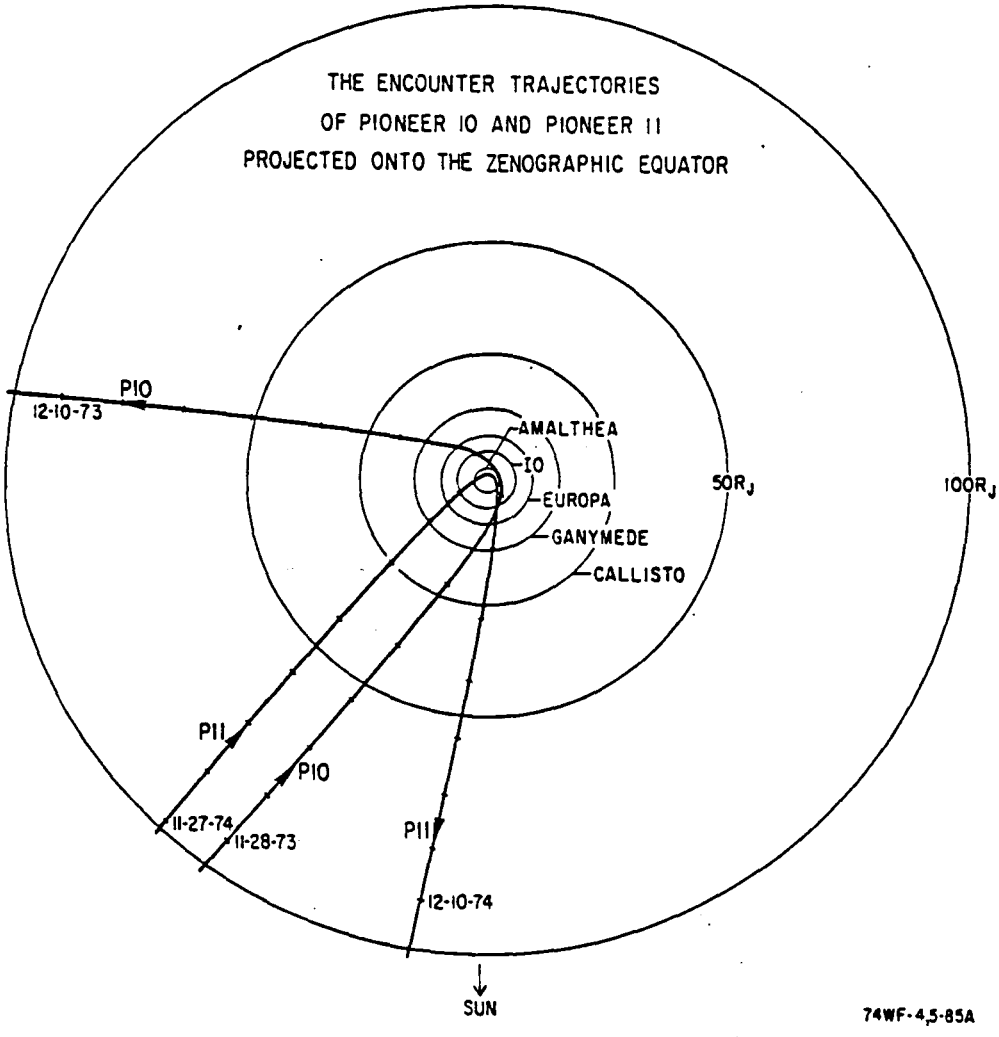

Fig. 1 Projection of the Pioneer 10 and Pioneer 11 trajectories on the equatorial plane of Jupiter. The dates mark the first and last magnetopause crossings for each flyby.

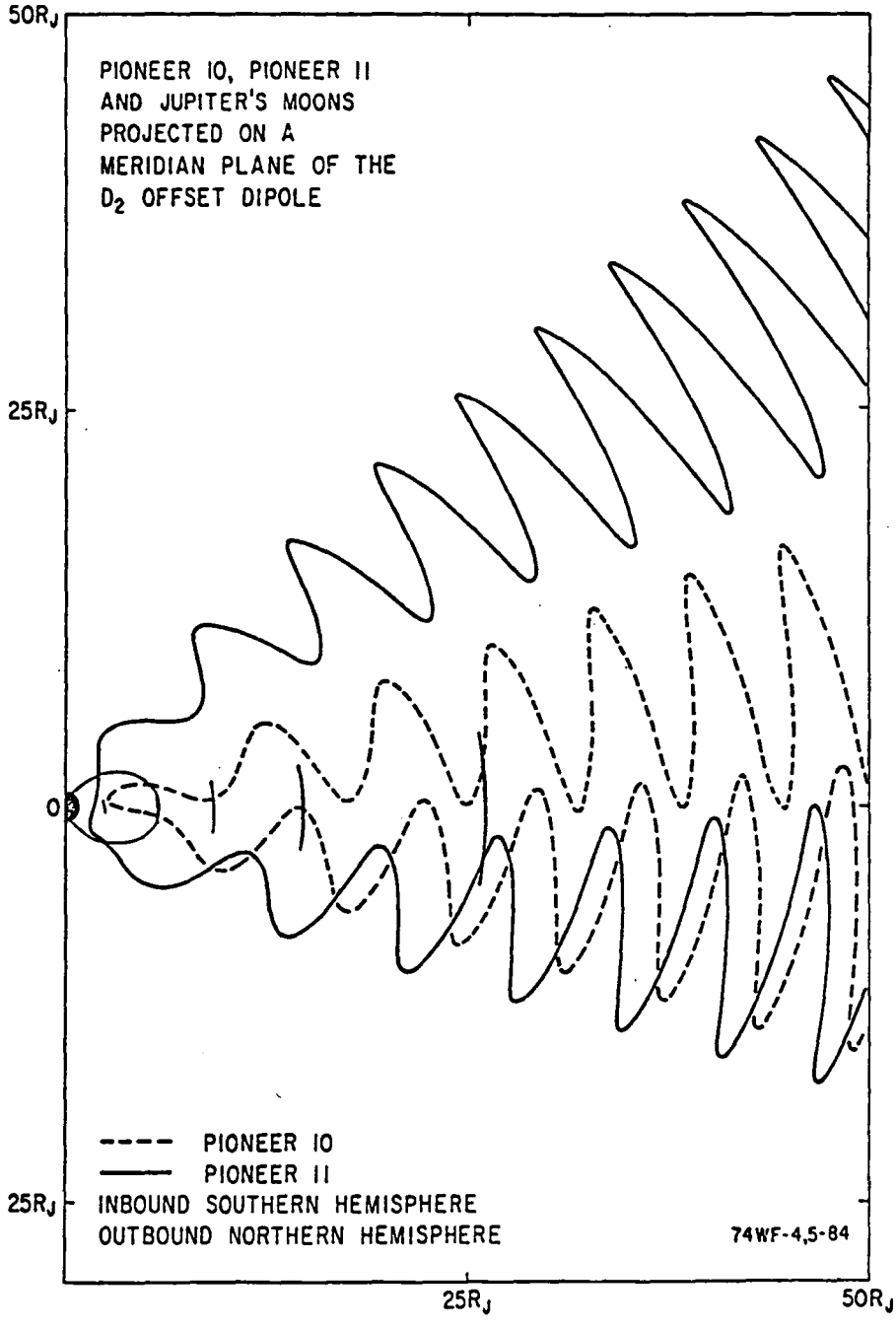

Fig. 2 The orbits of Jupiter's five innermost moons and the trajectories of Pioneers 10 and 11 projected on a magnetic meridian plane. The outbound leg of the Pioneer 11 flyby was at high magnetic latitude, whereas the other three legs were all near the magnetic equator. Although the magnetic field is not well represented by a dipole beyond 5 to 15 R_J, we show the projection farther out for illustrative purposes.

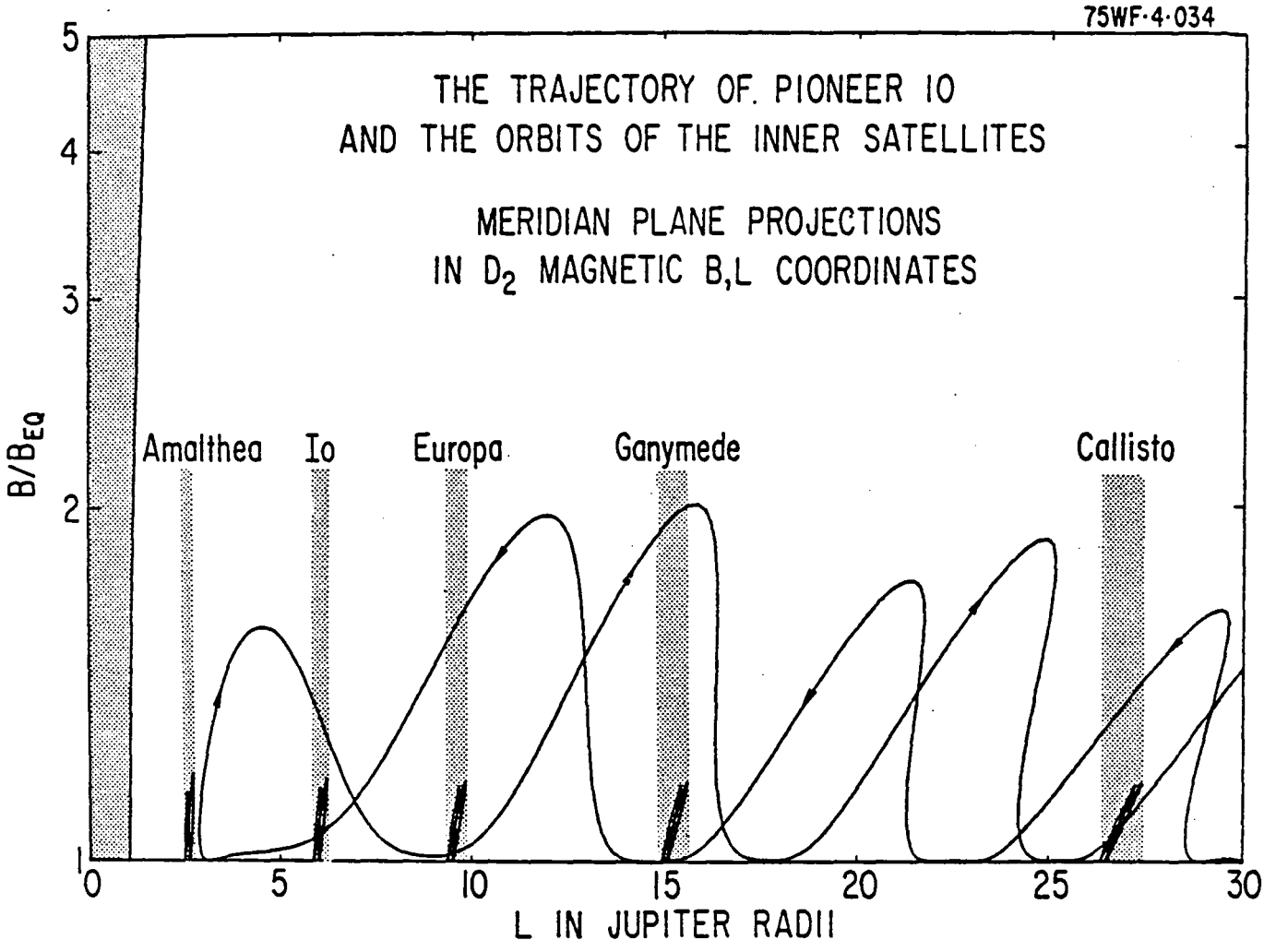

Fig. 3a Meridian plane projection in magnetic dipole coordinates. The equator lies along the abscissa, and the southern hemisphere is reflected into the upper quadrant. Magnetic lines of force are straight vertical lines from the equator to the planet's surface, which arches upward from the left side of the figure. The ordinate is the value of the scalar magnetic field normalized to the value at the equator. (Pioneer 10)

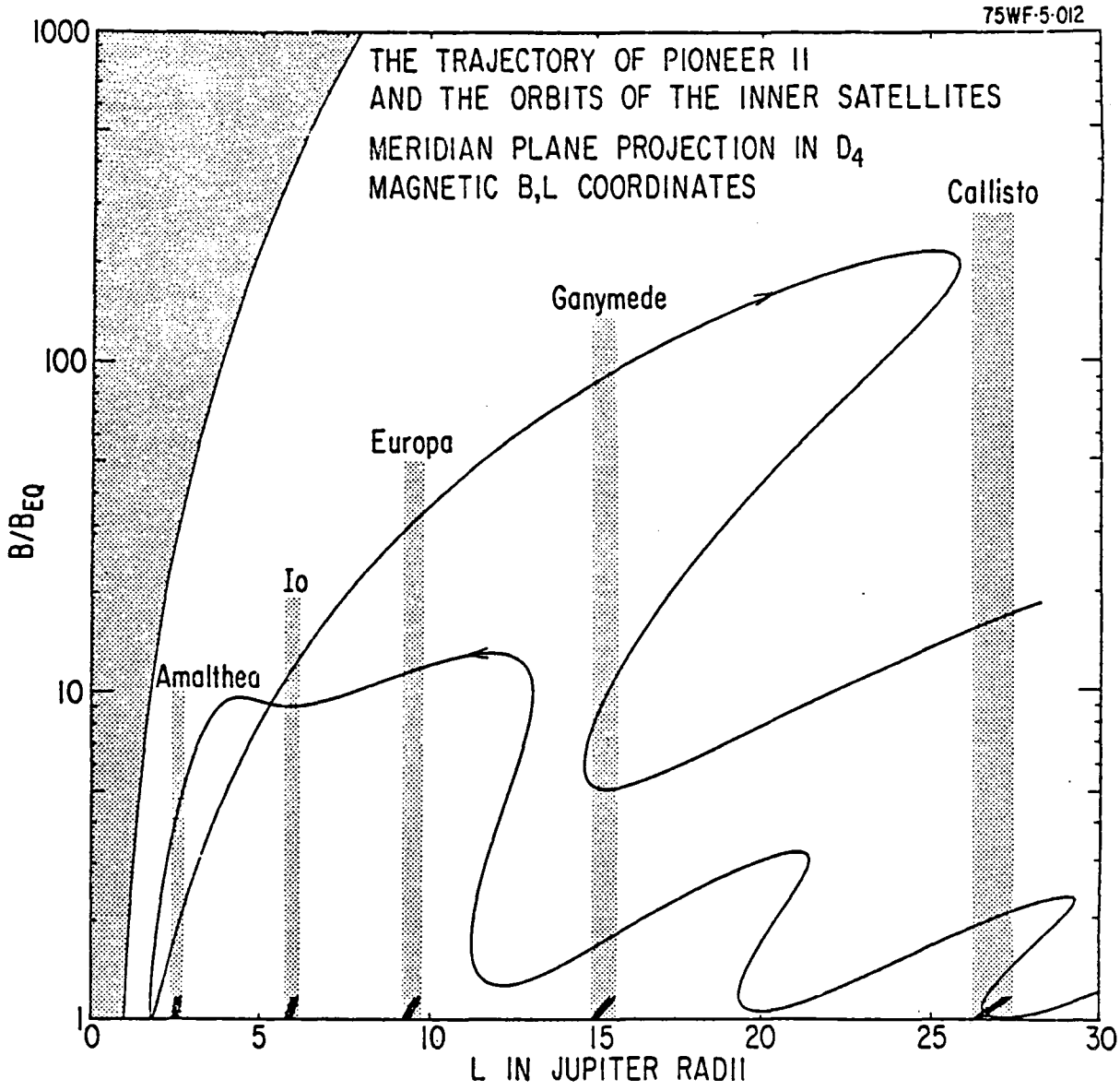

Fig. 3b Meridian plane projection in magnetic dipole coordinates. The equator lies along the abscissa, and the southern hemisphere is reflected into the upper quadrant. Magnetic lines of force are straight vertical lines from the equator to the planet's surface, which arches upward from the left side of the figure. The ordinate is the value of the scalar magnetic field normalized to the value at the equator. (Pioneer 11)

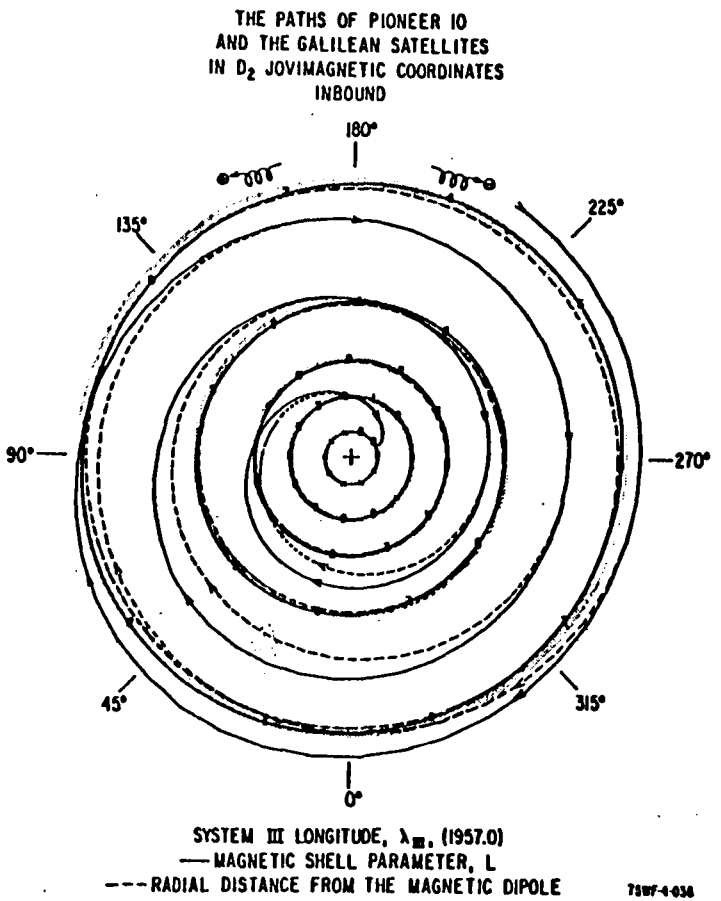

Fig. 4a
Vertigo Diagram for Pioneer 10 Inbound

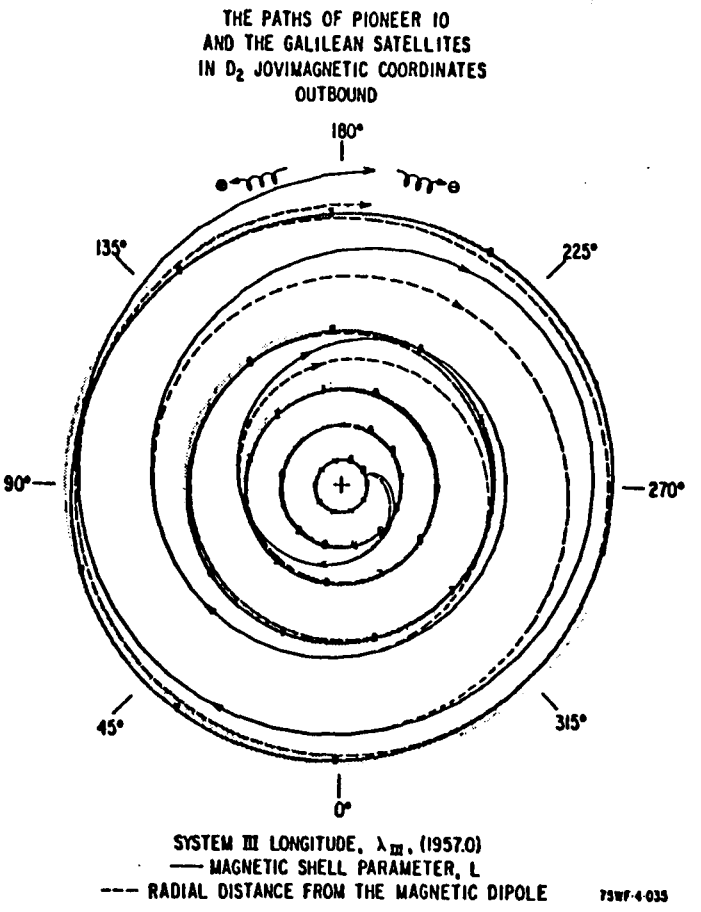

Fig. 4b
Vertigo Diagram for Pioneer 10 Outbound

The spacecraft trajectory and the five satelite orbits in a coordinate system fixed to Jupiter and rotating with the planet at the System III (1957.0) rotation rate. The track of each object is represented twice. The dashed lines represent the radial distance from the planet and the solid lines show the L values. Where the lines coincide an object is on the magnetic equator and where they are farthest apart it is at maximum latitude. The L shells traversed by each of the moons are shaded. Plasma and low energy trapped particles corotate with Jupiter and so remain fixed in this coordinate system, but high energy particles drift in circles, electrons westward and protons eastward. The zero on each moon's track indicates the position of the moon when the spacecraft crossed its L shell, and the other figures indicate where the moon was a given number of hours earlier. The large amount of information available in these figures makes them useful, but because it takes some concentration to interpret them, we call these figures vertigo diagrams.

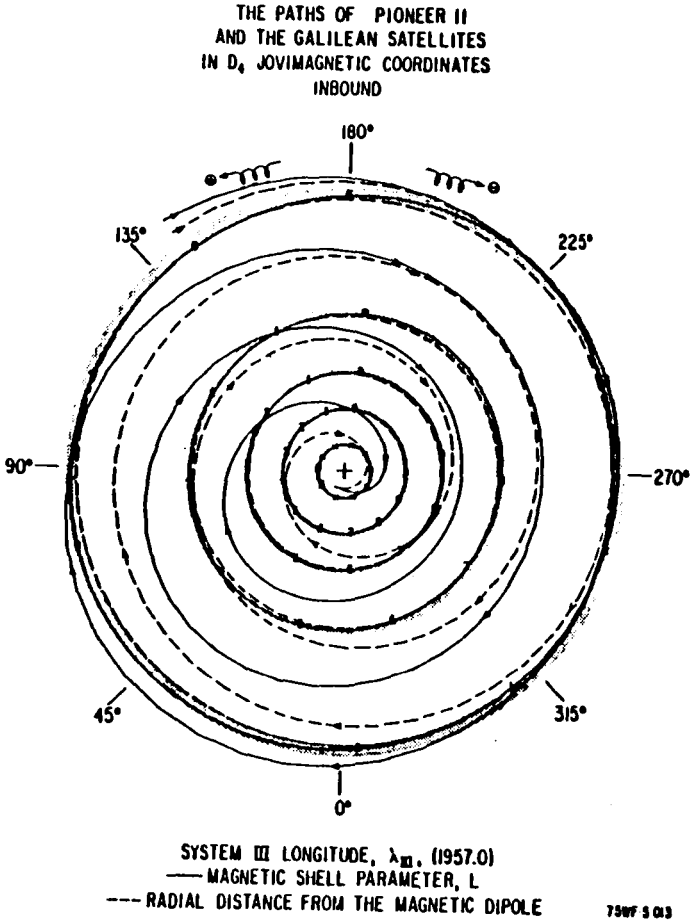

Fig. 5a

Vertigo Diagram for Pioneer 11 Inbound

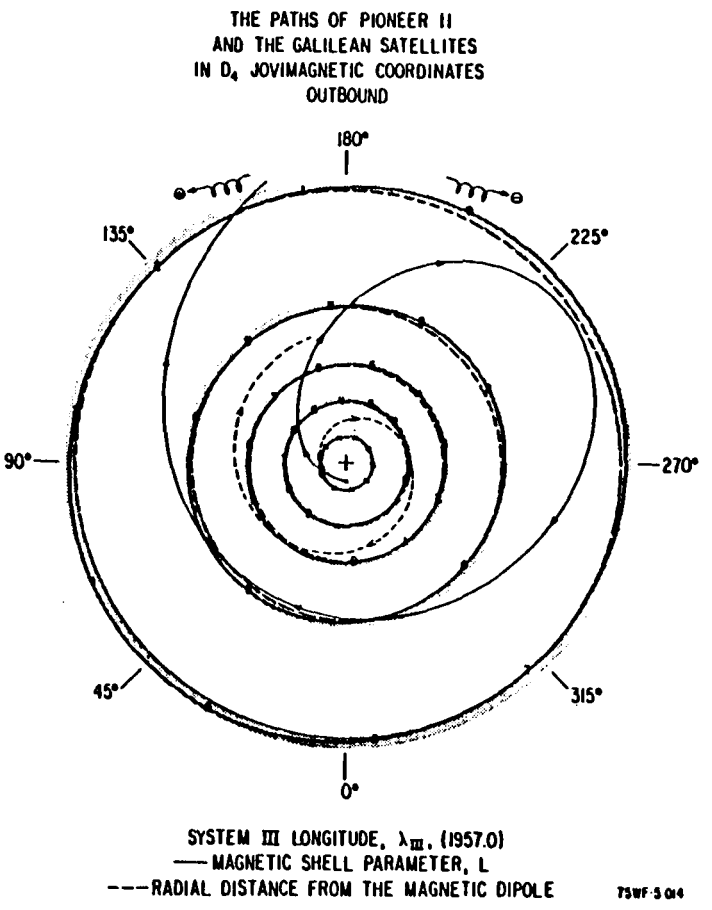

Fig. 5b

Vertigo Diagram for Pioneer 11 Outbound

The spacecraft trajectory and the five satelite orbits in a coordinate system fixed to Jupiter and rotating with the planet at the System III (1957.0) rotation rate. The track of each object is represented twice. The dashed lines represent the radial distance from the planet and the solid lines show the L values. Where the lines coincide an object is on the magnetic equator and where they are farthest apart it is at maximum latitude. The L shells traversed by each of the moons are shaded. Plasma and low energy trapped particles corotate with Jupiter and so remain fixed in this coordinate system, but high energy particles drift in circles, electrons westward and protons eastward. The zero on each moon's track indicates the position of the moon when the spacecraft crossed its L shell, and the other figures indicate where the moon was a given number of hours earlier. The large amount of information available in these figures makes them useful, but because it takes some concentration to interpret them, we call these figures vertigo diagrams.

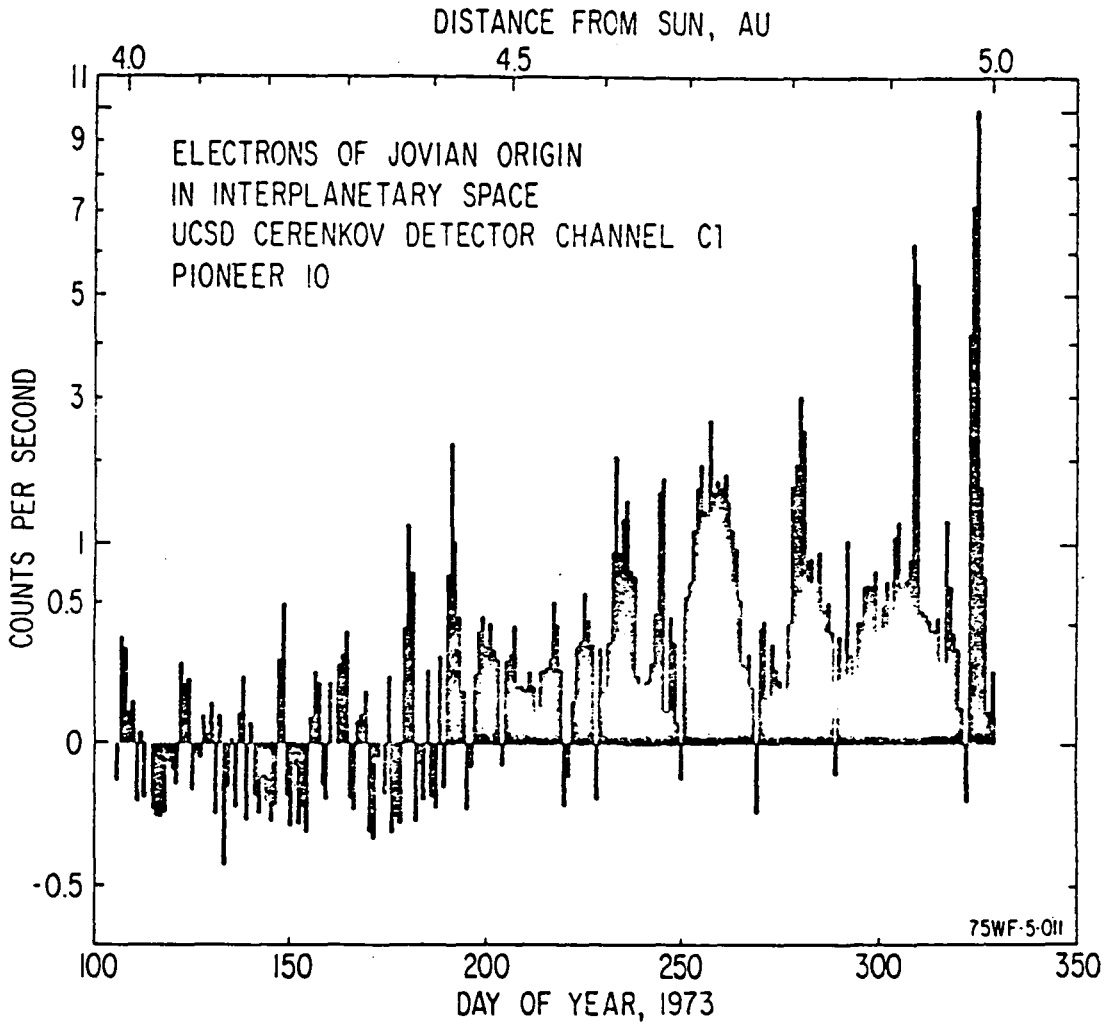

Fig. 6 Electrons from the Jovian magnetosphere found in interplanetary space before the Pioneer 10 encounter. The data points are one-day averages, and the counting rate from cosmic ray nucleons has been subtracted out. The contribution from cosmic ray nucleons has been eliminated by a linear subtraction procedure. Negative counting rates are caused by the errors and statistical uncertainties in this procedure.

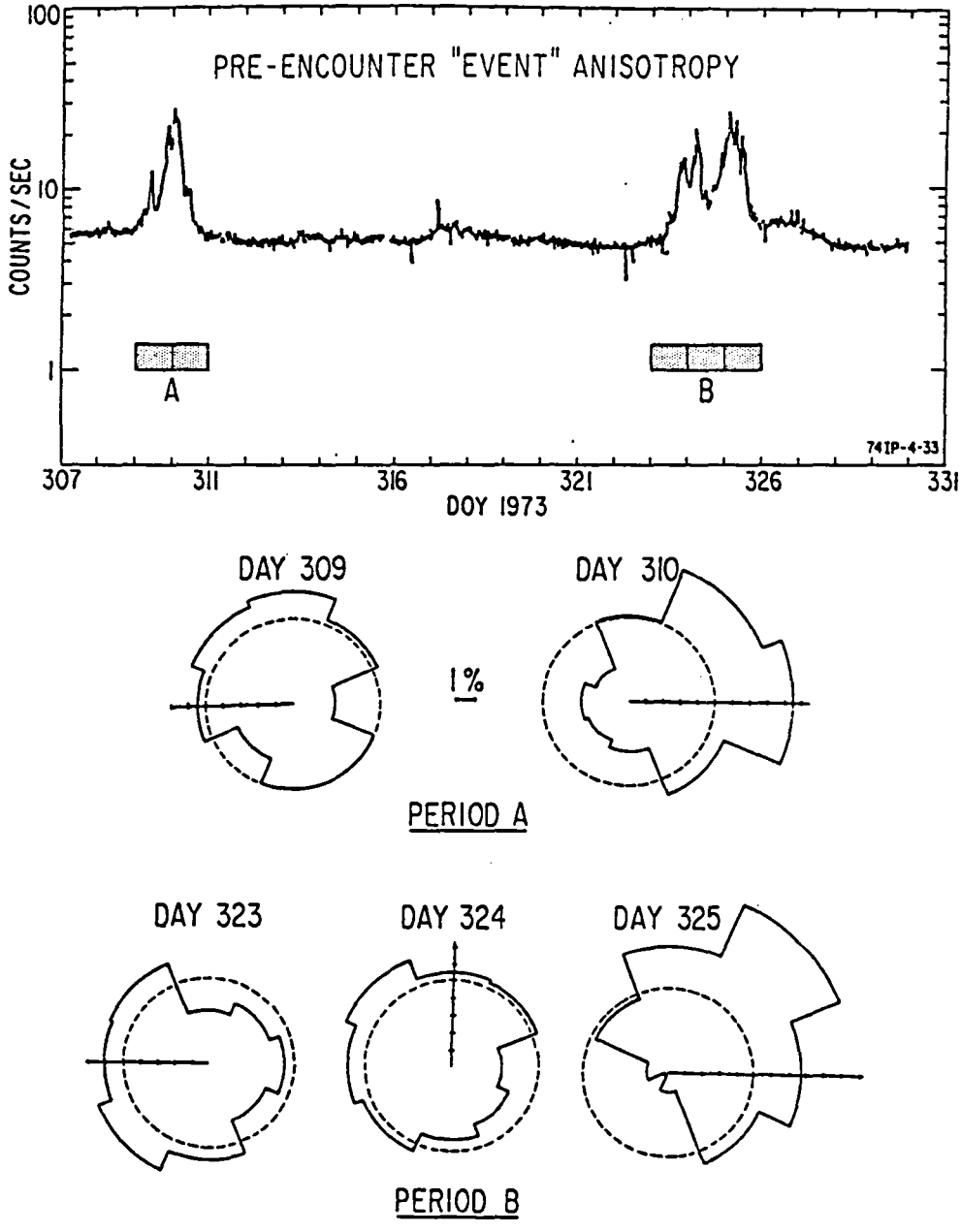

Fig. 7 Bursts of Jovian electrons that occurred in interplanetary space several days before encounter. No subtraction has been performed in this figure to eliminate the nucleonic cosmic ray counting rate of about 5 sec^{-1}. The cogwheels represent the directionality of the counting rates in the spacecraft equatorial plane, which is normal to the spacecraft-Earth vector. On days 310 and 325 there was a marked flow away from Jupiter.

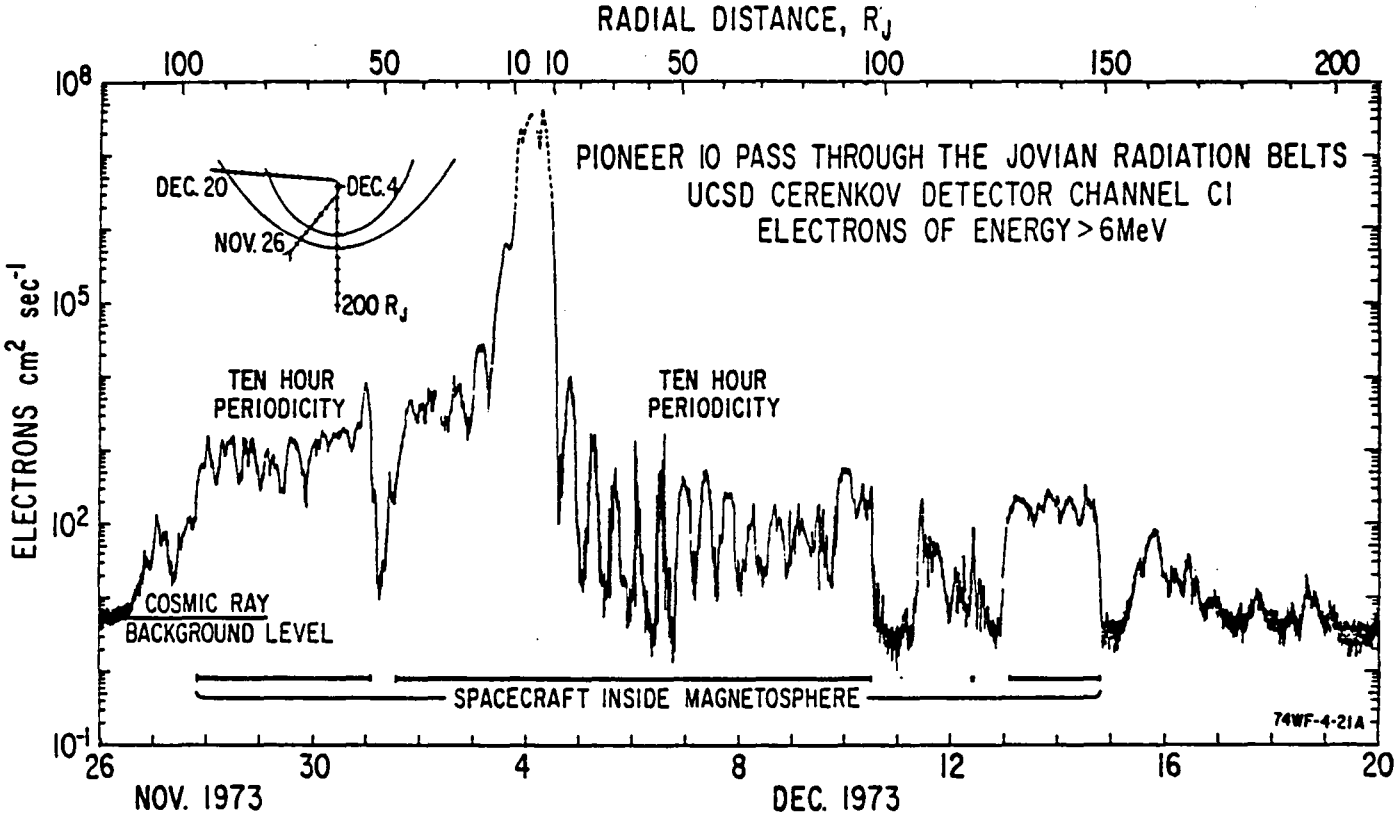

Fig. 8 Jupiter's radiation belts, end to end. It took about three weeks for each of the Pioneer spacecraft to fly through this enormous region of space. The radiation intensity in the inner magnetosphere is four orders of magnitude higher than in the surroundings. The outer magnetosphere is characterized by periodic fluctuations at the planetary rotation rate. Because of variations in the size of the outer magnetosphere, the spacecraft crossed and recrossed the magnetospheric boundary, or magnetopause, several times inbound and outbound.

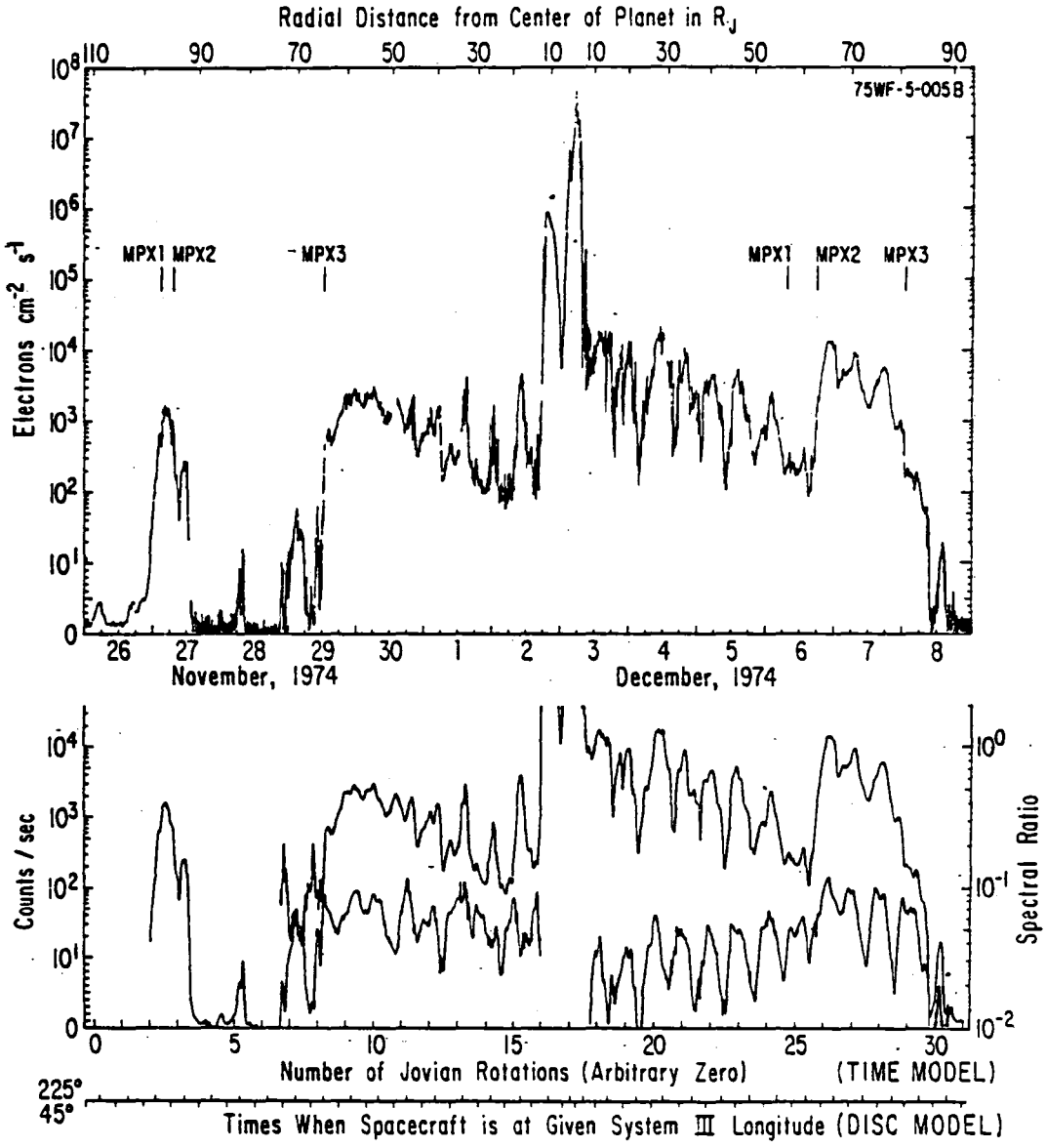

Fig. 9 (a) Time profile of Jupiter's radiation belts along the Pioneer 11 trajectory. The flux is of electrons of energy E > 5 Mev. The labels MPX-1, MPX-2, and MPX-3 mark the times when the spacecraft entered or left the magnetosphere.

(b) Running one-hour averages of data, filtered to show the ten-hour periodicity more clearly. The middle trace is the flux of > 5 Mev electrons, the same as in (a) above. The bottom trace is the ratio of two channels with energy thresholds above and below 5 Mev. Higher ratios indicate harder spectra.

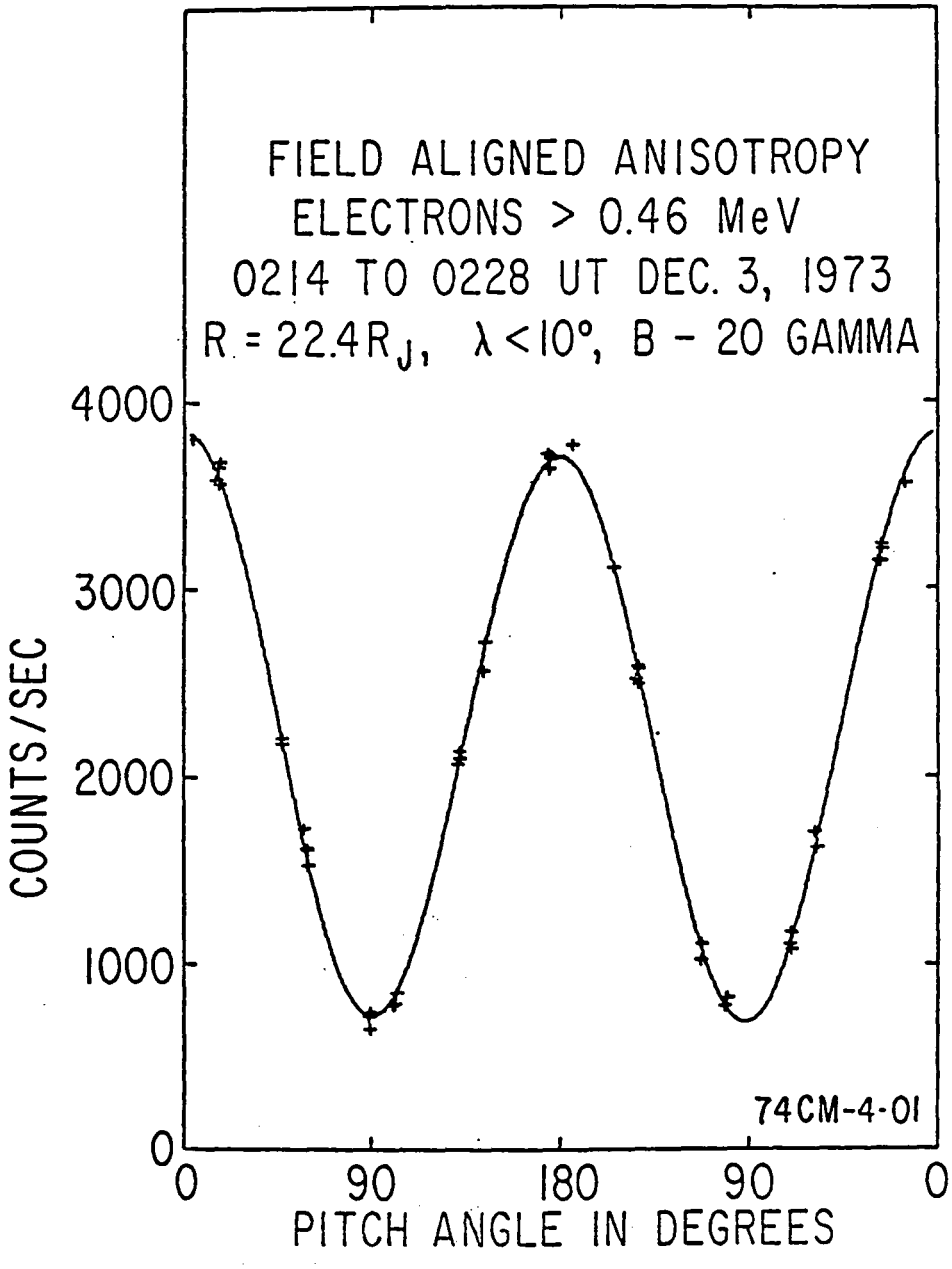

Fig. 10 The pitch angle distribution of ~ 1/2 Mev electrons during an episode of a field-aligned, or "dumbbell," angular distribution. This episode occurred while the inbound Pioneer 10 spacecraft was very near the equator at an L value of about 22 R_J.

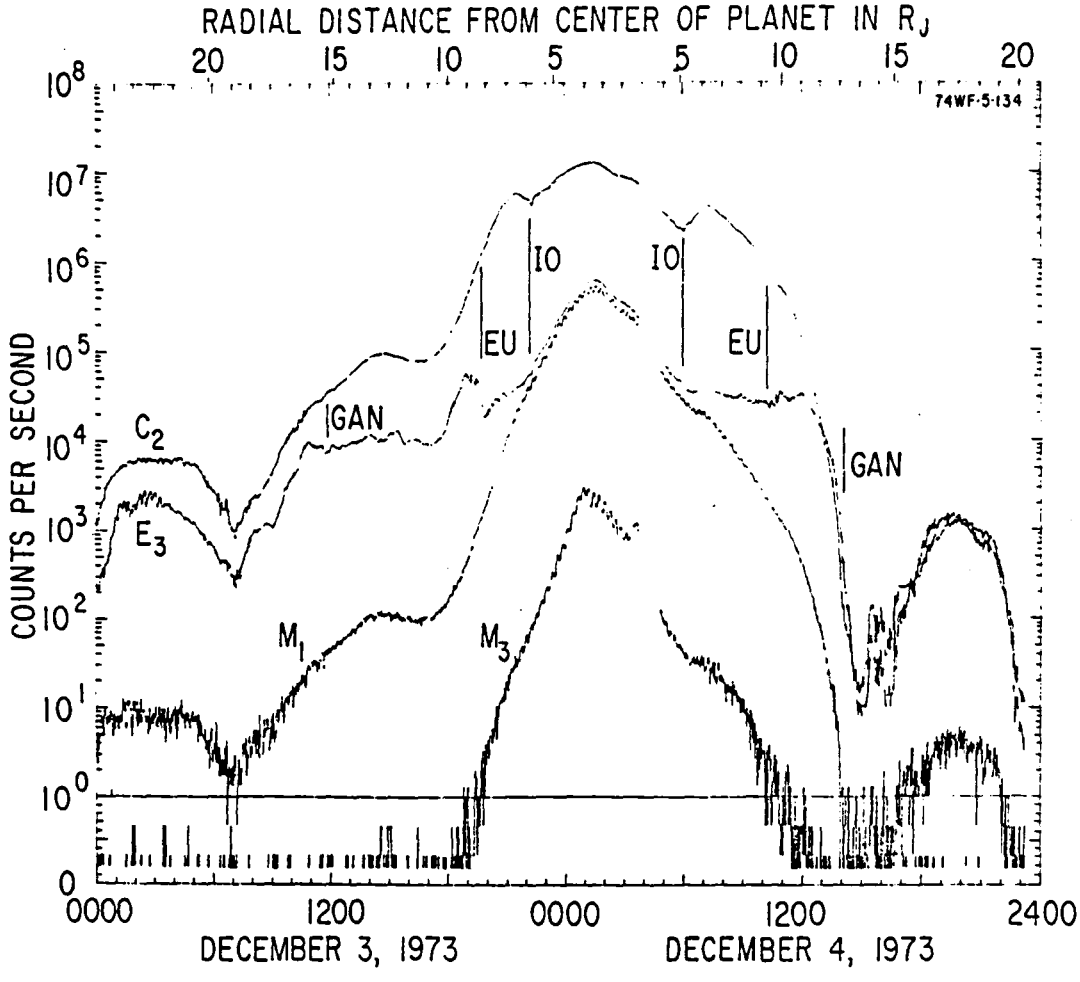

Fig. 11 Profile of Jupiter's inner radiation belt taken by Pioneer 10. Channel C2 counts electrons of energy E > 9 Mev; E3, electrons of E > .43 Mev; M1, electrons of E > 35 Mev; and M3, protons of E > 80 Mev. There are clear absorption features at the positions of Io and Europa, and a questionable one at Ganymede. The dumbbell pitch angle distribution shown in the last figure occurred during the subsidiary peak at the left of this figure.

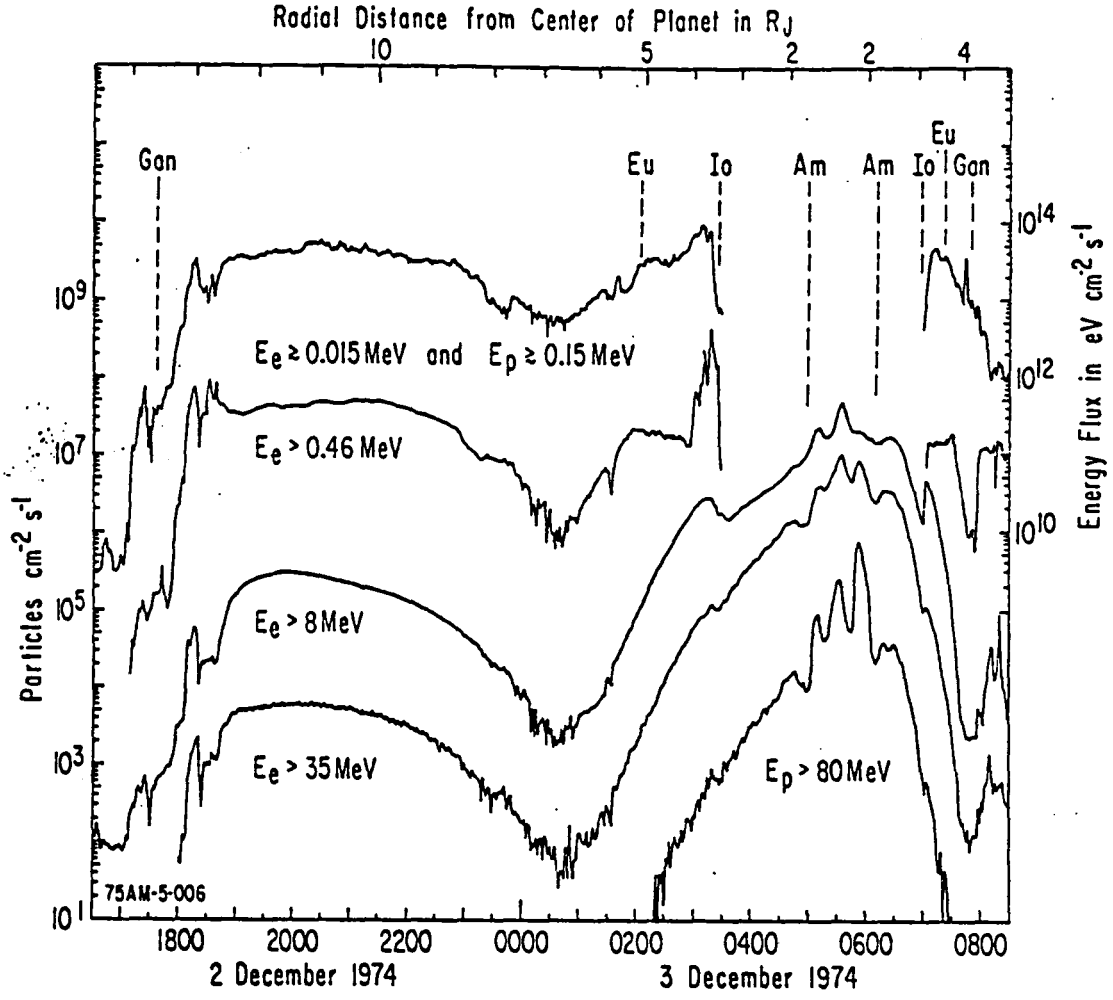

Fig. 12 Pioneer 11 profile of Jupiter's inner radiation belt. The uppermost trace shows the combined energy flux for electrons and protons above the lower threshold and below an upper limit of ~ 0.1 Mev for electrons and several Mev for protons. The right-hand scale refers to the uppermost trace only; all other profiles should be measured against the left-hand scale. Pioneer 11 passed the orbit of Amalthea in addition to the other satellites, and absorption features were seen for the inner moon as well.

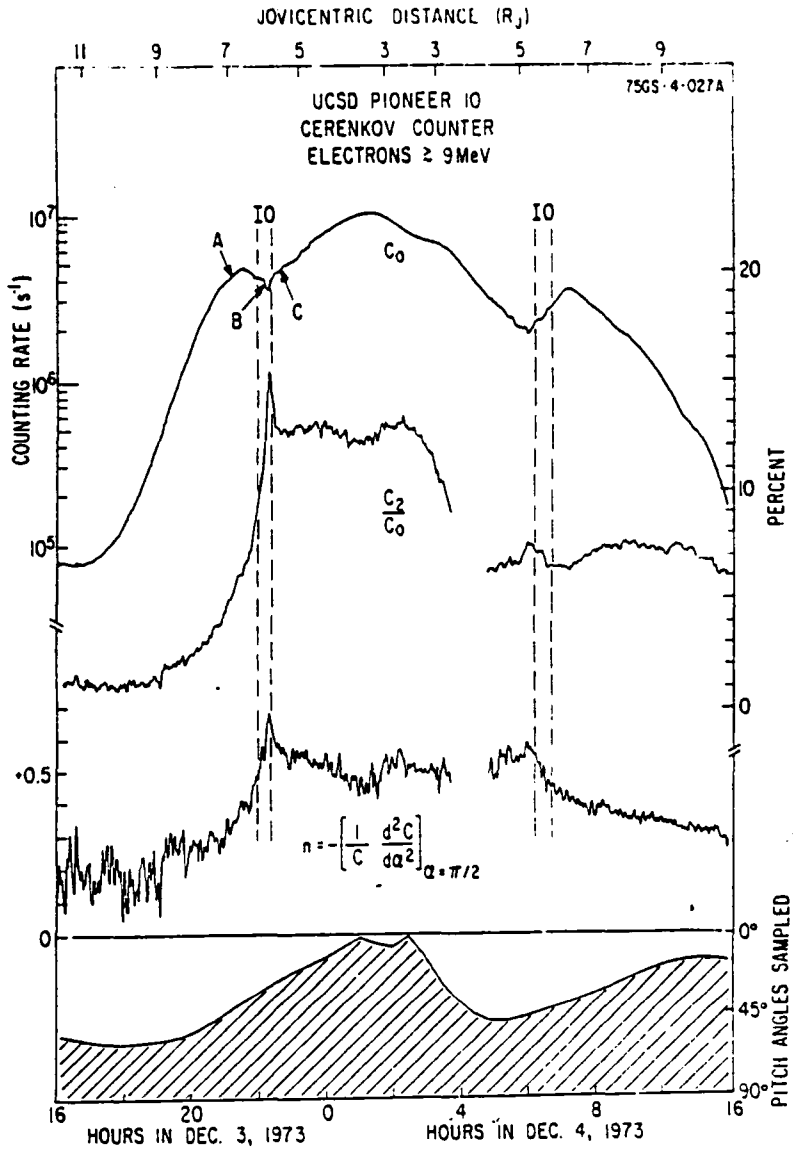

Fig. 13 Angular distribution data for the UCSD Cerenkov counter on Pioneer 10. The top trace is the spin-averaged count rate for electrons of E > 9 Mev, and shows the Io absorption features. The second trace shows the modulation amplitude at twice the spin frequency. In the region of Io the higher amplitude indicates a sharper pancake angular distribution, but because the detector is in the spacecraft equatorial plane, it samples the pitch angle distribution obliquely. The third trace shows the index, n, that would result from representing the pitch angle distribution near $\alpha = \pi/2$ in the form $\sin^n\alpha$. Again, higher values indicate a sharper pancake, and we see that the pitch angle distribution is sharper when Pioneer 10 crosses Io's L shell outbound as well.

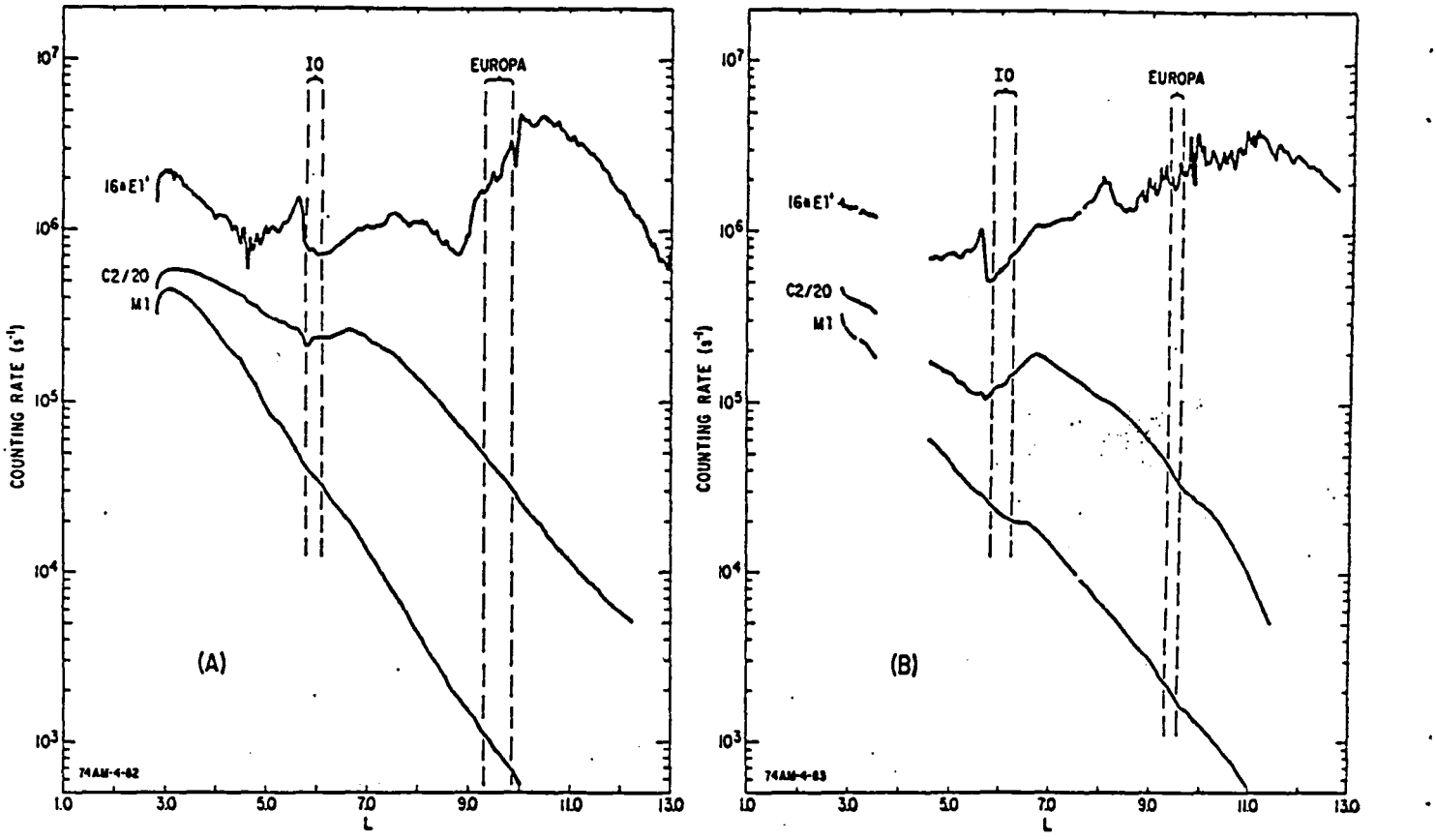

Fig. 14 Counting rates in the inner region plotted vs the magnetic parameter, L, calculated using D_2 magnetic coordinates. Channel E1 counts electrons of energy E > 0.16 Mev; C2 counts electrons of E > 9 Mev; and M1, electrons > 35 Mev. Note that the E1 and C2 counting rates are multiplied by scaling factors in order to share the same vertical axis.

(A) Pioneer 10 inbound

(B) Pioneer 10 outbound

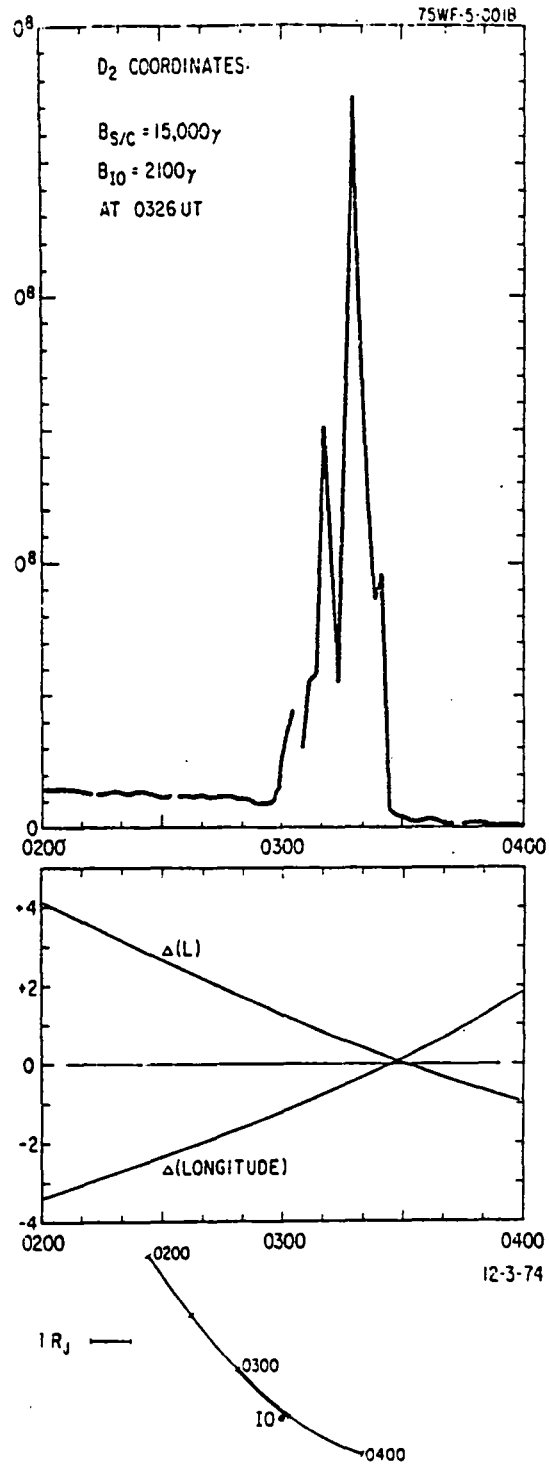

Fig. 15 Detail of the Pioneer 11 flyby of the Io flux tube, showing the local spike of energetic electrons. The relative magnetic coordinates of Io and Pioneer 11 were calculated using the D_2 field model. The relationship looks the same for D_4, but it might be different in a higher order model.

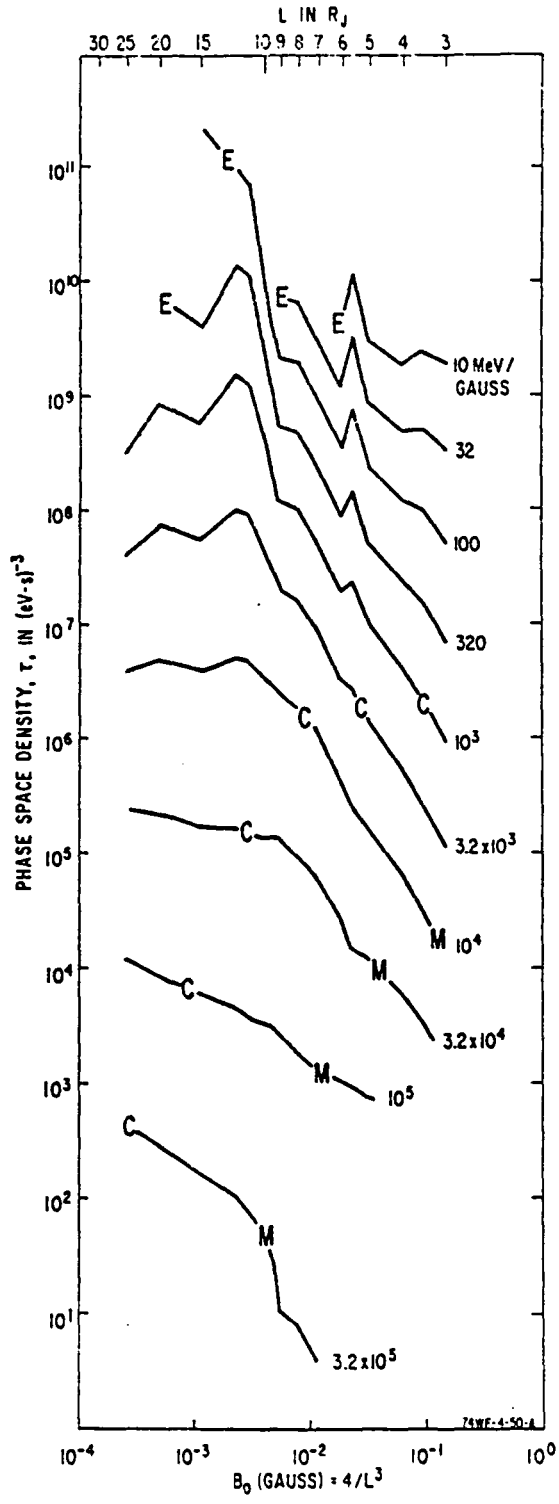

Fig. 16 Phase space density τ vs L at several values of the first adiabatic invariant. The second invariant is approximately zero. The physical processes acting on the particles are more apparent after the data have been converted to density in phase space.

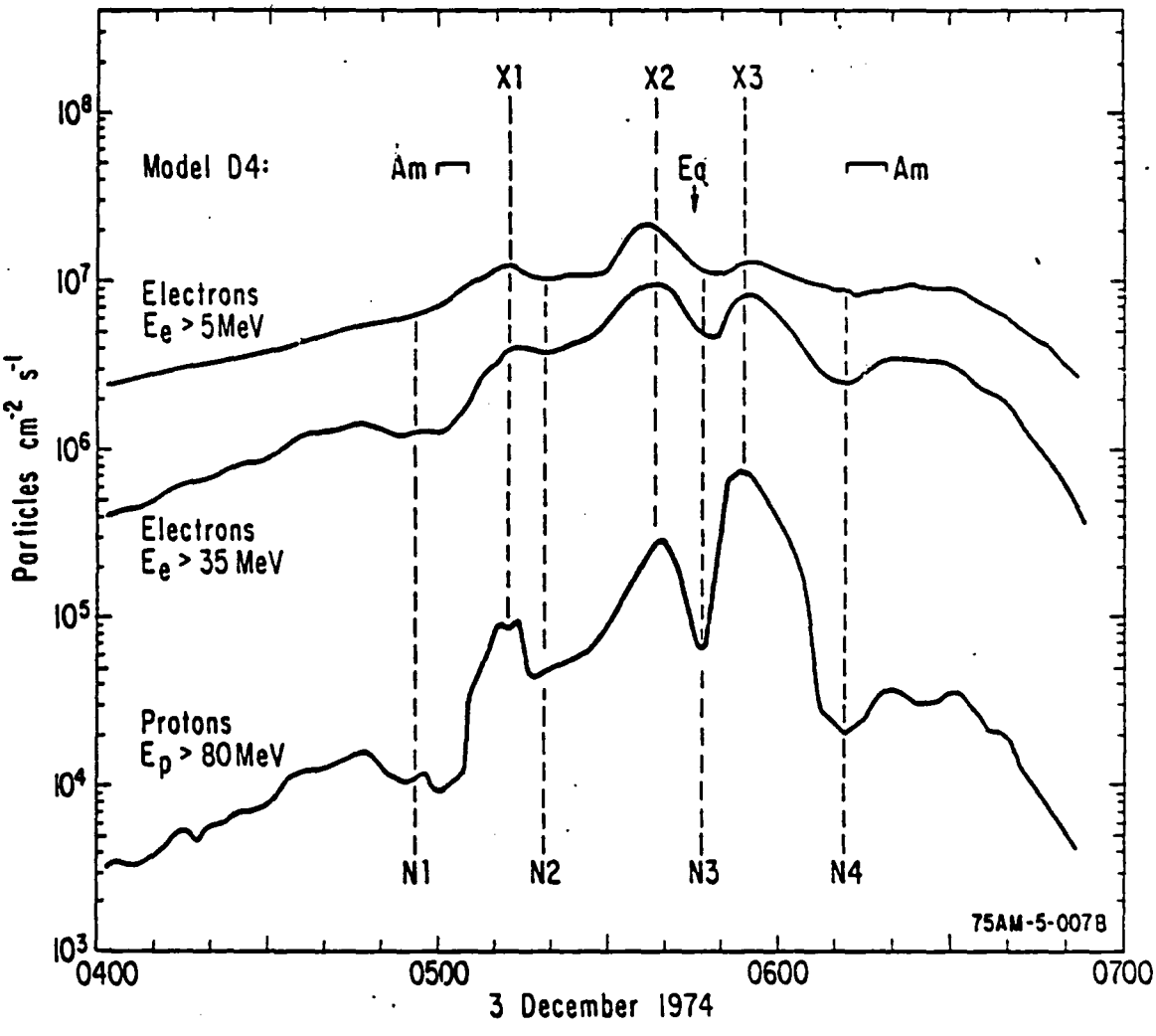

Fig. 17 Electron and proton fluxes measured near the closest approach of Pioneer 11 to Jupiter (1.6 R_J from the center of the planet at 0523). The multiple peak structure is unexplained, and could be accounted for by magnetic field anomalies, a dust ring, or some other cause.

Vol. 3, No. 1 Geophysical Research Letters January 1976

EVIDENCE THAT PITCH ANGLE SCATTERING IS AN IMPORTANT LOSS MECHANISM FOR ENERGETIC ELECTRONS IN THE INNER RADIATION BELT OF JUPITER

Walker Fillius, Carl McIlwain, Antonio Mogro-Campero and Gerald Steinberg

University of California, San Diego
La Jolla, California 92093

Abstract. Analysis of data from the Pioneer 10 flyby discloses that pitch angle scattering plays an important part in determining the distribution of energetic electrons in the inner magnetosphere of Jupiter. Angular distributions measured by the UCSD Cerenkov detector reveal that redistribution takes place in pitch angle. Additionally, the radial profile of phase space density along the equator demands simultaneous particle losses. The loss rates are too high to be accounted for by synchrotron radiation loss, but are reasonably attributed to pitch angle scattering into the planetary loss cone.

Introduction

Pitch angle scattering plays an essential role in determining the shape of the earth's trapped electron belts (Lyons and Thorne, 1973). It has been argued on theoretical grounds that the same mechanisms should be important at Jupiter (Coroniti, 1974). After Pioneer 10 discovered that significant numbers of trapped electrons were lost between 5 and 3 Jovian radii (Fillius and McIlwain, 1974), McIlwain and Fillius (1975) suggested pitch angle scattering as one of several processes that might explain the losses. In this paper we show angular distribution measurements which demonstrate pitch angle scattering of relativistic electrons, and we further examine the phase space density of equatorial electrons to obtain a quantitative estimate of the loss rate. We demonstrate that synchrotron energy loss is not a large factor for $L > 3$, and that pitch angle scattering can cause the required losses. Van Allen et. al. (1975) and Baker and Van Allen (1976) have also proposed that pitch angle scattering takes place in the same region, basing their arguments on the shape of the angular distributions and energy spectra. The evidence we cite in this paper comes from the phase space densities and the radial dependence of the angular distributions.

Evidence for Pitch Angle Scattering in the Angular Distribution Measurements

Independent of particle losses, the angular distributions measured by the UCSD instrument on Pioneer 10 require pitch angle scattering for their interpretation. To analyze our directional data we expand it in a partial Fourier series.

$$C(\alpha(\theta)) = f(\theta) = C_0 + C_1 \sin(\theta - \theta_1) + C_2 \sin 2(\theta - \theta_2) + C_4 \sin 4(\theta - \theta_4) \quad (1)$$

where α is the angle between the detector look axis and the magnetic field. θ is measured in the spacecraft equatorial plane to the detector look axis from the projection of the magnetic field vector. C is the observed count rate. It is obtained as a function of the spacecraft spin angle, θ, but it can be expressed as a function of the pitch angle, α, by using the magnetic field measurements (Smith, private communication) to give $\alpha(\theta)$.

For the period of interest the dominant modu-

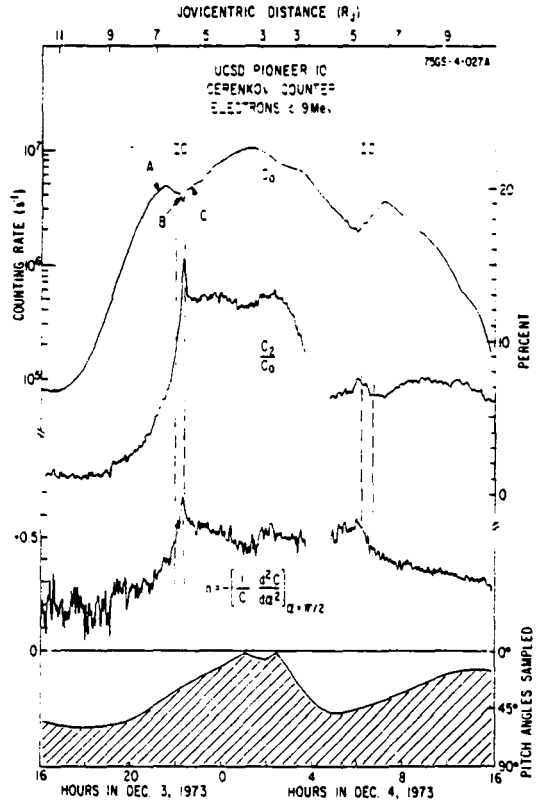

Fig. 1. The top trace shows the spin-averaged count rate for electrons of $E > 9$ Mev. The second trace shows the amplitude of the spin modulation at twice the spin frequency in the spacecraft equatorial plane. The third trace shows the normalized second derivative of the pitch angle distribution, evaluated at $\alpha = \pi/2$. The range of particle pitch angles sampled in the spacecraft equatorial plane is shown in the bottom trace. The labels A, B, and C point to the times of the angular distributions shown in Fig. 2.

lation was at twice the spacecraft spin frequency as represented by the first harmonic coefficient, C_2. The fundamental, C_1, and third harmonic, C_4, were less than 1% of C_0. After it was determined that the second harmonic coefficient, C_3, was consistently smaller than the error in its determination, the second harmonic term was removed from the series. Figure 1 shows the results of this analysis for channel two of a Cerenkov detector, counting electrons of energy E > 9 Mev. The first trace is shown for reference to the Io absorption features. The second and third traces are measures of the sharpness of the pancake pitch angle distribution, first as sectioned obliquely by the spacecraft equatorial plane, and then as projected to a pitch angle section. The pitch angle measure is based on the fact that, for a pitch angle distribution of the form

$$C(\alpha) = C_n \sin^n \alpha, \quad n = -\left[\frac{1}{C}\frac{d^2C}{d\alpha^2}\right]_{\alpha = \pi/2} \qquad (2)$$

This method of estimating n was chosen because it gives an estimate even when a limited range of α is sampled. The variation of this range is shown in the bottom trace. Note that the modulation in the spacecraft equatorial plane is biased by the range of pitch angles sampled, but that this bias is removed by the projection to a pitch angle section.

The parameters C_2/C_0 and n were chosen to indicate the sharpness of the distributions and to give a continuous profile throughout the near encounter. They can be compared with the complete angular distributions at times A, B, and C shown in Figure 2. The counting rate, C, is a convolution of the detector's angular response with the particles' angular dependence. Therefore, the particle angular distributions may be steeper than the representations we show.

To interpret these data we recall some previously known effects. The pitch angle distribution of particles diffusing inward under conservation of the first two adiabatic invariants will tend to become sharper if nothing acts to disturb it (Kaufmann, 1965). This happens because conservation of the second adiabatic invariant gradually draws inwardly diffusing particles toward the equator. In addition, Mead and Hess (1973) pointed out that absorption by a moon should operate with reduced effectiveness for particles that mirrored at magnetic latitudes lower than the moon's orbit. Thus, since the inbound crossing of the Io L shell was at low latitude, one expected to see, superimposed on the continuous change, a sudden step toward sharper angular distributions as the moon missed some particles with high equatorial pitch angles. Outbound, Pioneer 10 crossed the Io L shell at a higher magnetic latitude than the moon reaches, and here absorption should be at full efficiency, with no preference for one pitch angle over another.

These predictions are partially borne out in Figure 1. As we approach the orbit of Io inbound the pitch angle distribution steepens gradually, and it sharpens abruptly just where absorption appears in the spin-average profile. However, something unexpected happens inside Io. Instead of gradually becoming sharper still, the distribution relaxes to a less-peaked form. As there is conclusive evidence that the particles propagate inward, we conclude that pitch angle scattering redistributes them, with small angles gaining particles at the expense of large. Outbound, the absorption dip in C_0 is deeper than inbound, indicating increased absorption as expected, but there is another sharpening of the pitch angle distribution at Io's orbit. It looks as if absorption depends on pitch angle at high latitudes too, but this conclusion is not necessary in the presence of pitch angle diffusion. Our interpretation is that lunar sweeping created a pancake of electrons mirroring near the equator, and electrons from this source are scattering to the lower equatorial pitch angles that cross the latitude of the spacecraft. It is consistent with this interpretation that the pitch angle distribution at Io's orbit is sharper inbound than outbound.

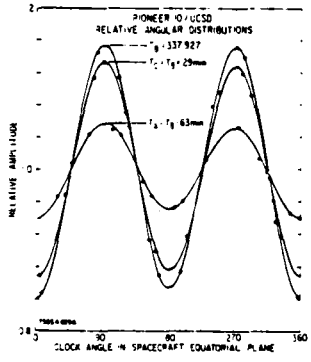

Fig. 2. Angular distributions in the spacecraft equatorial plane, normalized to the average count rate. The points are the actual data, and the lines are the fits from equation 1. Times A, B, and C are indicated in Fig. 1.

Evidence for Pitch Angle Scattering in the Phase Space Density Losses

As stated in the introduction, some accounting has to be made for the losses deduced from the radial intensity profile. Steady state conditions for electrons mirroring at the equator of Jupiter's radiation belts imply a balance between radial diffusion, acting as a source, and whatever losses occur locally. We consider synchrotron energy loss and pitch angle scattering. Thus

$$\frac{1}{\tau}\frac{\partial \tau}{\partial t} = \frac{1}{\tau}\left(\frac{\partial \tau}{\partial t}\right)_{DIF} + \frac{1}{\tau}\left(\frac{\partial \tau}{\partial t}\right)_{SYN} + \frac{1}{\tau}\left(\frac{\partial \tau}{\partial t}\right)_{SCA} = 0 \qquad (4a)$$

In this equation τ is the density in six-dimensional phase space $d^3x\, d^3p$, and it is related to the differential intensity, j, in particles $cm^{-2}s^{-1}sr^{-1}Mev^{-1}$, by $j = p^2\tau$. The diffusion source (Schulz and Lanzerotti, 1974; Birmingham et. al., 1974) is given by

$$\frac{1}{\tau}\left(\frac{\partial\tau}{\partial t}\right)_{DIF} = \frac{L^2}{\tau}\frac{\partial}{\partial L}\left(\frac{D}{L^2}\frac{\partial\tau}{\partial L}\right) \qquad (4b)$$

where D is the diffusion coefficient. The synchrotron term (Birmingham et. al., 1974; Coroniti, 1974) is

$$\frac{1}{\tau}\left(\frac{\partial\tau}{\partial t}\right)_{SYN} = -\frac{1}{\tau}\frac{\partial}{\partial I_1}\left(\dot{I}_1\tau\right) \qquad (4c)$$

where $\dot{I}_1$ is the rate of change of the particles' first adiabatic invariant due to synchrotron radiation. Without knowing the wave intensity and plasma density, we cannot predict the strength of the pitch angle scattering term. However, the loss rate has an upper bound that occurs when particles diffuse across the atmospheric loss cone in times much less than their bounce period. This bound is called the strong pitch angle diffusion limit, and it is given by Lyons (1973) and Schulz (1974):

$$-\frac{1}{\tau}\left(\frac{\partial\tau}{\partial t}\right)_{SCA} < \frac{v\sin^2\alpha_{LC}}{1.82\ L\ R_J} \qquad (4d)$$

where v is the particles' velocity, and α_{LC} is the equatorial pitch angle that defines the atmospheric loss cone. If there is asymmetry between the northern and southern hemispheres, this formula may require some modification, but we will see that the required loss rate is so far below this limit that we may ignore this refinement.

The diffusion term can be evaluated experimentally using the phase space densities obtained by McIlwain and Fillius (1975) and the diffusion coefficient profiles of Mogro-Campero (1975). Figure 4 of McIlwain and Fillius shows the phase space density vs L in log-log coordinates, and it can be seen that a power law is a good approximation to the L dependence between L = 3 and L = 10. Furthermore, the slope is nearly the same for different values of the first invariant, I_1, implying that the phase space density can be approximated as a separable function of I_1 and L:

$$\tau \cong \tau_1\,(I_1)\,L^{n_\tau} \qquad (5)$$

In fact a simple mathematical model, called MF5, was given in that paper to describe the differential intensity as a function of momentum and position for $3 < L < 5$. If one converts the independent variable from p to I_1 and considers only particles mirroring at the equator, MF 5 gives

$$\tau = \frac{1\times10^8\ L^4}{I_1\,(1+.02\sqrt{I_1})^3}\ (\text{ev s})^{-3} \qquad (6)$$

with I_1 expressed in Mev per gauss. Thus, MF5 conforms to equation (5) with $n_\tau = 4$. An L^4 dependence for τ has also been obtained by Baker and Van Allen (1976) from an independent analysis of data from the University of Iowa experiment on Pioneer 10.

Diffusion coefficients were estimated by Mogro-Campero (1975) at the orbits of Amalthea, Io, and Europa (L = 2.5, 5.9, and 9.4). Assembling values from the available data at these three locations, he found that the spatial dependence could be represented by a power law:

$$D\,(L) = D_{Io}\left(\frac{L}{5.9}\right)^{n_D} \qquad (7)$$

Although there is considerable scatter in the values of D_{Io} ($1.5\times10^{-8}s^{-1} < D_{Io} < 3.1\times10^{-7}s^{-1}$) and somewhat less in n_D ($3.6 < n_D < 4.0$), the conclusions of our present paper can tolerate this much uncertainty and more.

Substituting (5) and (7) in (4b) gives

$$\frac{1}{\tau}\left(\frac{\partial\tau}{\partial t}\right)_{DIF} = n_\tau\left(n_\tau + n_D - 3\right)\frac{D(L)}{L^2} \qquad (8)$$

The crucial point is that $n_\tau + n_D - 3$ is substantially positive, and no stretching of experimental errors will make it vanish. Because this coefficient is positive, more particles diffuse into an incremental element, ΔL, than diffuse out; i.e., radial diffusion is a local source. We now examine the other terms of the transport equation (equation 4) to see how to make it balance.

The synchrotron energy loss rate for gyrating electrons is derived in many textbooks (e.g. Panofsky and Phillips, 1955; Jackson, 1962). The following formulas are convenient for electrons on the equator of Jupiter's dipole field.

$$\frac{1}{\gamma}\frac{d\gamma}{dt} = -\frac{1}{T_y L^6}\frac{\gamma^2-1}{\gamma} \qquad (9)$$

$$\frac{1}{I_1}\frac{dI_1}{dt} = -\frac{2}{T_y L^6}\sqrt{1+\frac{16\ I_1}{L^3}} \qquad (10)$$

where γ is the ratio of the electron's total energy to its rest mass energy; I_1 is the electron's first adiabatic invariant in units of Mev/gauss; $T_y = 3.24\times10^7$ sec ≈ 1 year. Using equation 10 for $\dot{I}_1$ and equation 6 for τ, we can evaluate the synchrotron term (4c) in the transport equation between 3 and 5 R_J. It is a sink as expected for high energy electrons, but the energy spectrum becomes nearly flat at lower energies, and as electrons radiate less at these energies, there is a critical I_1, 613 Mev/gauss, below which synchrotron radiation acts as a source of particles into a differential band of I_1 rather than a sink.

The result is shown graphically in Figure 3. Other terms shown here are diffusion (equation 8) and the upper bound for pitch angle scattering (equation 4d). Synchrotron radiation does not have the right spatial and spectral profile, nor is it of sufficient magnitude to balance the radial diffusion source. Evidently it will be important below L = 3, however, and large loss rates for high energy particles can be expected to affect inward extrapolations of the model MF5. By contrast, pitch angle scattering has ample potential to compensate the radial diffusion source. We infer that it is the sink needed to balance the transport equation.

To estimate this loss rate, we neglect synchrotron radiation and equate the pitch angle scattering loss to the radial diffusion source. Inasmuch as the phase space density is a sep-

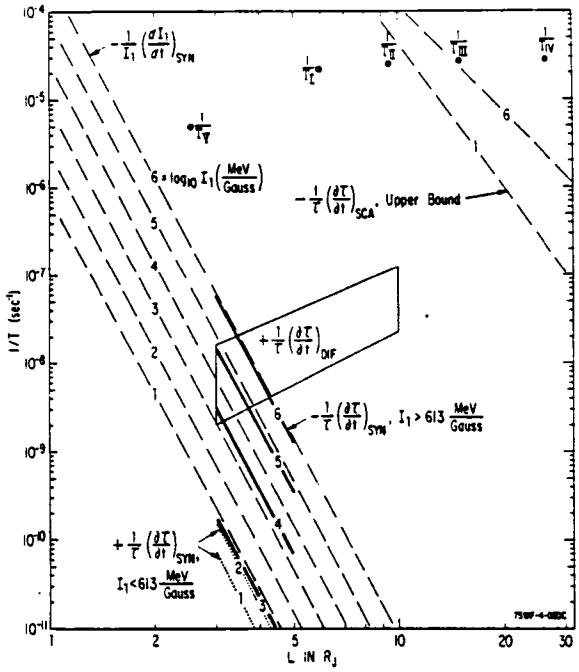

Fig. 3. Evaluation of the terms $1/\tau(\partial\tau/\partial t)$ in the electron transport equation. The radial diffusion term falls within the trapezoidal block, and in spite of experimental uncertainties, it is definitely a source. The synchrotron term is shown as a heavy black line when it is negative (a particle sink) and as a dotted line when it is positive (a particle source). The labels indicate that it is negative for $I_1 > 613$ Mev/gauss and positive for $I_1 < 613$ Mev/gauss. Pitch angle scattering is the only sink large enough to balance the radial diffusion source. The values shown are the upper bound for strong pitch angle diffusion, and far exceed the actual rates suggested in this paper. The numbers on the lines are equal to $\log_{10} I_1$ expressed in Mev/gauss. For additional reference, the dashed lines show values from equation 10 for $1/I_1\ (dI_1/dt)$ for individual electrons due to synchrotron radiation. Also shown for each of the five innermost moons of Jupiter is its sweeping rate, given as the reciprocal of the moon's period in a reference frame corotating with Jupiter's magnetosphere.

arable function of I_1 and L (equation 5), one can then deduce that the loss rate is independent of I_1 and varies spatially as L^2. It is orders of magnitude smaller than the strong diffusion limit.

It is interesting to note that if pitch angle scattering were at the strong diffusion limit near one of Jupiter's moons Amalthea, Io, or Europa, the pitch angle scattering lifetimes would be smaller than the moon's period. If this were the case, lunar sweeping would cause relatively small losses, and the lunar absorption features reported by all the particle experimenters on Pioneer 10 and 11 would not have been visible.

Conclusion

We have shown how pitch angle scattering affects the angular distributions observed for electrons in the inner magnetosphere of Jupiter, and how a local loss mechanism, inferred to be pitch angle scattering, causes large losses in the equatorial particle fluxes as they diffuse inward. We conclude that any treatment of the distribution and physical processes affecting electrons in the inner radiation belt of Jupiter must take the pitch angle scattering process into account.

Acknowledgments. We are indebted to Dr. Ed Smith and Dr. Allan Frandsen for Vector Helium Magnetometer data used to refer our detector look directions to the magnetic field direction. This work was supported in part by NASA contract NAS 2-6552 and NASA grant NGL 05-005-007.

References

Baker, D. N., and J. A. Van Allen, Energetic electrons in the Jovian magnetosphere, J. Geophys. Res., in press.

Birmingham, T., W. Hess, T. Northrop, R. Baxter, and M. Lojko, The electron diffusion coefficient in Jupiter's magnetosphere, J. Geophys. Res. 79, 87-97, 1974.

Coroniti, F. V., Energetic electrons in Jupiter's magnetosphere, Astrophys. J. Supplement Series No. 244 27, 261-282, 1974.

Fillius, R. W., and C. E. McIlwain, Measurements of the Jovian radiation belts, J. Geophys. Res. 79, 3589-3599, 1974.

Jackson, J. D., Classical Electrodynamics, John Wiley and Sons, Inc., New York, 1962.

Kaufmann, R. L., Conservation of the first and second adiabatic invariants, J. Geophys. Res. 70, 2181-2186, 1965.

Lyons, L. R., and R. M. Thorne, Equilibrium structure of radiation belt electrons, J. Geophys. Res. 78, 2142-2149, 1973.

Mead, G. D., and W. N. Hess, Jupiter's radiation belts and the sweeping effect of its satellites, J. Geophys. Res. 78, 2793-2811, 1973.

McIlwain, C. E., and R. W. Fillius, Differential spectra and phase space densities of trapped electrons at Jupiter, J. Geophys. Res. 80, 1341-1345, 1975.

Mogro-Campero, A., Absorption of radiation belt particles by the inner satellites of Jupiter, Jupiter, a Book and a Colloquium, Tucson, Arizona, May 18, 1975, Univ. of Ariz. Press, in press.

Panofsky, W. K. A., and M. Phillips, Classical Electricity and Magnetism, Addison-Wesley, Reading, Mass., 1955.

Schulz, M., and L. J. Lanzerotti, Particle Diffusion in the Radiation Belts, Springer-Verlag, New York, 1974.

Schulz, M., Particle lifetimes in strong diffusion, Astrophysics and Space Science 31, 37-42, 1974.

Van Allen, J. A., B. A. Randall, D. N. Baker, C. K. Goertz, D. D. Sentman, M. F. Thomsen, and H. R. Flindt, Pioneer 11 observations of energetic particles in the Jovian magnetosphere, Science, 188, 459-462, 1975.

(Received August 4, 1975;
revised October 14, 1975;
accepted November 24, 1975.)

INTERPLANETARY ELECTRONS: WHAT IS THE STRENGTH OF THE JUPITER SOURCE?

Walker Fillius, Wing-Huen Ip, and Paul Knickerbocker

University of California, San Diego
La Jolla, California USA

Abstract

Because there is not enough enformation to support a rigorous answer, we use a phenomenological approach and conservative assumptions to address the source strength of Jupiter for interplanetary electrons. We estimate that Jupiter emits $\sim 10^{24}$ - 10^{26} electrons s^{-1} of energy > 6 Mev, which source may be compared with the population of $\sim 3 \times 10^{28}$ electrons of the same energy in Jupiter's outer magnetosphere. We conclude that Jupiter accelerates particles at a rate exceeding that of ordinary trapped particle dynamical processes.

Introduction.

Almost all non-solar electrons of energy < 20 Mev found in interplanetary space are produced in the magnetosphere of Jupiter. This source was unsuspected until, as the Pioneer 10 spacecraft approached Jupiter, the electron fluxes increased drastically within 1 AU of the planet. (Chenette et al, 1974; Teegarden et al, 1974). It was then discovered that electron increases previously observed in the orbit of earth were tied to the relative positions of earth and Jupiter, and that these electrons originated at Jupiter, too (Teegarden et al, 1974; Krimigis et al, 1975; L'Heureux and Meyer, 1976; Mewaldt et al, 1976). The interplanetary propagation of these particles has been the subject of many papers and much lively debate (Gold et al, 1976; Gold and Roelof, 1976; Jokipii, 1976; Smith et al, 1976; Chenette et al, 1977; Conlon, 1977; Conlon and Simpson, 1977). Additionally, various authors have tried to deduce the existence and length of a Jovian magnetotail from observations of these particles (Krimigis et al, 1975; Mewaldt et al, 1976; Pesses and Goertz, 1976), but there is disagreement over this interpretation of the data (Pyle and Simpson, 1977). In this paper we address the question of how many energetic electrons per unit time Jupiter supplies to interplanetary space and we consider the significance of this number relative to the magnetospheric source region and the particle acceleration mechanism.

Instrumentation.

We will use data from the Cerenkov counter in the UCSD Trapped Radiation Detector package on Pioneers 10 and 11. This sensor counts electrons of energy > 6 Mev and nucleons of energy > 480 Mev/nucleon. (Fillius and McIlwain, 1974b; Axford et al, 1976) During the planetary encounter, its response is overwhelmingly dominated by trapped electrons, but in interplanetary space a special procedure is needed to distinguish between cosmic ray nucleons and electrons. This procedure makes use of the pulse height spectrum (3 integral channels are available) and takes advantage of the difference in the pulse height spectra of nucleons and electrons. Let N_i and E_i be the counting rates in channel i caused by nucleons and electrons, respectively, so that

$$S_i = N_i + E_i \qquad (i = 1,3) \qquad (1)$$

where S_i is the total counting rate. Define $\alpha_{ij} \equiv N_i / N_j$ and $\beta_{ij} \equiv E_i / E_j$. Far from Jupiter $E_i \ll N_i$, and we can determine α_{ij} from $\alpha_{ij} \approx S_i / S_j$. Close to Jupiter, fluctuations in the electron flux are much greater than fluctuations in the nucleon flux, and β_{ij} can be determined by a linear regression between S_i and S_j; $\beta_{ij} \approx \partial S_i / \partial S_j$. After the α's and β's have been determined, the electron (or nucleon) counting rate in a given channel can be evaluated by solving two of the simultaneous equations (1). Define E_{ij} as the electron counting rate in channel i evaluated by solving equations i and j. One gets

$$E_{ij} = \left(S_i - \alpha_{ij} S_j\right) \Big/ \left(1 - \alpha_{ij}/\beta_{ij}\right) \qquad (2)$$

There are three ways to evaluate the electron counting rate of a particular channel; E_{ij}, E_{ik}, and $\beta_{ij} E_{jk}$. Because of statistical fluctuations and imperfections in the procedure, the results differ slightly. As these errors are reduced by averaging the three results, the data shown in this paper are the average of three solutions for channel 1.

Interplanetary Electron Fluxes.

Figure 1 shows the interplanetary electron fluxes obtained by using this procedure. Each data point is averaged over a ten hour interval. The periods

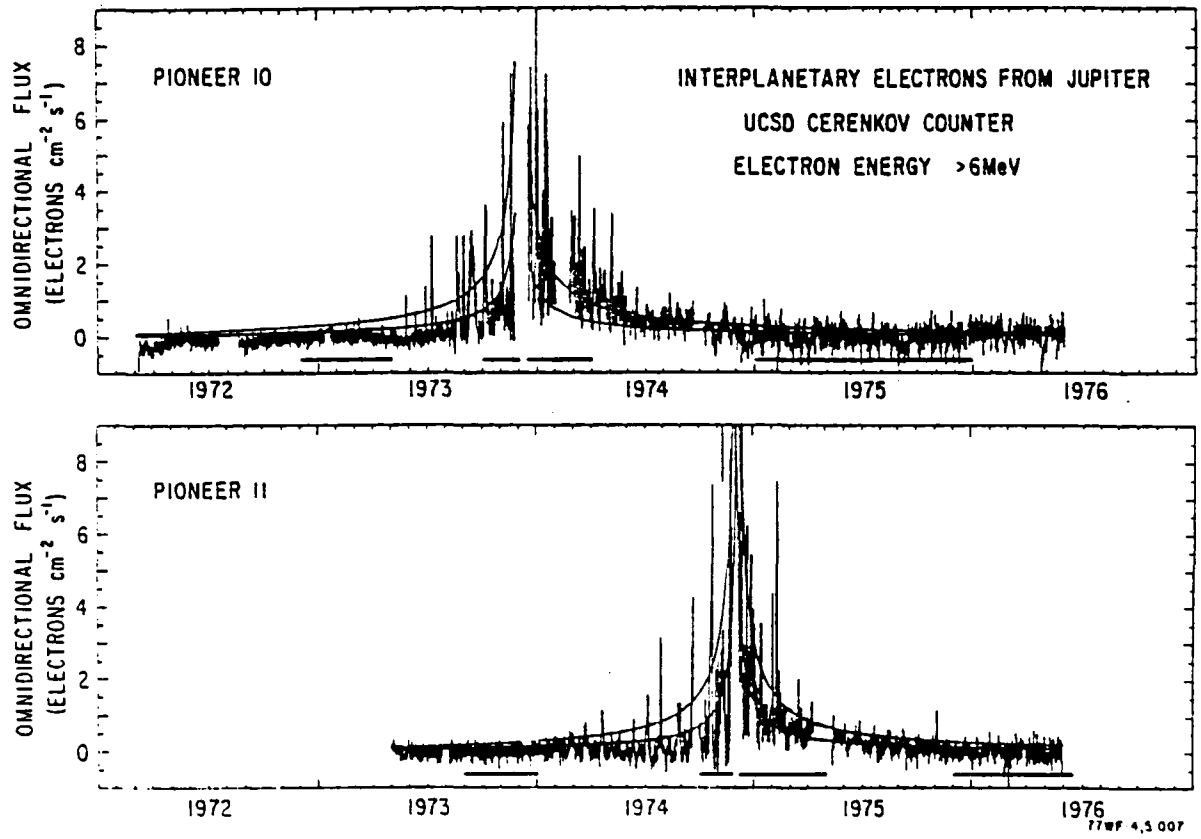

Figure 1

used to determine the α's and the β's are marked by horizontal bars. The nucleonic background typically corresponds to ~ 5 $cm^{-2}s^{-1}$, and the apparently negative electron fluxes are due to the limits of resolution of the subtraction procedure and statistical fluctuations. The data record starts at launch and continues through encounter with gaps for several solar particle events and the Jovian magnetosphere. Gain changes ($\sim$ 10%) occurred in the detectors at encounter, but these have been compensated for. The planetary encounter occurred in December, 1973 and December, 1974 for Pioneer 10 and Pioneer 11 respectively, and the two smooth reference lines superimposed on the data are inversely proportional to the distance between the spacecraft and Jupiter. It is clear that the appearance of electrons at the spacecraft is variable and impulsive, but the intensities are highest near encounter.

Figure 2 shows the electron fluxes plotted vs distance to Jupiter on log-log coordinates. Some of the impulsiveness has been smoothed out by taking running 27-day averages, and the inbound and outbound passes for both spacecraft are plotted together. It is clear that a 1/R dependence (where R is the distance from the observation point to Jupiter) describes each pass well. A 1/R-dependence has previously been noted for the peak fluxes by Chenette et al (1974) for Pioneer 10 inbound, and by Pyle and Simpson (1977). Because of negative excursions after nucleon subtraction this plot cannot be extended beyond $\sim$ 2 AU from Jupiter, but as mentioned in the introduction, there is plenty of evidence that the electrons extend as far as the earth's orbit. Using simultaneous data from Pioneer 11 and earth-bound Imp 7, McDonald and Trainor (1 (1976) deduced an intensity gradient of $\sim$ 150%/AU between the two spacecraft. Being a two-point observation, this gradient can as well be quoted as a power law, and their result is equivalent to a 1/R-dependence also.

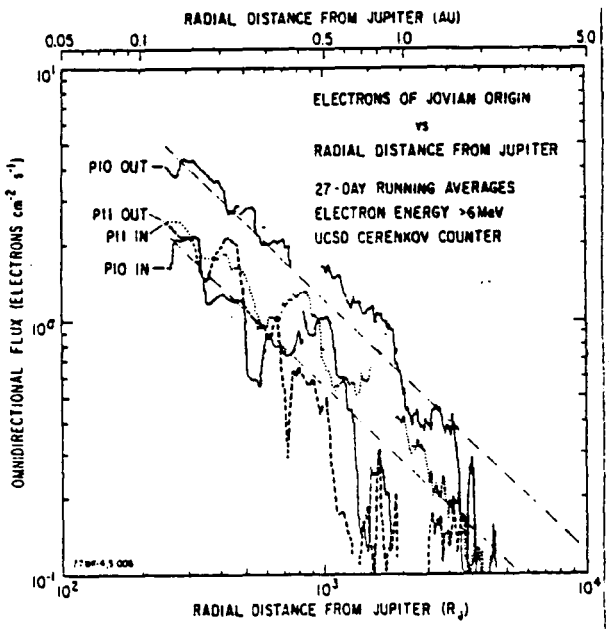

Figure 2

The two dashed lines are the same reference lines seen in Figure 1. The data from three of the four passes are intertwined and are equally well represented by a single line, while the Pioneer 10 outbound data are clearly higher by about a factor or two. Although it is incidental to our argument, this difference is certainly attributable to a better connection via the predominantly azimuthal interplanetary field lines between the source region and the spacecraft on the dawn side of the planet. What is significant to us is that there is bad connection on the other three passes, in which the spacecraft are more or less radially upstream of Jupiter in the solar wind, where the electrons must propagate across the interplanetary field lines.

The Source Strength.

It is impossible to get a firm value for the source strength without

more data or a full understanding of the propagation characteristics and parameters. However, by combining a phenomenological approach with conservative assumptions, we arrive at a value which suggests a significant relationship between the source strength and the population of the outer magnetosphere:

$$\text{source strength} \gtrapprox \frac{\text{population of the outer magnetosphere}}{\text{rotation period of the planet}}$$

Because of the simplicity of our approach, we believe this relationship will stand even after the numbers have been refined or changed using better knowledge.

The simplest approach to the source strength is to estimate the number of electrons in interplanetary space and divide by their residence lifetime. For the spatial distribution of electrons we choose the 1/R-dependence shown in Figure 3:

$$\rho(R) = \bar{J}_o \Big/ c\left(R \Big/ 100R_J\right)^{-1}; \quad 5 \leq \bar{J}_o \leq 13 \text{ cm}^{-2}\text{s}^{-1} \qquad (3)$$

where $\bar{J}_o$ is the time-averaged omnidirectional flux. Now these measurements were made on the dawn and daylight sides of Jupiter, but not over the poles or on the dusk and night sides. However, the noon side should be the most difficult for the electrons to get to, and so it is reasonable to suppose that the noonside profile is a lower limit. Furthermore, there is only a factor of two difference between the relatively accessible and inaccessible profiles sampled, and this is a minor factor. Equation (3) is thus a conservative estimate based on what information we do have. Integrated over a sphere out to the noise threshold of our data at 2 AU from Jupiter, this density profile yields an estimate of $\sim 10^{30}$ particles, and to 5 AU, $\sim 10^{31}$ particles.

To proceed to the source strength, we need to divide by the particles's residence lifetime in the integration volume. The impulsiveness of the data in Figure 1 gives a hint, but a better measure is provided by a solar event where the source is known to be a delta function in time. Electrons generated in the August, 1972 solar flares were monitored by Pioneer 10 at 2 AU, and they decayed exponentially with a lifetime of ~ 1.5 days. Using this lifetime we estimate that the source strength is $\sim 10^{25} - 10^{26}$ electrons second^{-1}.

A second approach to the source strength is to imagine a surface enclosing the Jovian magnetosphere and to estimate the net flow of particles outward through that surface. This flow can be expressed by the integral

$$\int \bar{j} \cdot \overline{dS}\, d\Omega = \iint \frac{J_o}{4\pi}\left(1 + \xi\cos\vartheta\right)\left(dA\cos\vartheta\right)\left(2\pi\sin\vartheta\, d\vartheta\right) = \frac{1}{3} J_o\, \xi\, A \qquad (4)$$

where ϑ is measured from a normal to the surface and ξ is the anisotropy with respect to the surface normal. Only in the Pioneer 10 outbound pass was our detector oriented so as to measure ξ. From a preliminary analysis, the average value is about 6% near Jupiter, and it decreases as the spacecraft recedes from Jupiter. If we use this value for the average anisotropy, take the average omnidirectional flux from equation (3), and integrate over a sphere at $100R_J$, the result is a source strength of $\sim 10^{24}$ electrons s^{-1}.

If electrons are channeled out of the magnetosphere is some preferential direction (e.g. from the polar caps, or down the magnetotail), our spacecraft has probably missed the main stream. Then our recourse is to take the surface of integration out so far that the escape channel looks like a point in the center and the electrons are relatively homogeneous over the surface. In so doing we note that, because the density and anisotropy both fall off inversely with R, particles are conserved only if the surface grows as something like the second power of R. Thus an integration over a spherical surface at, say, 2 AU should yield the same result as above.

The Population of the Jovian Magnetosphere.

In the outer magnetosphere of Jupiter the population of electrons of energy > 6 Mev numbers 3×10^{28} plus or minus an order of magnitude. Figure 3 shows four radial profiles of this region made by the same detector used for Figures 1 and 2. Large temporal and/or local time differences are apparent among the four passes. The number above was obtained by integrating the electron density represented by the dashed line over the volume of a dipole field between 25 and $100R_J$. The volume is probably somewhat less than this because the field lines are actually not dipolar in this region, but seem to be distended centrifugally. However, a generous estimate serves our purpose well, and a dipolar geometry is probably the best approximation near the equator where the flux tubes have most of their volume, anyway.

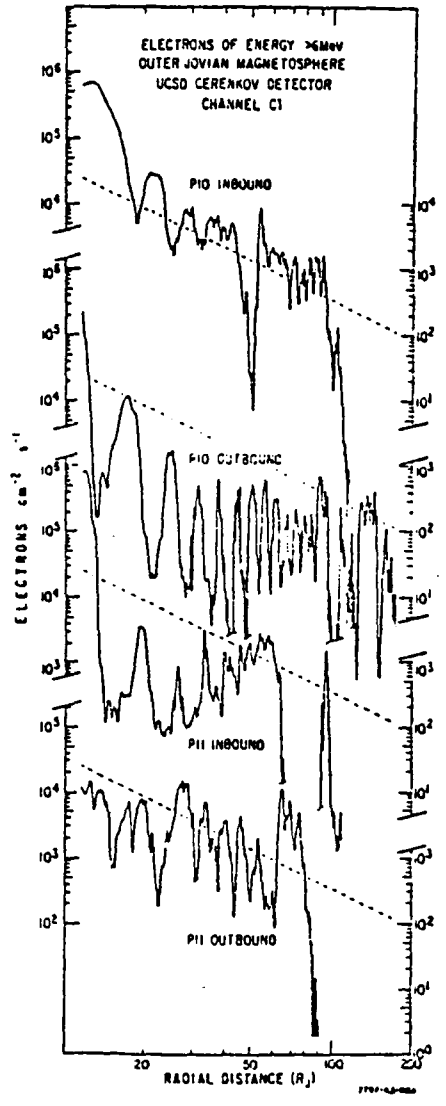

Figure 3

Discussion.

We have obtained estimates of $\sim 20^{24}$-$10^{26} s^{-1}$ for the source strength of > 6 Mev electrons, and $\sim 3 \times 10^{28}$ for the population of Jupiter's outer magnetosphere. As the rotation period of Jupiter is ~ 10 hours, this generation rate matches or exceeds the capacity of the outer magnetosphere in less than the planetary rotation period. Although there are other possibilities, these numbers lend credence to the hypothesis of McKibben and Simpson (1974) that the outer magnetosphere empties and fills with electrons every rotation. We conclude that Jupiter accelerates particles at a rate exceeding those of ordinary trapped particle dynamical processes (e.g. inward diffusion by violation of the third adiabatic invariant), and remarkable acceleration mechanisms are needed to produce this source rate. One possibility, suggested earlier by Fillius and McIlwain (1974a), is that the electric field of up to 360 megavolts associated with Jupiter's rotation couples by means of differential rotation and parallel electric fields to the charged particle population.

Acknowledgement

This work was supported by NASA through contract NAS 2-6552 and grant NGR 05-009-081.

References

Axford, W. I., W. Fillius, L. J. Gleeson, and W. -H. Ip, Ap. J. 210, 603, 1976.
Chenette, D. L., T. F. Conlon, and J. A. Simpson, J. Geophys. Res. 79, 3551, 1974.
Chenette, D. L., T. F. Conlon, K. R. Pyle, and J. A. Simpson, Ap. J. 215, L95, 1977.
Conlon, T. F., submitted to J. Geophys. Res., 1976.
Conlon, T. F., and J. A. Simpson, Ap. J. 211, L45, 1977.
Fillius, R. W., and C. E. McIlwain, Science, 183, 314, 1947a.
Fillius, R. W., and C. E. McIlwain, J. Geophys. Res. 79, 3589, 1974b.
Gold, R. E., and E. C. Roelof, submitted to J. Geophys. Res., 1976.
Gold, R. E., E. C. Roelof, and S. M. Krimigis, submitted to J. Geophys. Res. 1976.
Jokipii, J. R., Geophys. Res. Let. 3, 281, 1976.
Krimigis, S. M., E. T. Saris, and T. P. Armstrong, Geophys. Res. Let. 2, 561, 1975.
L'Heureux, Jacques, and Peter Meyer, Ap. J. 209, 955, 1976.
McDonald, F. B., and J. H. Trainer, Jupiter, T. Gehrels, Ed., pp 961, University of Arizona Press, Tucson.
McKibben, R. B., and J. A. Simpson, J. Geophys. Res. 79, 3545, 1974.
Mewaldt, R. A., E. C. Stone, and R. E. Vogt, J. Geophys. Res. 81, 2397, 1976.
Pesses, M. E., and C. K. Goertz, Geophys. Res. Let. 3, 228, 1976.
Pyle, K. R., and J. A. Simpson, Ap. J. 215, L89, 1977.
Smith, E. J., B. T. Tsurutani, D. L. Chenette, T. F. Conlon, and J. A. Simpson, J. Geophys. Res. 81, 65, 1976.
Teegarden, B. J., F. B. McDonald, J. H. Trainor, W. R. Webber, and E. C. Roelof, J. Geophys. Res. 79, 3615, 1974.

VOL. 84, NO. A10 JOURNAL OF GEOPHYSICAL RESEARCH OCTOBER 1, 1979

The Phase of the Ten-Hour Modulation in the Jovian Magnetosphere (Pioneers 10 and 11)

WALKER FILLIUS AND PAUL KNICKERBOCKER

University of California, San Diego, La Jolla, California 92093

We have systematized and recorded our study of the phase of the 10-hour modulation of energetic electrons seen by Pioneers 10 and 11 in the Jovian magnetosphere. To start with, we focus on the peaks rather than the valleys of each cycle because the peaks are where physically interesting features occur, such as particle acceleration, current sheets, etc. To identify the peaks, we demand that the instantaneous intensity be higher than the 5-hour running average and the 5-hour running average be greater than the 10-hour running average. These criteria select an interval rather than a point and we feel that this interval is an appropriate estimate of the experimental uncertainty. When the phases of the peaks are plotted together, they create patterns which we discuss in terms of disk-like, clock-like, and rotating anomaly models of the magnetosphere. Each model fits some of the data, but no model explains all of the data convincingly. We conclude that we still do not understand the configuration of the outer Jovian magnetosphere.

INTRODUCTION

The configuration of the magnetosphere of Jupiter has received attention for over a decade. Before any direct measurements were made, some of the key dynamical features were foreseen by *Piddington* [1969] and by Brice and his co-workers [*Brice and Ioannidis*, 1970; *Brice and McDonough*, 1973]. Figure 1*a* shows how Piddington visualized the spiraling of the magnetic field lines into a wrapped around tail where the magnetic flux tubes lag behind the rotation of the planet. Some evidence for lag appears in the Pioneer 10 and 11 data [*McKibben and Simpson*, 1974; *Northrup et al.*, 1974; *Fillius and McIlwain*, 1974; *Smith et al.*, 1974], and Piddington's analogy with the earth's tail seems to be at least partially sound. The Pioneer data provided many clues to the configuration of this region, but they do not add up to a complete picture. One of the outstanding clues is the strong ten-hour periodicity in the energetic particle intensities encountered by the spacecraft [*McKibben and Simpson*, 1974; *Van Allen et al.*, 1974*b*; *Fillius and McIlwain*, 1974; *Trainor et al.*, 1974].

This periodicity was initially explained as being caused by a disk-like concentration of particles near the tilted magnetic equator which approached and receded from the spacecraft as the planet rotated every ten hours. (Jupiter's rotation period is 9 hours 55 min, 29.711 ± 0.04 s [*Seidelmann and Divine*, 1977]. We shall refer to it as 10 hours.) Figure 1*b* shows how this 'magnetodisk' was pictured by *Van Allen et al.* [1974*a*]. However, the magnetodisk model ran into trouble on the outbound leg of Pioneer 11, which sampled latitudes higher than the envelope of the previous passes. If the cyclical minima in the earlier data were due to the spacecraft latitude's being above the magnetodisk, the Pioneer 11 outbound pass should have been entirely outside the magnetodisk, and the radiation intensities should not have risen above the levels of the previous minima. The data contradicted this expectation, exhibiting the familiar 10-hour cycle with maxima at least as high as on the previous passes. Rather than give up on the model, *Van Allen et al.* [1975] concluded that the magnetodisk is much thicker in the direction of the Pioneer 11 outbound pass, where the sun-Jupiter-spacecraft angle was 7°, compared with 40° for both inbound passes of Pioneers 10 and 11. If this local time difference was too small, *Fillius et al.* [1975] and *Jones* [1979] suggested that there might be a minimum B region at high latitude producing a secondary trapping region populated by particles that never cross the equator.

An alternative interpretation of the 10-hour periodicity was offered by *Chenette et al.* [1974]. (Also see *McKibben and Simpson* [1974].) They suggested that the inner magnetosphere is disklike, but outside 40 planetary radii (R_J) the particle intensity is independent of magnetic latitude and longitude but is a function only of time. We shall call this the 'magnetoclock' model. The mechanism by which the clock works has never been explained, nor is this model so appealing as the straightforward magnetodisk model.

Beginning with the clock idea, the Rice University group began work on a theory which has evolved into a separate model based on a rotating magnetic anomaly [*Hill et al.*, 1974; *Dessler and Hill*, 1975; *Carbary et al.*, 1976; *Dessler and Vasyliunas*, 1979]. According to these authors, a weak magnetic field region on the planetary surface near System III (1965) longitude 205° has profound effects on the flux tube which has its foot on the anomaly. This model attempts to account for a wide variety of observable phenomena. Presumably the modulation of the outer magnetospheric electrons is caused by the rotation of this flux tube. Like the University of Chicago magnetoclock, this model concedes that the inner magnetosphere has a conventional disklike configuration, and like the magnetoclock, this model suffers from having no precedent at Earth to guide its development and give it familiarity.

Obviously, the phase of the ten-hour modulation carries important information, and it has not been ignored [*Goertz et al.*, 1976; *McKibben and Simpson*, 1974; *Northrup et al.*, 1974; *Fillius and McIlwain*, 1974; *Simpson et al.*, 1975; *Fillius et al.*, 1975; *Simpson and McKibben*, 1976; *Kivelson et al.*, 1978]. Although the simplest forms of the disk, clock, and rotating anomaly models would be easily recognizable, comparison with the data has been indecisive.

The present paper is to present a review of the phase data from UCSD detectors on Pioneer 10 and 11. We have attempted to provide an objective methodology and to invent displays that illuminate the systematic, and nonsystematic, trends in the data. We find it heuristically useful to discuss what evidence there is for and against the several models, but

Paper number 9A0758.
0148-0227/79/009A-0758$01.00

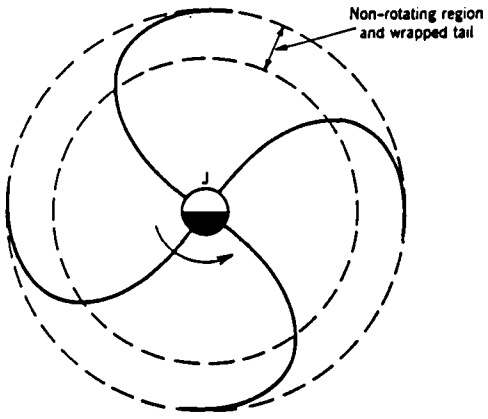

Fig. 1*a*. Spiraling of field lines in the Jovian magnetosphere as foreseen by *Piddington* [1969]. Copyright 1974 by the American Association for the Advancement of Science.

we do not rule out the possibility of separate models, or of compromise.

INSTRUMENTATION

The UCSD instrumentation is essentially identical on the two spacecraft. We concentrate on the Cerenkov detector, which measures the fluxes of relativistic particles which can penetrate the detector housing and radiator. Three integral pulse height channels have thresholds for electrons at about 6, 9, and 13 MeV and for nucleons at about 500 MeV/nucleon (all three channels). In interplanetary space the detector responds primarily to cosmic ray nucleons, and inside the magnetosphere, primarily to trapped electrons. For more detail, refer to *Fillius and McIlwain* [1974], *Fillius* [1976], and *Axford et al.* [1976]. In this paper we will use only the spin-averaged data, consisting of 12-s samples from each channel taken every 108 s.

We will present both an integral electron flux and a spectral index. For the electron flux we will use the counting rate of channel C1 (6 MeV threshold), and for the spectral index we will use the ratio of the counting rates from channels C3 and C1. On all but the Pioneer 10 outbound pass this ratio is raised to the fourth power to increase the contrast between maxima and minima. There are detector gain changes (~10%) and statistical uncertainties in the cosmic ray background, but we leave these factors uncorrected as they do not alter the phase.

METHODOLOGY

As soon as one looks at real data, identifying the phase of the 10-hour cycle becomes a problem. In preliminary analysis we, and others, plotted the position of the maxima and/or minima of the data. This procedure is expedient, but the counting rates often have an impulsive, or spiky profile so that the maxima or minima are not necessarily centered on the ten-hour wave. The work of *Kivelson et al.* [1978] on the magnetic field data has provoked us to introduce a methodology comparable to theirs. For our selection criteria we demand that the instantaneous value be higher than the 5-hour running average and the 5-hour running average be greater than the 10-hour running average. These criteria select an interval rather than a point. After many inspections of the data, we feel that the width of the interval places an appropriate error bar on the phase data. Previous work on the positions of minima has been criticized on the basis that there may be no importance to locating the middle of nothing (M. Kivelson, private communication, 1978). By focusing on intensity peaks rather than valleys, we intend to locate the sites of physical processes such as particle acceleration, current sheets, etc.

DATA EXHIBITS: STRIP CHARTS

To display detailed data we have plotted the intensity and the spectral index versus longitude (System III (1965)) for a large number of planetary rotations during the Pioneer 10 and 11 flyby's (Figures 2–5). The abscissa on each of these figures has a length of only two rotations; the data trace has been cut and stacked by shifting vertically through enough decades to prevent consecutive traces from crossing. A new trace starts every 360°. However, two rotations are shown so that an entire cycle can be seen without a break at an inconvenient point. Thus each rotation appears twice; once from 360° to 720°, and again from 0° to 360°. The longitude is plotted from right to left because it is defined such that it increases westward from the zero meridian, making it a left-handed system [*Riddle and Warwick*, 1976; *Seidelmann and Divine*, 1977]. Therefore the timeline runs from right to left also. The letters 'X, R' to the right of the graph beside each trace indicate (X) the amount by which the vertical scale is shifted, and (R) the radial distance from the spacecraft to Jupiter at the time of the zero meridian crossing. For example, in Figure 2, the fifth trace from the top of the left-hand strip starts at the right-hand edge with an intensity of $10^{22\cdot19}$, or 10^3 counts/s at a radial distance of 46 planetary radii (R_J). Except for the cycle nearest periapsis the local time of the spacecraft changes very

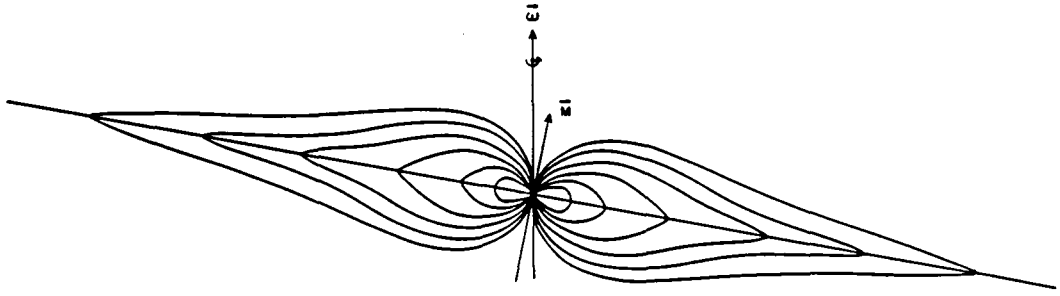

Fig. 1*b*. Early picture of the outer Jovian magnetosphere drawn by *Van Allen et al.* [1974*a*]. Copyright 1974 by the American Association for the Advancement of Science.

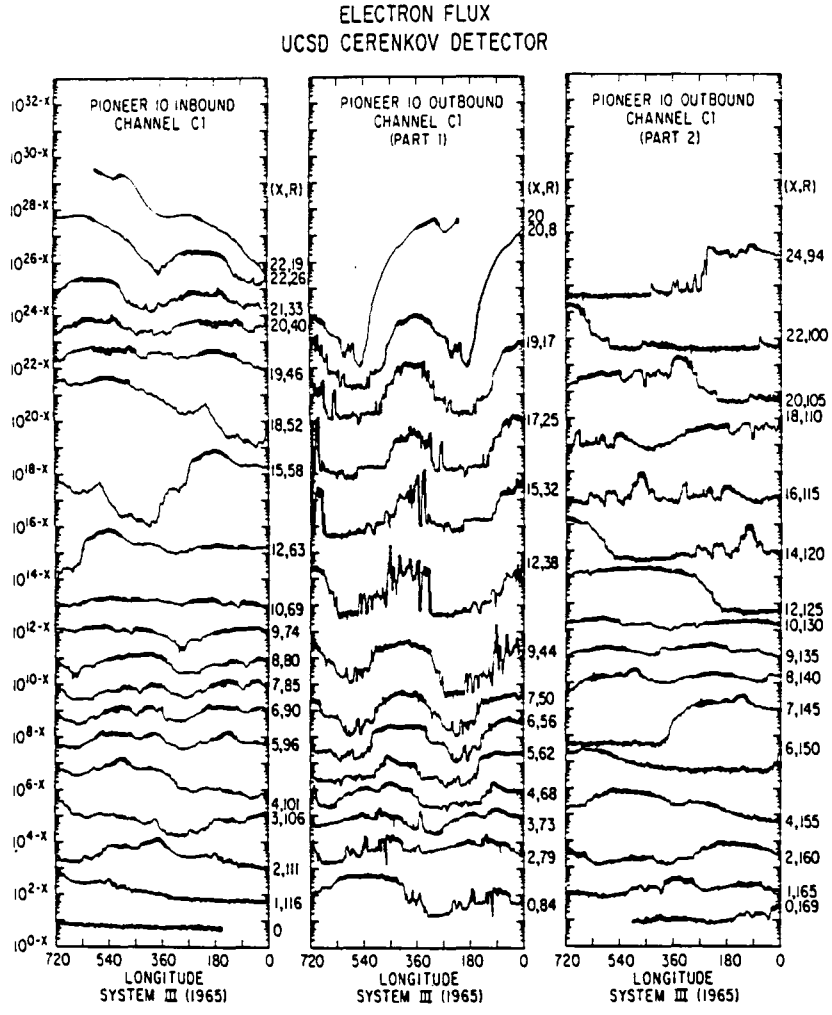

Fig. 2. Strip chart showing the electron flux for the Pioneer 10 flyby. The longitude scale is repeated in order to avoid inconvenient breaks in the data. See the text for an explanation of the format.

little during a cycle. Therefore these plots are nearly equivalent to plots of the data versus time, with the data cut and stacked every 10 hours. The darker trace identifies data meeting the criteria for peaks (see the section on methodology).

By running one's eye up and down the strip one can see similarities and dissimilarities between different cycles of the ten-hour wave. Although the wave is obvious throughout, it is not so consistent as to suggest a stable mechanism. Disk, clock, anomaly, or something else, the outer magnetosphere is apparently a very dynamic region.

As all investigators have noted, the ten-hour wave is particularly prominent on the Pioneer 10 outbound pass. Here the minimum frequently falls to cosmic ray levels, with the peaks jumping instantaneously one or two orders of magnitude above background. These features suggest that the spacecraft passes between closed field lines that contain particles and open field lines that cannot. *Goertz et al.* [1976] have shown that the magnetometer data for this pass are consistent with a nightside magnetic field model which includes just such field lines.

Other features can be picked out that are consistent with the models discussed in the introduction. Double-humped peaks occur on the Pioneer 10 inbound pass from the magnetopause to 63 R_J. One can explain these in terms of a magnetodisk if one supposes that the spacecraft passed through the equatorial plane and briefly emerged in the other hemisphere before recrossing the disk.

Another feature on the Pioneer 10 outbound pass recalls the prediction of Piddington for spiraling of the field lines into a wrapped-around tail (see introduction). In Figure 2 the maxima move to the left as one scans down the center column. This shift corresponds to an increasing phase lag as the spacecraft moves outward from Jupiter, and so the peaks fall on a spiral-like locus. Lest too much be made of this feature, it deserves saying that the Pioneer 10 outbound pass was unique: no such evidence appears in the other passes. Apparently the crucial difference is in the local time. Pioneer 10 exited from the magnetosphere at about 0530 local time, the only pass in the predawn sector. Pioneer 10 and 11 entered the magnetosphere at about 1000 local time, and Pioneer 11 exited at 1200.

Evidence is strong that the field is partially wrapped-around in the predawn sector. The phase lag in the particle maxima and minima has been remarked upon by all of the particle ex-

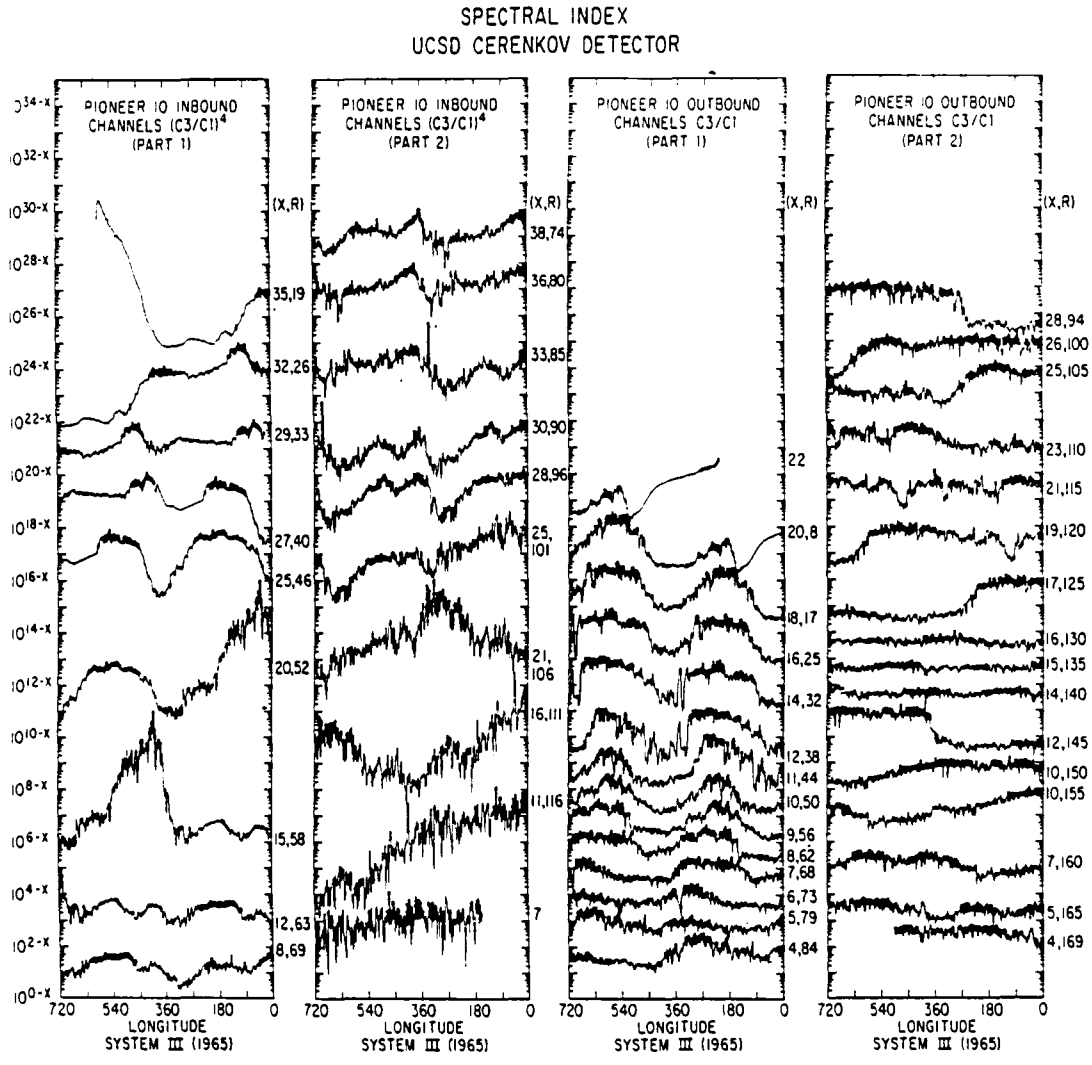

Fig. 3. Strip chart showing the spectral index for electrons in the Pioneer 10 flyby. The longitude scale is repeated in order to avoid inconvenient breaks in the data. See the text for an explanation of the format.

perimenters. Also, an increasing phase lag appears in the plasma sheet locations and current sheet crossings determined by the magnetic field experiment [E. J. Smith, private communication, 1978; *Kivelson et al.*, 1978]. Independently, the magnetic field vector has a radially increasing azimuthal component that causes it to point in the spiral direction [*Goertz et al.*, 1976; *Smith et al.*, 1974].

Data Exhibits: Slash Charts

To focus on just the phase of the 10-hour modulation, we have plotted in Figures 6 and 7 only the times when the data meet the peak criteria repeated below. In these figures the near-vertical slashes trace the spacecraft longitude (Figure 6) and clock phase (Figure 7) versus time. The slashes are drawn in only where the instantaneous data are greater than the 5-hour running average and the 5-hour running average is greater than the ten-hour running average as discussed under methodology. These are the same intervals that are darkened in Figures 2–5. The stippling indicates times when the spacecraft are inside the magnetosphere. (The occurrence of magnetopause crossings and the compressibility of the magnetosphere are discussed by *Smith et al* [1978].)

For most of Figures 6 and 7 the slashes group together to form patterns, and it is the information given by these patterns that we want to discuss. In Figure 7, for instance, the diagonal pattern of the Pioneer 10 channel C1 peaks corresponds to an increasing delay which results in a complete rollover between days 334 and 345. The spectral index does not roll over. These features were also noted by *McKibben and Simpson* [1974], plotting positions of minima. The fact that the flux ended up just in the same phase as it started, encouraged them to postulate that the outer magnetosphere behaves like a clock. If the clock mechanism applied to the entire magnetosphere, the pattern should be horizontal throughout.

A rotating feature such as a magnetic anomaly, on the other hand, would be expected to have a synodic period which varied with the motion of the observer. As Pioneer 10 entered at a sun-Jupiter-spacecraft angle of 35°, passed around the planet in a prograde sense, and exited near dawn at a sun-Jupiter-spacecraft angle of 100°, a net lag of 295° or 8 hours

would be expected. Pioneer 11 entered at the same place as Pioneer 10, passed around Jupiter in a retrograde sense, and exited at noon; then a net phase advance of 325° or 9 hours would follow. The patterns in Figure 7 do correspond to a phase lag for Pioneer 10, and suggest an advance for Pioneer 11. However, Pioneer 11 does not appear to roll over, and both these changes are gradual whereas the predicted changes would mostly occur in the day or two nearest periapsis.

The slash patterns do not fit the expectations for a magnetodisk very convincingly either. In Figure 6 the parabola-like reference curves indicate the loci where the spacecraft tracks cross a plane through Jupiter oriented perpendicular to the dipole moment. For a simple, unwarped, non-spiraled magnetodisk this is the magnetic equator, and the flux maxima would be expected to fall on this plane. No locus is shown for the Pioneer 11 outbound pass because this spacecraft track was at medium latitudes and never approached the magnetic equator. We pointed out in the Introduction that the presence of peaks here requires a departure from a simple disk.

As shown by the reference curves, the magnetodisk model implies a 180° phase difference between hemispheres which should be apparent when the spacecraft crosses the Jovigraphic equatorial plane. The equator crossings occur nearly simultaneously with periapsis at day 338.1 for Pioneer 10 and 337.2 for Pioneer 11. In Figure 6, the patterns in three out of four graphs shear abruptly by 180° at the appropriate time. This is clearly evidence for a disklike configuration in the inner magnetosphere, but the outer magnetosphere is more problematical.

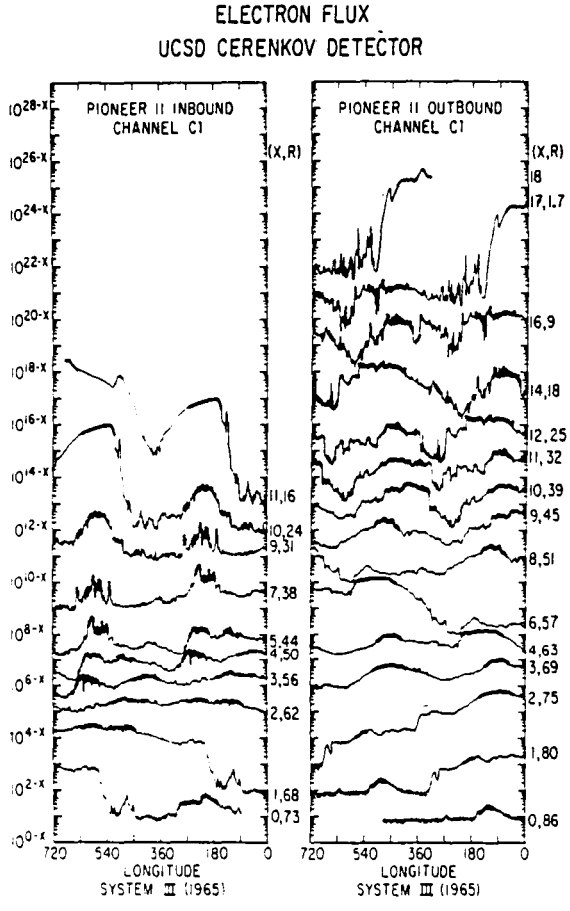

Fig. 4. Strip chart showing the electron flux for the Pioneer 11 flyby. The longitude scale is repeated in order to avoid inconvenient breaks in the data. See the text for an explanation of the format.

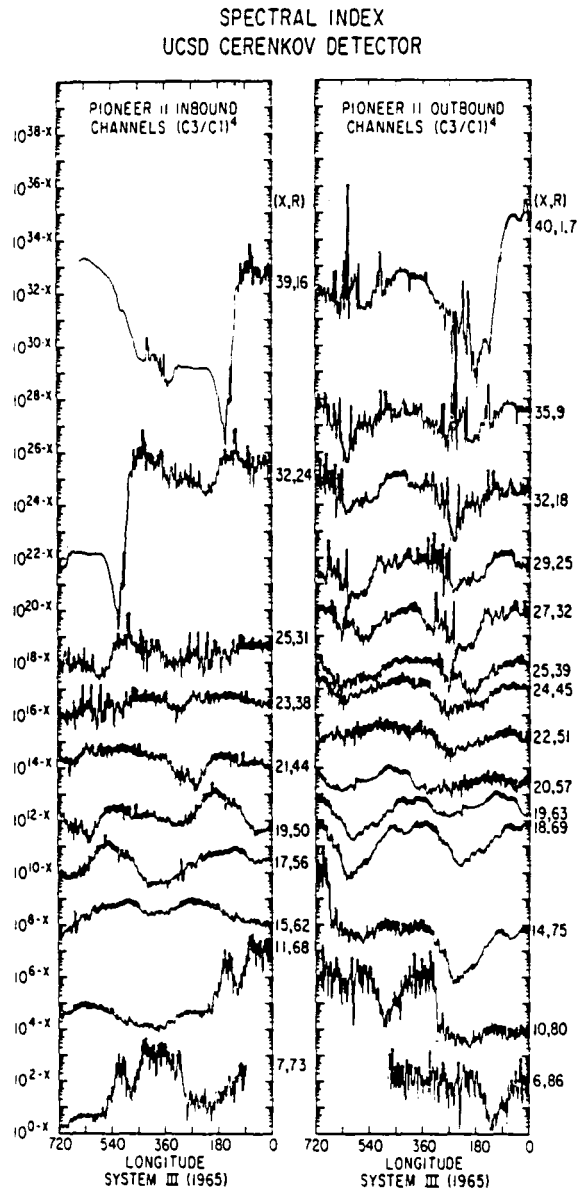

Fig. 5. Strip chart showing the spectral index for electrons in the Pioneer 11 flyby. The longitude scale is repeated in order to avoid inconvenient breaks in the data. See the text for an explanation of the format.

The Pioneer 10 inbound pass contains a particularly intriguing mystery. From day 331 through day 334, the particle intensity peaks lead the simple magnetodisk in phase. The Pioneer 11 inbound pass does not relieve this mystery, exhibiting a peculiar and possibly similar phase, too.

Other phase shifts are visible. We have already mentioned the gradually increasing phase lag on the Pioneer 10 outbound pass. This is clearly visible, and appears to have a slope of about 36° per day. Since the spacecraft velocity is about 12 R_J per day, the lag then appears to be about 3° per R_J.

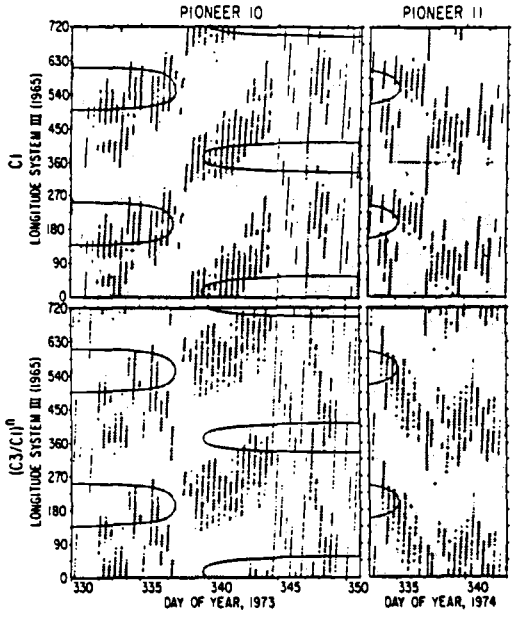

Fig. 6. Slash chart showing the longitude dependence of energetic electron maxima for Pioneers 10 and 11. The longitude scale is repeated in order to avoid inconvenient breaks in the data. See the text for an explanation of the format.

Another feature that we have already mentioned shows up prominently on the slash charts. The double peaks that occurred on the Pioneer 10 inbound pass form a distinctive cleft pattern. Although the slashes are not in the right phase (as mentioned above) the separation across the cleft is about the same as that between crossings of the magnetic dipole equator shown by the reference lines. If the magnetosphere is a disk, this agreement indicates that the tilt angle of the disk is about the same as that of the dipole.

CLOCK OR DISC?

A specific intercomparison of clock versus disk illustrates the difficulty of matching any model to the data. In Figures 8 and 9 we have plotted the positions of minima on a grid of clock phase versus longitude. We had to plot points for these graphs because the preferred criteria we used previously made too many indistinguishable lines falling on top of one another. Also we selected minima because there is somewhat less ambiguity in locating them. In this coordinate system a pure magnetoclock should produce points falling in a horizontal band across the graph. Similarly, a perfect magnetodisk should produce two vertical bands, one inbound and one outbound, separated by 180°. Histograms at the top and right-hand edges of the graph show the distribution of points projected to each axis. The data cannot be said to fall in either vertical bands or horizontal, but seem to have chosen a diagonal pattern instead.

There is a reason for this. In this coordinate space a stationary point at a given local time produces a diagonal trace as the planet rotates under it. Because of the commensurability of the clock and disc periods, every subsequent planetary rotation produces a retracing of the same diagonal. For each local time there is a different diagonal, and for each diagonal a corresponding local time. Consider a spacecraft trajectory in these coordinates. Far out from the planet, the spacecraft local time changes very little during a planetary rotation, and lies close to a single asymptotic diagonal. As the spacecraft approaches Jupiter, its trajectory still traces diagonals, but these creep slightly away from the asymptote. Near periapsis the spacecraft swings around the planet, changing local times very rapidly. In the plot the trajectory trace peels away from the tight cluster of its previous diagonals, and takes a curved path across the graph toward its outbound asymptote, which is a new diagonal corresponding to its outbound local time. The Pioneer trajectories, with periapses at 2.85 and 1.60 R_J, made most of their local time change in only one planetary rotation. Thus there is the chance for only one point per spacecraft away from the clusters of inbound and outbound diagonals. The spread of points is further limited by the fact that both approach asymptotes were at nearly the same local time. This asymptote at 35° before noon, and the outbound asymptotes, at noon and 100° before noon, span only 100° out of a possible 360°. It would obviously be desirable to sample other local times. As it is, the points are necessarily restricted to a diagonal belt, and the data are too noisy to describe anyting but the space sampled.

We are now in a good position to comment on other missions. Any spacecraft on a minimum-energy trajectory from earth is going to enter the Jovian magnetosphere at the same local time as the two Pioneers. Thus the Voyager and Solar Polar missions will all retrace the same diagonal on their approach. The Voyager outbound trajectories are on the dawn side, closer to midnight than Pioneer 10 outbound, but still displaced only about 100° from the inbound direction. Voyager periapsis is higher than Pioneer's, and so there will be more time on the nondiagonal transfer curve between inbound and outbound asymptotes. However, this takes place in the inner magnetosphere where the configuration is known to be disklike, and so there is no new phase data here. To form a decisive spread of points in these coordinates, one will need

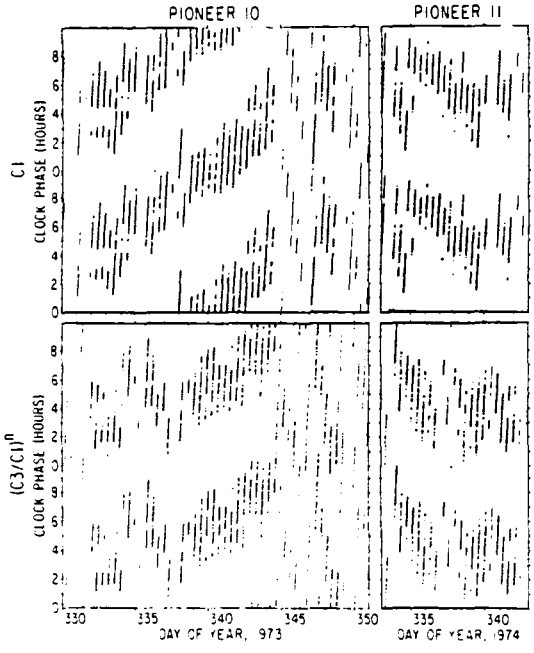

Fig. 7. Slash chart showing the clock time dependence of energetic electron maxima for Pioneers 10 and 11. The clock scale is repeated in order to avoid inconvenient breaks in the data. See the text for an explanation of the format.

data from the night and dusk quadrants, possibly obtainable by Galileo. In the meantime, the problem of the configuration of Jupiter's magnetosphere may be solved by deduction from other kinds of data, such as the double-humped peaks discussed below [see also *Dessler and Vasyliunas*, 1979].

ROTATING ANOMALY?

The rotating anomaly model predicts that at any given radial distance in the outer magnetosphere the energetic particles will always appear near the same longitude. (A. J. Dessler, private communication, 1979). This longitude may increase with distance if it spirals backward as foreseen by Piddington. To test this model, we have made slash charts with distance as the abscissa instead of time (Figure 10). The inbound and outbound passes are readily distinguishable by the slant of the slashes. (Because longitude increases with time, inbound slashes go from lower right to upper left, and outbound slashes from lower left to upper right.) Data are shown only for those times when the named spacecraft is inside the magnetosphere. Disklike structure is apparent in the inner magnetosphere, where the southern and northern hemisphere maxima are separated by 180°. However, outside 50 R_J there appears to be a change. At least for Pioneer 10, the two sets of slashes begin to merge, as called for by the anomaly model. The situation is unclear for Pioneer 11, partly because this spacecraft was outside the magnetosphere between 95 and 65 R_J on its inbound leg. However, the slashes for Pioneer 11 outbound do appear in the same range of longitude as for Pioneer 10.

We can investigate how these slashes stand with respect to the anomalous flux tube. According to *Dessler and Vasyliunas* [1979], the anomaly touches Jupiter's surface between 170° and 235°, and because of spiral lagging, it reaches the magnetopause between 220° and 350° System III (1965) longitude. Comparison with Figure 10 shows that the energetic electrons beyond 50 R_J seem to be found in that region of space complementary to the anomalous flux tube.

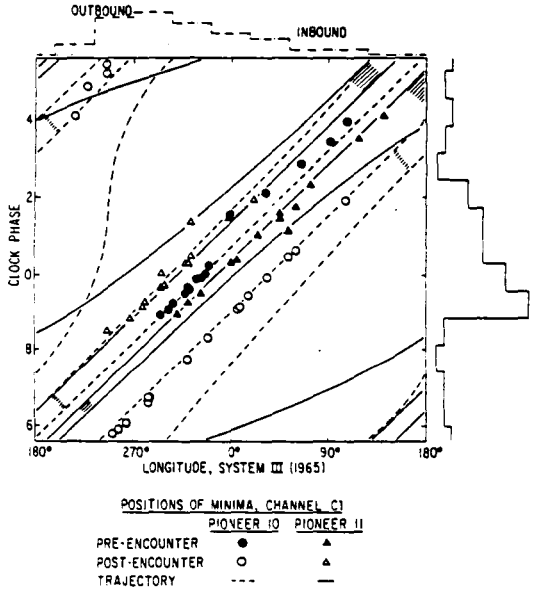

Fig. 8. Positions of minima in the energetic electron flux seen by Pioneers 10 and 11. The coordinates are chosen to emphasize the difference between clock and disk models.

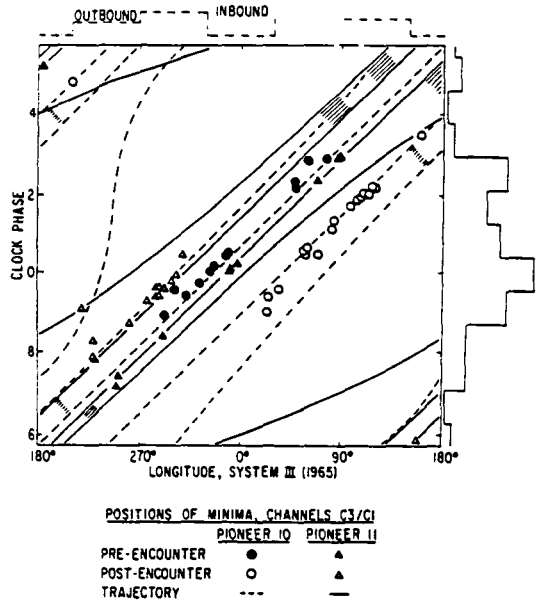

Fig. 9. Positions of minima in the electron spectral index seen by Pioneers 10 and 11. The coordinates are chosen to emphasize the difference between clock and disk models.

Whether this result confirms or contradicts the rotating anomaly model is unclear. At this point it seems up to the theorists to develop the model so that it accounts for this result.

DISCUSSION

Double-Humped Peaks

Double-humped peaks were apparent in both the strip charts and the slash charts (see the data presentation sections). If one accepts the explanation in terms of a magnetodisk, one can estimate the amplitude of the wobble and the thickness of the disk in this region at this time. Assuming that the Jovimagnetic equator performs simple harmonic motion with respect to the Jovigraphic equator, its displacement above the Jovigraphic equator is given by $Z_{max} \cos(\gamma - \gamma_0)$. If the spacecraft at $Z_{s/c}$ encounters the equator at longitudes γ_1 and γ_2, it is easy to calculate the amplitude of the magnetic equator's motion by

$$Z_{max} = Z_{s/c}/\cos[(\lambda_1 - \lambda_2)/2]$$

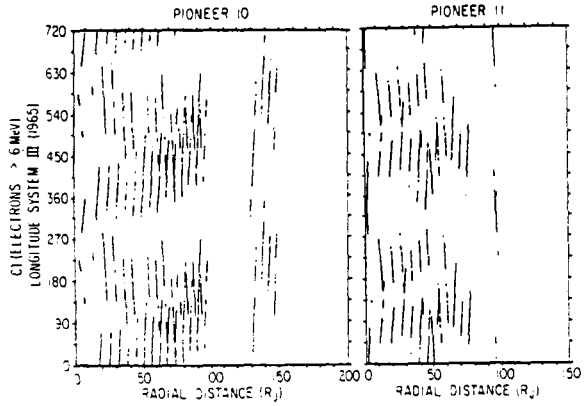

Fig. 10. Slash chart to test the rotating magnetic anomaly model.

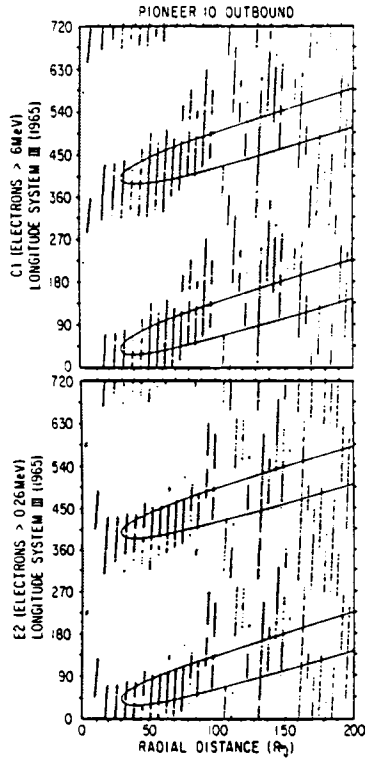

Fig. 11. Slash charts for two different electron energies during the Pioneer 10 outbound pass. The abscissa is the radial distance to Jupiter. The parabola-like curve represents the intersection of the spacecraft trajectory with the neutral sheet of *Kivelson et al.* [1978].

If the particle intensity falls to half its equatorial value at longitude γ_3, the full width of the disk at half of maximum intensity is given by

$$T = 2[Z_{s/c} - Z_{max} \cos(\lambda_3 - \lambda_0)] \quad (1)$$

Five cases on the Pioneer 10 inbound trajectory yield estimates of 15 R_J for the disk thickness, T, and 10.7° for the tilt of the magnetic equator. The scatter among these cases is 4 R_J and 2.3°, respectively, but there are likely to be greater systematic errors because the data are not entirely comfortable with the model. We note here that the Voyagers will approach Jupiter at a lower latitude than the Pioneers. If they encounter a disklike magnetosphere, they are likely to see double-humped peaks much of the time as the magnetic equator swings above and below the spacecraft. The modulation could then exhibit more of a 5-hour periodicity than 10. Such behavior would, of course, be strong evidence for a magnetodisk. Furthermore, calculations like those above could provide more information about the rigidity and thickness of the disk.

Particle Lifetimes

Implicit to the debate over magnetospheric configuration is the question of particle trapping lifetimes. The clock model implies that the particle lifetime is less than 10 hours. At the most, the rotating magnetic anomaly model implies that the lifetime is less than the dispersion in the drift period of the particles involved, which might be several times 10 hours. The magnetodisk model, on the other hand, is consistent with particle lifetimes as long as you like. It is clear that the first two models demand a prolific source of energetic particles, whereas the disk model makes no requirement.

Although the particle source and acceleration mechanism have not been identified, there is evidence that an adequate source exists to satisfy even the clock model. We have made estimates of the number of energetic electrons Jupiter emits into interplanetary space (10^{24}–10^{26} s^{-1}) and the number of electrons contained in the outer magnetosphere ($\sim 3 \times 10^{28}$) [*Fillius et al.*, 1977]. It is remarkable that these figures encompass what would be produced if the magnetosphere filled and emptied every 10 hours into interplanetary space, as suggested by the clock and anomaly models. Although the estimate of the source strength does not determine a model for the outer magnetosphere, it does relieve doubts about the particle lifetimes and show that this requirement of the clock and anomaly models is probably satisfied.

Magnitude of the Spiral Angle in the Predawn Sector

The magnitude of the spiral angle in the predawn sector can be inferred independently from several different measurements, and surprisingly, the results are not in very good agreement. The direction of the magnetic field vector has been shown to be well approximated by

$$\tan^{-1}(B_\phi/B_\rho) \simeq \tan^{-1}(7 \times 10^{-3}\rho) \quad (2)$$

where ρ is the radial distance in R_J (see Figure 3 of *Goertz et al.* [1976]). This can be integrated to give the net lag of the field line:

$$\phi(\rho) - \phi_0 = \int_{\rho_0}^{\rho} B_\phi/\rho' B_\rho \, d\rho' = 0.40(\rho - \rho_0) \quad \text{deg} \quad (3)$$

Jones [1979], modeling Jupiter's current disk, found that a linear fit to the twisting of the disk followed the form

$$\phi(\rho) - \phi_0 = 0.9\rho \quad \text{deg} \quad (4)$$

The near-equatorial neutral sheet has been studied by *Kivelson et al.* [1978], who used dips in the magnetic field strength to infer the presence of diamagnetic plasma. They obtained the following expression for its position:

$$\tan(\text{latitude}) = -0.19 \cos[-\phi + 0.85°(\rho - 14)] \quad (5)$$

At any constant latitude the spiral lag of the neutral sheet is then described by

$$\phi(\rho) - \phi_0 = 0.85(\rho - 14) \quad \text{deg} \quad (6)$$

A spiral angle can also be obtained from particle data. The phase lag of 6 Mev electron peaks can be estimated using our Figure 6 and the information that the spacecraft moves about 12 R_J per day. This lag is described by

$$\phi(\rho) - \phi_0 \simeq 3(\rho - \rho_0) \quad \text{deg} \quad (7)$$

A similar study on electrons of energy >0.255 Mev (UCSD channel E2) produces the result

$$\phi(\rho) - \phi_0 \simeq 1(\rho - \rho_0) \quad \text{deg} \quad (8)$$

Note the differences in the lag rates, or slopes, of these formulas. It is hard to assign error bars, but there seems to be real disagreement. Figure 11 displays some of these data graphically. The parabola-like curve represents the intersection of the spacecraft trajectory with the lagging neutral sheet described by (5) [*Kivelson et al.*, 1978]. This lag rate

agrees with that deduced by *Jones* [1979] and with the electrons of energy >0.255 Mev. However, the channel C1 electrons ($E_e > 6$ Mev) have a larger lag rate and the vector magnetic field (3) has a smaller lag rate.

If this difference is real, it demands of the disk model some departure from time invariance of axial symmetry. With no time variations and an axially symmetric disk, the intensity versus time profiles would be symmetrical about the times of latitude extrema, where the intensity extrema would occur. Since our assumptions apply to all particle energies, all channels would have symmetrical peaks at the same place, and no energy dependence could be introduced in the lag rate.

Time variations could explain the energy dependence if, for instance, it took more time to boost the 6 Mev electron intensity than the 0.25 Mev electron intensity.

Axial symmetry could be broken by letting either the radial intensity profiles or the pitch angle distributions vary with longitude. An energy-dependent lag rate could be produced if this variation were a function of energy. Suppose, for instance, that the pitch angle distribution at some energy varied with longitude so that the magnetodisk became cyclically thinner and thicker. Intensity extrema would still occur in the same place as before, but the time profiles would be asymmetric, with maxima skewed toward longitudes where the disk is thicker. If this process were energy-dependent, the amount of skew could be different at different energies, and the lag rate could be energy-dependent. Alternatively, if the radial intensity profiles were longitude-dependent, different energies might peak at different longitudes, and an energy-dependent lag rate could result.

These departures from time invariance or axial symmetry might not have to be large. However, time variation is the essence of the clock model, and axial asymmetry is the essence of the rotating anomaly model. Thus if the lag rate really is energy dependent, the disk model is forced to concede something to one of the other models.

The difference between the vector field spiral and the positions of the plasma and particle maxima might be caused by a kind of lag different from that which has been discussed before. It is widely believed that the centrifugal force exerted by the plasma upon the magnetic field lines causes them to bend so that their direction becomes more nearly perpendicular to the spin axis than to the magnetic dipole axis (see Figure 15 of *Smith et al.* [1974]). This bending causes the equatorial point on any line of force to occur at a lower latitude than it would have otherwise. If the lines of force at one longitude are bent more than those at a later longitude, it can be envisioned that the later longitude will have the higher equatorial latitude. If this longitude-dependent kind of bending occurs, the lines of force need not have the same spiral lag rate as the maximum latitudinal excursion of the equatorial surface.

CONCLUSIONS

The central conclusion emerging from this study is that the Pioneer data simply do not support a clear cut choice to be made between several fundamentally different competing scenarios proposed to account for the 10-hour modulation.

Each of the models discussed seems to have enough problems to make it less than convincing. The critical problems with the disk model are the high intensities on the Pioneer 11 outbound pass and the phase lead on the Pioneer 10 inbound pass. The critical problems with the clock model are the ambiguity of the data, the unconventional nature of the postulated magnetosphere, and the lack of any plausible mechanism to run the clock. The principal problems with the rotating anomaly model are the ambiguity of the data, the unconventional nature of the postulated magnetosphere, and the underdeveloped state of the theoretical mechanism.

Better understanding of this problem may come with more theoretical development or with more experimental data (Voyagers I and II in 1979 and Galileo in 1985). Whatever models emerge in the future will clearly have to be reconciled to the Pioneer data. Although it would have been more gratifying to demonstrate that the Pioneer data favor one model over another, it still seems worthwhile to present the data so that they may challenge and guide future work.

Acknowledgments. We thank our many colleagues who have discussed this problem with us and offered arguments, suggestions, and encouragement. Special thanks are due to Alex Dessler for suggesting Figure 10 and discussing the rotating anomaly model with us. This research was supported by NASA contract NAS2-6552 and NASA grant NGL 05-005-007.

The Editor thanks R. B. McKibben and D. Sentman for their assistance in evaluating this paper.

REFERENCES

Axford, W. I., W. Fillius, L. J. Gleeson, and W.-H. Ip, Cosmic-ray gradients from Pioneer 10 and Pioneer 11, *Astrophys. J., 210*, 603–613, 1976.

Brice, N. M., and G. A. Ioannidis, The magnetosphere of Jupiter and Earth, *Icarus, 13*, 173–183, 1970.

Brice, N. M., and T. R. McDonough, Jupiter's radiation belts, *Icarus, 18*, 206–219, 1973.

Carbary, J. F., T. W. Hill, and A. J. Dessler, Planetary spin period acceleration of particles in the Jovian magnetosphere, *J. Geophys. Res., 81*, 5189–5195, 1976.

Chenette, D. L., T. F. Conlon, and J. A. Simpson, Bursts of relativistic electrons from Jupiter observed in interplanetary space with the time variation of the planetary rotation period, *J. Geophys. Res., 79*, 3551–3558, 1974.

Dessler, A. J., and T. W. Hill, High-order magnetic multipoles as a source of gross asymmetry in the distant Jovian magnetosphere, *Geophys. Res. Lett., 2*, 567–570, 1975.

Dessler, A. J., and V. M. Vasyliunas, The magnetic anomaly model of the Jovian magnetosphere: Predictions for Voyager, *Geophys. Res. Lett., 6*, 37–40, 1979,

Fillius, W., The trapped radiation belts of Jupiter, in *Jupiter*, edited by T. Gehrels, University of Arizona Press, Tucson, 1976.

Fillius, R. W., and C. E. McIlwain, Measurements of the Jovian radiation belts, *J. Geophys. Res., 79*, 3589–3599, 1974.

Fillius, R. W., C. E. McIlwain, and A. Mogro-Campero, Radiation belts of Jupiter: A second look, *Science, 188*, 465–467, 1975.

Fillius, W., W.-H. Ip, and P. Knickerbocker, Interplanetary electrons: What is the strength of the Jupiter source?, *Proc. Cosmic Ray Conf., 15*, 1977.

Goertz, C. K., D. E. Jones, B. A. Randall, E. J. Smith, and M. F. Thomsen, Evidence for open field lines in Jupiter's magnetosphere, *J. Geophys. Res., 81*, 3393–3398, 1976.

Hill, T. W., J. F. Carbary, and A. J. Dessler, Periodic escape of relativistic electrons from the Jovian magnetosphere, *Geophys. Res. Lett., 1*, 333–336, 1974.

Jones, D. B., On the phase relationship between the energetic particle flux modulation and current disc penetrations in the Jovian magnetosphere: Pioneer 10 inbound, *Geophys. Res. Lett., 6*, 45–48, 1979.

Kivelson, M. G., P. J. Coleman, Jr., L. Froidevaux, and R. L. Rosenberg, A time dependent model of the Jovian current sheet, *J. Geophys. Res., 83*, 4823–4829, 1978.

McKibben, R. B., and J. A. Simpson, Evidence from charged particle studies for the distortion of the Jovian magnetosphere, *J. Geophys. Res., 79*, 3545–3549, 1974.

Northrup, T. G., C. K. Goertz, and M. F. Thomsen, The magnetosphere of Jupiter as observed with Pioneer 10, 2, Nonrigid rotation of the magnetodisc, *J. Geophys. Res., 79*, 3579–3582, 1974.

Piddington, J. H., *Cosmic Electrodynamics*, John Wiley, New York, 1969.

Riddle, A. C., and J. W. Warwick, Redefinition of System III Longitude, *Icarus*, *27*, 457–459, 1976.

Seidelmann, P. K., and N. Divine, Evaluation of Jupiter longitudes in system III (1965), *Geophys. Res. Lett.*, *4*, 65–68, 1977.

Simpson, J. A., and R. B McKibben, Dynamics of the Jovian magnetosphere and energetic particle radiation, in *Jupiter*, edited by T. Gehrels, pp. 738–766, University of Arizona Press, Tucson, 1976.

Simpson, J. A., D. C. Hamilton, G. A. Lentz, R. B. McKibben, M. Perkins, K. R. Pyle, and A. J. Tuzzalino, Jupiter revisited: First results from the University of Chicago charged particle experiment on Pioneer 11, *Science*, *188*, 455–459, 1975.

Smith, E. J., L. Davis, Jr., D. E. Jones, P. J. Coleman, Jr., D. S. Colburn, P. Dyal, C. P. Sonett, and A. M. A. Frandsen, The planetary magnetic field and magnetosphere of Jupiter: Pioneer 10, *J. Geophys. Res.*, *79*, 3501–3513, 1974.

Smith, E. J., R. W. Fillius, and J. H. Wolfe, Compression of Jupiter's magnetosphere by the solar wind, *J. Geophys. Res.*, *83*, 4733–4742, 1978.

Trainor, J. H., F. B. McDonald, B. J. Teegarden, W. R. Webber, and E. C. Roelof, Energetic particles in the Jovian magnetosphere, *J. Geophys. Res.*, *79*, 3600–3613, 1974.

Van Allen, J. A., D. N. Baker, B. A. Randall, M. F. Thomsen, D. D. Sentman, and H. R. Flindt, Energetic electrons in the magnetosphere of Jupiter, *Science*, *183*, 309–311, 1974*a*.

Van Allen, J. A., D. N. Baker, B. A. Randall, and D. D. Sentman, The magnetosphere of Jupiter as observed with Pioneer 10, 1, Instrument and principal findings, *J. Geophys. Res.*, *79*, 3559–3577, 1974*b*.

Van Allen, J. A., B. A. Randall, D. N. Baker, C. K. Goertz, D. D. Sentman, M. F. Thomsen, and H. R. Flindt, Pioneer 11 observations of energetic particles in the Jovian magnetosphere, *Science*, *188*, 459–462, 1975.

(Received February 26, 1979;
revised May 4, 1979;
accepted May 7, 1979.)

VOL. 80, NO. 10 JOURNAL OF GEOPHYSICAL RESEARCH APRIL 1, 1975

Differential Spectra and Phase Space Densities of Trapped Electrons at Jupiter

CARL E. MCILWAIN AND R. WALKER FILLIUS

Physics Department, University of California at San Diego, La Jolla, California 92037

Using Pioneer 10 data, we have constructed differential spectra and phase space densities of trapped electrons at Jupiter. These quantities should assist in calculating synchrotron radiation from these particles and in evaluating the diffusion mechanisms that accelerate the particles. Absorption by the moons Io and Europa is evident, and injection by Io is demonstrated by a density peak in phase space, which demands a local source. There is also a rapid decrease in density between the moons, which could call for either a local loss mechanism or nonlocal losses fed by diffusion.

INTRODUCTION

In a previous paper [*Fillius and McIlwain*, 1974, henceforth referred to as FM 1974] we described the University of California at San Diego instrument on Pioneer 10 and presented preliminary findings. Our most important electron measurements were displayed in a graph showing intensities of electrons of energy above 0.16, 9, and 35 MeV during the day surrounding periapsis. Whereas our sensors respond to particles of energy above these thresholds, many studies can best be carried out with differential spectra, or better, with the distribution function. These studies include computation of the synchrotron emission spectrum, the quantitative evaluation of particle transport mechanisms, and also the homely business of integrating the detector responses over the input spectrum to develop self-consistent values for the measured intensities.

In these studies, merely taking differences between a few integral channels will not do; there is a need for continuous derivatives. However, differential measurements of the energy spectrum are difficult to make and beyond reasonable limitations for exploratory spacecraft, so that it will be years before direct measurements will be made. Therefore there is strong motivation to make the best of what we have now.

FITS TO A THREE-PARAMETER FUNCTION

With the three integral channels already mentioned we can obviously fit a three-parameter mathematical function. Not just any three-parameter function will do, because we require that it must be physically reasonable and not contradict the data points. Although it is not necessary, it is satisfying to note that the function to be introduced later satisfies a third criterion: the same form gives an adequate fit at all positions calculated. In using such a procedure we of course make assumptions. First, it is implicit that the spectrum must be very smooth, containing no sharp features that fall in the gaps between our channels. Second, the three data points must give adequate definition of the spectrum.

Choice of a model function was prompted by the observation that between 9 and 35 MeV the spectrum is steep throughout encounter, but at the lowest energies the spectrum becomes flat inside Io. This suggests a threshold energy at which the spectrum changes character. These features are represented in the following form:

$$J_0 = 4\pi K(1 + pc/H)^{-\gamma} \qquad (1)$$

where

J_0 the omnidirectional intensity per unit energy in units of el cm^{-2} s^{-1} MeV^{-1};
p the relativistic electron momentum;
c the velocity of light;
γ a fitting parameter giving the slope at high energies;
H a fitting parameter giving the threshold where the spectrum changes character;
K a fitting parameter giving the intensity;
E kinetic energy.

The independent variable was chosen to be p rather than E because this simplifies usage of the relativistic energy momentum equation.

This function was fit to our data at a number of points on the inbound pass between $L = 25$ and $L = 3$. Table 1 is a list of the spacecraft positions and the fitting parameters, and Figure 1 is a graph of differential spectra given by the model. Several alternative spectra were computed at $L = 3$, corresponding to different values of the flux above 0.16 MeV. As explained in FM 1974, there is a large uncertainty in this measurement because of the background created by penetrating electrons. The fit labeled 3A corresponds to the correction used in the reference, but fits 3B and 3C represent possible values that result from subtractions of only 6 and 9% more background.

The data recorded by our instrument can be represented by an integral of the input intensity over energy and angle with appropriate weighting for the detector response. Formally, this leads to a complex integral (equation (A2) of the appendix) which needs simplification. For FM 1974 we calculated the integral for a large number of artificial spectra and angular distributions to arrive at an approximation which is easy to use and reasonably accurate for most cases. However, some spectra occurred at Jupiter which are outside the valid range of the approximation. For these cases the approximation is in error, and as we noted in FM 1974, these spectra require special treatment. For the present paper we integrate the model spectra over the detector responses (appendix equation (A5)) so as to develop self-consistent solutions for the flux and energy spectra.

Figure 2 shows the actual count rates plotted versus L for comparison with the count rates computed using equation (A5) and the fits. The symbols M1, C2, and E1 refer to the data channels used, and E1 − 2.6 * M1 is the low-energy channel with background subtracted as explained in FM 1974. The slight misfit to channel C2 below $L = 8$ is deliberate. The photomultiplier tube in this detector experienced some slight (~15%) gain loss caused by radiation damage, and the fits were made after correcting the count rates by the rough formula

TABLE 1. Fitting Parameters Used for Model Spectra of the Form $J_0\ dE = 4\pi K(1 + pc/H)^{-\gamma}\ dE$

L, R_J	λ_M, deg	K, el cm^{-2} s^{-1} sr^{-1} MeV^{-1}	H, MeV	γ
25	11	4.0×10^5	1.3	4.39
20	21	6.2×10^6	0.9	4.30
15	2	6.0×10^6	2.1	4.85
12	27	7.6×10^7	1.9	5.00
11	25	6.2×10^7	2.7	5.35
10	23	9.4×10^6	7.8	6.8
9	20	1.65×10^6	75.	25.1
8	16	2.20×10^6	60.	18.7
7	11	1.55×10^6	150.	33.
6	6	9.4×10^5	45.	9.0
5.56	4	4.1×10^6	7.0	3.58
5.	2	1.26×10^6	15.	3.89
4.	0	1.72×10^6	7.4	2.44
3.5	1	4.7×10^6	2.6	1.93
3A*	4	1.19×10^7	1.1	1.74
3B†	4	1.88×10^6	4.4	1.89
3C‡	4	3.24×10^5	40.	3.33

Magnetic coordinates calculated from D_1 model of *Smith et al.* [1974*a*]. Differences between the D_1 model and the newer D_2 models of *Smith et al.* [1974*b*] are not critical in this paper.

*E1 - 2.6 * M1 as used in FM 1974.

†6% background subtracted (reduces net by factor of 2).

‡9% background subtracted (reduces net by factor of 4).

$$R' = R \qquad L > 7.9 \text{ inbound} \tag{2}$$

$$R' = R/[0.75 + 0.05(L - 2.9)] \qquad L < 7.9 \text{ inbound}$$

This formula was obtained crudely by matching the inbound and outbound passes and by letting the correction be linear between $L = 7.9$ inbound and $L = 7.9$ outbound. Figure 2 demonstrates that equation (A5) is satisfied by the spectra and illustrates the degree to which the sample of fits in Table 1 describes the spatial dependence of the electron fluxes.

Differential Intensities

Using the fits above, we have computed differential electron intensities and plotted them versus L in Figure 3. The dashed lines are constant energy profiles at the thresholds of the integral channels from Figure 2. The differential and integral intensity profiles clearly exhibit the same features.

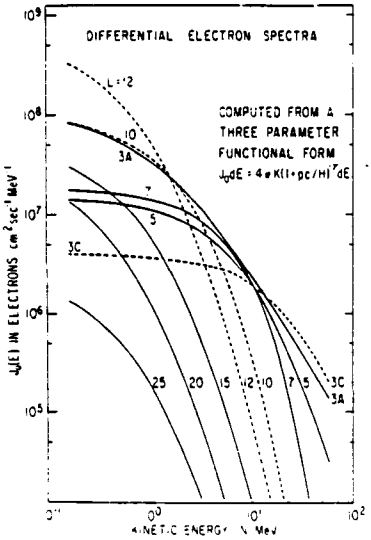

Fig. 1. Differential electron spectra computed from the fitting parameters in Table 1.

For investigations of particle transport it is pertinent to study profiles with the first adiabatic invariant I_1 held constant:

$$I_1 = (p^2 \sin^2 \alpha)/2m_0B \tag{3}$$

where α is the pitch angle, B is the local magnetic field, and m_0 is the electron rest mass. Since all pitch angles are included in the omnidirectional flux, there is a range of I_1 values for each fit in Table 1. However, we assign to each spectrum only one value of I_1, that of the locally mirroring particles, and we represent the directional flux of these particles as $J_0/4\pi$. This value is strictly accurate only if the angular distribution is isotropic. From the data the angular distribution is nearly isotropic, and we introduce a factor of 2 error at the most.

These profiles are shown by the solid lines in Figure 3. Intensities can be calculated for a very wide range of I_1. Energies were restricted to 0.16–60 MeV or 2½ orders of magnitude, an appropriate range for our data; but for relativistic particles, $I_1 \propto E^2$, and B varies through almost 3 orders of magnitude. Differences in the second adiabatic invariant are ignored because the spacecraft was always near the magnetic equator, and the intensities did not have a strong latitude dependence in this region.

The differential intensity as a function of energy and position is needed to calculate the synchrotron radiation from the trapped electron belt. Equation (1) gives a continuous energy dependence, but the coefficients are evaluated only at discrete positions. However, by restricting attention to $L \leq 5$ one can find a consensus spectrum that gives a passable replica of these discrete fits.

Such a model, which we are calling MF5, is given by

$$j_\perp(E) \cong 5 \times 10^5 L(B/B_Q)^{-20/L^3}(1 + pcL^{3/2}/100)^{-3} \tag{4}$$

$$J_0(E) \cong j_\perp(E)/(0.054 + 0.27L^{-1} + 0.1L^{-2}) \tag{5}$$

$$J_0(>E) \cong J_0(E)50/L^{3/2}(1 + pcL^{3/2}/100) \tag{6}$$

where

- $j_\perp(E)\ dE\ d\Omega$ the differential intensity within dE and $d\Omega$ perpendicular to the local magnetic field in units of el cm^{-2} s^{-1} sr^{-1} MeV^{-1};
- $J_0(E)\ dE$ the differential omnidirectional intensity within dE in units of el cm^{-2} s^{-1} MeV^{-1};
- $J_0(>E)$ the omnidirectional intensity with energies greater than E in units of el cm^{-2} s^{-1};
- B/B_Q the local magnetic field divided by the equatorial field on that line of force;
- pc the particle momentum multiplied by the velocity of light in units of MeV;
- L in units of R_J (71,372 km).

The angular distribution, and particularly the relationship between $j_\perp$ and J_0, is discussed in appendix 2. Equation (6) is the integral of (5) in the relativistic limit $v \approx c$. Because $v/c = 0.65$ for our lowest energy (0.16 MeV), this approximation is better than the roughness of the fit. These formulas are not supported by data outside the region

$$3 \leq L \leq 5 \qquad 1 \leq B/B_Q < 3 \qquad 0.16 \leq E < 60 \tag{7}$$

Inside this region, (5) falls within 30% of the tabulated fits above 9 MeV but deviates systematically at lower energies. This deviation is in the direction of lower intensities and falls

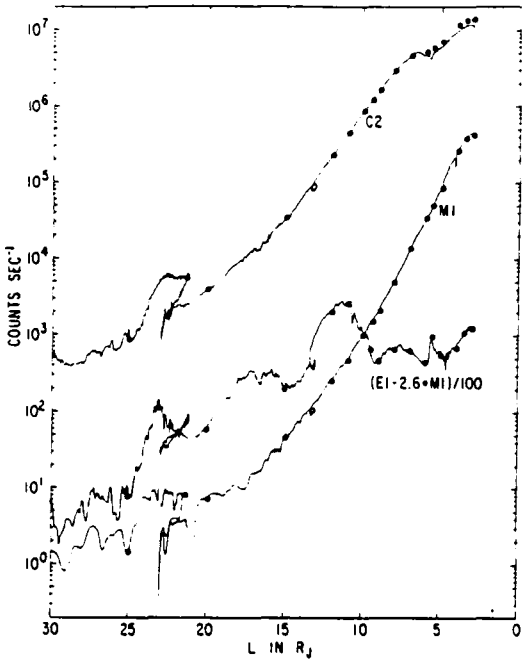

Fig. 2. Comparison between observed count rates and count rates computed by integrating the model spectra over the efficiency of each channel.

within the uncertainties in background subtraction discussed in FM 1974 and represented by the alternate spectra in Table 1 at $L = 3$. For $L > 5$, data contradict the formulas, and for $L < 3$, there are no data to compare with the formulas. In consideration of their limited domain, (4)–(7) should be treated with caution. However, they provide a reasonable representation that is continuous in energy, position, and angle, and they will be useful for some purposes.

Phase Space Density

Considering Liouville's theorem, we can evaluate sources and losses in the radiation belts by calculating the phase space density. Because [*Schulz and Lanzerotti*, 1974]

$$j = p^2\tau \tag{8}$$

where j is the differential intensity in particles $cm^{-2}\ s^{-1}\ sr^{-1}\ MeV^{-1}$ and τ is the density in six-dimensional phase space $d^3x\ d^3p$. Using the approximation as before that the angular distribution is isotropic, we can obtain from our fits the quantity $\bar{\tau}$, which is the phase density of particles with magnetic moment I_1 and 90° pitch angle:

$$\bar{\tau} = (K/2m_0BI_1)[1 + (2m_0c^2BI_1)^{1/2}/H]^{-\gamma} \tag{9}$$

Profiles of $\bar{\tau}$ are shown in Figure 4 for constant I_1. Except for a small spike in the vicinity of Io ($L = 5.6$), we see a monotonic decrease toward lower L values. This is the expected behavior for inward radial diffusion from an external source. The spike at $L = 5.6$ for $I_1 \approx 10$ MeV/G calls for a source at this point. This is apparently injection by Jupiter's moon Io, a phenomenon predicted by several authors [*Goldreich and Lynden-Bell*, 1969; *Shawhan et al.*, 1973].

Sudden losses take place at $L = 9.5$ and $L = 5.6$, evidently caused by absorption at Europa and Io. However, $\bar{\tau}$ decreases continuously between moons as well. This decrease could result from additional loss mechanisms such as synchrotron radiation or pitch angle scattering, or it could come from non-local losses fed by diffusion. In case there are no local losses the concavity of the τ versus L profile demands that the diffusion coefficient increase toward the planet so as to maintain equilibrium of diffusive flow. An inverse radial dependence of the diffusion coefficient had not been expected. We will treat the diffusion coefficient more thoroughly in a subsequent paper.

Appendix 1. Derivation of Particle Flux From the Count Rate

The instantaneous count rate may be described by the following integral over energy and angle:

$$R(\theta) = \iint A_{eff}(E, \eta, \zeta)j[E, \alpha(\eta, \zeta, \theta, \xi)]\, dE \sin\eta\, d\eta\, d\zeta \tag{A1}$$

where

- R instantaneous count rate;
- θ phase of spacecraft spin motion;
- η, ζ polar angles measured from detector look axis;
- ξ angle between B vector and spacecraft spin vector;
- α particle pitch angle, is equal to $\alpha(\eta, \zeta, \theta, \xi)$ because the aperture has an appreciable solid angle (η, ζ) and thus detector look axis varies with θ and ξ.

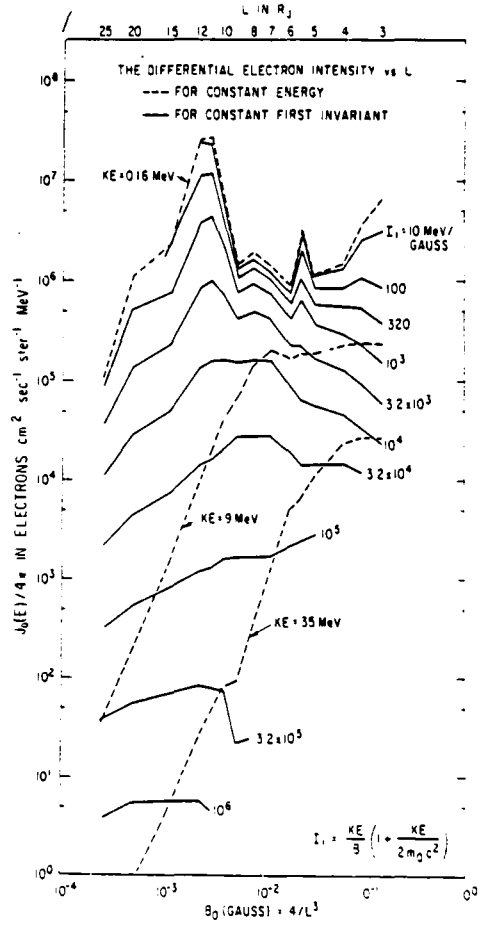

Fig. 3. Differential electron intensities computed from the fits, evaluated at constant energy (dashed lines) and at constant first invariant (solid lines).

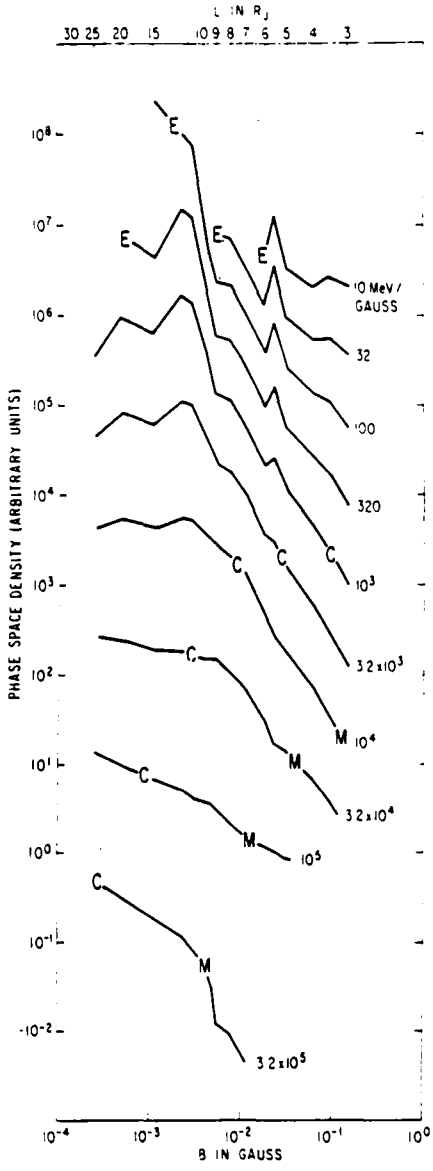

Fig. 4. Phase space density $\bar{r}$ versus L evaluated at constant first invariant I_1. The symbols E, C, and M indicate where the particle energy crosses the threshold of the named detection channel for each I_1.

We do not measure the instantaneous count rate, however, because our counters accumulate for 1.5 s and then read out. With a period of 12.62 s the spacecraft spin phase changes by $\Delta\theta \approx 43°$ in this interval. Thus our data are described by an integral over phase:

$$C(\theta) = \left(\int_{\theta-(\Delta\theta/2)}^{\theta+(\Delta\theta/2)} R(\theta)\, d\theta\right)\left(\int_{\theta-(\Delta\theta/2)}^{\theta+(\Delta\theta/2)} d\theta\right)^{-1}$$

$$= \frac{1}{\Delta\theta}\int_{\theta}\int_{\eta,\zeta}\int_{E} A_{\mathrm{eff}}(E,\eta,\zeta)$$

$$\cdot j[E,\alpha(\eta,\zeta,\theta,\xi)]\, dE \sin\eta\, d\eta\, d\zeta\, d\theta \qquad \text{(A2)}$$

where C is the number of counts accumulated divided by the time (1.5 s). We are generally able to fit a Fourier series to the data points to give us a continuous representation of $C(\theta)$. Thus we can evaluate

$$C_\perp \equiv C(\theta_\perp) \qquad C_\omega \equiv (1/2\pi)\int C(\theta)\, d\theta \qquad \text{(A3)}$$

where $\theta_\perp$ is the phase where the look direction is perpendicular to B.

Equation (A2) is as unwieldly as it looks. In the first place, the unknown $j(E,\alpha)$ is given by an integral equation for which there is no straightforward inversion technique. Second, the integral involves the additional variables η, ζ, which represent the appreciable opening of the aperture, and θ, ξ, which describe the fact that the scan direction is not a direct function of α. Published fluxes obtained by detector systems such as this all involve approximations used to solve this integral equation.

The technique used in this paper is to obtain the omnidirectional intensity

$$J_\omega(E) = 2\pi\int_0^{\pi} j(E,\alpha)\sin\alpha\, d\alpha \qquad \text{(A4)}$$

from the following approximation to (A2):

$$C_\perp \cong \frac{1}{4\pi}\int g(E)\, J_\omega(E)\, dE \qquad \text{(A5)}$$

where

$$g(E) = \int_{\eta,\zeta} A_{\mathrm{eff}}(E,\eta,\zeta)\sin\eta\, d\eta\, d\zeta \qquad \text{(A6)}$$

We call $g(E)$ the energy-dependent geometric factor, and we can evaluate it from laboratory calibrations. Figure 3 of FM 1974 displays $g(E)$ for two of our detectors.

This approximation removes the angle variables, but there remains a knotty integral equation in energy. In this paper we assume a spectral form (equation (1)) with as many fitting parameters as independent data channels, and through an iterative search we find values of the fitting parameters that satisfy the equation. These values are listed in Table 1.

The differences between this technique and that used in FM 1974 occur in the approximation used for the angular integration and in the approach to the energy integral. In quoting our results in FM 1974 we felt that the errors introduced by the former were smaller than those introduced by the latter. The fluxes obtained in this paper should be more accurate because of the improved method of handling the energy integral.

Appendix 2. Relationship Between $j_\perp$ and J_0

The angular distribution is implicit in (4)–(6), and it was handled in the following manner. Because it is often a good approximation in the earth's radiation belts, we represented the omnidirectional flux along a line of force as a power law in the field strength:

$$J_0 = C(B/B_0)^{-\nu} \qquad \text{(A7)}$$

where B/B_0 is the ratio of the local magnetic field to the magnetic field at the equator for that line of force. With two intersections of each L shell (inbound and outbound) we obtained empirical values for the exponent as a function of L. It is known from theory that a representation of the omnidirec-

TABLE 2. Relationship Between $j_\perp$ and J_0

ν	$f(\nu)$	$J_0/j_\perp$
0	1	12.6
1	1.5	8.1
2	1.9	6.6
3	2.2	5.7
4	2.5	5.0

tional flux all along a line of force implies the complete angular distribution and particularly the value $j_\perp$ of locally mirroring particles [*Ray*, 1960]. One can write

$$j_\perp = p(\nu)J_0/4\pi \qquad \text{(A8)}$$

where values for $p(\nu)$ can be calculated from Ray's equations and are tabulated in Table 2. Using our empirical exponents and values for $p(\nu)$, we obtained an empirical formula for the ratio of $j_\perp$ to J_0 (equation (5)).

Acknowledgments. We thank Antonio Mogro-Campero for helpful comments. This work was supported in part by NASA contract NAS 2-6552 and by NASA grant NGL 05-005-007.

The Editor thanks T. J. Birmingham for his assistance in evaluating this report.

References

Fillius, R. W., and C. E. McIlwain, Measurements of the Jovian radiation belts, *J. Geophys. Res.*, *79*, 3589, 1974.

Goldreich, P., and D. Lynden-Bell, Io, a Jovian unipolar inductor, *Astrophys. J.*, *156*, 59, 1969.

Ray, E. C., On the theory of protons trapped in the earth's magnetic field, *J. Geophys. Res.*, *65*, 1125, 1960.

Schulz, M., and L. J. Lanzerotti, Particle diffusion in the radiation belts, in *Physics and Chemistry in Space*, vol. 7, edited by J. G. Roederer, 215 pp., Springer, New York, 1974.

Shawhan, S. D., D. A. Gurnett, R. F. Hubbard, and G. Joyce, Io-accelerated electrons: Predictions for Pioneer 10 and Pioneer 11, *Science*, *182*, 1348, 1973.

Smith, E. J., L. Davis, Jr., D. E. Jones, D. S. Colburn, P. J. Coleman, Jr., P. Dyal, and C. P. Sonett, Magnetic field of Jupiter and its interaction with the solar wind, *Science*, *182*, 305, 1974*a*.

Smith, E. J., L. Davis, Jr., D. E. Jones, P. J. Coleman, Jr., D. S. Colburn, P. Dyal, C. P. Sonett, and A. M. A. Frandsen, The planetary magnetic field and magnetosphere of Jupiter: Pinoneer 10, *J. Geophys. Res.*, *79*, 3501, 1974*b*.

(Received August 19, 1974;
accepted December 20, 1974.)

Space Research XV — Akademie-Verlag, Berlin 1975

ELECTRONS AND PROTONS IN JUPITER'S RADIATION BELTS

A. Mogro-Campero, R. W. Fillius and C. E. McIlwain

Department of Physics, University of California, San Diego, La Jolla, Calif., USA

The UCSD experiment on Pioneer 10 measured fluxes of electrons and protons in Jupiter's magnetosphere. We present radial profiles of electrons with energies greater than 0.16, 9 and 35 MeV and of protons of energy > 80 MeV for the region $R \lesssim 13$ Jovian radii. We discuss particle absorption by the inner Jovian satellites. It is shown that the particle-satellite collision time, the radial diffusion coefficient, and the resulting absorption probability are expected to be functions of particle energy and species, in qualitative agreement with our observations. We also discuss possible causes for the observed decrease of proton flux at $R \lesssim 3.5$ Jovian radii.

1. Introduction

The existence and some characteristics of trapped relativistic electrons and the Jovian magnetic field were deduced from synchrotron models for the decimetric radiation observed at the earth [e.g. 1, 2]. However, information on the trapped protons and non-relativistic electrons has only recently become available as a result of direct measurements by experiments on Pioneer 10 (preliminary reports of these results were published in the 25 January 1974 issue of *Science*).

In December 1973 Pioneer 10 became the first spacecraft to traverse the magnetosphere of Jupiter. The University of California at San Diego (UCSD) experiment on Pioneer 10 measured protons with energies $E_p \geqq 80$ MeV and electrons with energy thresholds in the range $0.1 \leqq E_e \leqq 35$ MeV. Some aspects of the results of this experiment, including the description and characteristics of the instrument have been published [3, 4].

The analysis in this paper was performed by using the magnetic field model derived from direct measurements on Pioneer 10 [5]. In particular, the values of the magnetic shell parameter L ($\equiv R \cos^{-2} \lambda$), where λ is the magnetic latitude and R is the jovicentric distance in units of the planetary radius R_J, are a function of the magnetic field model. In the present paper we restrict our analysis to the region $R \lesssim 15 R_J$, where a dipole representation of the magnetic field is usable [5]. Based on particle measurements, the Jovian magnetosphere is also naturally divided into two regions with the boundary at $R \sim 20 R_J$ [e.g. 3, 4].

In §2. we present radial profiles of electrons with $E_e > 0.16$ MeV, $E_e > 9$ MeV, and $E_e > 35$ MeV and of protons with $E_p > 80$ MeV. In §3. we develop the concepts needed for an analysis of the interaction of the Jovian satellites with the

trapped particles, and we show why the published treatments of particle absorption by Jupiter's satellites are inadequate for some of the energies and values of L for which we have measurements. We find that there is a considerable variation in the drift frequencies for the particles we measure, and we discuss particle absorption by the innermost Jovian satellites with an emphasis on the effects due to the differences which can be expected as a function of particle energy. We show that the qualitative characteristics of the particle-satellite interactions which we observe can be understood in terms of these ideas. In § 4 we discuss possible causes for the observed decrease of proton flux at $L \lesssim 3.5$. We conclude that loss due to pitch angle scattering and absorption by Amalthea are possible explanations, but that there is insufficient information in our data to decide between these.

2. The Data

The data reduction procedures, including calculations of the geometrical factors and background corrections when necessary have been described in [4]. To illustrate the structure in the radial profiles of electrons we have chosen three integral flux measurements ($E_e > 0.16$ MeV, $E_e > 9$ MeV, and $E_e > 35$ MeV), as shown in Fig. 1. Although the satellites revolve around Jupiter at a fixed jovicentric distance, the non-centered and tilted position of the magnetic dipole with respect to jovigraphic coordinates results in a spread in the L values traversed by each

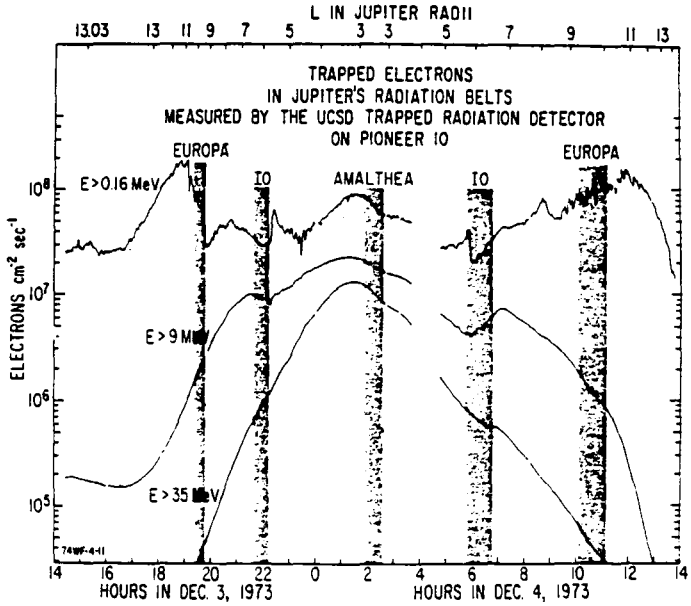

Fig. 1. Radial profiles of electron fluxes in the inner Jovian magnetosphere. The hours are in spacecraft time. The shaded bands indicate times when Pioneer 10 was on L shells traversed by Jupiter's satellites.

satellite as shown in the figure. As can be easily seen, some prominent features in the radial profile seem to be due to absorption of particles by satellites, but it is immediately evident that all energies do not behave in the same manner (e.g., at Europa electrons with $E_e > 0.16$ MeV are affected strongly, whereas those with $E_e > 9$ MeV seem to pass by with no effect). We discuss why an energy dependence would be expected in the next section.

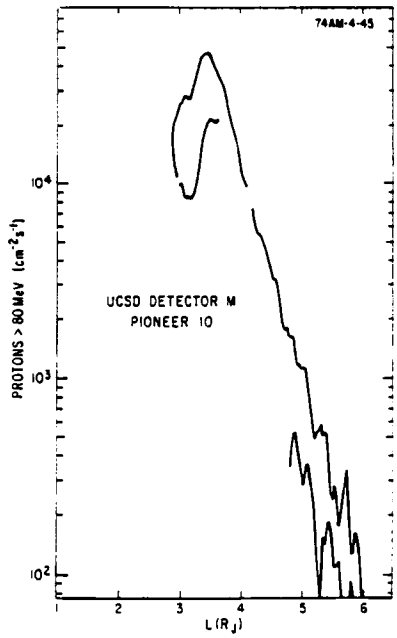

Fig. 2. The integral flux of protons > 80 MeV as a function of L.

We also see from Fig. 1 that the energy spectrum flattens toward lower L values, since with decreasing L the fluxes of higher energy electrons are rising at a faster rate than those of lower energy electrons. The peaks in the lowest energy electrons inside of Io on both the inbound and outbound trajectories are suggestive of acceleration effects at Io as proposed, for example, in [6].

In Fig. 2 we show the proton flux ($E_p > 80$ MeV) as a function of L. The inbound pass corresponds to the higher fluxes, and the data gap on the outbound trajectory is due to occultation of the spacecraft by Jupiter. These data were stored in the spacecraft and transmitted to earth after occultation. Although the reduction procedure has not been completed due mainly to timing problems, it is clear from the occultation data that a good approximation to the actual profile is a straight line connection for the missing portion in the figure. Therefore, it is established that the narrow peak observed inbound at $L \sim 3.5$ occurs also on the outbound trajectory, where the reduction in flux can be understood in terms of magnetic latitude (i.e. the inbound pass was closer to the magnetic equator). In § 4 we discuss possible reasons for this dramatic decrease in proton flux for $L \lesssim 3.5$.

3. Particle Absorption by Jupiter's Satellites

It appears likely that the radial diffusion of trapped particles in the inner region of the Jovian magnetosphere may be driven by electric fields associated with the upper atmosphere dynamo which is driven by neutral winds in the ionosphere [7, 8]. It seems natural then to consider motion in an inertial reference frame, in which steady state winds in the planet's upper atmosphere produce electric field fluctuations at zero frequency [7].

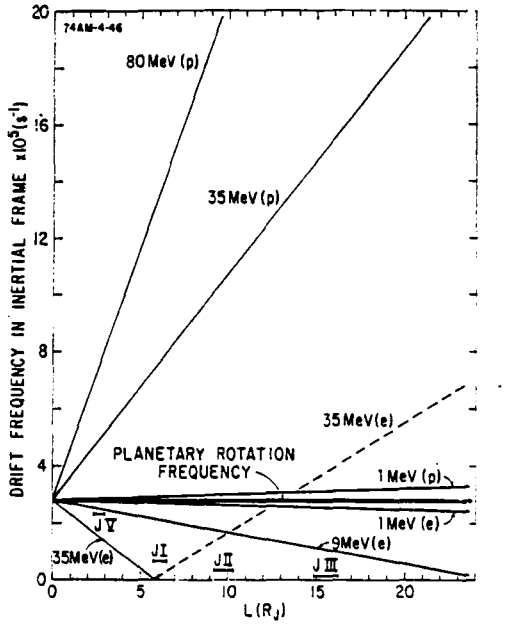

Fig. 3. Drift frequencies of protons and electrons of selected energies as a function of L in an inertial frame. The ranges of L values traversed by the satellites are indicated at their appropriate rotation frequencies (JV is Amalthea, JI is Io, JII is Europa, and JIII is Ganymede). The dashed line corresponds to negative frequencies (i.e. opposite to the direction of planetary rotation).

In this frame, the frequency of rotation around Jupiter of protons and electrons of different energies is shown in Fig. 3. This drift frequency is a combination of the usual drift frequency produced by the curvature and the gradient of the magnetic field and the planetary rotation frequency (assuming co-rotation). We see that for both species drift frequencies at a fixed energy are represented by straight lines which intersect $L = 0$ at the planetary rotation frequency, and that larger slopes correspond to higher energies. The range of L values traversed by each of the innermost four satellites is shown in this figure at the rotation frequency of the satellite. The range of L values for each satellite is a measure of the radial extent

of its "sweeping region". For the electrons there is a characteristic energy E_f at a fixed L value at which the drift frequency f is zero, and at the average L value traversed by a satellite there is an energy E_s at which the particle drift frequency equals the satellite rotation frequency. At the average L values of the satellites these electron energies in MeV are (E_f, E_s): Amalthea (90, 14.5), Io (39, 30), Europa (24, 21), and Ganymede (15, 14).

Theoretical treatments of Jovian trapped particle diffusion and their interactions with the satellites [8—10] have been limited to particles whose drift frequency equals the planetary rotation frequency, and therefore, as illustrated in Fig. 3, they may be inapplicable at the higher energies for which we have measurements. As noted in [9], because of the tilt of the magnetic dipole axis with respect to the planetary rotation axis, particles with large pitch angles will have less probability of being absorbed by the satellites. An examination of pitch angle distributions both before and after the traversal by Pioneer 10 of the orbit of Io reveals that this effect is occurring, but we postpone a detailed discussion of this effect and others related to pitch angle distributions to a future publication. We also defer treatment of the effects of radial and latitude excursions of the satellites, since the preliminary magnetic field model [5] may soon be improved (E. J. Smith, private communication). These latter effects have not been dealt with in the theoretical treatments, but have recently been considered in [11].

We proceed by exploring the consequences of the frequency distribution illustrated in Fig. 3, realizing that the effects we are omitting and which are mentioned above may modify this simplified treatment.

Two characteristic parameters determine particle absorption by satellites: the time T_s taken by the particles to traverse the sweeping region of the satellite, and the time T_i taken by the particles to impact the satellite once they find themselves in its sweeping region. The probability of absorption by a satellite is high for $T_s \gg T_i$, and low for $T_i \gg T_s$. It will be shown that the probability of absorption of electrons has two minima. We assume that T_i is inversely proportional to the relative drift frequencies between the particles and the satellite. This means that for electrons T_i will be very large at energies near E_s, the energy at which the particle drift frequency equals the satellite rotation frequency. For radial motion, $T_s \propto D^{-1}$, where D is the radial diffusion coefficient, so that the absorption probability will have an additional energy dependence if the diffusion coefficient is a function of energy, as it is likely to be.

As an example of the energy dependence of D, we proceed as follows. The diffusion coefficient for motion produced by fluctuating electric fields is proportional to the power spectrum of these fields at the drift frequency [12]; therefore the diffusion coefficient can be constant only if the fields have a white spectrum. A frequency dependence of the power spectrum will result in an energy dependence for T_s. As an example, we assume a power spectrum which is inversely proportional to the square of the frequency. In this case the diffusion coefficient for electrons will have a maximum at E_f, the energy at which the drift frequency is zero. Other forms of the power spectrum might be preferable, for example a maximum might be expected at the planetary rotation frequency. However, for simplicity, in this paper we consider only the case described above. In Fig. 4 we show T_i and T_s as a function of energy for electrons at $L = 9.5$ (the average location of Europa) with the assumptions stated above. Since the time scale is independently arbitrary for T_s and T_i, we have fixed their relative positions so that low energy electrons will suffer some absorption ($T_s > T_i$).

whereas high energy electrons (3 MeV $\lesssim E_e \lesssim$ 42 MeV) will not, as is observed (Fig. 1).

Fig. 4 shows that large variations in T_i and T_s can be expected. Our assumption for the frequency dependence of the power spectrum is not critical, since even a constant T_s would lead to a rather broad energy window of easy particle access across the satellites, with absorption at the low energies. We find that at Io, a

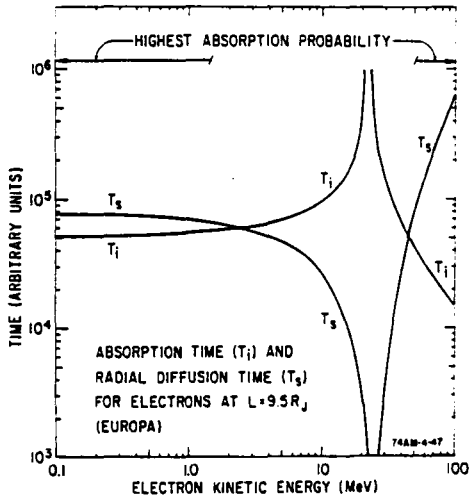

Fig. 4. The absorption time T_i and the radial diffusion time T_s as a function of energy for electrons at the average L value traversed by Europa. The highest absorption probability occurs for $T_s > T_i$, at the energies shown at the top of the figure.

similar analysis results in the energy window for little or no absorption moving to higher energies (since both E_i and E_s are larger than at Europa). Therefore, at Io our electron observations shown in Fig. 1 can again be understood qualitatively. Our observations near Amalthea can also be made consistent with these ideas by a similar analysis. It seems reasonable that both T_i and T_s should be the same for protons and electrons in the low energy limit, so that once the positions of T_s and T_i are fixed with respect to each other to satisfy the observations at a given electron energy, qualitative predictions can be made for electrons and protons of all other energies.

4. The Maximum in the Radial Profile of Protons

In Fig. 2 we have seen that the protons with $E_p > 80$ MeV decrease abruptly at $L \lesssim 3.5$. In this section we consider possible causes for this decrease. These causes have also been recently considered in [11] with respect to their data.

If the decrease in protons is produced by a loss mechanism, this mechanism will become effective for $T_L < T_S$, where T_L and T_S are the characteristic loss and source times. If the source of particles is radial diffusion, we may use $T_S \sim R_J^2/D$.

For loss due to pitch angle scattering into the loss cone, $T_L \gtrsim 4L^4 R_J/a$ [13], where a is the velocity of the particle. If we use for a the velocity of an 80 MeV proton, and $L = 3.5$, we obtain an upper limit for the diffusion coefficient, $D \lesssim 2.2 \times 10^{-3} R_J^2(s^{-1})$. This upper limit is ~ 5 orders of magnitude greater than the diffusion coefficient derived in [8] for this L value. However, we point out that the diffusion coefficient derived in [8] to explain the observed Jovian decimetric radio emission is only valid for particles with drift periods near the planetary rotation frequency; the drift frequency of 80 MeV protons at $L = 3.5$ is a factor of ~ 3 greater than the planetary rotation frequency.

For Jovian trapped protons, plasma turbulent precipitation loss by electromagnetic ion cyclotron waves and by quasi-electrostatic loss-cone waves have been considered [13]. The maximum flux of protons we observe (Fig. 2) is well below the limiting flux expected as a result of the instabilities considered in [13]. This is consistent with the notion that most of the particles being limited are below our threshold energy. The electrons are not observed to decrease as the protons do (Fig. 2), but this might be due to their lower drift frequencies and consequently higher diffusion coefficients (§ 3), and to the limiting effect of synchrotron radiation. For the ion cyclotron wave, significant wave growth results only if $E \gtrsim E_c = B^2/8\pi n$ [13], where n is the cold plasma density, so that our observations in Fig. 2 imply that $E_c < 80$ MeV. Therefore, at $L = 3.5$ this means $n > 4.5$ cm^{-3}. The lower limit of n is more than an order of magnitude higher than the plasma density at $1 \leqq L \leqq 5$ derived for Jupiter in [14], but we note that this model does not take into account the plasma contributed by the satellites.

It may be that absorption by Amalthea is responsible for the drastic reduction even though the electrons we observe do not behave similarly. An analysis for Amalthea similar to that shown for Europa in Fig. 4, shows that this is possible. Since T_l is smaller for protons than for electrons at the relevant energies, and T_s is larger, both of these lead to a higher probability of absorption for protons (see § 3).

In summary, on the basis of our data, it seems possible in principle that the proton decrease at $L \lesssim 3.5$ may be due to a pitch angle scattering loss mechanism. If the plasma density is $n > 4.5$ cm^{-3}, the ion cyclotron instability is a possibility. Proton absorption at Amalthea is also plausible for explaining this phenomenon. However, it is clear that many more data are needed to solve this problem; the behavior of the radial profile at $L < 3$ (Pioneer 11) and proton measurements at other energies can be expected to throw more light on this puzzle.

Acknowledgment

This work was supported by NASA contracts NAS 2-5602 and NAS 2-6552, and by NASA Grant NGL 05-005-007.

References

[1] J. W. Warwick, Space Sci. Rev. 6, 841 (1967).
[2] J. N. Clarke, Radio Sci. 5, 529 (1970).
[3] R. W. Fillius and C. E. McIlwain, Science 183, 314 (1974).
[4] R. W. Fillius and C. E. McIlwain, J. Geophys. Res. 79, 3589 (1974).
[5] E. J. Smith et al., Science 183, 305 (1974).

[6] S. D. Shawhan et al., Science 182, 1348 (1973).
[7] N. Brice and T. R. McDonough, Icarus 18, 206 (1973).
[8] T. Birmingham et al., J. Geophys. Res. 79, 87 (1974).
[9] G. D. Mead and W. N. Hess, J. Geophys. Res. 78, 2793 (1973).
[10] W. N. Hess, T. J. Birmingham and G. D. Mead, J. Geophys. Res. 79, 2877 (1974).
[11] J. A. Simpson et al., J. Geophys. Res. 79, 3522 (1974).
[12] C.-G. Fälthammar, J. Geophys. Res. 70, 2503 (1965).
[13] F. V. Coroniti, C. F. Kennel and R. M. Thorne, Astrophys. J. 189, 383 (1974).
[14] G. Ioannidis and N. Brice, Icarus 14, 360 (1971).

ABSORPTION OF RADIATION BELT PARTICLES BY THE INNER SATELLITES OF JUPITER

A. MOGRO-CAMPERO
University of California, San Diego

The study of trapped particle absorption by the inner Jovian satellites is reviewed from the viewpoint of radiation belt physics. Both pre- and post-Pioneer work is discussed but the emphasis is on methods used to deduce radial diffusion coefficients of particle transport from particle data. The phenomenon of particle absorption as observed by experiments on Pioneers 10 and 11 is considered; absorption effects are found to depend on the satellite, and on particle energy and species. Approximate diffusion coefficients derived from the data are found to follow a steeper spatial dependence than previously expected. The assumptions and limitations of absorption analysis and diffusion coefficient estimation are pointed out.

In this paper we discuss the absorption of radiation belt particles by the satellites from the standpoint of radiation-belt physics. We are concerned with the passive role of satellites as absorbers of trapped radiation and with the implications relevant to trapped particle transport throughout the inner magnetosphere of Jupiter.

Since Pioneer 10 was the first spacecraft which traversed the Jovian magnetosphere, it is convenient to divide the development of the problem into pre- and post-Pioneer 10 phases, which we label Phase 1 and Phase 2. This division is obviously chronological, and in the following sense conceptual. During Phase 1 the central question can be summarized as: given a dynamic situation in which trapped particles undergo radial diffusion, what is the effect of satellite absorption on the particle intensity profiles for values of the diffusion coefficient assumed or derived independently? In Phase 2 the question becomes: given that trapped particle intensity profiles have been observed which indicate absorption by the satellites, what values can we deduce for the diffusion coefficient of radial transport?

We review the work done in Phases 1 and 2, and summarize the methods and results obtained in Phase 2. Values are then presented for the radial

diffusion coefficient as a function of particle energy, drift frequency and L (throughout this chapter L is the dimensionless McIlwain shell parameter). These values are derived by using one of the methods presented here and all of the Pioneer 10 and 11 data.

The reader who wishes background information on radiation-belt physics may consult books by Hess (1968), Roederer (1970), or more specifically on trapped particle diffusion, by Schulz and Lanzerotti (1974).

I. PHASE 1

Before spacecraft measurements in the close environment of Venus and Mars were performed, it was thought possible that these planets might have significant radiation belts. In this context, the absorption effect of a planetary satellite was considered for the first time. Phobos, which orbits Mars at ~ 3 Martian radii from the center of the planet, was a natural candidate for study. Thus, Singer (1962) treated the sweeping effect of Phobos on the Martian radiation belt. He obtained expressions for the particle absorption lifetime in the case of a magnetic dipole field displaced by an arbitrary amount from the center of the planet in the equatorial plane, and he concluded that trapped particle intensity measurements in the region of Phobos could be used to deduce the particle injection rate and ultimately the source of the trapped radiation.

About a decade later, in July 1971, a group of scientists and engineers met for a Workshop at the Jet Propulsion Laboratory, Pasadena, California, in order to review the current state of Jupiter radiation belt knowledge and to recommend a best set of models for the determination of spacecraft design requirements. Two papers at that meeting (one by Hess and one by Mead) dealt with the effects of Jupiter's satellites on the trapped radiation: one of these (Mead 1972) can be found in the Workshop Proceedings. In Mead's paper, characteristic spatial and temporal parameters of trapped protons and of the inner satellites were evaluated and discussed with respect to particle absorption. The radiation belt models resulting from the Workshop (Divine 1972) did not include the effect of the satellites, since it was assumed that the diffusion of protons past the satellites occurs without interference. It was realized, however, that alternative models with a strong absorption effect by the Jovian satellites were also plausible (Davis 1972). A few months later, in an extension of the discussions of the Workshop, Jacques and Davis (1972) solved the trapped particle equations of transport for diffusion of particles by violation of the third adiabatic invariant, including losses due to satellite absorption and synchrotron radiation. They estimated values for diffusion coefficients due to (a) deformation of the magnetic field by the solar wind ($\propto L^{10}$); (b) randomly fluctuating electric fields ($\propto L^{6}$), and (c) interchange of flux tubes by ionospheric winds [$\propto L^{2}(L-1)$]. The first two are processes thought to be important at Earth, and the third is based on

a mechanism suggested at the Workshop by Brice (1972). Jacques and Davis concluded that only the third mechanism could explain the electrons required to produce the observed synchrotron radiation, and that in this case the effect of Io would be neither overwhelming nor negligible.

All studies of particle absorption by the satellites have assumed that trapped particles co-rotate with the planet. Mead and Hess (1973) made a thorough study of the absorption process for low-energy particles, i.e., those for which the drift period is close to the planetary rotation period. They pointed out that because of the tilt of the magnetic dipole field with respect to the planetary rotation axis, the absorption process would be pitch-angle dependent. Assuming violation of the third adiabatic invariant by deformation of the magnetic field due to the solar wind (resulting in a diffusion coefficient $D \propto L^{10}$), they concluded that the inner satellites would act as a barrier to the inward diffusion of particles, in agreement with the conclusion of Jacques and Davis (1972) for this type of diffusion coefficient.

Brice and McDonough (1973) estimated the strength of the diffusion coefficient due to electric field fluctuations produced by neutral winds in the ionosphere, following an earlier suggestion by Brice (1972). For slowly drifting particles, i.e., those whose drift period is close to the planetary rotation period, they found that the diffusion coefficient $D \propto L^3$. For fast drift particles, $D \propto L^5$ and $D \propto L^{3.5}$ for nonrelativistic and relativistic particles, respectively. Their values for D led them to conclude that no serious losses would occur due to particle absorption by the Jovian satellites, in agreement with the conclusion of Jacques and Davis (1972) for a similar type of diffusion coefficient.

Coroniti (1974) also considered radial diffusion driven by fluctuating electric fields originating from atmospheric neutral wind turbulence, and derived a diffusion coefficient $D \propto L^3$. He investigated plasma instabilities which could limit the intensity of stably trapped electron fluxes and absorption of particles by the satellites. His estimate for the value of the diffusion coefficient led him to conclude that the satellites would not act as major barriers to the passage of inward diffusing particles.

Hess *et al.* (1973, 1974) estimated sizable reductions in the trapped particle intensities (up to one order of magnitude, depending on equatorial pitch angle) near the orbits of Ganymede, Europa and Io due to particle absorption by these satellites. They used a diffusion coefficient $D = kL^a$, with the values of k and a (1.7×10^{-9} sec^{-1} and 2, respectively) deduced by Birmingham *et al.* (1974) by fitting the observed radial distribution of Jupiter's decimeter radio emission to a model of trapped electrons. Birmingham *et al.* noted that their diffusion coefficient had roughly the same radial dependence, but was considerably smaller in magnitude than the upper limit diffusion coefficients for field-line exchange driven by ionospheric winds suggested by Brice and McDonough (1973), and by Jacques and Davis (1972).

In summary, prior to the first flyby of Jupiter by Pioneer 10, many authors had considered the possible effect of absorption of trapped particles by the

Jovian satellites. It was generally felt that some of the inner Jovian satellites would produce observable effects on the trapped particle intensities, and that the diffusion coefficient of radial transport was probably of the type $D \propto L^a$, with $a \simeq 2$ to 3 for slow-drift particles.

II. PHASE 2

All charged particle experimenters on Pioneer 10 reported features in the trapped particle intensity profiles which could clearly be attributed to satellite absorption (Fillius and McIlwain 1974*a*,*b*; Simpson *et al.* 1974*a*,*b*; Trainor *et al.* 1974*a*,*b*; Van Allen *et al.* 1974*a*,*b*). Similar results have been reported recently for Pioneer 11 (Fillius *et al.* 1975*a*;[1] Simpson *et al.* 1975;[2] Trainor *et al.* 1975;[3] Van Allen *et al.* 1975[4]). Electron absorption is also evident when one considers the particle phase-space densities computed from the data (McIlwain and Fillius 1975; Baker and Van Allen 1975). Vesecky (1975) has collected the Pioneer 10 observations relevant to satellite absorption and compared them with theoretical expectations developed in Phase 1.

Since data are available for both inbound and outbound passes of Pioneers 10 and 11, it is possible to investigate whether absorption is a strong function of longitude. In spite of the wide range of longitudes involved (Table 1), the large-scale features in the particle intensity profiles of a given detector which are attributable to satellite absorption are similar in the four Pioneer passes with the exception of the MeV protons at Europa as reported by Trainor *et al.* (1975). A possible local rapid diffusion process may be partly responsible for the longitudinal uniformity (Huba and Wu 1975).

A discernible energy and species dependence of particle absorption is clearly identifiable in the Pioneer data. For example, in Fig. 1 are shown the counting rate profiles of three electron detectors for the inbound and outbound passes of Pioneer 10. The average energies to which these detectors are sensitive are ~ 1, 10, and 25 MeV, so that the energy dependence of absorption at Io and Europa is evident. A dependence of particle absorption on spacecraft magnetic latitude should be observable due to the expected preferential absorption of small equatorial pitch-angle particles (Mead and Hess 1973). The Pioneer 10 trajectory is suitable for the observation of this effect at Io (from Table I we see that the magnetic latitude of Pioneer 10 was $-6°$ and 14° for the inbound and outbound passes, respectively). Figure 1 is especially tuned to observe this effect, since the particle counting rates shown are those measured perpendicular to the local magnetic field vector. The pitch-angle dependence of absorption is qualitatively confirmed by the middle trace in Fig. 1, where a larger absorption effect is evident in the case of the higher-latitude outbound pass. An analysis of particle anisotropies in

[1] See also p. 913.
[2] See also p. 743.
[3] See also p. 964.
[4] See also p. 929.

TABLE I

Pioneer-Satellite Longitude Intervals and Pioneer Magnetic Latitude at Times When the Spacecraft Traversed the L Shells of a Satellite

Pioneer 10 or 11 and Satellite	Inbound or Outbound	Longitude Interval[a] (deg)	Spacecraft Magnetic Latitude[b] (deg)
P10–Europa	I	334	−19
	O	126	+4
P11–Europa	I	76	−43
	O	204	+53
P10–Io	I	51	−6
	O	157	+14
P11–Io	I	(a few)	−41
	O	163	+45
P11–Amalthea	I	129	−34
	O	30	+23

[a]This longitude interval is relevant for particle absorption, and is defined as the longitude angle (0° to 360°) from the spacecraft to the satellite in the direction of motion of the satellite in the frame co-rotating with Jupiter. The accuracy of these values is a few degrees. This has been emphasized in the table by the entry for P11–Io, I. A study of the Pioneer 11 proximity to the Io flux tube requires a more accurate description.

[b]Magnetic latitudes are those given by the D2 magnetic field model of Smith *et al.* (1974). The magnetic latitude of the satellites is bounded by ± 11°.

the vicinity of Io's orbit (e.g., see Fig. 2) was also found to be consistent with the concept that particles with small equatorial pitch angles are absorbed preferentially (Simpson *et al.* 1974*b*; Trainor *et al.* 1974*a*; Fillius *et al.* 1975*b*). In the case of electrons > 0.06 MeV, however, Sentman and Van Allen (1975) do not observe clearly identifiable effects on the angular distributions associated with passage through the magnetic shells of Ganymede, Europa, and Io. Angular effects for electrons may be more difficult to observe because of pitch-angle scattering (Fillius *et al.* 1975*b*).

We have seen that the absorption effect is observed to depend on particle species and energy. This fact seemed at first puzzling from the viewpoint of the theoretical framework developed in Phase 1 (Hess *et al.* 1974). However, the slow drift approximation which is prevalent in these models is not valid for many of the particle energies. Simpson *et al.* (1974*b*) have studied particle absorption by Io and showed that the impact probability is depen-

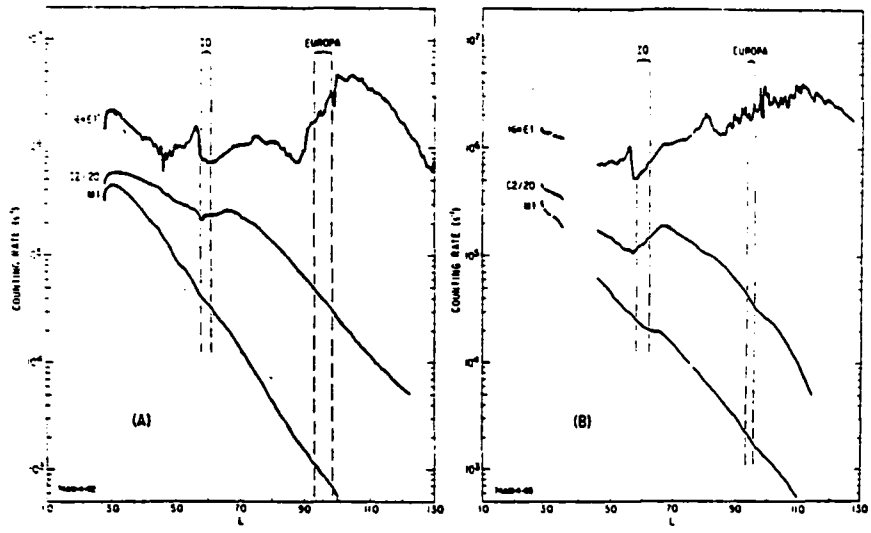

Fig. 1. The energy dependence of particle absorption at Io and Europa. Counting rates of three electron detectors of the University of California, San Diego experiment for (A) the inbound trajectory, and (B) the outbound trajectory of Pioneer 10. These are the counting rates perpendicular to the local magnetic field vector. The average energy of response varies with location in the Jovian magnetosphere. Approximate values are 1, 10, and 25 MeV from top to bottom (from Mogro-Campero and Fillius 1976).

dent on energy and species. Furthermore, they have obtained a probable value for the radial diffusion coefficient of ~ 1 MeV protons at Io. Mogro-Campero *et al.* (1975) have discussed particle absorption by the inner satellites and they showed that the particle-satellite collision time, the radial diffusion coefficient, and the resulting absorption probability are expected to be dependent on species and energy. They also showed that the energy dependence of absorption exhibited by their electron detectors was in qualitative agreement with the expected energy dependence. Mogro-Campero and Fillius (1976) discussed several approaches to obtain estimates of the radial diffusion coefficient. They have derived an expression for the sweeping time at a given satellite, and by using Pioneer 10 electron data they obtained values for the diffusion coefficient at Europa and Io in the energy range of ~ 0.7 to 14 MeV. They concluded that the diffusion coefficient is a function of energy and L. Based on this formulation and on Pioneer 11 data, Fillius *et al.* (1975*a*) have recently reported values for the diffusion coefficient of ~ 100 MeV protons and ~ 90 MeV electrons at Amalthea, providing a stronger basis for contentions of energy and spatial dependences of the diffusion coefficient.

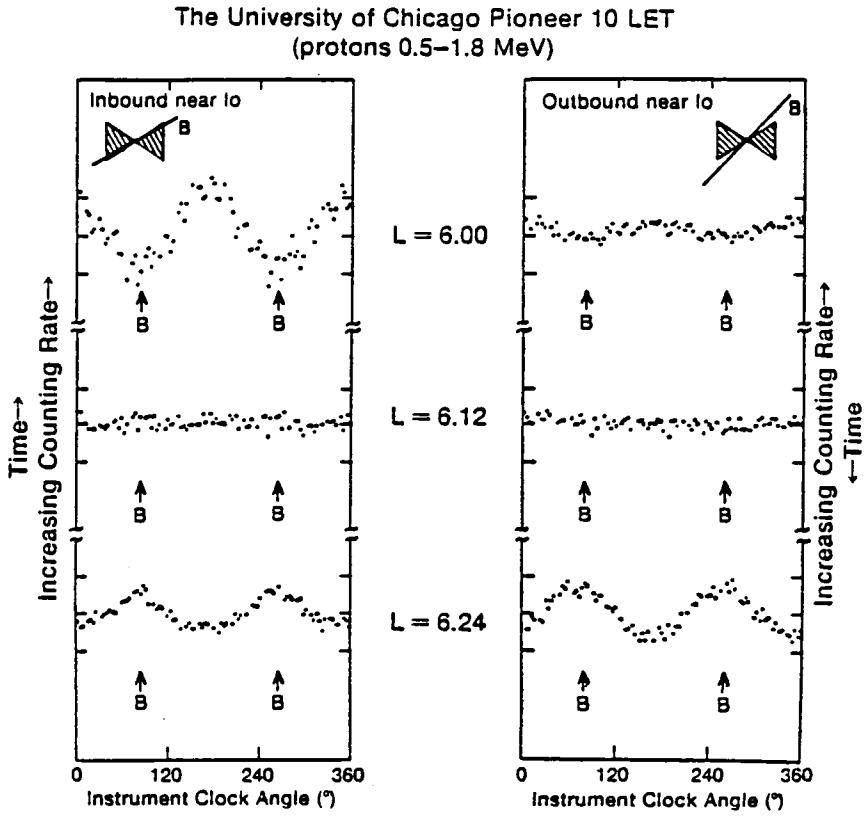

Fig. 2. The change in the low-energy (0.5–1.8 MeV) proton anisotropy as the orbit of Io is crossed, both inbound and outbound, as observed with the University of Chicago experiment on Pioneer 10. The diagrams near the top of the figure show the relationship between the magnetic field direction and the detector acceptance band (from Simpson *et al.* 1974*b*).

III. METHODS USED IN PHASE 2

The Sweeping Time

The sweeping time is defined as the time required for the satellite to absorb a given fraction of the trapped particles within its sweeping region. The following considerations apply:

1. It is always assumed that the trapped radiation co-rotates with the planet.
2. Because of our ignorance of the electric and magnetic field configuration in the immediate vicinity of the satellites, it is assumed that trapped-particle motion is determined exclusively by the undistorted planetary

magnetic field (the D2 dipole model of Smith *et al.* 1974 is used throughout this paper). Thus, if a trapped particle trajectory intersects a satellite, the particle is removed from the trapped particle population. The electron/proton energy in MeV at which the gyroradius equals the satellite radius is 680/220 at Amalthea, 970/410 at Io, and 220/25 at Europa. These energies are all above those measured on the Pioneer missions where absorption effects have been noticed. It is therefore not possible for these particles to avoid impact with the satellite when their center of gyration lies within the satellite.

3. Particles may escape absorption by leapfrogging the satellite in their longitudinal drift motion during half a bounce period. This is not possible for electrons of the energies in consideration ($0.1 \lesssim E \lesssim 100$ MeV) for the four innermost Jovian satellites (Mogro-Campero and Fillius 1976), but it is an important point to consider e.g., in the case of protons with $\lesssim 7$ MeV at Europa. For convenience at this time, we restrict our attention to cases where this longitude skipping mechanism is unimportant.
4. The extent of the sweeping region ΔL, is a function of equatorial pitch angle. This is equivalent to the preferential absorption of small pitch-angle particles mentioned previously. This concept, as well as the geometry of particle absorption, can be illustrated by considering satellite trajectories in magnetic field coordinates. Such a trajectory for Io is shown in Fig. 3. It is clear from this figure that particle absorption is more likely for small equatorial pitch-angle particles, since their magnetic latitude coverage is wider than that of the satellite.

The time required for removal by Io of 90% of the electrons and protons at $L = 6.19$ has been evaluated by computer simulation as a function of energy by Simpson *et al.* (1974*b*), and is shown in Fig. 4. At low energies the smooth behavior corresponds to complete absorption within one drift period. At higher energies the fine structure is produced by particles whose drift velocity is in some simple ratio to the velocity of Io in the co-rotating frame. The effects of radial diffusion were not considered.

When reviewing the Pioneer data we have concluded that longitudinal uniformity of the particle intensity profiles in the vicinity of the satellites is probably a good approximation. Processes contributing to this uniformity are the combined effects of the particle's drift motion, random radial displacements characteristic of their radial diffusive motion, and possible localized turbulent diffusion (Huba and Wu 1975).

By postulating that longitudinal uniformity would be achieved in time scales comparable or shorter than the satellite orbital period in the co-rotating frame, Mogro-Campero and Fillius (1976) derived the following expression for the sweeping time at a satellite:

$$T_s = -g\, t_c \ln y \qquad (1)$$

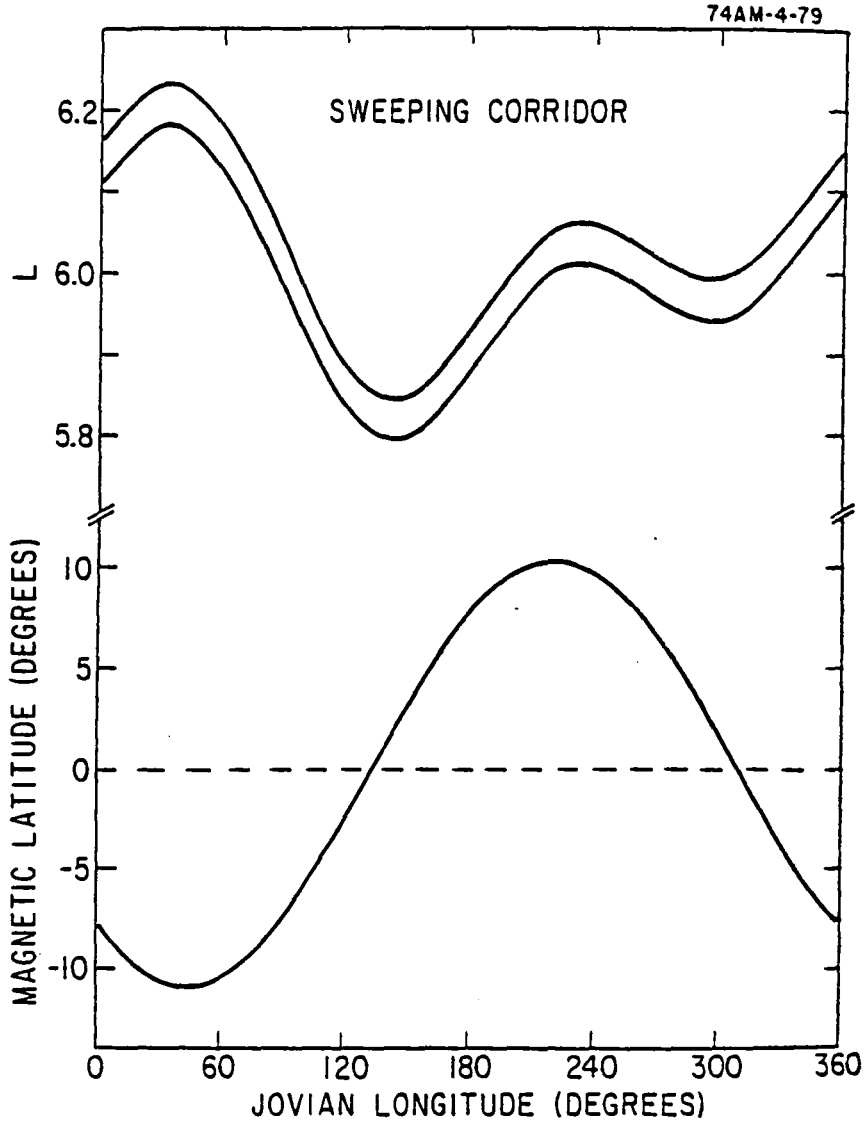

Fig. 3. Io's trajectory in the magnetic field coordinates L and magnetic latitude versus Jovian System III longitude (Mead 1974). The width of the band in L corresponds to Io's diameter and determines the sweeping corridor for particles with gyroradii $\ll$ Io's radius. Io passes through a given longitude in the sweeping corridor once every orbital period in the frame of reference co-rotating with Jupiter (from Mogro-Campero and Fillius 1976).

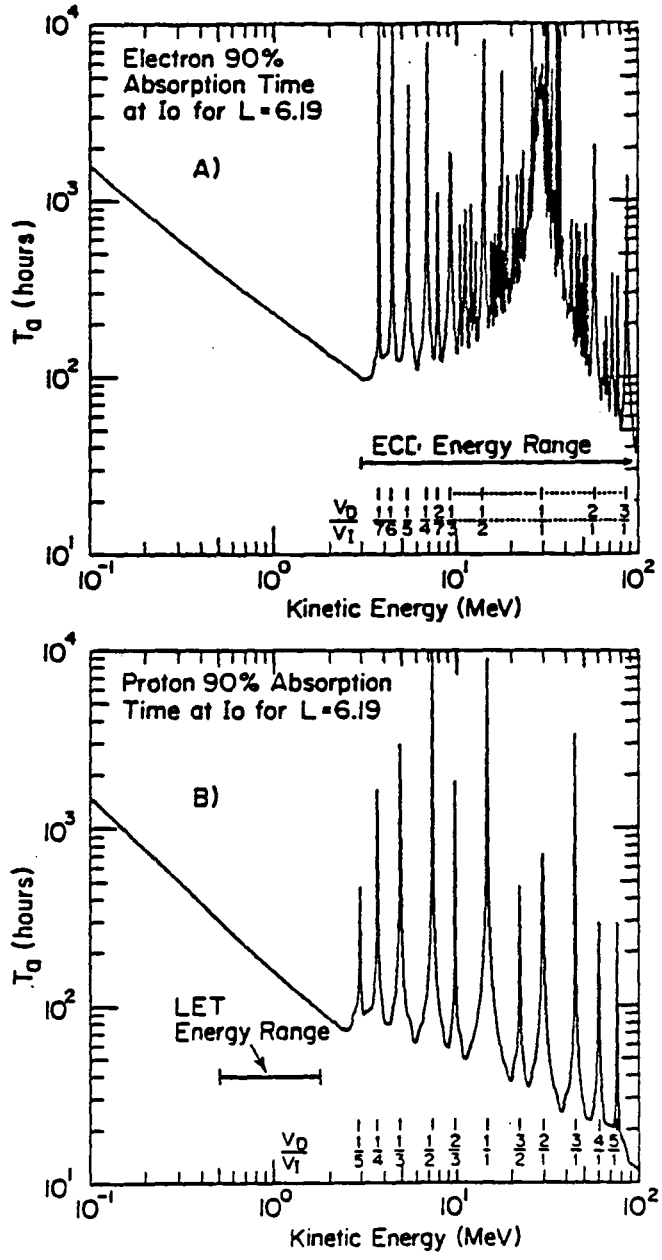

ig. 4. The time required for removal by Io of 90% of the (A) electrons and (B) protons initially present in a uniformly populated drift shell at $L = 6.19$ in the absence of radial diffusion, computed as a function of energy. The ratio of particle drift velocity to Io's orbital velocity in the co-rotating frame is labeled V_p/V_I (from Simpson *et al.* 1974*b*).

where g is a geometrical factor which depends on the satellite and the particle equatorial pitch angle, y is the fraction of particles surviving absorption (to be determined from the data), and $t_c = |f_s \mp f_p|^{-1}$ with f_s = satellite orbital frequency and f_p = particle drift frequency (−/+ refers to electrons/protons). $T_s \propto t_c$ had been suggested earlier by Mogro-Campero *et al.* (1975). Although it has always been assumed that the relevant satellite diameter for particle absorption is the physical diameter d of the satellite, it is illustrative to discuss the dependence of the geometrical factor g on d. This is useful in considering for example the result of changing the effective satellite diameter by internally or externally generated magnetic fields. In the simplest case of trapped particles with equatorial pitch angles $< 67°$, $g \propto d^{-1}$ (Mogro-Campero and Fillius 1976).

The sweeping time given by Eq. (1) is shown in Fig. 5 as a function of particle energy at Io. In comparing the energy dependence of the solutions in Figs. 4 and 5, we notice that at the higher energies ($E \gtrsim 3$ MeV), the smooth energy dependence in Fig. 5 approximately follows the envelope of minima in Fig. 4. In order to compare absolute values we have evaluated Eq. (1) at $L = 6.19$ and for $y = 0.1$, and we find that in this high-energy region Eq. (1) gives values of a factor of ~ 3 higher than the envelope of minima in Fig. 4. At the lower energies Fig. 4 is relatively energy independent and a comparison of absolute values results in a maximum discrepancy at 0.1 MeV, where Eq. (1) lies a factor of ~ 6 lower than the value in Fig. 4.

In Fig. 5, the strong energy dependence of the electron sweeping time at ~ 30 MeV is a consequence of the inefficient particle absorption which occurs with zero relative velocity between the drifting particles and the satellite. The other "resonant" energies for electrons are 14.5 MeV at Amalthea, 21 MeV at Europa, and 14 MeV at Ganymede. The strong energy dependence makes it difficult to estimate sweeping times for particles of energy near the resonant energies. The fact that the observations are consistent with inefficient absorption at these energies (e.g., see the higher-energy electrons in Fig. 1) is an indirect confirmation of the assumption of trapped particle co-rotation. It is interesting to note that if no co-rotation is assumed, the situation is reversed in the sense that protons and not electrons will exhibit the resonance phenomenon. For example, ~ 5 MeV protons at Io, and ~ 40 MeV protons at Amalthea would diffuse past these satellites with ease. Protons of ~ 1 to 2 MeV and those of ~ 18 MeV are observed to be significantly absorbed at Io, but no measurements exist at ~ 5 MeV so that this possibility cannot be excluded. On the other hand, if particles do not co-rotate, the observed inefficient absorption of high-energy electrons discussed above would remain unexplained.

The Radial Diffusion Coefficient

The equation describing the radial diffusion of particles by violation of the third adiabatic invariant is (Schulz and Lanzerotti 1974):

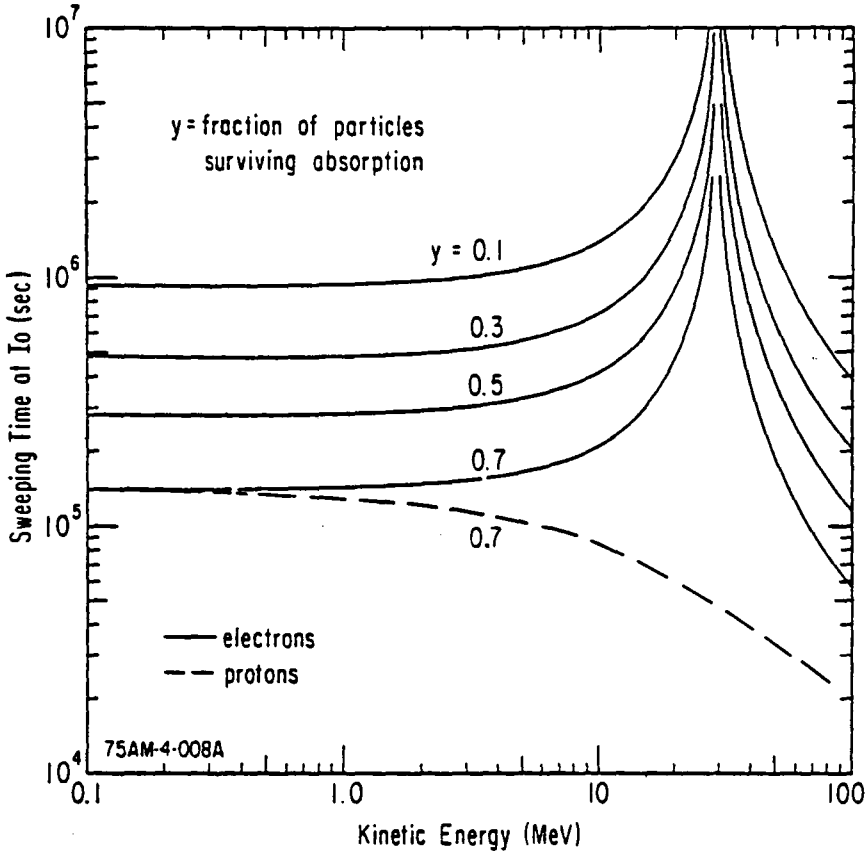

Fig. 5. The sweeping time at Io as given by Eq. (1) in the text, as a function of particle energy. Selected values of the fraction of particles surviving absorption are indicated. The value used for the geometrical factor g in Eq. (1) corresponds to particles which mirror at magnetic latitudes $\gtrsim 11°$.

$$\frac{\partial f}{\partial t} = L^2 \frac{\partial}{\partial L}\left(\frac{D}{L^2}\frac{\partial f}{\partial L}\right) \tag{2}$$

where f is the phase space density of particles such that $f\ d^3x\ d^3p$ is the number of particles in the spatial volume element d^3x and in the momentum volume element d^3p; it must be evaluated at constant first and second invariants. The relationship between the differential particle flux j (cm^{-2} sec^{-1} $ster^{-1}$ MeV^{-1}) measured perpendicular to the magnetic field vector and $f = j/p^2$. Since L is the dimensionless shell parameter, the dimension of the diffusion coefficient D is inverse time.

Particle absorption in the satellite sweeping region ΔL can be treated by adding a loss or sink term $S = -\rho / T_\ell$ to the right-hand side of Eq. (2). The time T_ℓ is the exponential decay time of particles in the absence of diffusive flow as can be readily seen from Eq. (2) with sink term but no diffusion term. From Eq. (1) we see that the particle population may in fact be considered to decay exponentially with time, so that $T_\ell = g\, t_c$.

Since the objective is to obtain values for the diffusion coefficient, Eq. (2) with sink term must be solved for D. For $D \propto L^n$ and steady state conditions ($\partial\rho/\partial t = 0$), Mogro-Campero and Fillius (1976) obtain

$$D = \frac{\rho / T_\ell}{\left[\frac{(a-2)}{L}\frac{\partial \rho}{\partial L} + \frac{\partial^2 \rho}{\partial L^2}\right]} \tag{3}$$

valid in the sweeping region ΔL. The parameter a can be obtained by solving Eq. (2) in the steady state in an L-region with no satellite absorption, resulting in

$$a = 2 - L\,\frac{\partial^2 \rho / \partial L^2}{\partial \rho / \partial L}. \tag{4}$$

In order to evaluate these expressions we require a substantial set of differential energy measurements covering a wide range of spatial locations and energies. Similar approaches have been profitable in the case of Earth's radiation belt (Schulz and Lanzerotti 1974), but other methods may be more appropriate for the analysis of the first stage of Jovian radiation belt exploration. An estimate of the diffusion coefficient can be obtained by solving the diffusion Eq. (2) with sink term for the phase space density ρ, and comparing this with ρ determined by the observations. The value of D for the best fit can then be chosen. Mogro-Campero and Fillius (1976) have used this method for a particular case where they could determine ρ. The following expressions derived from the diffusion equation by different approximations have been used in considering Jovian radiation belt data [Mogro-Campero and Fillius (1976); and similar expressions in a paper by Simpson *et al.* (1974*b*)]:

$$D \simeq \frac{(\Delta L)^2}{4T_s} \tag{5}$$

$$D \simeq -\frac{\Delta L}{T_s \dfrac{\partial}{\partial L}(\ell n\, \rho)} \tag{6}$$

where T_s is the sweeping time and ΔL the sweeping region, both defined above. Another approximate expression can be obtained by solving Eq. (27) of Mead and Hess (1973) for D. In the notation of this paper one obtains

$$D \simeq \frac{(\Delta L)^2}{T_s \left(\cosh^{-1} \frac{1}{y}\right)^2}. \tag{7}$$

If T_s from Eq. (1) is used in (5), Eqs. (5) and (7) give results which differ at most by a factor of 2 in the range $0.001 < y < 0.9$ (by definition y must be in the range $0 \leq y \leq 1$).

IV. VALUES OF THE RADIAL DIFFUSION COEFFICIENT

Values of the diffusion coefficient based on the approximate formulas (5) and (6) have been evaluated at the orbits of satellites: for ~ 1 MeV protons at Io (Simpson *et al.* 1974*b*), for ~ 0.8 MeV and ~ 12 MeV electrons at Io and Europa (Mogro-Campero and Fillius 1976), and for ~ 100 MeV protons and ~ 90 MeV electrons at Amalthea (Fillius *et al.* 1975*a*). Mogro-Campero and Fillius (1976) find evidence for an energy and spatial dependence of the diffusion coefficient.

Any given experiment is limited in its coverage of energy and species. It is also difficult to compare diffusion coefficients deduced by different experimenters since their methods are not identical. Furthermore, estimates of diffusion coefficients have not yet been made by all Pioneer experimenter teams. It therefore seemed of interest to compute diffusion coefficients using all of the Pioneer 10 and 11 data reported so far, by one method. This has been done by using Eq. (5), with T_s given by Eq. (1). It must be cautioned that Eq. (5) is a crude approximation, but since most of the Pioneer data has not been reduced to produce particle phase space densities, better approximations such as that of Eq. (6), and especially of Eqs. (3) and (4) are not yet possible for the whole set of data.

The diffusion coefficients as a function of particle kinetic energy are shown in Figs. 6 and 7. An overall positive slope is apparent. A more reasonable parameter is probably the particle-drift frequency, since radial diffusion is caused by violation of the third adiabatic invariant in a time comparable to the particle-drift period in an inertial frame. Therefore, particles with the same drift frequency at a given L should have the same diffusion coefficient. The relationship between particle species, energy, L value, and drift frequency is illustrated in Fig. 8. The diffusion coefficients as a function of particle-drift frequency are shown in Figs. 9 and 10. The frequency dependence shows a minimum near the co-rotation frequency and is an indirect measure of the power spectrum of the electric and magnetic field irregularities which are responsible for violating the particles' third adiabatic invariant (e.g., see Schulz and Lanzerotti 1974). Since the diffusion coefficient depends on drift frequency, the L dependence is displayed in three frequency regimes in Fig. 11.

From the results in Fig. 11 we see that it is not possible to identify a simple spatial dependence for the diffusion coefficient. There is uncertainty

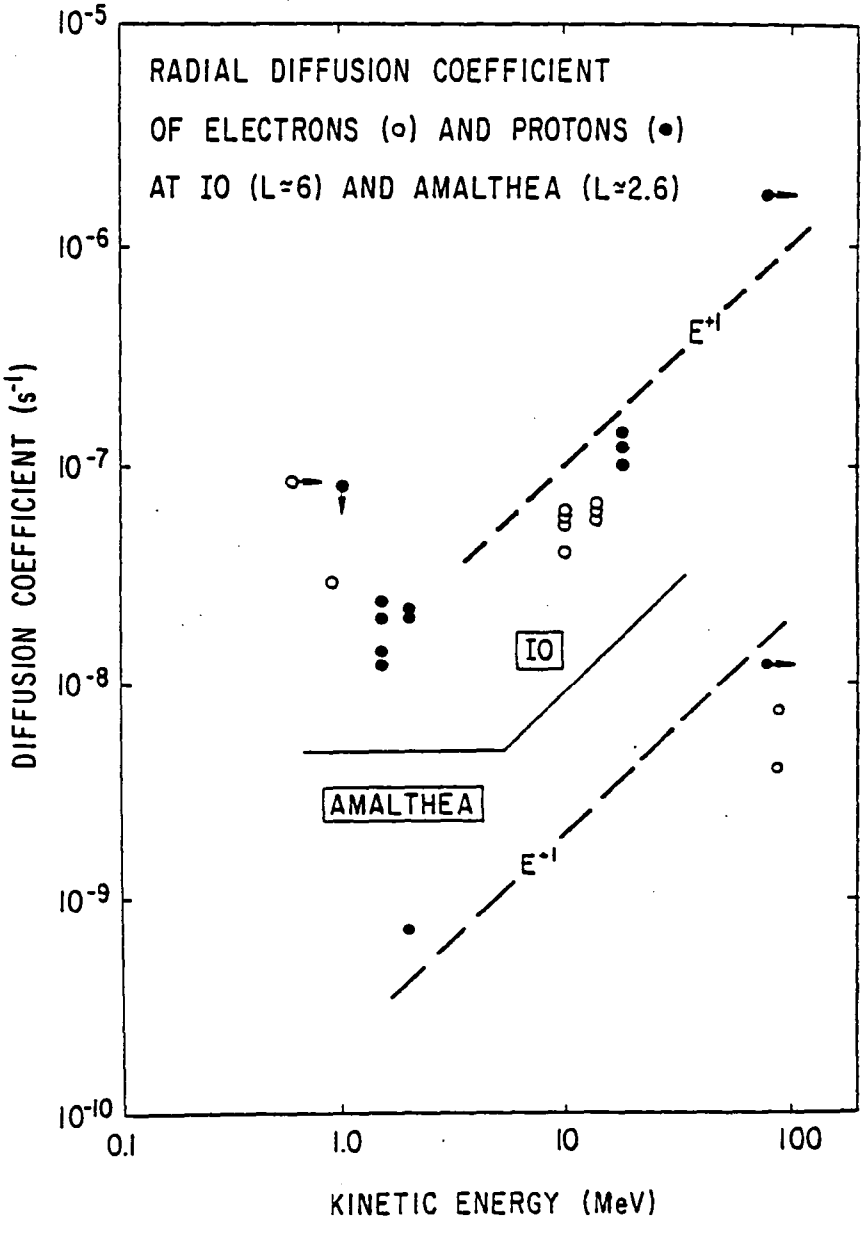

Fig. 6. Diffusion coefficients as a function of particle kinetic energy for protons and electrons at Io and Amalthea. The dashed line is meant to serve as a reference slope.

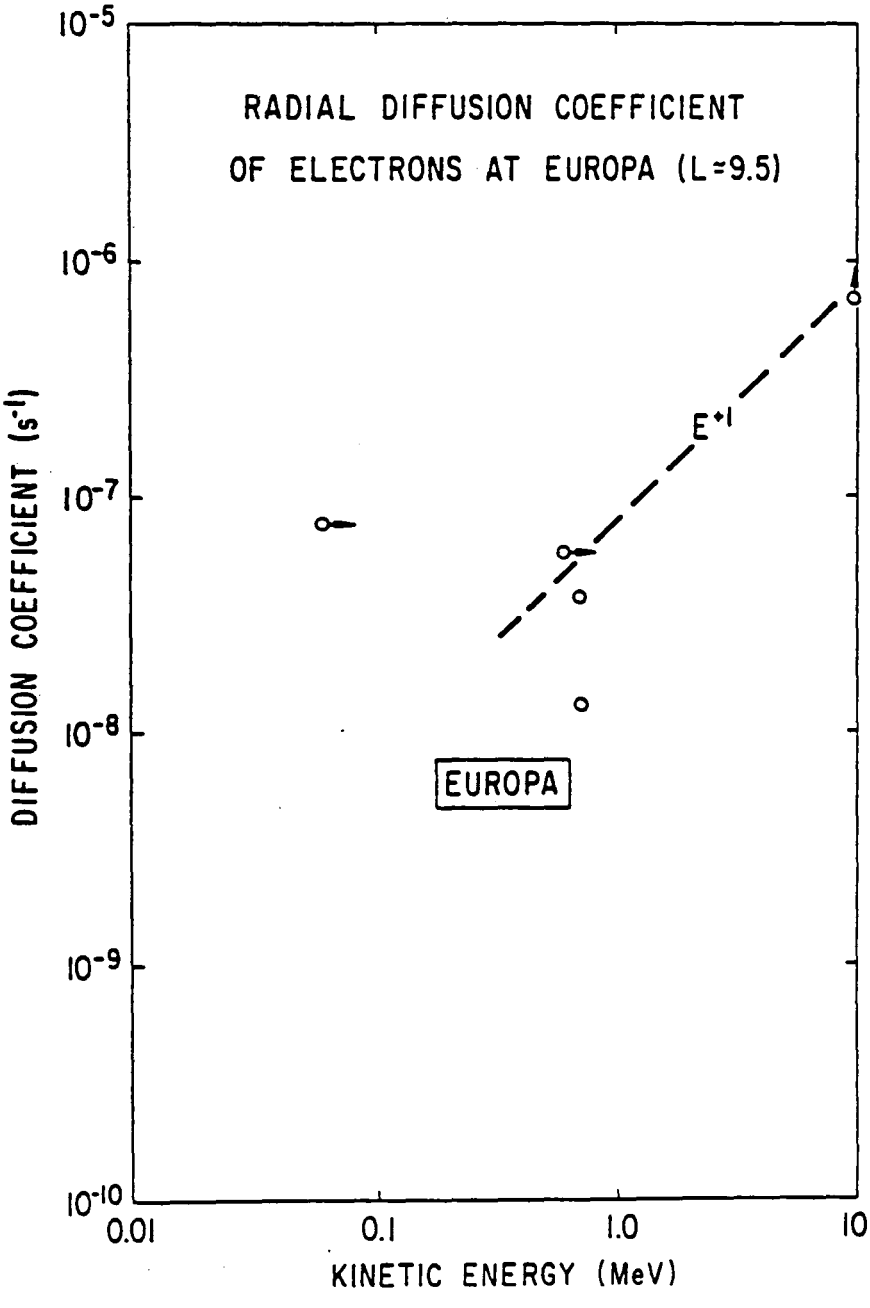

Fig. 7. Same as Fig. 6 but for Europa.

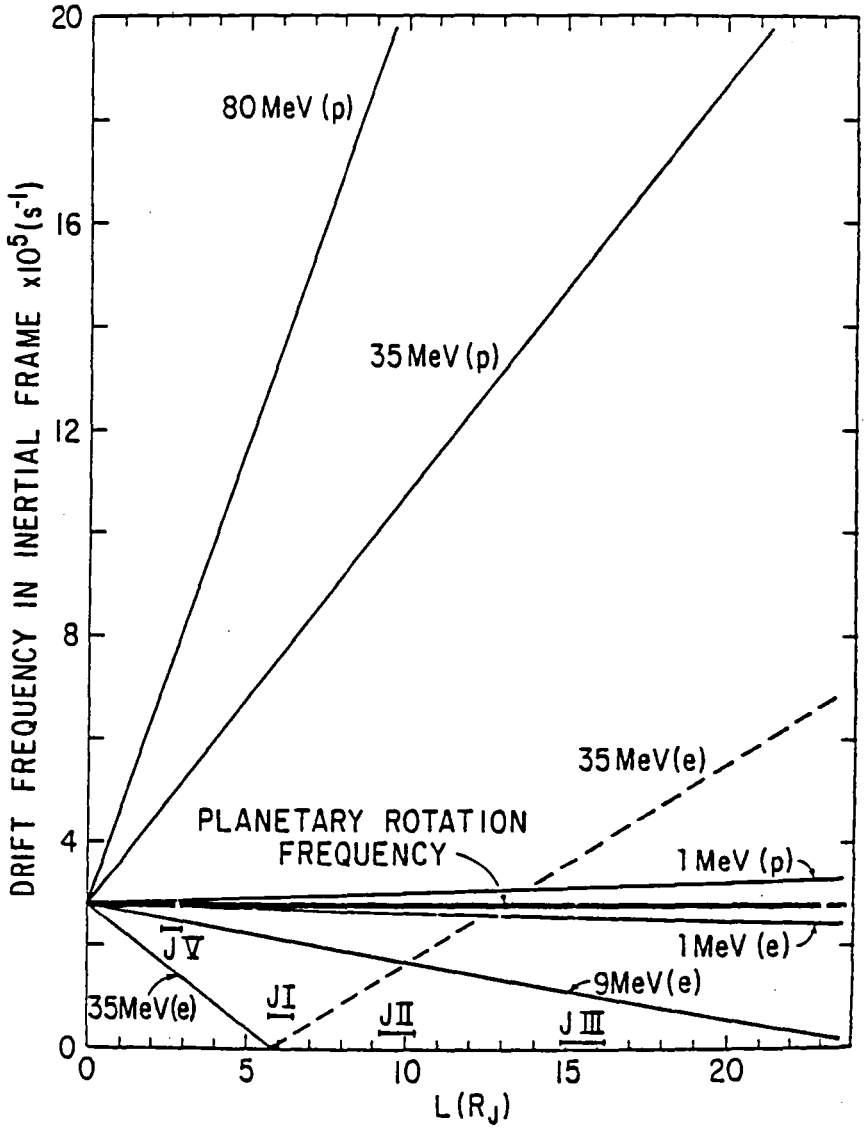

Fig. 8. Drift frequencies of protons and electrons of selected energies as a function of L in an inertial frame. The ranges of L values traversed by the satellites are indicated at their appropriate orbital frequencies (J V is Amalthea, J I is Io, J II is Europa, and J III is Ganymede). The dashed line corresponds to negative frequencies i.e., opposite to the direction of planetary rotation (from Mogro-Campero *et al.* 1975).

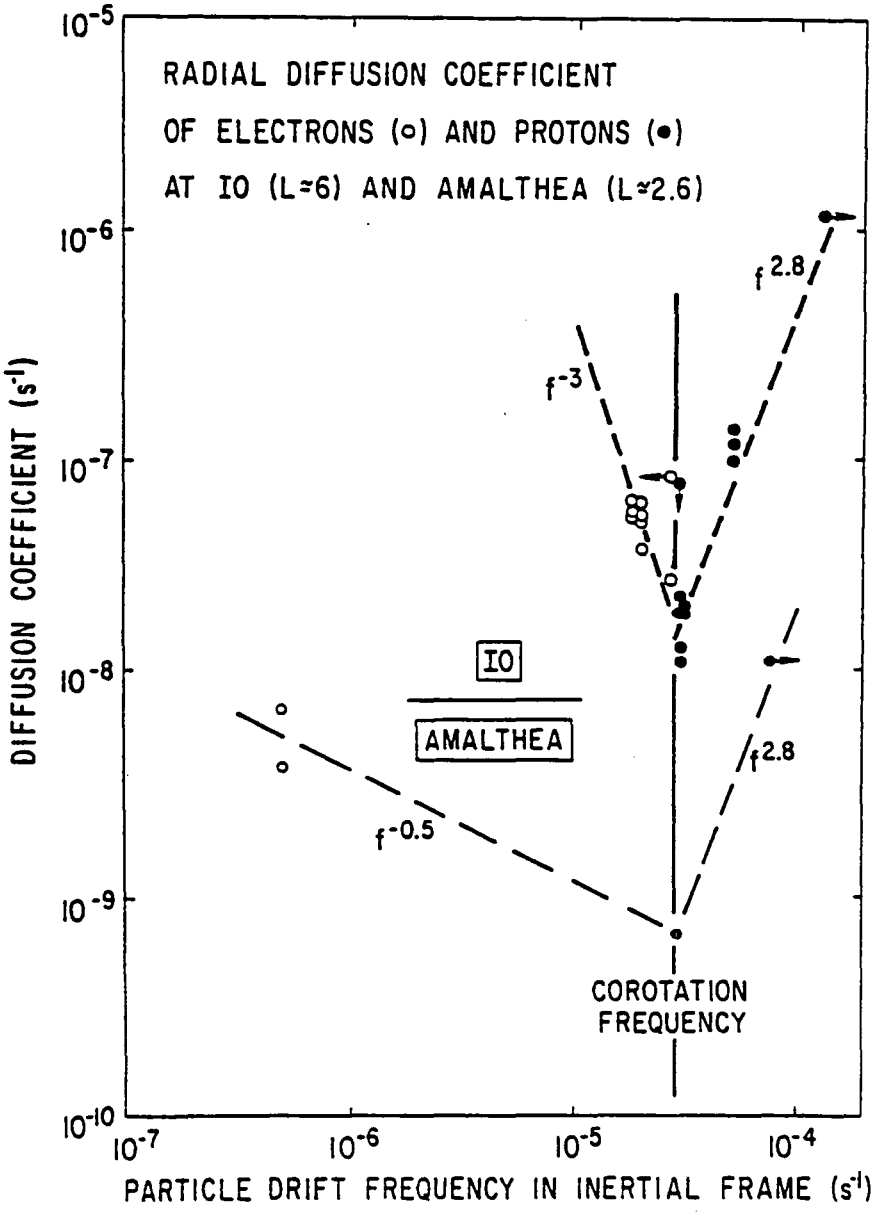

Fig. 9. Diffusion coefficients as a function of particle drift frequency in an inertial frame for protons and electrons at Io and Amalthea. A minimum seems to occur at the planetary rotation frequency (co-rotation frequency).

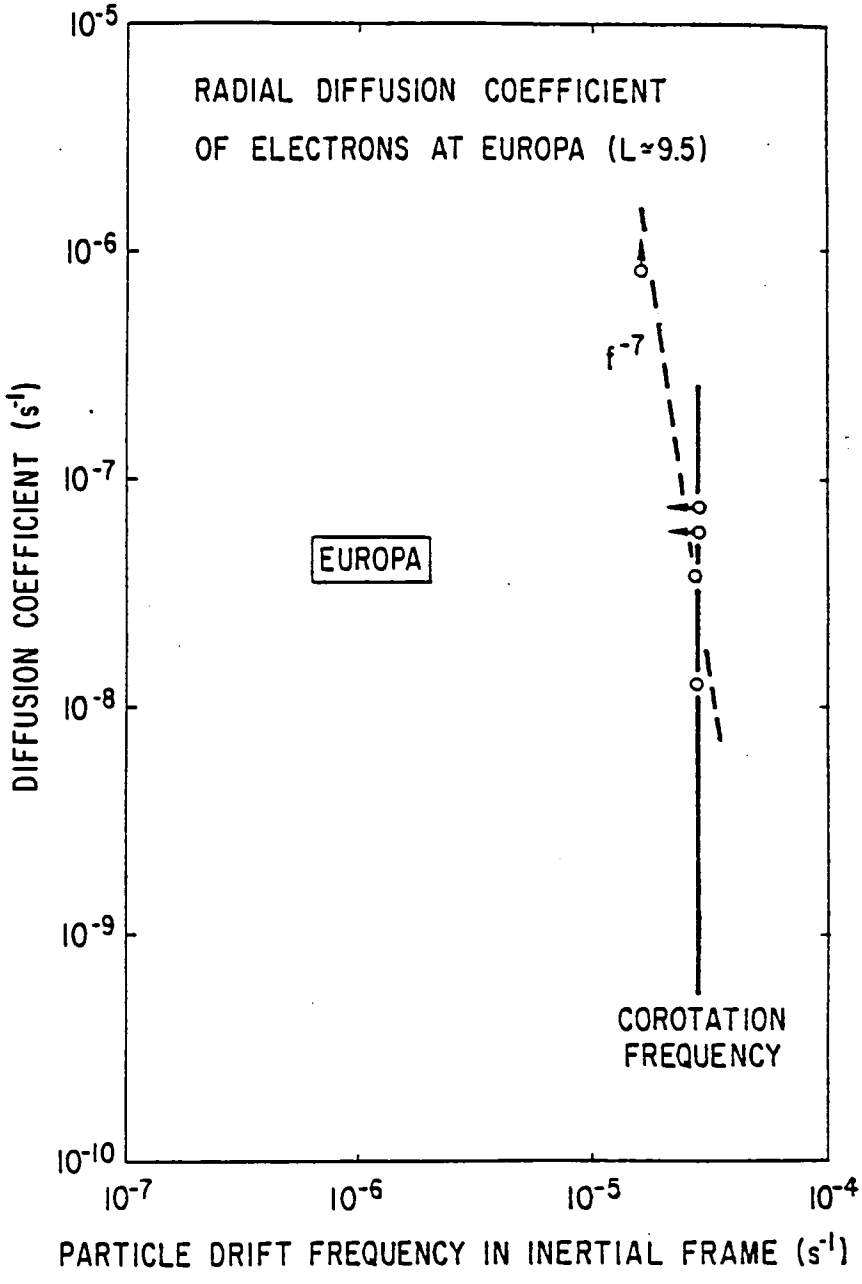

Fig. 10. Same as Fig. 9 but for Europa.

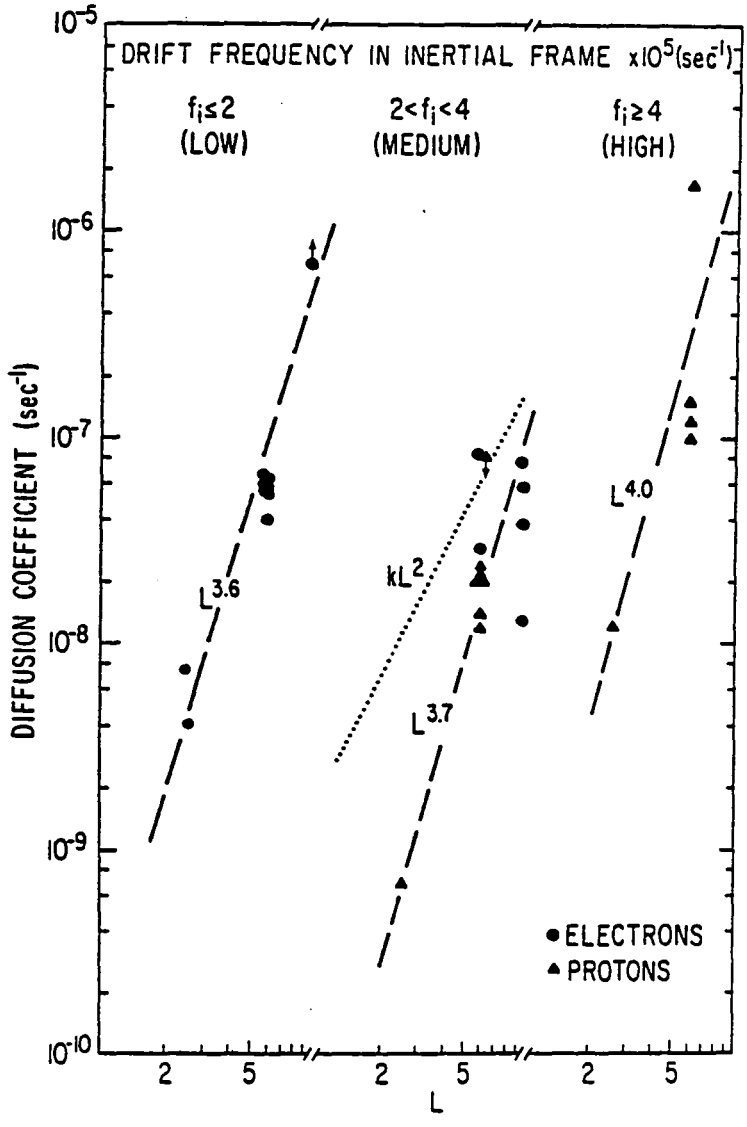

Fig. 11. The diffusion coefficient as a function of L based on Pioneer 10 and 11 trapped particle data in the vicinity of the orbits of Amalthea ($L \simeq 2.6$), Io ($L \simeq 6$) and Europa ($L \simeq 9.5$). The approximations used are described in the text. The diffusion coefficients have been classified into low-, medium-, and high-frequency regimes, with arbitrary boundaries. The planetary rotation frequency (the low-energy limit of the particle-drift frequency in the inertial frame) lies approximately in the middle of the medium-frequency regime. The dashed lines are rough visual fits drawn to illustrate the steepness of spatial dependences. The dotted line with $k \simeq 2 \times 10^{-4}$ sec^{-1} was deduced from radio observations by Birmingham *et al.* (1974) before the Pioneer particle data became available.

particularly at medium frequencies in going from Io to Europa. An overall simplifying statement would be to deduce from these results that if a power law must be chosen, the exponent $a \simeq 4$ is a reasonable value. The urge to fit the spatial dependence into a power law comes from our experience at Earth and from theoretical considerations (see Sec. I), where $D \propto L^a$ is a reasonable approximation with $a = 10$, 6 or ~ 3 depending on whether the mechanism responsible for the violation of the third adiabatic invariant is due to, respectively,

(a) deformation of the magnetic field by the solar wind,
(b) randomly fluctuating electric fields, or
(c) field-line exchange driven by ionospheric winds.

We also have $D = kL^2$, with $k = 2 \times 10^{-9}$ sec^{-1} given by Birmingham *et al.* (1974) from their fits to radio observations at $L \lesssim 4$ (this result has been included in Fig. 6 as a dotted line). The value $a \simeq 4$ is higher than the favorite pre-Pioneer values of $a \simeq 2$ or 3.

V. SUMMARY AND COMMENTS

In Sec. I we have reviewed the work done on the absorption of trapped particles by the Jovian satellites in the pre-Pioneer 10 era. The emphasis at that stage was on determining the relative importance of such absorption, and it was generally felt to be a relevant process in the inner magnetosphere. Much of the conceptual framework needed to study the absorption process and its consequences for the trapped particle distributions was developed at this time. The power law exponent $a \simeq 2$ to 3 in $D \propto L^a$ was favored.

In Sec. II we have reviewed the work performed after Jupiter encounter data became available from Pioneer 10. Absorption effects at the inner satellites were observed by charged particle detectors on Pioneers 10 and 11. Particle angular distributions are consistent with expected absorption effects, and the absorption effects seem to have little or no longitude dependence. An energy and species dependence is clearly observable in the data, and progress has been made in accounting for this effect.

In Sec. III, the methods used in the analysis of particle data have been reviewed. A major uncertainty in considerations of the absorption process is the electric and magnetic field configuration in the vicinity of the satellites. These fields may change the absorption cross section which is presently taken to be the geometrical one. Methods are available for computing the time required for a satellite to absorb a given fraction of the trapped particles within its sweeping region. It is possible to calculate the diffusion coefficient of particle radial motion by using parameters obtained in considering the absorption process and by neglecting other terms (such as pitch-angle diffusion) in the diffusion equation. The data currently available probably are too unsophisticated to use the more powerful theoretical methods so that

approximate expressions for the diffusion coefficient have been derived and used.

In Sec. IV we have referenced current values of the diffusion coefficient and presented a first attempt at a unified approach based on the complete set of available particle data. For self-consistency in the absorption analysis, diffusion coefficients derived from the data should be inserted into the diffusion equation which can then be used to predict the particle intensity profiles. The spatial dependence of the diffusion coefficient derived from particle observations appears steeper ($a \simeq 4$ in $D \propto L^a$) than the pre-Pioneer expectations. It should be noted, however, that the early studies were concerned mostly with the region around $L = 2$, where the synchrotron radio source is important.

Substantial improvement in absorption analysis is probably not to be expected from more refined magnetic field models, except possibly near Amalthea (Fillius *et al.* 1975*a*). For example, the maximum sweeping regions ΔL for the D2 model of Smith *et al.* (1974) are 0.28, 0.40, and 0.55 for Amalthea, Io and Europa. The corresponding values for the O_3 magnetic field model of Acuña and Ness (1975)[3] are 0.44, 0.57, and 0.63.

Acknowledgements. I thank R. W. Fillius and C. E. McIlwain for helpful comments and discussions. This work was supported in part by NASA Contract NAS 2-6552 and by NASA Grant NGL 05-005-007.

DISCUSSION

T. R. McDonough: The L^3 dependence of the diffusion coefficient which we got in the Brice theory was dependent on the model of the fluctuating winds in the upper atmosphere which we assumed. The real behavior of these winds may give a different L-dependence.

A. Mogro-Campero: I agree. I would like to mention, in that connection, that the L^2 or L^3 dependence in the pre-Pioneer literature was derived to fit the radio data, which is mainly around $L = 2$. The Pioneer data, however, cover larger values of L, and the dependence of the diffusion coefficient on L might become less steep as one approaches the planet.

C. K. Goertz: I would like to point out that the actual problem of deriving a diffusion coefficient from the observed absorption of particles by the satellites is much more complicated.

1. The satellites absorb the particles every 15 or 20 hours and thus the problem becomes strongly time dependent.
2. The solution of the diffusion equation depends on the initial and boundary conditions which are time dependent. Every time the satellite passes a particular L shell it interacts with the holes created previously.

---

[3]See, however, p. 38.

3. The holes created by the satellites drift in azimuth. I do not believe that azimuthal symmetry is a valid assumption.

A. Mogro-Campero: I think it is clear to all who have worked on this problem that its treatment can be made more complicated. What is not clear is whether the additional complications provide a better description of the physical phenomena. Furthermore, in obtaining numerical values for diffusion coefficients one must take into account the nature of the observations available and our current knowledge of Jovian magnetospheric parameters.

The effect of the holes created by the satellites and their drift in time has been discussed by Simpson *et al.* (1974*b*). Justifications for the assumptions made by different authors are given in their papers. The relative merit of the approach you have outlined will be judged when it is presented in the literature.

D. Harris: Could these data be used to compute the net charge on Io?

A. Mogro-Campero: The net charge on Io, due to its absorption of electrons and protons of the energies which have been measured, can be estimated. The contribution to the net charge from the probably more numerous lower-energy particles, whose fluxes have not been measured, is unknown, so that the computed net charge would be of little value.

REFERENCES

Acuña, M. H., and Ness, N. F. 1975. Jupiter's main magnetic field measured by Pioneer 11. *Nature* 253:327–328, and personal communication.

Baker, D. N., and Van Allen, J. A. 1975. Energetic electrons in the Jovian magnetosphere. *J. Geophys. Res.* In press.

Birmingham, T.; Hess, W.; Northrop, T.; Baxter, R.; and Lojko, M. 1974. The electron diffusion coefficient in Jupiter's magnetosphere. *J. Geophys. Res.* 79:87–97.

Brice, N. 1972. Energetic protons in Jupiter's radiation belts. *Proceedings of the Jupiter radiation belt workshop.* (A. J. Beck, ed.) Tech. Mem. 33–543, pp. 283–302. Pasadena, California: Jet Propulsion Laboratory.

Brice, N., and McDonough, T. R. 1973. Jupiter's radiation belts. *Icarus* 18:206–219.

Coroniti, F. V. 1974. Energetic electrons in Jupiter's magnetosphere. *Ap. J. Suppl.* 27:261–281.

Davis, Jr., L. 1972. Comments on models of the Jovian radiation belts. *Proceedings of the Jupiter radiation belt workshop.* (A. J. Beck, ed.) Tech. Mem. 33–543, pp. 517–525. Pasadena, California: Jet Propulsion Laboratory.

Divine, N. 1972. Post-workshop models of Jupiter's radiation belts. *Proceedings of the Jupiter radiation belt workshop.* (A. J. Beck, ed.) Tech. Mem. 33–543, pp. 527–542. Pasadena, California: Jet Propulsion Laboratory.

Fillius, R. W., and McIlwain, C. E. 1974*a*. Radiation belts of Jupiter. *Science* 183:314–315.

———. 1974*b*. Measurements of the Jovian radiation belts. *J. Geophys. Res.* 79:3589–3599.

Fillius, R. W.; McIlwain, C. E.; and Mogro-Campero, A. 1975*a*. Radiation belts of Jupiter: a second look. *Science* 188:465–467.

Fillius, W.; McIlwain, C. E.; Mogro-Campero, A.; and Steinberg, G. 1975*b*. Pitch angle scattering as an important loss mechanism for energetic electrons in the inner radiation belt of Jupiter. Submitted to *Geophys. Res. Lett.*

Hess, W. N. 1968. *The radiation belt and magnetosphere.* Waltham, Mass.: Blaisdell Pub. Co.

Hess, W. N.; Birmingham, T. J.; and Mead, G. D. 1973. Jupiter's radiation belts: can Pioneer 10 survive? *Science*, 182:1021–1022.

———. 1974. Absorption of trapped particles by Jupiter's moons. *J. Geophys. Res.* 79:2877–2880.

Huba, J. D., and Wu, C. S. 1975. A local diffusion process associated with the sweeping of energetic particles by Io. *University of Maryland preprint.* College Park, Maryland.

Jacques, S. A., and Davis, Jr., L. 1972. Diffusion models for Jupiter's radiation belt. *California Inst. Technology Report.* Pasadena, California.

McIlwain, C. E., and Fillius, R. W. 1975. Differential spectra and phase space densities of trapped electrons at Jupiter. *J. Geophys. Res.* 80:1341–1345.

Mead, G. D. 1972. The effect of Jupiter's satellites on the diffusion of protons. *Proceedings of the Jupiter radiation belt workshop.* (A. J. Beck, ed.) Tech. Mem. 33–543, pp. 271–276. Pasadena, California: Jet Propulsion Laboratory.

———. 1974. Magnetic coordinates for the Pioneer 10 Jupiter encounter. *J. Geophys. Res.* 79: 3514–3521.

Mead, G. D.; and Hess, W. N. 1973. Jupiter's radiation belts and the sweeping effect of its satellites. *J. Geophys. Res.* 78:2793–2811.

Mogro-Campero, A., and Fillius, R. W. 1976. The absorption of trapped particles by the inner satellites of Jupiter and the radial diffusion coefficient of particle transport. *J. Geophys. Res.* In press.

Mogro-Campero, A.; Fillius, R. W.; and McIlwain, C. E. 1975. Electrons and protons in Jupiter's radiation belts. *Space Research.* Vol. XV. Berlin: Akademie Verlag. In press.

Roederer, J. G. 1970. *Dynamics of geomagnetically trapped radiation.* Berlin: Springer-Verlag.

Schulz, M., and Lanzerotti, L. J. 1974. *Particle diffusion in the radiation belts.* Berlin: Springer-Verlag.

Sentman, D. D., and Van Allen, J. A. 1975. Angular distributions of electrons of energy $E_e >$ 0.06 MeV in the Jovian magnetosphere. *J. Geophys. Res.* In press.

Simpson, J. A.; Hamilton, D.; Lentz, G.; McKibben, R. B.; Mogro-Campero, A.; Perkins, M.; Pyle, K. R.; Tuzzolino, A. J.; and O'Gallagher, J. J. 1974*a*. Protons and electrons in Jupiter's magnetic field: results from the University of Chicago experiment on Pioneer 10. *Science* 183:306–309.

Simpson, J. A.; Hamilton, D. C.; Lentz, G. A.; McKibben, R. B.; Perkins, M.; Pyle, K. R.; Tuzzolino, A. J.; and O'Gallagher, J. J. 1975. Jupiter revisited: first results from the University of Chicago charged particle experiment on Pioneer 11. *Science* 188:455–459.

Simpson, J. A.; Hamilton, D. C.; McKibben, R. B.; Mogro-Campero, A.; Pyle, K. R.; and Tuzzolino, A. J. 1974*b*. The protons and electrons trapped in the Jovian dipole magnetic field region and their interaction with Io. *J. Geophys. Res.* 79:3522–3544.

Singer, S. F. 1962. Radiation belts of Venus and of Mars (with consideration of sweeping effect of Phobos). *Space Age Astronomy.* (A. J. Deutsch and W. B. Klemperer, eds.) pp. 444–461. New York: Academic Press.

Smith, E. J.; Davis, Jr., L.; Jones, D. E.; Coleman, Jr., P. J.; Colburn, D. S.; Dyal, P.; Sonett, C. P.; and Frandsen, A. M. A. 1974. The planetary magnetic field and magnetosphere of Jupiter: Pioneer 10. *J. Geophys. Res.* 79:3501–3513.

Trainor, J. H.; McDonald, F. B.; Stilwell, D. E.; Teegarden, B. J.; and Webber, W. R. 1975. Jovian protons and electrons: Pioneer 11. *Science* 188:462–465.

Trainor, J. H.; McDonald, F. B.; Teegarden, B. J.; Webber, W. R.; and Roelof, E. C. 1974*a*. Energetic particles in the Jovian magnetosphere. *J. Geophys. Res.* 79:3600–3614.

Trainor, J. H.; Teegarden, B. J.; Stilwell, D. E.; McDonald, F. B.; Roelof, E. C.; and Webber, W. R. 1974*b*. Energetic particle population in the Jovian magnetosphere: a preliminary note. *Science* 183:311–313.

Van Allen, J. A.; Baker, D. N.; Randall, B. A.; and Sentman, D. D. 1974*a*. The magnetosphere of Jupiter as observed with Pioneer 10. 1. Instrument and principal findings. *J. Geophys. Res.* 79:3559–3578.

Van Allen, J. A.; Baker, D. N.; Randall, B. A.; Thomsen, M. F.; Sentman, D. D.; and Flindt, H. R. 1974*b*. Energetic electrons in the magnetosphere of Jupiter. *Science* 183:309–311.

Van Allen, J. A.; Randall, B. A.; Baker, D. N.; Goertz, C. K.; Sentman, D. D.; Thomsen, M. F.; and Flindt, H. R. 1975. Pioneer 11 observations of energetic particles in the Jovian magnetosphere. *Science* 188:459–462.

Vesecky, J. F. 1975. Features of Jupiter's trapped particle environment associated with Jovian satellites—Pioneer 10 results and X-ray observations. *Geophys. J. Roy. Astron. Soc.* 41: 331–346.

VOL. 81, NO. 7 JOURNAL OF GEOPHYSICAL RESEARCH MARCH 1, 1976

The Absorption of Trapped Particles by the Inner Satellites of Jupiter and the Radial Diffusion Coefficient of Particle Transport

ANTONIO MOGRO-CAMPERO[1] AND WALKER FILLIUS

Physics Department, University of California at San Diego, La Jolla, California 92093

The process of trapped particle absorption by the inner Jovian satellites is considered in detail by taking into account both the particle and the satellite motions in a magnetic dipole field which is displaced from the center of the planet and tilted with respect to the planetary rotation axis in the manner found by magnetic field measurements on Pioneer 10. It is assumed that particle motion is controlled exclusively by the planetary field and that a particle is removed from the trapped particle population when its trajectory intersects the physical boundary of a satellite. We derive an expression for computing the sweeping time at a given satellite, defined as the time required for the satellite to sweep up a given fraction of the trapped particles within its sweeping region. By making use of the sweeping time and the radial diffusion equation of particle transport we derive approximate expressions for the diffusion coefficient. Measurements performed in the Jovian magnetosphere by the University of California at San Diego experiment on Pioneer 10 are then used to obtain estimates of the diffusion coefficient at the orbits of Io ($L \simeq 6$) and Europa ($L \simeq 9.5$). We find that the diffusion coefficient is a function of energy and L for electrons in the energy range ~0.7–14 MeV.

The absorption of trapped particles by the Jovian satellites was treated by *Mead and Hess* [1973] and by *Hess et al.* [1974]. These authors considered the effect of satellite absorption on the trapped particle distribution function by assuming certain boundary conditions for particle injection into the radiation belts and by using diffusion coefficients derived independently.

Since December 1973, when Pioneer 10 flew by Jupiter, direct measurements of the Jovian trapped radiation and magnetic field have become available for the first time (for the latest reports, see special Pioneer 10 issue of the *Journal of Geophysical Research, 79*, 3487–3694, 1974). These measurements have permitted a more detailed consideration of the absorption process and have led to an extension of its treatment to include higher energies [*Simpson et al.*, 1974; *Mogro-Campero et al.*, 1975].

Since the particle fluxes have now been measured, the observed absorption of particles by the Jovian satellites can be used to obtain values for the radial diffusion coefficient. In this paper we discuss the process of trapped particle absorption by satellites in a dipole magnetic field, and we derive expressions for the satellite sweeping time. We show how values for the radial diffusion coefficient can be obtained from data on particle fluxes and the satellite sweeping time. Finally, data obtained with the University of California at San Diego experiment on Pioneer 10 are used to arrive at values for the diffusion coefficient in the inner Jovian magnetosphere.

1. Absorption of Trapped Particles by the Inner Satellites of Jupiter

Preliminary Considerations

Satellite absorption cross section. The fundamental assumption is that if a trapped particle trajectory intersects a satellite, the particle is removed from the planetary trapped particle population. The absorption process need not be specified but might be magnetic field confinement to the vicinity of the satellite, neutralization by charge exchange in the satellite atmosphere, energy loss by ionization, pitch angle scattering into the planetary loss cone, nuclear interactions, etc. The magnetic field configuration in the vicinity of the Jovian satellites is unknown but is of critical importance for the particle absorption process. Depending on the conductivity of the satellite this field configuration could be such as to reduce the number of particles absorbed by deflecting particles away from the satellite; on the other hand, the magnetic field geometry could be such as to guide particles toward an impact with the satellite. The effective cross section for trapped particle absorption may therefore be smaller or larger than the actual satellite dimensions and can be expected to be a function of gyroradius and pitch angle. In addition, the effective cross section may be a function of particle species, since the absorption processes are. There is evidence from the Pioneer 10 data that Io is a local source of electrons at low energies [*McIlwain and Fillius*, 1975]. As is discussed by *Shawhan et al.* [1973], their model for the acceleration of electrons at Io requires that Io have a sufficiently good conductivity to act as a unipolar generator. However, since trapped particle absorption is observed at the orbits of the inner satellites, we believe that some magnetic field lines intersect these bodies. In the absence of more concrete information we assume here that particle motion is controlled exclusively by the Jovian magnetic field and that the effective absorption cross section is determined by the satellite radius. This assumption corresponds to the satellite being a perfect insulator. Even in this simple case we will see that the absorption is dependent on gyroradius and pitch angle.

Planetary magnetic field. For the evaluation of characteristic particle parameters which depend on the magnetic field we assume that the field is given by $B = 4G/L^3$, where L is determined from the most recent best estimate of the magnetic field, i.e., the D2 noncentered dipole model of *Smith et al.* [1974], which appears to be a reasonable approximation for $L \lesssim 15$. The satellites included in this range of L are Amalthea, Io, and Europa (their physical and orbital characteristics can be found in the paper by *Mead and Hess* [1973]).

Frame of reference. We assume that the trapped radiation corotates with the planet [*Brice and Ioannidis*, 1970], so that it is convenient in this paper to consider motion in a corotating frame of reference. In this frame the four inner Jovian satellites rotate clockwise as viewed from the north, and the trapped

[1] Now at Energy Science and Engineering, General Electric Company, Schenectady, New York 12301.

electrons and protons drift around the planet clockwise and counterclockwise, respectively.

Longitudinal skipping. Particles may escape absorption by leapfrogging the satellite in their longitudinal (drift) motion during half a bounce period. If the satellite radius and particle gyroradius are R_s and R_g, respectively, the effective cross-sectional radius of absorption is $R_g + R_s$. For simplicity, we restrict our attention to cases for which $R_g \ll R_s$, so that the cross-sectional radius is $R_g + R_s \simeq R_s$ (e.g., at Io, $R_g < 0.1R_s$ for $E < 100$-MeV electrons).

If we measure the satellite diameter in longitude units and represent it as D and if $\Delta l(s, e)$ and $\Delta l(e)$ are the absolute values of the changes in longitude of the satellite and electron during half a particle bounce period, respectively, we conclude that electrons may escape absorption only if $|\Delta l(s, e) - \Delta l(e)| > D$. For protons we obtain a plus sign in the previous inequality. In Figure 1 we show these changes in longitude as a function of energy for protons and electrons in the energy range 0.1–100 MeV for Europa. From this figure we conclude that longitudinal skipping is not possible for electrons of the energy shown at Europa but that it is possible for protons (it is important to replace $D = 2R_s$ by $2(R_g + R_s)$ for the higher-energy protons, since $R_g \gtrsim 0.7R_s$ for $E > 10$ MeV). By a similar analysis for the four innermost Jovian satellites we conclude that longitudinal skipping of electrons is not possible for any of these satellites over the energy interval $0.1 \lesssim E \lesssim 100$ MeV.

Henceforth, we restrict our attention to particle energies for which the effective absorption cross-sectional radius is equal to the satellite radius and for which longitudinal skipping is not possible.

Absorption Process and Satellite Sweeping Time

Satellite sweeping corridor and particle-satellite sweeping region. In Figure 2 we show the trajectory of Io displayed in the coordinates convenient for an analysis of trapped particle motion (L and magnetic latitude versus Jovian system 3 longitude). The width shown in the L coordinate corresponds to Io's diameter, so that for particles with gyroradii much smaller than Io's radius the band shown in the figure defines the sweeping corridor of the satellite. The sweeping corridor is retraced by Io with a frequency f_s given by the inverse of its orbital period in the corotating frame.

Since the orbits of the inner satellites are in the Jovian equatorial plane and since the tilt of the magnetic dipole axis with respect to the rotation axis is 11°, the maximum magnetic latitude excursion of a satellite is 11°. Particles which mirror at magnetic latitudes of <11° (i.e., those with equatorial pitch angles $\alpha_e > 67°$) will not intersect the sweeping corridor at some longitudes. Therefore particles with $\alpha_e < 67°$ have the highest probability of being absorbed, and the absorption probability decreases with increasing α_e for $\alpha_e > 67°$. It is convenient to define a particle-satellite sweeping region ΔL, which is the effective extent in L of the sweeping corridor. If the sweeping corridor extends from L_1 to L_2, the sweeping region ΔL, which is a function of particle mirror latitude, is $\Delta L \le L_2 - L_1 = 0.4$ for Io.

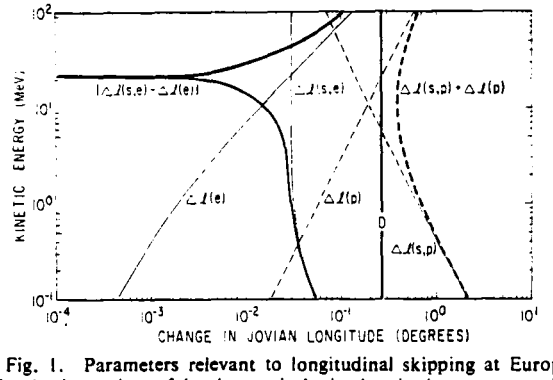

Fig. 1. Parameters relevant to longitudinal skipping at Europa. The absolute values of the changes in Jovian longitude are measured in the frame of reference which corotates with the planet. Here, $\Delta l(s, e)$ is the change in longitude of the satellite during half an electron bounce period, and $\Delta l(e)$ is the change in longitude of the electron during half its bounce period (e is replaced by p in the case of protons). D is the longitude range occupied by the satellite diameter.

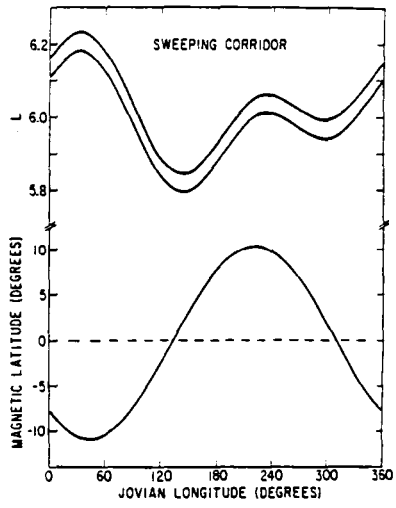

Fig. 2. Io's trajectory in the magnetic field coordinates L and magnetic latitude versus Jovian system 3 longitude [*Mead*, 1974]. The width of the band in L corresponds to Io's diameter and determines the sweeping corridor for particles with gyroradii much smaller than Io's radius. Io passes through a given longitude in the sweeping corridor once every orbital period in the frame of reference corotating with Jupiter.

Satellite sweeping time. Let us first consider the sweeping process at a fixed value of L, where the sweeping corridor intersects a longitude interval α. For example, from Figure 2 we see that at $L = 6.2$, $\alpha = 0.7$ rad. The time that the satellite spends at this L value is $T_L = \alpha/(2\pi f_s)$, where f_s is the satellite orbital frequency. The time required to absorb all particles if the satellite were at this L value continuously is $t_c = |f_s \pm f_p|^{-1}$, where f_p is the particle drift frequency and the plus or minus refers to protons or electrons. All particles in a longitude range $\beta = 2\pi T_L/t_c = \alpha/(f_s t_c)$ will be absorbed during the time that the satellite spends at that L value. We know that trapped particles are subject to longitudinal drift motion and random radial displacements which characterize their radial diffusive motion. We assume that these processes produce an effective uniform distribution of particles such that on the average a constant fraction of particles within the sweeping region will be absorbed during every satellite orbital period. Since t_c is nearly constant across the sweeping region, this average fraction will be $B = A/(2\pi f_s t_c)$, where A is the average over L of the longitude range intersected by the sweeping corridor. The area of the sweeping corridor is $A\Delta L$, which may also be evaluated by integrating along the longitude coordinate. Since the width of the corridor in L is the satellite diameter d, the area is $2\pi d$ for particles which mirror at magnetic latitudes of >11° ($\alpha_e < 67°$), and in this case, $B = d/(\Delta L f_s t_c)$.

We define the satellite sweeping time as the time that it takes the satellite to absorb a given fraction of the particles contained within its sweeping region. In section 3 we discuss how a value for the fraction of particles absorbed can be obtained from the data. Since a constant fraction B are absorbed during every satellite rotation period (f_s^{-1}), the fraction of particles surviving absorption will be $y = \exp(-Btf_s)$. Solving for t, we find the following expression for the satellite sweeping time:

$$T = -2\pi t_c \ln y/A \tag{1}$$

For $\alpha_e < 67°$, $2\pi/A = \Delta L/d$. The sweeping time is a function of energy, as is shown in Figure 3 for electrons at Io. We have used the following values: $f_s = 2.1 \times 10^{-5}$ s^{-1}; $f_p = 1.16 \times 10^{-7} LE(\gamma + 1)/\gamma$, where E is the kinetic energy of the particle and γ is the total particle energy in units of the rest energy; and $\Delta L = 0.4$, which is valid for particles mirroring at magnetic latitudes greater than ~11° (see Figure 2), i.e., for particles which have access to the sweeping corridor at all longitudes. The structure of T as a function of energy is due entirely to $t_c = |f_s - f_p|^{-1}$, which has a singularity at $f_s = f_p$, reflecting the inefficient absorption which occurs with zero relative velocity between the drifting particles and the satellite.

We conclude this section by comparing our expression for the sweeping time with others given in the literature. In the notation of this paper, the energy dependence of the sweeping time was given as $T \propto t_c$ by *Mogro-Campero et al.* [1975], which is consistent with our equation (1).

Simpson et al. [1974] have computed the sweeping time for electrons and protons at $L = 6.2$ and for 10% of the particles surviving absorption (see their Figure 22). Their sweeping time is not directly comparable to ours, since it refers to a specific L value within the sweeping region, where they have assumed no radial displacements of the particles. In that case it is important to consider the longitude interval through which particles drift during one satellite orbital period ($\delta = 2\pi f_p/f_s$) and to compare this with the longitude interval swept up by the satellite ($\beta = \alpha/(f_s t_c)$, as derived above). When $\delta > \beta$, corresponding to $E \gtrsim 2.3$ MeV electrons for $L = 6.2$, particles may escape absorption by drifting past the particle-satellite interaction interval during one satellite orbital period. This leads to a resonant behavior of the sweeping time when the drift period is a multiple of the satellite orbital period. Our expression (1) smooths out these narrow energy spikes (see Figure 22 of *Simpson et al.* [1974]) and at the same time maintains the broad energy dependence inherent in t_c. For low-energy particles ($\delta < \beta$) a fraction of particles $\delta/2\pi \propto f_p$ are absorbed during every satellite period, so that the sweeping time $T \propto f_p^{-1}$ (see Figure 22 of *Simpson et al.* [1974]), and T increases with decreasing energy. From our equation (1) (see also Figure 3) we see that the sweeping time becomes constant at low energies. This difference in behavior of the solutions at low energies is due to the randomizing effect of particle radial motion which we have included in our case.

2. Radial Diffusion Coefficient of Particle Transport

The equation describing particle transport for radial diffusion by violation of the third adiabatic invariant φ is [*Schulz and Lanzerotti*, 1974]

$$\frac{\partial \tau}{\partial t} = \frac{\partial}{\partial \varphi}\left(D_\varphi \frac{\partial \tau}{\partial \varphi}\right) \tag{2}$$

The $D\varphi$ is the diffusion coefficient in the coordinate φ. The phase space density of particles τ is defined such that $\tau d^3x d^3p$ is the number of particles contained in the spatial volume element d^3x and in the momentum volume element d^3p. In (2), τ is to be evaluated at constant first and second invariants. The relationship between the differential particle flux j (cm^{-2} sr^{-1} s^{-1} MeV^{-1}) measured perpendicular to the magnetic field vector and τ is $\tau = j/p^2$, where p is the particle momentum.

A first estimate of the diffusion coefficient can be obtained by finding the characteristic time that it takes particles to move a distance ΔL equal to the satellite sweeping region while they are undergoing diffusion as described by (2). We first change coordinates to L by noting that $\varphi \propto L^{-1}$ and $D_\varphi \propto (d\varphi)^2$ [*Roederer*, 1970], and we obtain

$$\frac{\partial \tau}{\partial t} = L^2 \frac{\partial}{\partial L}\left(\frac{D}{L^2}\frac{\partial \tau}{\partial L}\right) \tag{3}$$

where $D = D_L$ is the diffusion coefficient in the coordinate L, which we henceforth refer to as the radial diffusion coefficient. We now calculate the mean square displacement in L, $(\Delta L)^2$, of an infinitesimally thin particle distribution starting from time $t = 0$. We assume that D is independent of L across the thin developing distribution. Using (3) and following the derivation of *Reif* [1965], we obtain $t = (\Delta L)^2/4D$. Equating this time to the satellite sweeping time T gives

$$D \simeq \Delta L^2/4T \tag{4}$$

Although (4) should give correct order of magnitude estimates of the diffusion coefficient, it is not expected to be very accurate. The shortcoming, which is fundamental, is that the radiation belt is not a spreading particle sheet, and the correspondence between model parameters and measurables is imperfect.

A second estimate can be obtained by considering a diffusive inward particle flow and calculating the fraction of particles lost in crossing the sweeping region.

Equation (2) is of the form of an equation of continuity, the right-hand side corresponding to the divergence of a current $I = -D_\varphi(\partial \tau/\partial \varphi)$. One can then define a diffusion velocity $\Delta\varphi/\Delta t$ such that $I = \tau(\Delta\varphi/\Delta t)$. We again change coordinates to the more useful radial dimensionless coordinate L, and the expression containing the diffusion velocity becomes

$$\Delta L/\Delta t = -D\, \partial/\partial L\, (\ln \tau) \tag{5}$$

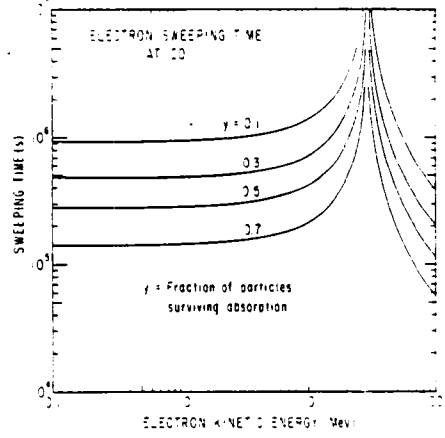

Fig. 3. Sweeping time T (equation (1)) at Io as a function of electron kinetic energy and for selected values of the fraction of particles surviving absorption.

In order to use (5) to obtain quantitative estimates of D in the neighborhood of the Jovian satellites we set the diffusion velocity $\Delta L/\Delta t$ equal to the width of the sweeping region ΔL divided by the sweeping time T that it takes to absorb a fraction $1 - y$ of the particles (equation (1)). For convenience we denote the slope $\partial(\ln \tau)/\partial L = n$, so that our expression for the diffusion coefficient becomes

$$D \simeq -\Delta L/nT \tag{6}$$

Equation (5) can be used to describe a fundamental characteristic of particle transport. Since the diffusion coefficient D is a positive quantity, a determination of $\tau(L)$ allows one to deduce the sign of the diffusion velocity. Thus in the case of the inner Jovian magnetosphere, *McIlwain and Fillius* [1975] conclude that particles move toward the planet, since they find that the slope $n = \partial(\ln \tau)/\partial L$ is positive. We feel that (6) is more accurate than (4). Note, however, that there is an increased demand on the experimental measurements. Whereas (4) requires only the fraction of particles surviving absorption, (6) requires both this fraction and the first spatial derivative of the phase space density τ.

Expressions of the type $D \sim(\Delta L)^2/T$ and (5) have been used to obtain estimates of the absorption effectiveness of the Jovian satellites (S. A. Jacques and L. Davis, Jr., unpublished manuscript, 1972) and the diffusion coefficient at the orbit of Io [*Simpson et al.*, 1974].

If the measurements also allow a determination of the second spatial derivative of τ, one can obtain the diffusion coefficient directly by use of the diffusion equation (3) by adding a sink term $-s$ to the right-hand side to describe particle absorption in the sweeping region of a satellite. If the number of particles decays exponentially, as we found in the subsection on satellite sweeping time in section 1, the sink term can be expressed as $s = \tau/T_i$, where T_i is given by (1), with $\ln y = -1$. Equation (3) with sink term can now be solved for the diffusion coefficient D ($\propto L^m$) for steady state conditions ($\partial\tau/\partial t = 0$), and we obtain

$$D = \frac{\tau}{T_i}\left[\frac{(m-2)}{L}\frac{\partial\tau}{\partial L}\frac{\partial^2\tau}{\partial L^2}\right]^{-1} \tag{7}$$

which is valid in the sweeping region ΔL. To obtain m, we consider an L region where there is no satellite absorption, and we solve (3) in the steady state to obtain

$$m = 2 - L\frac{\partial^2\tau/\partial L^2}{\partial\tau/\partial L} \tag{8}$$

Although (7) and (8) give a complete solution, they demand more of the experimental data than we can deliver at our present level of data analysis. Therefore when we obtain numerical values for D in section 3, we use only the first two methods (equations (4) and (6)).

The ultimate test of a value for D is whether or not the diffusion equation reproduces the experimental results when it is integrated away from some boundary conditions. If one uses a constant value of D within the sweeping region, (3) with sink term can be reduced to Bessel's equation, and the solution can be compared with the observations. In section 3 such a comparison is made for one case where the data allowed us to obtain a rather good profile of the phase space density τ.

3. VALUES FOR THE RADIAL DIFFUSION COEFFICIENT

The University of California at San Diego instrument on Pioneer 10 made measurements at Jupiter of electrons with energy thresholds in the range $0.1 \lesssim E \lesssim 35$ MeV. In Figure 4 we show an overall view of the behavior of counting rates for three integral energy measurements. We also show the locations of the sweeping regions of the relevant Jovian satellites. We see that there is evidence for absorption at Io and Europa. The differences in absorption as a function of energy can be understood qualitatively by considering the dependence of the absorption and radial diffusion processes on the particle drift period [*Mogro-Campero et al.*, 1975].

In this section we explain the handling of the experimental data and other parameters needed to obtain the diffusion coefficient. In Table 1 we present our values for the diffusion coefficient and related parameters at Io and Europa.

The energy response of our detectors is determined by the product of the geometric factor [*Fillius and McIlwain*, 1974], as given, e.g., in their Figure 3, and the differential energy spectrum [*McIlwain and Fillius*, 1975]. For example, the average energy of particles measured by the C2 detector of Figure 4 in the neighborhood of the orbit of Io is $\bar{E} = 14$ MeV, and the energy response has a full width at half maximum of 11 MeV, extending from 6 to 17 MeV. Therefore although the detectors are sensitive to all particles above a threshold energy, a differential energy spectrum of negative exponent will lead to the detection of a majority of particles within an energy window. We use $\bar{E}$ for the evaluation of parameters which are functions of energy.

Evaluation of the sweeping time. The sweeping time T (equation (1)) depends on y, the fraction of particles surviving passage across the sweeping region ΔL of a satellite. We can obtain an estimate of y by using the flux profiles in Figure 4. If one extrapolates the rate of rise of flux as a function of L which is observed outside the satellite range of influence across the region of absorption, one obtains the flux which would have been present in the absence of the satellite. The ratio of the actual flux observed to the flux obtained in this manner is the value of y. Thus at Io, for example, we obtain $y = 0.6$ for the inbound pass and $y = 0.4$ for the outbound pass of the curve labeled C2 in Figure 4 ($\bar{E} = 14$ MeV).

The extent of the sweeping region ΔL and the geometrical function A in (1) for the sweeping time are functions of magnetic latitude and can be obtained as in the following example. At the orbit of Io ($L = 6$) the magnetic latitude of Pioneer 10 was 6° for the inbound trajectory. From Figure 2 we deduce that in this case the sweeping region extends from $L = 5.8$ to $L = 6.1$, so that $\Delta L = 0.3$. We also find from this figure that the average longitude range intersected by the sweeping corridor is $A = 0.9$ rad.

We can now find the absorption time of electrons with $\bar{E} = 14$ MeV at Io from (1). For the inbound pass we obtain $T = 3.8 \times 10^6$ s.

Evaluation of the diffusion coefficient. Except for (6) the expressions for the diffusion coefficient in section 2 require a knowledge of the phase space density τ at constant first and second invariants.

The fluxes in Figure 4 are those measured perpendicular to the local magnetic field vector, so that they correspond to particles which mirror at the magnetic latitude of the instrument. At a given energy all particles with common mirror points have the same value of the second invariant. Therefore the second invariant is constant for a trajectory along the magnetic equator if one measures particles with 90° pitch angles. In fact, the Pioneer 10 trajectory was nearly equatorial with a maximum magnetic latitude excursion of 23°. Our criterion for conservation of the second invariant then reduces

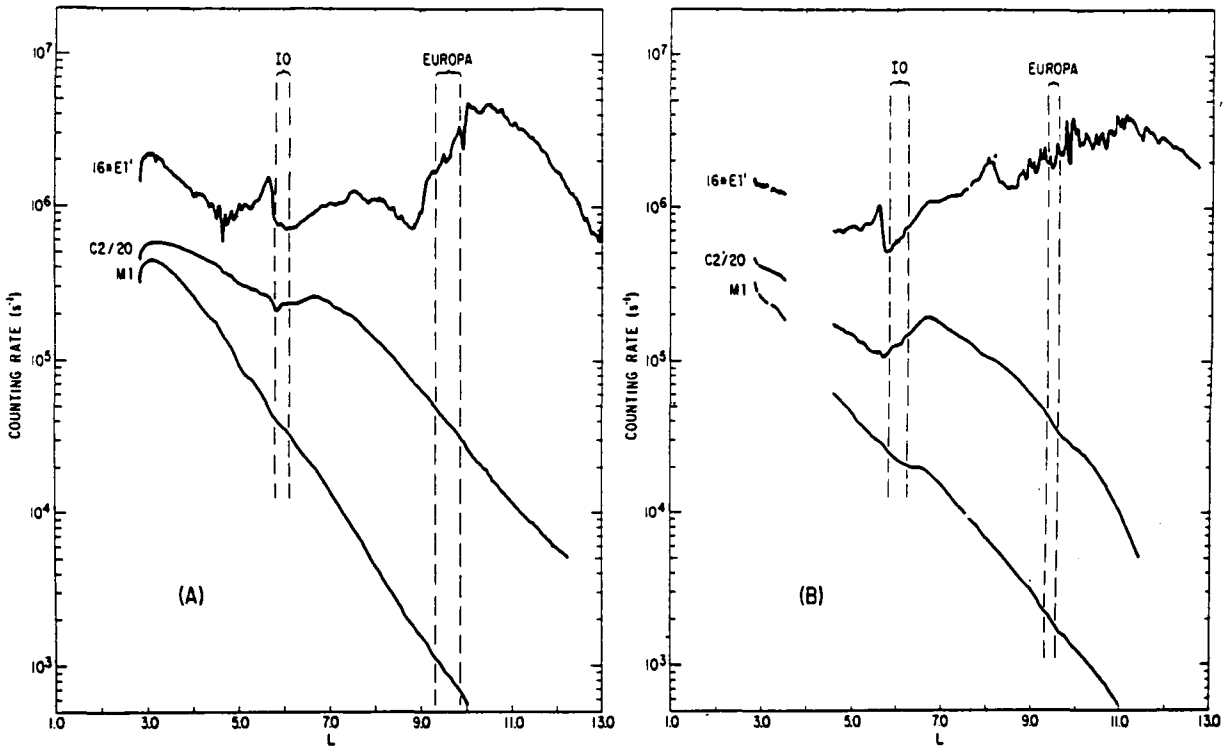

Fig. 4. Counting rates of three electron detectors of the University of California at San Diego experiment for (*a*) the inbound trajectory and (*b*) the outbound trajectory of Pioneer 10. These are the counting rates measured perpendicular to the local magnetic field vector. The energy response of each detector is determined by its geometrical factor and the electron differential energy spectrum. Therefore the average energy of response varies with location in the Jovian magnetosphere (see Table 1). Approximate values for illustrative purposes are 1, 10, and 25 MeV from top to bottom on both sides of the figure. The sweeping regions of Io and Europa are indicated by dashed lines.

to the use of the flux of particles perpendicular to the local magnetic field vector.

We now discuss the procedure for obtaining the phase space density τ at constant first invariant μ. *McIlwain and Fillius* [1975] have computed τ for electrons at constant μ at discrete points in the Jovian magnetosphere and for a wide range of values of μ. We have used the results of their calculations to get values for the slope of the phase space density τ ($n = \partial(\ln \tau)/\partial L$) in the neighborhood of Europa. Their computations lack detail in the vicinity of Io, so for that case we devised the approximate method described below.

Conservation of the first invariant μ for relativistic particles implies $E^2L^3 = \text{const}$. The phase space density τ at energy E is $\tau = j(E)/p^2$, where p is the particle momentum. Since $p = E$ in the relativistic limit used here, $\tau = j(E)/E^2$. As was shown above, because of the geometric factor of our detectors and for the differential energy spectra in consideration the major contribution to an integral energy measurement will be from particles within an energy window. The window thresholds will remain constant for a constant particle spectral index. For a window detector with energy thresholds E_a and E_c the differential particle flux at energy E_b ($E_a < E_b < E_c$) is given by $j(E_b) = [J(E_a) - J(E_c)]/(E_c - E_a)$, where J is the integral particle flux above the energy specified (i.e., $j = dJ/dE$). $J(E_a) - J(E_c)$ is the particle flux which the detector measures, so that the counting rate of the detector is proportional to $j(E_b)$. We now assume that the spectral index remains constant for a limited region in L space, namely, the sweeping region of Io. The energy E_b is then a constant, and from conservation of μ, $\mu_0 = E_b^2L_0^3 = E^2L^3$, where we arbitrarily choose L_0. For a power law spec-

TABLE 1. Values of the Diffusion Coefficient and Relevant Parameters for Trapped Electrons at Jupiter

L	Average Energy $\bar{E}$, MeV	Orbit*	First Invariant μ, MeV/G	Electron Drift Frequency, s^{-1}	Sweeping Region ΔL	y†	Slope of τ ($n = \partial(\ln \tau)/\partial L$)	Sweeping Time T From (1), s	Diffusion Coefficient D, s^{-1} From (4)	From (6)
6 (Io)	14	I	10^4	1.0×10^{-5}	0.3	0.55	1.8	3.8×10^5	5.9×10^{-6}	4.4×10^{-7}
6 (Io)	14	O	10^4	1.0×10^{-5}	0.4	0.38	1.8	7.1×10^5	5.6×10^{-6}	3.1×10^{-7}
6 (Io)	0.9	I	90	8.5×10^{-7}	0.3	0.1		7.8×10^5	2.9×10^{-6}	
9.5 (Europa)	10	I	2×10^4	1.2×10^{-5}	0.55	>0.9	0.16	$<1.1 \times 10^5$	$>6.9 \times 10^{-7}$	$>3.1 \times 10^{-5}$
9.5 (Europa)	0.7	I	300	1.1×10^{-6}	0.55	0.03	1.8	2.0×10^6	3.8×10^{-6}	1.5×10^{-7}
9.5 (Europa)	0.7	O	300	1.1×10^{-6}	0.25	0.1		1.2×10^6	1.3×10^{-6}	

*I indicates inbound, and O outbound.
†Fraction of particles surviving absorption.

trum, $j(E)/j(E_0) = (E_0/E)^k$, and τ at $\mu = \mu_0$ is $\tau = j(E)E^{-2} = E_0^k j(E_0)E^{-2-k}$, so that finally, we have

$$\tau(\mu = \mu_0) \propto j(E_0)(L/L_0)^{3+1.5k} \quad (9)$$

Since $j(E_0)$ is proportional to the counting rate of the detector, given the spectral index k, we can transform the measured flux profile of relativistic electrons into τ at constant μ. The result of this calculation for curve C2 of Figure 4*a* in the vicinity of Io's sweeping region is shown in Figure 5. The differential energy spectrum given by *McIlwain and Fillius* [1975] for $L = 6$ was used ($k = 2$), and the choice $L_0 = 6$ implies $\mu_0 \sim 10^4$ MeV/G. Our method is valid to the extent that our detectors can be considered as window detectors and the spectral index can be assumed as constant over this limited domain. The large-scale behavior of τ in Figure 5 is in good agreement with the results of the precise treatment of *McIlwain and Fillius* [1975], whose values are shown for comparison in Figure 5, so that we believe that we have produced a reasonable approximation to τ in the vicinity of Io's sweeping region.

We feel that the values of the slope $n = \partial(\ln \tau)/\partial L$ which can be obtained from Figure 5 (e.g., $n \simeq 2$ in the sweeping region) are reliable but that second spatial derivatives cannot be trusted. Therefore our estimates of the diffusion coefficient in this paper make use of (4) and (6) of section 2, namely, $D \simeq (\Delta L)^2/4T$ and $D \simeq \Delta L/nT$, where ΔL is the sweeping region of the satellite, T is the sweeping time, i.e., the time required for the satellite to absorb an observed fraction $x = 1 - y$ of particles, as given by (1) and as evaluated above, and n is the spatial slope of the logarithm of the phase space density τ, as defined above. The values of n and x are extracted from the data. The precision with which these parameters can be obtained leads to the overall estimate of accuracy of a factor of 2 for the values of D as represented by (4) and (6). However, as was stated previously, (4) and (6) are only expected to give order of magnitude estimates of the diffusion coefficient.

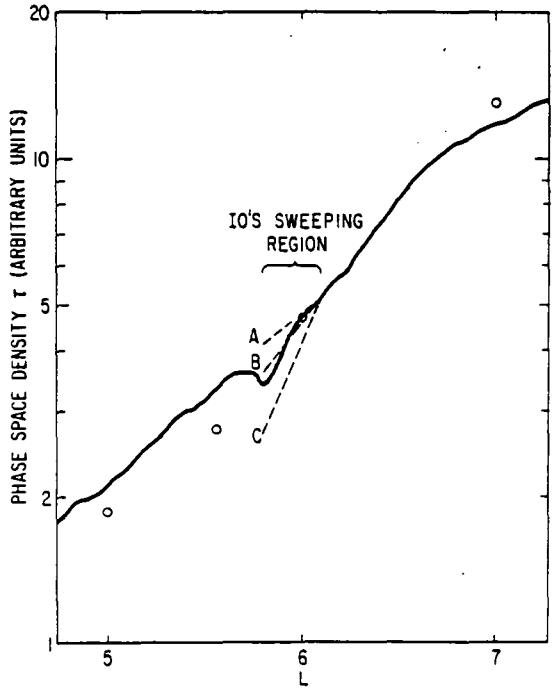

Fig. 5. The phase space density τ at constant first invariant μ ($= 10^4$ MeV/G) as derived from the counting rate profile C2 of Figure 4*a*. The overall positive slope of this curve indicates the net diffusive flow of particles toward the planet, as explained in section 2. The sweeping region of Io is based on the D2 magnetic field model [*Smith et al.*, 1974]. The open circles are the values of τ taken from *McIlwain and Fillius* [1975], normalized at $L = 6$. A, B, and C are solutions to the diffusion equation with a sink term due to particle absorption by Io; the solutions are normalized to the value of τ at the outer edge of the sweeping region and correspond to values of the diffusion coefficient of 6.4×10^{-6}, 1.6×10^{-6}, and 4×10^{-7} s^{-1}, respectively.

The values for the diffusion coefficient are shown in Table 1. The two expressions that we have used for the diffusion coefficient are different approximations to this quantity (see the derivations in section 2), and therefore it is not surprising that the values of D obtained by these two methods are not in agreement. A comparison of values of D obtained by the same equation for inbound and outbound passes is consistent within the uncertainty of a factor of 2, as can be seen for $\bar{E} = 14$ MeV at Io and $\bar{E} = 0.7$ MeV at Europa.

For the first case in Table 1 we have also obtained an estimate of D by solving (3) with sink term in the sweeping region of Io. The solutions are shown by dashed lines in Figure 5 for different values of D. The boundary conditions used were the value and slope of τ at the outer boundary of the sweeping region. The best fit value $D \simeq 1.6 \times 10^{-6}$ s^{-1} (case B in Figure 5) is higher than both estimates in Table 1.

For the low-energy electrons at Europa the calculations based on the outbound pass are probably more reliable, since the sharp rise and fall of the flux profile on the inbound pass and the fact that the spacecraft was within ~25° of longitude from Europa as it crossed its orbit may be an indication of local effects near this satellite. No estimates of D based on the highest electron energies (curve M1 of Figure 4) have been given, because the energy response of the detector overlaps the resonance in the sweeping time (Figure 3) for both Io and Europa. This resonance surrounds the energy at which the electron drift frequency equals the satellite rotation frequency, leading to extremely large sweeping times. We believe that this is the reason for the lack of absorption at Io and Europa as shown in Figure 4.

4. Discussion

Knowledge of the diffusion coefficient is obviously important for an understanding of the trapped radiation belt. In addition, it provides us with a measure of the power spectrum of the electromagnetic fluctuations at the particle drift frequency. A determination of the spatial dependence of D may permit us to identify or narrow down the choice of the mechanism producing the disturbances which violate the third invariant. For example, field line exchange driven by atmospheric-ionospheric winds seemed to be favored by pre-Pioneer 10 investigations [see *Birmingham et al.*, 1974, and references therein]. For this process it is expected that $D \propto L^2$. However, $D \propto L^8$ and L^{10} resulting from fluctuating convection electric fields and from magnetic pumping, respectively, are other possibilities, which appear to be dominant in the earth's case.

With regard to the absolute value of the diffusion coefficient, *Simpson et al.* [1974] have obtained a value of $D \simeq 6 \times 10^{-8}$ s^{-1} at $L \simeq 6$ from an analysis of the absorption of ~1-MeV protons by Io. This value is consistent with our results, and we note that their proton energy implies a drift period comparable to that of our low-energy electrons. For ~10-MeV electrons at Io, *Simpson et al.* [1974] deduce $D \simeq 2 \times 10^{-7}$ s^{-1} and $D \simeq 10^{-6}$ s^{-1}, depending on the method of analysis. These

values are also compatible with ours. *Birmingham et al.* [1974] obtained $D \simeq 2 \times 10^{-9} L^2 s^{-1}$ from a consideration of synchrotron radiation observed at earth. At $L = 6$ this gives $D \simeq 6 \times 10^{-8} s^{-1}$, and at $L = 9.5$, $D \simeq 1.5 \times 10^{-7} s^{-1}$. These values are consistent with ours for the low energies for which they are applicable.

In addition to obtaining the absolute value of D we may use Table 1 to look into the spatial and energy dependences of the diffusion coefficient.

From the results presented in Table 1 we conclude that in general, D is a function of L and electron energy. Specifically, we can say that (1) the diffusion coefficient is an increasing function of energy at $L \sim 9.5$ (Europa), based on values at 0.7 and 10 MeV, and (2) the diffusion coefficient increases with increasing L (for $E \sim 10$ MeV the values shown for $L \sim 6$ and $L \sim 9.5$ imply that if $D \propto L^m$, $m \geq 2$).

However, we note that at Io there is no evidence for an energy dependence of D over an energy range similar to that sampled at Europa. Therefore the spatial and energy dependences of the diffusion coefficient may not be separable; i.e., the spatial dependence may be a function of energy.

The conclusions on spatial and energy dependences of the diffusion coefficient can also be verified from Figure 4 in a qualitative manner. First, we note that the sweeping regions and physical dimensions of Io and Europa are similar and that resonance effects leading to extremely large sweeping times apply only to curve M1. We then conclude from the fact that curve C2 shows a much more pronounced absorption effect at Io than at Europa that the diffusion coefficient is larger at Europa. Similarly, the difference in absorption at Europa between curves E1′ and C2 indicates that in this case the diffusion coefficient is an increasing function of energy.

The diffusion coefficient for radial motion produced by fluctuating electric fields is proportional to the power spectrum of these fields evaluated at the particle drift frequency [*Fälthammar*, 1965]. In this case, from the values of the electron drift frequency and the diffusion coefficient at Europa we deduce that the power spectrum of electric field fluctuations is larger at $10^{-5} s^{-1}$ than at $10^{-6} s^{-1}$ (see Table 1). These drift frequencies are computed in the reference frame which corotates with Jupiter, but they are consistent with a power spectrum peaking at zero frequency in an inertial frame [*Mogro-Campero et al.*, 1975], as would be expected for electric fields associated with the upper atmosphere dynamo driven by neutral winds in the ionosphere [*Brice and McDonough*, 1973].

The best estimate of the net transport velocity of particles toward the planet can be obtained from the sweeping time T rather than from D. For example, at Io we find that for $\tilde{E} = 14$ MeV the sweeping time is such that the net transport velocity is $T/\Delta L \simeq 20$ days R_J^{-1}. It is interesting to note that the synchrotron radiation lifetime of electrons with $\mu = 10^4$ MeV/G is ~150 days at $L = 2$.

Acknowledgments. We thank Carl E. McIlwain for comments and discussions. We also thank G. Steinberg and W. Knight for assistance in the preparation of some of the figures. This work was supported by NASA contract NAS 2-6552 and grant NGL 05-005-007.

The Editor thanks T. J. Birmingham and D. J. Williams for their assistance in evaluating this paper.

REFERENCES

Birmingham, T., W. Hess, T. Northrop, R. Baxter, and M. Lojko, The electron diffusion coefficient in Jupiter's magnetosphere, *J. Geophys. Res.*, *79*, 87, 1974.

Brice, N., and G. A. Ioannidis, The magnetospheres of Jupiter and earth, *Icarus*, *13*, 173, 1970.

Brice, N., and T. R. McDonough, Jupiter's radiation belts, *Icarus*, *18*, 206, 1973.

Fälthammar, C.-G., Effects of time-dependent electric fields on geomagnetically trapped radiation, *J. Geophys. Res.*, *70*, 2503, 1965.

Fillius, R. W., and C. E. McIlwain, Measurements of the Jovian radiation belts, *J. Geophys. Res.*, *79*, 3589, 1974.

Hess, W. N., T. J. Birmingham, and G. D. Mead, Absorption of trapped particles by Jupiter's moons, *J. Geophys. Res.*, *79*, 2877, 1974.

McIlwain, C. E., and R. W. Fillius, Differential spectra and phase space densities of trapped electrons at Jupiter, *J. Geophys. Res.*, *80*, 1341, 1975.

Mead, G. D., Magnetic coordinates for the Pioneer 10 Jupiter encounter, *J. Geophys. Res.*, *79*, 3514, 1974.

Mead, G. D., and W. N. Hess, Jupiter's radiation belts and the sweeping effects of its satellites, *J. Geophys. Res.*, *78*, 2793, 1973.

Mogro-Campero, A., R. W. Fillius, and C. E. McIlwain, Electrons and protons in Jupiter's radiation belts, *Space Res.*, *15*, in press, 1975.

Reif, F., *Fundamentals of Statistical and Thermal Physics*, pp. 486–488, McGraw-Hill, New York, 1965.

Roederer, J. G., *Dynamics of Geomagnetically Trapped Radiation*, p. 129, Springer, New York, 1970.

Schulz, M., and L. J. Lanzerotti, *Particle Diffusion in the Radiation Belts*, p. 83, Springer, New York, 1974.

Shawhan, S. D., D. A. Gurnett, R. F. Hubbard, and G. Joyce, Io-accelerated electrons: Predictions for Pioneer 10 and 11, *Science*, *182*, 1348, 1973.

Simpson, J. A., D. C. Hamilton, R. B. McKibben, A. Mogro-Campero, K. R. Pyle, and A. J. Tuzzolino, The protons and electrons trapped in the Jovian dipole magnetic field region and their interaction with Io, *J. Geophys. Res.*, *79*, 3522, 1974.

Smith, E. J., L. Davis, Jr., D. E. Jones, P. J. Coleman, Jr., D. S. Colburn, P. Dyal, C. P. Sonnett, and A. M. A. Frandsen, The planetary magnetic field and magnetosphere of Jupiter: Pioneer 10, *J. Geophys. Res.*, *79*, 3501, 1974.

(Received December 16, 1974;
accepted September 12, 1975.)

VOL. 83, NO. A10 JOURNAL OF GEOPHYSICAL RESEARCH OCTOBER 1, 1978

Compression of Jupiter's Magnetosphere by the Solar Wind

EDWARD J. SMITH

Jet Propulsion Laboratory, California Institute of Technology, Pasadena, California 91103

R. WALKER FILLIUS

Department of Physics, University of California at San Diego, La Jolla, California 92093

JOHN H. WOLFE

Ames Research Center, Moffett Field, California 94035

A study of the major changes in the solar wind during the Pioneer 10 and 11 encounters and their influence on the size of the Jovian magnetosphere is reported. Simultaneous sets of encounter data acquired by the Jet Propulsion Laboratory vector helium magnetometer, the Ames Research Center plasma analyzer, and the University of California at San Diego trapped radiation detector have been compared with data acquired simultaneously in interplanetary space by the sister spacecraft. Of particular interest were four intervals during which it appeared that the spacecraft had reentered the magnetosheath near 50 R_J after having first entered the magnetosphere near 100 R_J. The principal outcome of the study is that in three of these cases the reentries into the magnetosheath occurred when high-speed solar wind streams and their associated interaction regions were expected to arrive at Jupiter. Thus the study supports the hypothesis advanced previously that the Jovian magnetosphere had undergone a large-scale compression. The results are contrary to an alternative hypothesis that the Pioneers had traversed a spatial region located inside the magnetosphere possibly associated with plasma outflow. The fourth case, which was observed by Pioneer 11 outbound, appears to have occurred during quiet interplanetary conditions. However, a detailed reinvestigation of magnetic field and plasma data during this interval shows that the spacecraft had reentered the magnetosheath and not a region interior to the magnetosphere. The reentry into the magnetosheath and the subsequent return to the magnetosphere were separated by an interval of 10 hours and would have been expected to occur when the spacecraft was at its highest magnetic latitude. It is concluded, tentatively, that this reentry was the result of a large-scale north-south motion intrinsic to the Jovian magnetosphere. The question of whether or not the magnetic field just inside the magnetopause is sufficiently strong to withstand the pressure of the incident solar wind has been reexamined within the context of this present study. The field appears able to hold off the solar wind both at 100 R_J and near 50 R_J. The compressibility of the Jovian magnetosphere is enhanced because the field inside the magnetopause is not the planetary field but is principally caused by currents inside the magnetosphere, presumably the equatorial current sheet. The possible acceleration of energetic trapped radiation when the magnetosphere was compressed has been investigated. Comparison of the increased particle fluxes and the magnetic field shows that gyrobetatron acceleration can be discounted. Based on the measured time difference between the particle enhancement and the arrival of the magnetopause at the spacecraft, an estimate is derived for the average plasma density inside the magnetosphere of 1–10 cm $^{-3}$. Finally, the characteristic time constants appropriate to an electric circuit model of Jupiter's magnetosphere have been estimated as being in the range between 15 and 50 hours.

INTRODUCTION

Both Pioneer 10 and Pioneer 11 first encountered the magnetosphere of Jupiter at nearly 100 planetary radii (96 and 97 R_J, respectively). During both encounters, field and particle observations showed that the two spacecraft subsequently returned to a region like that just outside the magnetosphere but at a Jovicentric distance of only $\simeq 50$ R_J [*Wolfe et al.*, 1974*a*; *Smith et al.*, 1974*a*, 1975; *Mihalov et al.*, 1975]. The observations were interpreted as a large-scale compression of Jupiter's magnetosphere presumably caused by a temporal change in the character of the solar wind. The compression of the magnetosphere by a factor of nearly 2, observed during both encounters, was further interpreted as evidence that Jupiter's magnetosphere is much more readily compressed than that of the earth. Compression of the earth's magnetosphere from its normal location of 10 to only 5 R_E has been found to occur only on rare occasions [e.g., *Opp*, 1968; *Cahill and Skillman*, 1973].

The question has persisted, however, of whether the observations actually represented a temporal change or were evidence of a spatial region, somewhat like the magnetosheath, located inside the magnetosphere. To some extent, this challenge has come from theorists who favor so-called plasma outflow models of Jupiter's magnetosphere. Outflow models have been proposed, for example, by *Michel and Sturrock* [1974], *Hill et al.* [1974], and *Kennel and Coroniti* [1975]. According to such models, regions would exist inside the magnetosphere within which centrifugal forces, associated with Jupiter's large scale and rapid rotation, overwhelm the restraining effect of the planetary magnetic field with the production of internal convective flows and possibly even some form of internal shock.

One test of these alternative hypotheses, temporal change or spatial variation, is to investigate changes in the solar wind in the vicinity of Jupiter during intervals in which the magnetosphere was supposedly compressed. Fortunately, during each encounter, simultaneous measurements in interplanetary space are available from the sister spacecraft. While Pioneer 10 was inside Jupiter's magnetosphere, Pioneer 11 was nearly radially aligned with Jupiter and at a heliocentric distance of 2.9 AU. During the Pioneer 11 encounter, Pioneer 10 was in inter-

Paper number 8A0455.
0148-0227/78/108A-0455$1.00

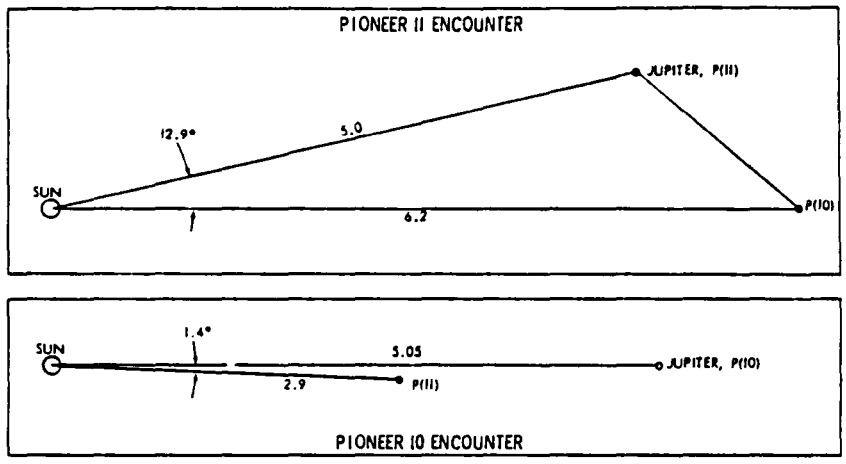

Fig. 1. Geometry of the observations during the Pioneer 10 and 11 encounters. During the Pioneer 10 encounter, Pioneer 11 was making interplanetary measurements upstream of Jupiter at 2.9 AU and was nearly radially aligned with the sun and Pioneer 10 (the longitude separation was only 1.4°). During the Pioneer 11 encounter, Pioneer 10 was beyond the orbit of Jupiter at 6.2 AU, and the radii from the sun to Pioneer 10 and Jupiter were separated in longitude by 12.9°.

planetary space beyond the orbit of Jupiter at a distance of 6.2 AU. We have compared these simultaneous sets of interplanetary and planetary data, with a view to identifying major changes in the solar wind and their possible influence on the Jovian magnetosphere.

Observations

The locations of the spacecraft at the times of the encounters are shown in Figure 1. Although simultaneous measurements are available at Jupiter and in interplanetary space, a time delay must be introduced to allow the solar wind that reaches one spacecraft from a given solar longitude to arrive at the other. This delay consists of two parts, one a consequence of the longitude separation of the two spacecraft and the other the result of their radial separation. The latter depends on the radial velocity of propagation of a specific solar wind feature. If a spread of velocities typical of the solar wind is assumed and the locations of the spacecraft are known, it is possible to compute characteristic time delays. Thus for constant solar wind speeds between 400 and 600 km/s the delays between the times of arrival of an interplanetary structure at Pioneer 11 and at Pioneer 10 or Jupiter would have been $T_{10} - T_{11} = 9.6$ and 6.4 days, respectively. The corresponding delays during the Pioneer 11 encounter, computed for the same two velocities, are $T_{10} - T_{11} = 6.2$ and 4.4 days.

In conducting this investigation we have benefited from the advantage of having already analyzed a substantial quantity of interplanetary data from Pioneer 10 and 11. Such studies have shown that the interplanetary medium beyond 1 AU can be classified into two distinct types of regions [*Smith and Wolfe*, 1976, 1977]. One region is disturbed and is characterized by enhancements in the magnitude of the magnetic field B, the plasma density n and temperature T, and the level of irregularity. Such regions occur in portions of high-speed solar wind streams that earlier contained a positive velocity gradient (increasing speed). The regions are sharply bounded, often with a forward shock at the leading edge and a reverse shock at the trailing edge, and are evidently the consequence of the interaction of fast solar wind with slower moving plasma preceding it. Within the interaction region the convective energy of the solar wind stream is converted into internal energy, partly in the form of enhanced plasma and magnetic field pressure ($B^2/8\pi + nkT$). The disturbed interaction regions alternate with quiet regions within which the solar wind velocity is monotonically decreasing and in which the field strength, density, and temperature are low.

The principal features at the encounter and in interplanetary space are summarized in Figures 2 and 3. The upper halves of the figures contain logarithmic plots of magnetic field and energetic particle data prior to, during, and following each encounter. The various regions surrounding Jupiter have previously been identified on the basis of high-resolution particle, magnetic field, and plasma data. The times when the spacecraft were thought to be inside Jupiter's magnetosphere are shown as shaded columns. At other times the spacecraft were in either the Jovian magnetosheath or interplanetary space. These designations are consistent with previous publications in which the details have been presented and described [*Wolfe et al.*, 1974*b*; *Smith et al.*, 1974*b*, 1976; *Intriligator and Wolfe*, 1976].

The lower halves of Figures 2 and 3 contain the simultaneous interplanetary data from the sister spacecraft. Two interplanetary parameters were selected as being representative of interplanetary structure, the magnetic field magnitude, which is plotted logarithmically, and the convective plasma pressure $P_c = nmV^2$. There is an obvious correspondence between these two parameters, as can readily be seen in the figures, so that they basically identify the same structures. The interaction regions discussed above are evident as distinct regions in which both parameters are enhanced by factors of 3–10 in comparison to those of the adjacent quiet regions.

An additional feature of the interplanetary magnetic field that is useful in identifying corresponding features at two widely separated locations is the field polarity or magnetic sector structure. The polarity of the interplanetary field is shown at both locations with the exception of intervals when the encounter spacecraft was inside the Jovian magnetosphere. A characteristic feature that may be noted is the tendency for the sector boundaries to occur in the vicinity of peaks in the field magnitude and the pressure.

The time scales in the upper and lower halves of these figures have been displaced to accommodate the corotation

and radial delays. It was found adequate, for this study, to use an average displacement of the data from one spacecraft relative to data from the other so that corresponding interaction regions were aligned. In doing this a reasonable velocity of propagation and a reasonable time delay were assumed in order to exclude some alignments which were possible but highly improbable. It can be seen that the pattern of interaction regions, as well as the magnetic sector structure, agrees at both locations and for both encounters.

The major features of the data in Figures 2 and 3 will now be discussed in some detail. The upper two panels containing encounter data are hatched when Pioneer was inside the magnetosphere. The entire encounter extending between the first and the last bow shock crossing is identified as the interval between the two vertical lines. The two 'white' intervals within the hatching are those within which the spacecraft 'returned to the magnetosheath.'

One of the principal features of the energetic particle data [*Fillius and McIlwain*, 1974] is the high count rates inside the magnetosphere. The particle data shown are from channel C1 of the University of California at San Diego Cerenkov counter. In interplanetary space this detector responds mainly to cosmic ray nucleons with energies of >500 MeV. Inside the magnetosphere, its response is dominated by electrons with energies of >6 MeV. The count rates are substantially larger inside than outside the magnetosphere and rise to very large values near periapsis.

A periodicity of approximately 10 hours is noticeable both inbound and outbound. Outside the magnetosphere and bow shock, bursts of energetic electrons can be seen. These are electrons that escape from the Jovian magnetosphere and propagate back along the interplanetary field into the inner solar system [*Chenette et al.*, 1974; *Teegarden et al.*, 1974]. Within the white intervals there is a precipitous drop of the count rates to near-interplanetary values.

The principal features of the magnetic field magnitude appear in the panel just below the energetic particle data. The white intervals during which Pioneer reentered the magnetosheath do not correspond to any very obvious changes in the field magnitude. The crossing of the magnetopause and evidence from the field data that the observations were again being made in the magnetosheath are based on other properties, such as the field direction and the character of the superposed irregularities, and on higher time resolutions. In particular, the field magnitude in the magnetosheath is comparable to its value inside the magnetosphere. In the past we have interpreted this approximate equality as evidence that the magnetosheath was disturbed, as would be anticipated if the magnetosphere were compressed by enhanced solar wind pressure and stronger-than-average fields. Evidence in support of this presumption will be presented below, where it will be shown that large interplanetary fields were expected in the vicinity of Jupiter during these intervals.

A periodicity associated with the rotation of Jupiter is evident in B, although not as noticeably as in the energetic particle data. In Figure 2 the irregular appearance of B between the last outbound magnetopause crossing and the last bow shock crossing is the result of numerous crossings of the bow shock as Pioneer 10 exited along the predawn flank of the magnetosphere. Two enhanced field regions are apparent before and after the Pioneer 10 encounter (designated regions a and d, respectively). These enhancements are a characteristic feature of the solar wind interaction regions that corotate with the sun, called corotating interaction regions (CIR's), that are discussed in the second paragraph above.

In Figure 2 the magnitude of the interplanetary field at Pioneer 11 is dominated by the large increases associated with CIR's. There are basically four such regions (designated a, b, c, and d), although the first region may actually be superposed on a smaller preceding CIR. In each case the interaction regions begin and end abruptly. Typically, they are enclosed within a forward shock and a reverse shock that are readily identifiable in both the field and the plasma data. The CIR's alternate with quiet regions within which the average magnitude is 0.7 γ, the value anticipated at 5 AU from a simple extrapolation of a 5-γ field at 1 AU, if the Parker spiral field model [*Parker*, 1963] is assumed.

The Pioneer 11 panel in Figure 2 shows that the convective pressure is dominated by the same CIR's that are visible in B. During the intervening quiet intervals the pressure is typically 10×10^{-10} dyn/cm^2. If an average solar wind pressure at 1 AU of $nMV^2 = 5 \times 2 \times 10^{-24} \times (360 \times 10^5)^2 = 130 \times 10^{-10}$ dyn/cm^2 is assumed, the pressure to be expected in the vicinity of Pioneer 11 is $130 \times 10^{-10}/2.9^2 = 15 \times 10^{-10}$ dyn/cm^2. Thus the observed pressure is approximately two thirds of the extrapolated pressure.

Similarly, Figure 3 shows that the pressure in the quiet regions at Pioneer 10 is typically 10^{-10} dyn/cm^2. This value is approximately one third of the value obtained from extrapolating the average solar wind to Pioneer 10, for which $P_c = 130 \times 10^{-10}/6.2^2 = 3.4 \times 10^{-10}$ dyn/cm^2.

The tendency for the pressure within the quiet regions to be less than that anticipated at large distances can be explained as a consequence of the rarefaction that occurs within the quiet regions. Evidently, the number density and hence the pressure fall off more rapidly than r^{-2} as the plasma expands in such regions, which are characterized by a negative speed gradient (decreasing velocity).

There is an excellent correlation between the signatures of the CIR's in the plasma and field data. Within the interaction regions the convected pressure is increased by about an order of magnitude. Although the solar wind velocity remains high within the quiet region, the density is typically very low, so that large pressure is confined to the interaction regions.

The principal correlation between the interplanetary and the encounter data involves the CIR's. The two interaction regions (a and d) that were observed at Pioneer 10 prior to and following the encounter can also be seen in the Pioneer 11 data. In particular, the 'double-step' structure associated with the first CIR is evident at both locations. These correlations are part of a much longer sequence of correlated interaction regions extending over a period of 1.5 years following the Pioneer 11 launch [*Smith and Wolfe*, 1976]. Thus there is no ambiguity in the identification of corresponding interaction regions.

The main feature to be noted is the correspondence between the white columns within the hatching and the intervals in which CIR's b and c would be expected to have arrived at Jupiter. The arrival of the interaction regions at Jupiter was coincident with the return of Pioneer to the magnetosheath both inbound and outbound. Thus the Pioneer 10 and 11 correlation supports the hypothesis that the Jovian magnetosphere was compressed by regions of enhanced solar wind pressure.

Figure 3, which contains data acquired during the Pioneer 11 encounter, follows the same format as Figure 2. All of the

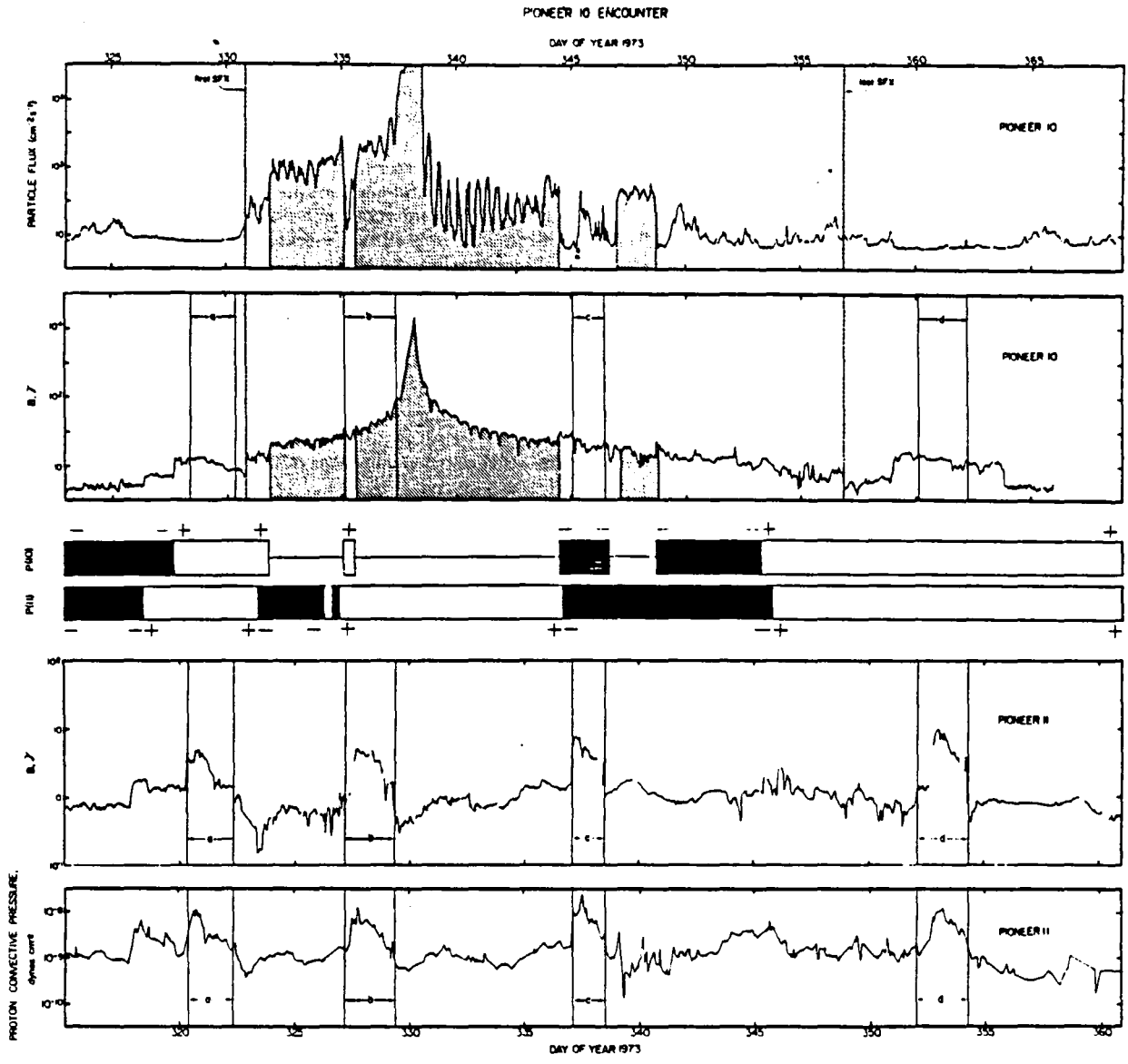

Fig. 2. Planetary and interplanetary observations during the Pioneer 10 encounter. The upper three panels contain the Pioneer 10 energetic particle flux, magnetic field magnitude, and interplanetary field polarity. The three lower panels contain Pioneer 11 observations of the magnetic field polarity and magnitude and the solar wind pressure. Details associated with the figure are described in the text.

comments made above regarding the energetic electrons also apply to the Pioneer 11 encounter: high count rates inside the magnetosphere rising to a large peak near periapsis, a periodicity associated with the rotation of Jupiter, and bursts of magnetospheric electrons in the magnetosheath and interplanetary space.

The magnetic field data show the arrival of a CIR (designated *e*) in the interval prior to encounter (days 320–328). This interaction region contained a sector boundary that was seen both at Pioneer 11 near Jupiter and at Pioneer 10. Elsewhere in interplanetary space the Pioneer 11 data show a relatively low field magnitude ($<1\ \gamma$) characteristic of quiet intervals.

The magnetic field measurements at Pioneer 10 show that two CIR's were observed in interplanetary space within this 34-day interval. The CIR mentioned above (*e*) was also observed at Pioneer 10. The Pioneer 10 data have been displaced in time by approximately 5 days corresponding to a solar wind speed of 400 km/s. Following a quiet interval of only 2 days a second interaction region (*f*) was observed at Pioneer 10. This interaction region would have arrived at Jupiter at about day 330.

The convected solar wind pressure again shows a good correlation with the field magnitude. Two distinct increases from the background level of $P_c \simeq 10^{-10}$ dyn/cm² coincide with interaction regions *e* and *f* in the field data. The Pioneer 10 interval from days 343 to 353 is devoid of activity and appears to be a prolonged quiet region.

The second CIR (*f*) visible in the Pioneer 10 data coincides nicely with the apparent compression of Jupiter's magnetosphere as recorded in the Pioneer 11 data (the CIR is corre-

lated with the white column). During this 2.5-day interval, Pioneer 11 exited from the magnetosphere into the magnetosheath, was crossed by the bow shock to reenter interplanetary space, and then recrossed the shock and passed through the magnetosheath back into the magnetosphere.

Additional support for the interpretation that the compression coincides with the CIR is provided by the relatively large field magnitude in interplanetary space between the second and the third bow shock crossing, which can be seen to be comparable to the large field magnitudes within the preceding interaction region (*e*). Furthermore, a sector boundary was observed at Pioneer 10 within the CIR. A sector boundary was also observed at Pioneer 11 during the relatively short interval when the spacecraft was in interplanetary space. As Figure 3 shows, the time delay between the arrivals of the sector boundary at Pioneer 11 and Pioneer 10 strongly suggests that the same feature was being observed at both locations.

On the other hand, a striking feature of the two middle panels in Figure 3 is the absence of a CIR corresponding to the interval when Pioneer 11 reentered the magnetosheath outbound on day 340 (the second white column inside the hatching). There is no evidence for a CIR at Pioneer 10 in either the field or the plasma data. This observation is in contrast to the two encounter intervals in Pioneer 10 and the inbound Pioneer 11 interval, which were all correlated with the presence of a CIR in the immediate vicinity of Jupiter. It is interesting to note that the two Pioneer 10 compressions and the inbound Pioneer 11 compression are correlated with sector boundaries (−+, +−, and +−, respectively) and that no sector boundary is associated with this anomalous Pioneer 11 magnetopause crossing.

DISCUSSION

Variations in Magnetopause Location

The principal outcome of this study has been that three out of four cases in which the Pioneers reentered the magnetosheath were the result of time variations associated with changing interplanetary conditions. The Pioneer 10 reentries inbound and outbound and the Pioneer 11 entry inbound all occurred when high-speed solar wind streams and their associated interaction regions were expected to arrive at Jupiter. Thus in three fourths of the possible cases under consideration the evidence is clearly opposed to the hypothesis that the Pioneers had encountered unusual spatial regions inside the magnetosphere. This study also supports the previous assertion that the Jovian magnetosphere is much more compressible than the terrestrial magnetosphere.

The absence of any evidence that the fourth Pioneer 11 outbound reentry was correlated with changing solar wind conditions prompted us to reconsider these data very carefully. We seriously considered the possibility that Pioneer 11 had traversed a region interior to the magnetosphere and reexamined the available data to determine whether or not the magnetopause was crossed twice and whether the intervening region was actually the magnetosheath. Fortunately, the Pioneer data produced seven other bona fide magnetopause crossings on the dayside and six other examples of data acquired inside the Jovian magnetosheath. We carefully compared the Pioneer 11 data outbound (Figure 4) with these earlier examples.

There is very little doubt that on this occasion also, Pioneer 11 did penetrate the magnetopause, spend time in the magnetosheath, and then reenter the magnetosphere. Both of the magnetopause crossings appear typical in every respect. The field on the innerside of the crossing is principally southward. There is an abrupt decrease in field strength from inside to outside, and the direction of the normal to the discontinuity is consistent with the direction expected for the magnetopause normal. The data in the intervening interval between the two crossings have the polarity and the direction anticipated for an interplanetary field that is draped around the magnetosphere. Finally, one of the strongest pieces of evidence favoring reentry into the magnetosheath is provided by the observation in this interval of the large-amplitude compressional pulses that have been found to be a characteristic feature of the Jovian magnetosheath [*Smith et al.*, 1975]. As a corollary, we conclude that this set of observations cannot be considered to be representative of some region interior to the magnetosphere.

In view of the foregoing, the question which we considered next was: Why, in this instance, did Pioneer 11 cross the magnetopause so close to Jupiter?

One possibility is that the solar wind stream or interaction region was actually in the vicinity of Jupiter but was missing from the 'simultaneous' solar wind data at Pioneer 10. In support of this hypothesis it should be recognized that the geometries of the Pioneer 10–Pioneer 11 match-ups were significantly different for the two encounters (see Figure 1). At the time of the Pioneer 10 encounter the two spacecraft were nearly radially aligned, a condition that is very favorable for comparing observations separated by the relatively large distance of ≃2 AU. The only correction that needed to be made was a time delay associated with the radial propagation of the solar wind from Pioneer 11 to Pioneer 10. The situation was more complicated during the Pioneer 11 encounter, for which the largest part of the delay was associated with the difference in the heliographic longitude of the two spacecraft. In particular, it is difficult to exclude the possibility of significant time variations at the solar source during the interval that it rotated from the longitude of Pioneer 11 and Jupiter to the longitude of Pioneer 10.

Although this hypothesis cannot be completely ruled out, it is rendered rather unlikely by the observation of numerous interaction regions at both spacecraft, both before and after the Pioneer 11 encounter. In general, the 2- or 3-year interval encompassing the Pioneer 11 encounter was one in which the interplanetary conditions were dominated by a few very stable solar wind streams which reoccurred for many successive solar rotations.

Another possibility is that the Pioneer 11 crossing was the result of large-scale motions intrinsic to the Jovian magnetosphere. It has been suggested, for instance, that the disclike character of the magnetosphere might lead to fluting motions or to an up and down flapping of the magnetosphere [e.g., *Hill et al.*, 1974]. Since the Pioneer encounters, it has been recognized that the magnetodisc concept applies to the shape of the field lines and trapped radiation contours inside the magnetosphere near the equatorial plane and not to the shape of the magnetosphere as a whole. Nevertheless, the possibility exists that a systematic motion of the magnetodisc might be communicated to the rest of the magnetosphere causing it also to oscillate up and down.

Evidence that the two innermost magnetopause crossings seen outbound on Pioneer 11 might be associated with an intrinsic magnetospheric motion is provided by the intervals at which they occurred. The times of the three successive magnetopause crossings are 0850 and 1830 on day 340 and 0130 on day 342. It is seen that the interval from the first to the second crossing is approximately 10 hours, the rotation period of

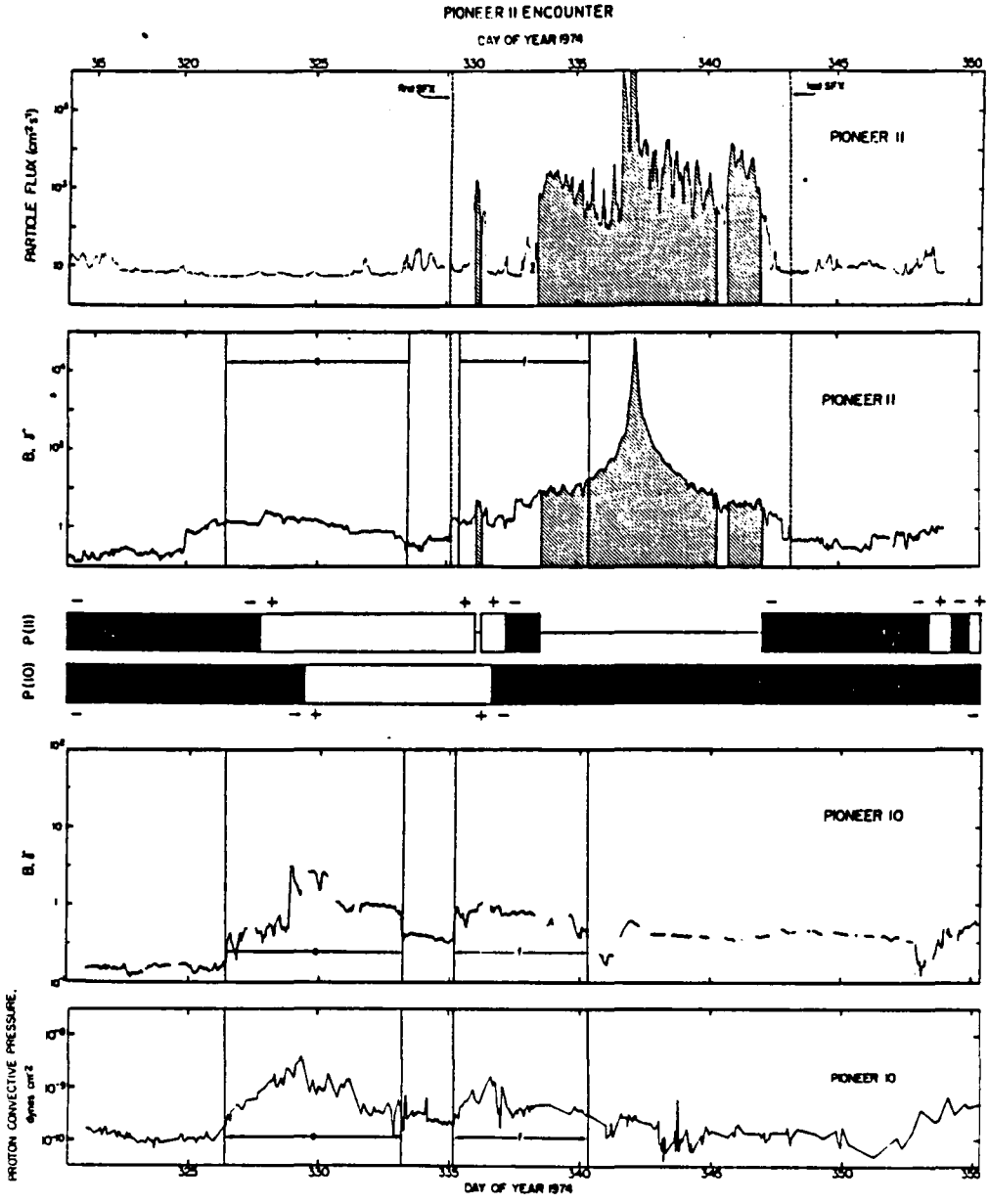

Fig. 3. Planetary and interplanetary observations during the Pioneer 11 encounter. The format is the same as that in Figure 2. The text contains a description of the details.

Jupiter, and that the interval from the second to the third crossing is 32 hours, which is also nearly a multiple of 10.

Prior to the first outbound magnetopause crossing, a definite periodicity of 10 hours is evident in both the field and the energetic particle data. In particular, the behavior of the magnetic field direction is consistent with the changing magnetic latitude of the spacecraft that would be expected as Jupiter's magnetic dipole rotated. It should be recalled that the outbound Pioneer 11 pass was at a relatively high Jovigraphic latitude of 32° in contrast to the other three Pioneer passes, which were all nearly equatorial. If the 10° tilt of the dipole is taken into account, the magnetic latitude of the spacecraft would be expected to vary between 22° and 42° with a period of 10 hours.

It is interesting and suggestive that the first magnetopause crossing occurred when Pioneer 11 was expected to be at its highest latitude. However, some hours before the crossing the direction of the field was much more southward than it had been observed to be previously even when Pioneer was at its lowest magnetic latitude. The spacecraft also reentered the magnetosphere again when it was expected to be at a high, rather than a low, latitude.

This pattern is as though the magnetosphere had first been deflected northward and then, when the spacecraft was north, was deflected southward, the southward deflection causing Pioneer to exit from the magnetosphere. The reentry could have been the consequence of the recovery of the magnetosphere toward its neutral position during the next northward

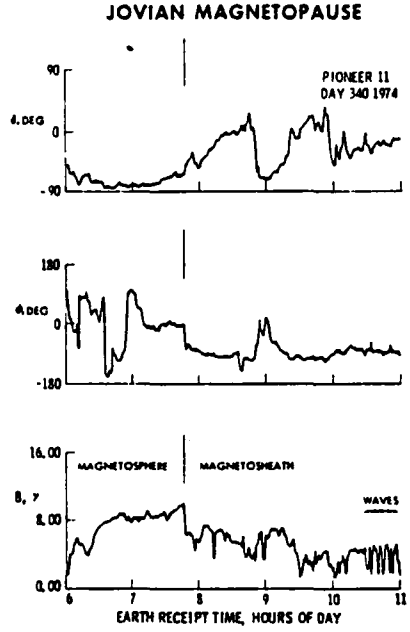

Fig. 4. Magnetic measurements in the vicinity of the magnetopause. The field magnitude (B), longitude (ϕ), and latitude (δ) are shown near the first of two magnetopause crossings as Pioneer 11 was outbound along the postencounter trajectory. The coordinate system in which the data are displayed has one axis (X) directed toward the sun and an orthogonal axis (Z) lying in the plane formed by X and the rotation axis of Jupiter and pointing northward. The third axis (Y) completes the orthogonal, right-handed system. Vertical lines show the magnetopause location as identified in both the plasma and the magnetic field data.

cycle. If the magnetosphere were then to be deflected northward for essentially two successive rotations, the spacecraft would not have been able to leave the magnetosphere even at its highest magnetic latitude. Another deflection of the magnetosphere southward in the next interval could then account for the third penetration of the magnetosphere. By the time the magnetosphere would have been deflected northward again, the radial distance of the Pioneer would have reached 100 R_J, and the spacecraft would have permanently escaped the magnetosphere.

Thus by invoking an asynchronism between two sinusoidal motions, one associated with the period of rotation of Jupiter and the other with a longer period associated with a north-south deflection of the magnetosphere, it appears possible to account for the observed pattern of the magnetopause crossings.

Although the above hypothesis is not well established, it merits serious consideration. It is a plausible explanation that is qualitatively consistent with the apparent periodicity of the magnetopause crossings. The latter we consider to be good evidence that a temporal variation of some sort intrinsic to the Jovian magnetosphere is responsible for the anomalous magnetosheath observations in the outbound Pioneer 11 data.

Although we are thus able to account for all four anomalous magnetosheath reentries in terms of time variations, this result does not necessarily imply that the outflow model, with its distinct spatial regions, is definitely ruled out. Recently, *Coroniti and Kennel* [1977] proposed a scenario that combines an outflow model with time variations of the kind being considered here and that places the two spacecraft at precisely the improper locations to observe outflow effects. Their hypothesis is that outflow was occurring when the magnetosphere was most distended, e.g., when Pioneer 10 was inbound after the first magnetopause crossing. It is further proposed that the spacecraft would have entered the outflow region nearer to Jupiter but that before that could happen the enhanced solar wind pressure reduced the size of the magnetosphere and temporarily stopped the outflow. The magnetosphere was in this latter state when the spacecraft passed through it and proceeded into periapsis. This sequence would have to be repeated outbound on Pioneer 10 and inbound on Pioneer 11. In fairness to the model, however, it is not necessary to appeal to this sequence of happenings to explain the lack of observation of a distinctive outflow region on Pioneer 11 outbound. Presumably, the outflow occurs predominately near the equatorial region and may be absent at higher latitudes. The Coroniti and Kennel suggestion appears to be a plausible hypothesis that cannot be ruled out on the basis of the available data.

Pressure Balance at the Magnetopause

It having been established that the changes in the solar wind pressure alter the location of the magnetopause, it is possible to study the following question: Is the magnetic field strength just inside the magnetopause sufficient to withstand the incident pressure of the solar wind? A related issue is whether or not additional pressure associated with magnetospheric plasma is required to hold off the solar wind. This question has been investigated in earlier studies of specific magnetopause crossings [*Wolfe et al.*, 1974*b*; *Intriligator and Wolfe*, 1976]. However, the observation of a massive shift in the position of the magnetopause coincident with the large increase in the solar wind pressure makes it possible to reconsider this question. The answer is likely to have important implications for the nature of the Jovian magnetosphere under quiet and disturbed interplanetary conditions.

An accurate assessment of the pressure balance across the magnetopause must include the effect on the solar wind as it passes through the bow shock and the location at which the observations were made with respect to the Jupiter-sun direction. If one ignores these important factors, it might be concluded that the magnetic pressure is inadequate to withstand the solar wind. For example, the convected pressure of the solar wind at Jupiter during quiet conditions, based solely on an r^{-2} decrease in density, is $P_c \simeq 5 \times 10^{-10}$ dyn/cm^2. The equivalent magnetic pressure $B^2/8\pi$ implies $B = 12$ γ, whereas the field just inside the magnetopause at 100 R_J is typically 5 γ, a factor which is 2.4 times too small in field strength and 6 times too small in pressure. It must be recognized, however, that the shocked solar wind exerts a pressure on the magnetosphere that is less than the convective pressure of the solar wind in interplanetary space. Passage through the shock may lead to a modest decrease in convective pressure, and more important, it leads to a substantial deflection of the flow around the magnetosphere, so that the plasma is not generally incident on the magnetopause from the normal direction. Both the Pioneer 10 and the Pioneer 11 data showed a large deflection of the solar wind flow in the magnetosheath. It is therefore necessary to use some means to estimate the pressure exerted inward at the point of observation which, in the case of the two inbound Pioneer passes, was at an angle ψ with respect to the sun-Jupiter direction of 45°.

We have adopted an approach based on scaling the magnetic field pressure observed at the corresponding point of observation just inside the terrestrial magnetopause. The

earth's magnetosphere can be considered to be the prototype of a model in which magnetic field pressure compensates the solar wind pressure. At a sun-earth observation angle of ψ = 45° a typical observed value at the magnetopause during quiet intervals is 35 γ [*Mead and Fairfield*, 1975]. This value may be compared with the corresponding field strength at the nose of the magnetopause (ψ = 0) of 55 γ.

In support of the comment made in the paragraph above, it may be noted that a 55-γ field is equivalent to a magnetic pressure of 120×10^{-10} dyn/cm², which may be compared with a quiet solar wind pressure at 1 AU of $P_e = 5 \times 2 \times 10^{-24} \times (3.6 \times 10^7)^2 = 130 \times 10^{-10}$ dyn/cm². Thus at the earth the magnetic pressure at ψ = 45° is 2.5 times smaller than the pressure of the unshocked solar wind at perpendicular incidence at the subsolar point.

The measured solar wind pressures at Pioneer 11 and Pioneer 10, when they are extrapolated to Jupiter, yield values of $10 \times 10^{-10}/(5/2.9)^2 = 3.4 \times 10^{-10}$ and $10^{-10}/(5/6.2)^2 = 1.5 \times 10^{-10}$ dyn/cm², respectively. If, as is expected, the pressure within quiet regions falls off faster than r^{-2}, the Pioneer 11 value will tend to be too high, and the Pioneer 10 value will tend to be too low. It therefore seems likely that the quiet pressure at Jupiter was somewhere between 1.5 and 3.4×10^{-10} dyn/cm².

The magnetopause field strength that would be expected at ψ = 45°, $(8\pi P/2.5)^{1/2}$, is then either 3.9 or 5.8 γ, corresponding to the two extrapolated pressures above. This calculated value compares well with the observed value of $\simeq$5 γ, especially if, as was noted above, the actual pressure is intermediate to the two extrapolated pressures. This result can be taken to imply that negligible pressure must be supplied by magnetospheric plasma or that β, the ratio of the plasma to magnetic pressure, was much less than 1. Therefore the magnetic field strength at the Jovian magnetopause is sufficient to balance the pressure of the magnetosheath plasma during quiet solar wind conditions.

The same type of calculations may be applied to the Jovian magnetosphere when it is compressed. Figures 2 and 3 suggest that the average value of the pressure associated with the interaction regions is increased over quiet values by a factor of $\simeq$6. If the shape of the magnetosphere is assumed to be unchanged by compression, the magnetopause field at ψ = 45° would then be expected to be $5 \times (6)^{1/2} = 12$ γ. This value is reasonably close to the values of 15 and 17 γ that were observed when the magnetosphere was compressed to 54 and 47 R_J, respectively. Thus in this instance also there appears to be very little doubt that the interior field was able to balance the pressure of the shocked solar wind. In the above calculations we have ignored the pressure exerted by the magnetic field and the high-temperature plasma external to the magnetopause. The observed changes in field magnitude across the Jovian magnetopause show this to be a reasonable assumption.

It is interesting to note that when the magnetosphere is at its greatest extent, most of the field inside the magnetopause must be derived not from the planetary field but from currents within the magnetosphere. The dipole field at 100 R_J is only 0.4 γ, and if the field just inside the magnetopause is approximately double its value in the absence of confinement, the most it could contribute to the observed field of 5 γ would be 1 γ. A likely source of the major component of the field inside the magnetopause is the equatorial current sheet that is a characteristic feature of the middle magnetosphere.

When the magnetosphere is compressed, the contribution of the dipole field to the field at the magnetopause becomes increasingly significant. Thus near 50 R_J the strength of the dipole field is 3.2 γ, which confinement will increase to 6.4 γ. Thus the dipole field now contributes over 40% of the total field.

A comparison of the magnetopause field strengths at the various locations (48, 54, 65, 95, 96, and 97 R_J) shows that the field magnitude varies with radial distance approximately as $r^{-1.6}$. This dependence, which is approximately r^{-2} and suggests that a relatively constant amount of magnetic flux is being compressed, helps explain why the Jovian magnetosphere is compressed more readily than the earth's magnetosphere. Thus an increase in the solar wind pressure by a factor of 6 will cause the Jovian magnetopause to move inward by a factor of 1.64, e.g., from 100 to 61 R_J. Since a dipole field varies as r^{-3}, the radial distance to the terrestrial magnetopause varies as $P_r^{1/6}$. Thus the terrestrial magnetosphere under the same circumstances would be compressed by a lesser factor of 1.35, e.g., from 10 to 7.4 R_E. Alternatively, the pressure ratio needed to decrease the size of the magnetosphere by a factor of 2 at Jupiter is 12, while at the earth the ratio is 64. The compressibility of the Jovian magnetosphere may also be enhanced if the current sheet that is responsible for the dominant part of the field just inside the magnetopause is interrupted or reduced as the magnetosphere is compressed.

Acceleration of Energetic Trapped Radiation

During the two Pioneer 10 events the spacecraft was deep enough within the magnetosphere to observe effects on trapped particles. As can be seen in Figures 2 and 3, there was an enhancement of particle intensity preceding the appearance of the magnetosheath at the spacecraft. In both cases the enhancements appear out of context with the surrounding data, and they are almost certainly caused by the compression. Such an increase in intensity could only arise in two ways. Either particles were accelerated during the compression or else a region of higher particle intensity was transported to the spacecraft. The latter is not probable because under normal conditions, intensities this high were only found closer to the planet. On the other hand, acceleration seems likely during such a compression event.

The electric fields that accelerated the particles could be local or nonlocal, curl-free or solenoidal. Comparison of the particle intensities with magnetic field values at higher resolution reveals that the time profiles do not match. Therefore we can discount gyrobetatron acceleration driven by the local solenoidal field. Of the remaining possibilities, drift betatron effects or acceleration by curl-free electric fields, there is no way to distinguish between the many possible models [e.g., *Carbary et al.*, 1976].

A great deal of energy is released by the compression—more than enough to produce the observed particle acceleration. In pushing the magnetopause 40 R_J inward the solar wind does as much as 10^{20} J of work. For example, consider the work w done by pressure p in compressing a hemispherical volume of radius r. If it is assumed that the radial pressure of the shocked solar wind p_0 varies as $\cos^2\psi$, then

$$w = \int_0^{\pi/2} \int_0^{2\pi} \int_{r_1}^{r_2} r^2 p_0 \cos^2\psi \sin\psi \, d\psi \, d\phi \, dr = 2\pi p_0 (r_2^3 - r_1^3)/9$$

For values of $p_0 = 20 \times 10^{-10}$ dyn/cm², $r_1 = 60$ R_J, and $r_2 = 100$ R_J, $w \simeq 10^{20}$ J. Since the outer magnetosphere contains about 10^{17} J above the threshold of the detector used, Figures 2 and 3

show that the observed particle acceleration is not even the main energy receptor during these events.

The Plasma Density From the Response Time of Jupiter's Magnetosphere

It is significant to note that the particle acceleration precedes the arrival of the magnetopause at the spacecraft by approximately 5 hours in the inbound case and 15 hours in the outbound case. The unimpeded solar wind would cover a distance of 40 R_J in only about 2 hours. Thus the measured time difference is determined by the properties of the magnetosphere. Indeed, one can make a guess at the plasma density on the basis of this time lag. It may be that the energetic particles, which drift and mirror rapidly and which sample a large volume of the magnetosphere, are able to respond quickly to changes in magnetospheric topology. If the jump in particle intensity marks the start of the compression and the speed of motion of the magnetopause is assumed to be of the order of the hydromagnetic wave velocity V_A, internal to the magnetosphere, then $\tau = \int dr/V_A = (\mu_0 Mn)^{1/2} \int dr/B$. We take the integrand to be constant with $B \approx 10\,\gamma$. Then $n \approx 0.6\,\mathrm{cm}^{-3}$ (inbound) and $\sim 6\,\mathrm{cm}^{-3}$ (outbound), corresponding to $V_A \simeq 150$ and ≈ 50 km/s, respectively. These densities are of the same order of magnitude ($1\,\mathrm{cm}^{-3}$) as that inferred by *Smith et al.* [1974*b*] from the density of the magnetodisc current and also of the same order ($4\,\mathrm{cm}^{-3}$) as that inferred by *Eviatar and Ershkovich* [1976] from estimates of the hydromagnetic wave velocity based on diurnal magnetic field variation. Although all of these indirect methods are questionable, it is noteworthy that they lead to results that are in reasonable agreement.

Time Constants of Magnetospheric Circuit Models

To pursue these deductions further, we can estimate the time constants of electrical circuits on the scale of Jupiter's magnetosphere. The current systems in the magnetopause and the equatorial plane have large inductances which must contribute to the time constant. It is hard to guess the circuit parameters of the magnetopause system, but we know a good deal about the equatorial ring current. The linear current density is typically $K = 2 \times 10^{-2}$ A/m or 1.5×10^{9} A/R_J. Then the total current I is $\simeq 10^{6}(r_o - r_i)$, where r_o and r_i are the outer and inner radii of the current sheet. When the magnetosphere is distended to 100 R_J, the current sheet extends from about 30 to 80 R_J, so that $I \simeq 5 \times 10^{7}$ A. A circular loop carrying this current and located at a mean distance of 55 R_J would roughly correspond to an inductance of $L \simeq \mu_0 r \simeq 5 \times 10^{3}$ H.

An alternative estimate of inductance is provided by considering the magnetic flux Φ linking the distributed current disc. The magnetic field interior to a flat current disc, obtained from the Biot-Savart law, is $B = (\mu_0 K/2) \ln (r_o/r_i)$. For the above parameters this equation implies $B = 4\pi \times 10^{-7} \times 10^{-2} \ln (8/3) \simeq 10\,\gamma = 10^{-8}$ Wb/m^2. The flux interior to the current is then $\Phi = 10^{-8} \times \pi \times (30 \times 7.3 \times 10^{7})^2 \simeq 1.5 \times 10^{11}$ Wb, and the inductance $L = \Phi/I = 3 \times 10^{3}$ H. If the current is interrupted by the compression, the energy associated with it ($LI^2/2 = 10^{19}$ J) must be dissipated or displaced.

Since the plasma-filled space of the magnetosphere has a high dielectric coefficient, large capacitances are possible too. In general, capacitance can be evaluated by the formula $C = \eta \varepsilon_0 G$, where η is the dielectric constant and G is a purely geometric term with the dimension of length. For instance, $G = A/s$ for parallel plates, where A is the area and s is the separation, and for concentric spheres, $G = 4\pi[ab/(b - a)]$, where b and a are the outer and inner radii. Without knowing the geometry we are dealing with, we may nevertheless estimate a lower limit for G based on the scale of the Jovian magnetosphere. Using the formula for a concentric spherical capacitor, take the inner plate to be the planetary surface and the outer plate to be at the magnetopause. Then $G \approx 4\pi R_J \approx 10^{8}$ m. This is the minimum reasonable value; it can be lowered only by assuming the inner plate to be below the surface or by supposing that the capacitance is on a local rather than a global scale. The dielectric constant is given by $\eta = (c/V_A)^2$, and for the densities cited above, $\eta \approx 2 \times 10^{6}$ to 2×10^{7}. Then $c \gtrsim 20$–200 kF.

If this capacitance received the energy from the ring current, the charging time would have to be about one half of the resonant period, which is given by $\tau = 2\pi(Lc)^{1/2}$. Our figures then give charging times of 15–50 hours, which are longer than the observed compression times but not unreasonable.

A more complex equivalent circuit is likely. Energy can be transferred by mutual inductance between ring and magnetopause currents or between ring currents in the inner and outer magnetosphere. We would expect the turns ratio to be of the order of unity and the magnetospheric capacitance to interact with the circuit as before, however, so that the time constant would not be altered drastically. Alternatively, if the energy were dissipated, we would require a resistance of about 1 Ω (calculated from $\tau = L/R$). We find that the observed lag can be duplicated by reasonable circuits, but we don't know enough about magnetospheric processes to specify the proper equivalent circuit.

Note added in proof. The interval between magnetopause crossings has also been noticed by *Dessler* [1978], who points out that 11 of 14 crossings occurred in the same hemisphere. A model has been developed in which a lopsided outer magnetosphere results from asymmetries in the internal magnetic field [*Dessler and Hill*, 1975].

Acknowledgments. W. Fillius thanks Helmut Rosenbauer for suggesting that the response lag could be explained by hydromagnetic wave propagation and Hannes Alfvén for comments regarding the magnetospheric electrical circuit. Valuable assistance in analyzing the data from the three investigations was provided by Elaine Parker and Emilie Karspeck of the Jet Propulsion Laboratory. This report represents one aspect of research done by the Jet Propulsion Laboratory for NASA under contract NAS 7-100. The research carried out at the University of California at San Diego was supported in part by NASA contract NAS 2-6552.

The Editor thanks D. B. Beard and another referee for their assistance in evaluating this paper.

REFERENCES

Cahill, L. J., Jr., and T. L. Skillman, Inward movement of the magnetopause on August 4, 1972 (abstract), *Eos Trans. AGU*, *54*, 433, 1973.

Carbary, J. F., T. W. Hill, and A. J. Dessler, Planetary spin period acceleration of particles in the Jovian magnetosphere, *J. Geophys. Res.*, *81*, 5189, 1976.

Chenette, D., T. F. Conlon, and J. A. Simpson, Bursts of relativistic electrons from Jupiter observed in interplanetary space with the time variation of the planetary rotation period, *J. Geophys. Res.*, *79*, 3551, 1974.

Coroniti, F. V., and C. F. Kennel, Possible origins of time variability in Jupiter's outer magnetosphere, 1, Variations in solar wind dynamic pressure, *Geophys. Res. Lett.*, *4*, 211, 1977.

Dessler, A. J., Longitudinal control of Jovian magnetosphere motion, *Geophys. Res. Lett.*, *5*, 65, 1978.

Dessler, A. J., and T. W. Hill, High order magnetic multipoles as a source of gross asymmetry in the distant Jovian magnetosphere, *Geophys. Res. Lett.*, *2*, 567, 1975.

Eviatar, A., and A. I. Ershkovich, Plasma density in the outer Jovian magnetosphere, *J. Geophys. Res.*, *81*, 4027, 1976.

Fillius, R. W., and C. E. McIlwain, Measurements of the Jovian radiation belts, *J. Geophys. Res.*, *79*, 3589, 1974.

Hill, T. W., A. J. Dessler, and F. C. Michel, Configuration of the Jovian magnetosphere, *Geophys. Res. Lett.*, *1*, 3, 1974.

Intriligator, D. S., and J. H. Wolfe, Results of the plasma analyzer experiments on Pioneers 10 and 11, in *Jupiter*, edited by T. Gehrels, p. 848, University of Arizona Press, Tucson, 1976.

Kennel, C. F., and F. V. Coroniti, Is Jupiter's magnetosphere like a pulsar's or earth's?, *Space Sci. Rev.*, *17*, 857, 1975.

Mead, G. D., and D. H. Fairfield, A quantitative magnetospheric model derived from spacecraft magnetometer data, *J. Geophys. Res.*, *80*, 523, 1975.

Michel, F. C., and P. A. Sturrock, Centrifugal instability of the Jovian magnetosphere and its interaction with the solar wind, *Planet. Space Sci.*, *22*, 1501, 1974.

Mihalov, J. D., H. R. Collard, D. D. McKibbin, J. H. Wolfe, and D. S. Intriligator, Pioneer 11 encounter: Preliminary results from Ames Research Center plasma analyzer experiment, *Science*, *188*, 448, 1975.

Opp, A. G., Penetration of the magnetopause beyond 6.6 R_E during the magnetic storm of January 13–14, 1967: Introduction, *J. Geophys. Res.*, *73*, 5697, 1968.

Parker, E. N., *Interplanetary Dynamical Processes*, Interscience, New York, 1963.

Smith, E. J., and J. H. Wolfe, Observations of interaction regions and corotating shocks between one and five AU: Pioneers 10 and 11, *Geophys. Res. Lett.*, *3*, 137, 1976.

Smith, E. J., and J. H. Wolfe, Pioneer 10, 11 observations of evolving solar wind streams and shocks beyond 1 AU, in *Study of Travelling Interplanetary Phenomena*, edited by M. A. Shea, D. F. Smart, and S. T. Wu, p. 227, D. Reidel, Hingham, Mass., 1977.

Smith, E. J., L. Davis, Jr., D. E. Jones, D. S. Colburn, P. J. Coleman, Jr., P. Dyal, and C. P. Sonett, Magnetic field of Jupiter and its interaction with the solar wind, *Science*, *183*, 305, 1974*a*.

Smith, E. J., L. Davis, Jr., D. E. Jones, P. J. Coleman, Jr., D. S. Colburn, P. Dyal, C. P. Sonett, and A. M. A. Frandsen, The planetary magnetic field and magnetosphere of Jupiter: Pioneer 10, *J. Geophys. Res.*, *79*, 3501, 1974*b*.

Smith, E. J., L. Davis, Jr., D. E. Jones, P. J. Coleman, Jr., D. S. Colburn, P. Dyal, and C. P. Sonett, Jupiter's magnetic field, magnetosphere and interaction with the solar wind: Pioneer 11, *Science*, *188*, 451, 1975.

Smith, E. J., L. Davis, Jr., and D. E. Jones, Jupiter's magnetic field and magnetosphere, in *Jupiter*, edited by T. Gehrels, p. 788, University of Arizona Press, Tucson, 1976.

Teegarden, B. J., F. B. McDonald, J. H. Trainor, W. R. Webber, and E. C. Roelof, Interplanetary MeV electrons of Jovian origin, *J. Geophys. Res.*, *79*, 3615, 1974.

Wolfe, J. H., H. R. Collard, J. D. Mihalov, and D. S. Intriligator, Preliminary Pioneer 10 encounter results from the Ames Research Center plasma analyzer experiment, *Science*, *183*, 303, 1974*a*.

Wolfe, J. H., J. D. Mihalov, H. R. Collard, D. S. Intriligator, D. D. McKibbin, and L. A. Frank, Pioneer 10 observations of the solar wind interaction with Jupiter, *J. Geophys. Res.*, *79*, 3489, 1974*b*.

(Received December 28, 1977;
revised April 25, 1978;
accepted April 25, 1978.)

JOURNAL OF GEOPHYSICAL RESEARCH, VOL. 86, NO. A8, PAGES 6773–6780, AUGUST 1, 1981

Compression of Jupiter's Magnetosphere by the Solar Wind: Reexamination via MHD Simulation of Evolving Corotating Interaction Regions

Z. K. SMITH AND M. DRYER

Space Environment Laboratory, NOAA/ERL, Boulder, Colorado 80303

R. W. FILLIUS

Department of Physics, University of California at San Diego, La Jolla, California 92093

E. J. SMITH

Jet Propulsion Laboratory, California Institute of Technology, Pasadena, California 91109

J. H. WOLFE

Ames Research Center, NASA, Moffett Field, California 94035

We examine the major changes in the solar wind before, during, and after the Pioneer 10 and 11 encounters with the Jovian magnetosphere during 1973 and 1974, respectively. In an earlier study, Smith et al. (1978) concluded that the Jovian magnetosphere was subjected to large-scale compression during at least three of four intervals during which it appeared that the spacecraft had reentered the solar wind or magnetosheath near 50 R_J after having first entered the magnetosphere near 100 R_J. They based this suggestion on the observations of the sister spacecraft, which indicated—on the basis of a kinematic translation of corotating interaction regions (CIR's)—that these structures would be expected to arrive at Jupiter at the appropriate beginning of these three intervals. Our reexamination of this suggestion involved the numerical simulation of the multiple CIR evolutions from one spacecraft to the sister spacecraft. This approach, considered to be a major improvement, confirms the suggestion by Smith et al. (1978) that Jupiter's magnetosphere was compressed by interplanetary CIR's during three out of four of these events. Our MHD simulation also suggests that Jupiter's magnetosphere reacts to solar wind rarefactions in the opposite way—by expanding. A previously unexplained pair of magnetopause crossings on the Pioneer 11 outbound pass may simply be due to a delayed reexpansion of Jupiter's magnetosphere from a compression that occurred during the inbound pass.

INTRODUCTION

The question of the compression of Jupiter's magnetosphere by nearly a factor of 2 during the Pioneer 10 and Pioneer 11 encounters in late 1973 and 1974, respectively, has been examined by *Smith et al.* [1978]. These authors examined simultaneous sets of encounter data acquired by the Jet Propulsion Laboratory vector helium magnetometer, the NASA Ames Research Center plasma analyzer, and the University of California (San Diego) trapped radiation detector. These data, acquired before, during, and after the Jupiter encounter, were compared with the plasma and magnetic field data acquired simultaneously in interplanetary space by the sister spacecraft. A time delay based on the radial and (small) longitudinal separation was introduced to allow the solar wind that reached one spacecraft to arrive at the other. The interplanetary data were then kinematically translated to the observations in the neighborhood of Jupiter. A similar approach was used by *Bridge et al.* [1979] during the Voyager 1 flyby in early 1979. These authors also observed the dependency of magnetopause and bow shock motion on solar wind pressure as projected from Voyager 2, which was ~ 0.5 AU in the sunward direction from Jupiter. Also, *Siscoe et al.* [1980] compared the Voyager 2 bow shock crossings with those of Voyager 1.

Of particular interest in the Pioneer flyby data were four intervals during which it appeared that the spacecraft had reentered the magnetosheath near 50 R_J (where R_J is Jovian radius) after having first entered the magnetosphere near 100 R_J, as discussed earlier by *Wolfe et al.* [1974*a*, *b*], *Smith et al.* [1974, 1975] and *Mihalov et al.* [1975]. Earlier, the observations had been interpreted as a large-scale compression of the Jovian magnetosphere, presumably caused by pressure pulses in the solar wind. An alternative hypothesis was that the observations represented a spatial variation within the magnetosphere. This hypothesis [*Dessler and Vasyliunas*, 1979; *Michel and Sturrock*, 1974; *Hill et al.*, 1974; *Kennel and Coroniti*, 1975], and a combined temporal solar wind/spatial magnetospheric distortion caused by plasma outflow, suggested by *Coroniti and Kennel* [1977], asserts that regions exist inside the magnetosphere within which centrifugal forces (associated with Jupiter's large size and rapid rotation) overwhelm the restraining effect of the planetary magnetic field. The result is the production of internal outward convective flows, and possibly even some form of internal shock. A similar model (but without the intrinsic magnetic field) has been proposed for solar wind interaction with comets by *Wallis and Dryer* [1976].

The four intervals of time during which the spacecraft reentered the magnetosheath, as mentioned above, were notable by the observation of a precipitous drop-off of the energetic particle count rates to near-interplanetary values, followed some time later (hours) by a return to the characteristic high count rates [*Fillius and McIlwain*, 1974] inside the magnet-

Paper number 1A0681.
0148-0227/81/001A-0681$01.00

osphere. These particle data, presented by *Smith et al.* [1978], are from channel C1 of the UCSD Cerenkov counter. This detector responds mainly to cosmic ray nucleons with energies > 500 MeV in interplanetary space. On the other hand, its response within the magnetosphere is dominated by electrons with energies greater than 6 MeV. The count rates are substantially larger inside than outside the magnetosphere, rising near periapsis to very high values. The principal outcome of the study by *Smith et al.* [1978] was that in three of the four cases of precipitous drop-off in energetic particle flux (from $\sim 10^3$ to ~ 10 $cm^{-2}s^{-1}$) reentry into the magnetosheath occurred when high-speed solar wind streams, which are marked by a substantial increase in proton convective pressure, were expected to arrive at Jupiter. Thus their study supported the early hypothosis that the Jovian magnetosphere had undergone large-scale compression.

It is realized, however, that corotating interaction regions (CIRs) evolve as they move outward [c.f., *Smith and Wolfe*, 1976, 1977; *Dryer and Steinolfson*, 1976]; thus the plasma and field characteristics will change somewhat between the flyby spacecraft and its sister spacecraft in the interplanetary medium. Strong, significant evolution was clearly demonstrated by direct comparison of time-dependent MHD numerical simulations with Pioneer 9 and 10 observations during the August 1972 solar flare disturbances [*Dryer et al.*, 1978*a*]. The same theory [*Steinolfson et al.*, 1975*a*, *b*] was used again for a longer time scale (~60 days) by *Dryer et al.* [1978*b*] with a similar conclusion. They examined the evolution of the solar wind observed by Pioneer 11 at ~2.8 AU in 1973 into the well-developed CIRs observed by Pioneer 10 at ~4.9 AU just prior to the latter's first entry into the Jovian bow shock/magnetosphere system. The reader is invited to examine (for example) the detailed evolution of a single CIR from its observation on days 308–317 (1973) by Pioneer 11 at ~2.8 AU to its metamorphosis as observed on days 318–322 (1973) by Pioneer 10 at ~5 AU [*Dryer et al.*, 1978*b*, Figures 5–7]. Downstream, at 5 AU, the CIR was characterized by the classical fast forward and reverse MHD shock waves that bounded a clear interface (or piston) where the total pressure was a maximum; whereas upstream, at ~2.8 AU, the CIR was yet undeveloped. It was characterized by several weak forward, as well as several weak reverse, shocks or high-amplitude nonlinear MHD waves. Also, the interface in the CIR at 2.8 AU was still ill defined among strong magnetic and thermal fluctuations. It was not until the CIR became more fully developed near Jupiter that it started to approach the classical characteristics predicted by similarity theory [*c.f., Dryer*, 1974, 1975] for its structure at asymptotically large distances. We remark, in passing, that comparison of observations, similarity theory, and numerical simulations is still in progress [c.f., *Metzler et al.*, 1979; *Rosenau*, 1979].

It is our intention to use the MHD model to reexamine the original 'large-scale compression' hypothesis that was suggested by the authors noted earlier. We will show that the results, which are found by using a rational and self-consistent fluid theory, support the conclusions of *Smith et al.* [1978] that such compressions did indeed take place at or close to the appropriate time intervals mentioned above. Our MHD technique provides us with a more faithful representation of the variations in the solar wind pressure than we have had before, and these variations are followed in a remarkably detailed way by expansions and contractions of Jupiter's magnetosphere. Furthermore, the quantitative evaluation of the solar wind pressure at Jupiter enables us to estimate the subsolar magnetopause distance as a function of solar wind pressure.

DISCUSSION

Model. We first use the one-dimensional, time-dependent MHD theory described originally by *Steinolfson et al.* [1975*a*] and used by *Dryer et al.* [1978*b*] to simulate the CIRs observed by Pioneers 10 and 11 in 1973 just prior to the first penetration of the Jovian bow shock by the former spacecraft. The procedure, described in detail in this latter paper, can be summarized for the 1973 encounter as follows: (1) Approximately 60 days of observed plasma and magnetic field data at Pioneer 11 are used as an input forcing function for the numerical MHD model. (2) The simulation proceeds timewise into an ambient medium determined by the beginning of the input data. (3) The output at the desired position of Pioneer 10 prior to, during, and following magnetospheric penetration is compared with the Pioneer 10's solar wind data before and after this encounter. During this period in 1973 the radial, heliolongitudinal, and heliolatitudinal separation of the two spacecraft varied between 2.0 to 2.4 AU, 0°–5°, and 1°–½°, respectively, as shown by *Dryer et al.* [1978*b*, Figure 1]. The present study includes a refinement of this earlier one in the sense that the actual, varying spacecraft positions and spacecraft velocities during the 60-day interval are now taken into account; whereas they were previously not included.

The procedure for the 1974 encounter was modified for the first step (1) noted above. During the 35-day period used, the radial, heliolongitudinal, and heliolatitudinal separations were ~1.3 AU, 12.9°, and 1.4°, respectively, as shown by *Smith et al.* [1978, Figure 1]. Solar wind plasma and magnetic field data were available from the innermost spacecraft, Pioneer 11, before and after the Jovian magnetospheric encounter. These data were, of course, used for step (1). During the period of time when solar wind data were unavailable, linear interpolations were assumed between the data points on each side of the data gap. A time delay of 1 day was added to the simulation at 6.2 AU to account for the azimuthal corotation delay, thus allowing a direct comparison to the data.

Results: 1973 Encounter. The Pioneer 11 observations (~2.28 hour averages) of solar wind bulk velocity, density, proton temperature, and azimuthal magnetic field (V, n, T_p, and B_ϕ, respectively) are given in Figure 1 for days 301–361 in 1973. The average spacecraft separation of ~2.2 AU was used in the program. The time scale of the simulation was then corrected for the changes caused by variations in the spacecraft separation. This correction was $\leq \pm 20$ hours. It can be seen, particularly from the time series for n and T_p, that approximately seven CIR's—in various stages of development—were observed by Pioneer 11. These data, as noted above, served as the input forcing function for the MHD model. The simulation was performed for a time sufficient for a useful comparison with the Pioneer 10 solar wind observations downstream, before and after encounter with the Jovian magnetosphere.

Figure 2 shows this comparison at the position of Jupiter. The earlier CIR's, such as those discussed above for days 318–322 (1973), evolved into more mature ones, with well-developed forward and reverse shocks. The theoretical evolution of the seven CIR's, from their ~2.8 AU position to ~5 AU, is clearly seen to be in good agreement (phasing and magnitudes) with the observed CIR's before and after Jupiter encounter by Pioneer 10. The timing of the simulated and ob-

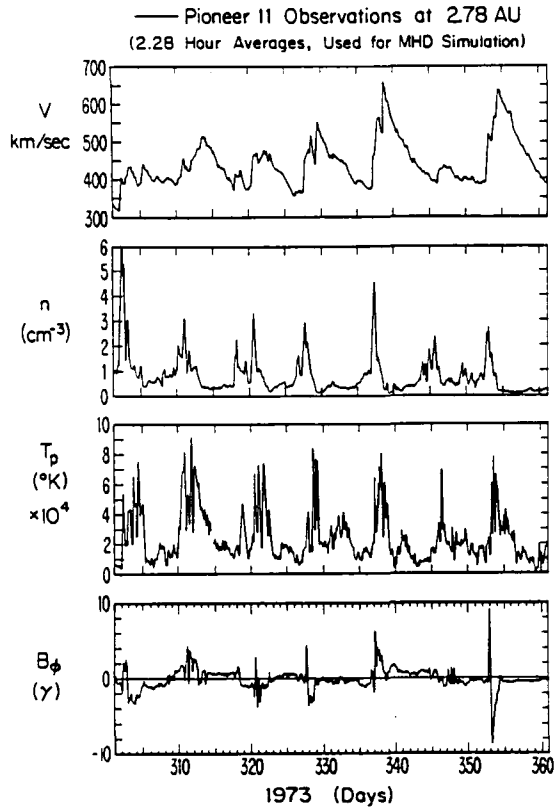

Fig. 1. Pioneer 11 solar wind observations (2.28 hour averages) at ~2.8 AU on days 301–361, 1973.

served pressure pulses, shown in Figure 3, all agree to within 3 hours, except for the first one and a partial one observed as the spacecraft left Jupiter's magnetosphere. Of particular interest to the test of the present hypothesis discussed in the Introduction are the two simulated CIR's that appeared at Jupiter when solar wind data were unavailable for local 'monitoring' purposes. The forward shocks arrived on days 335 (13 hours) and 344 (2 hours), respectively. The ensuing interaction of the interplanetary fast forward MHD shock with the Jovian bow shock-magnetopause system may be described by the theoretical quasistatic system described by *Dryer* [1973] and *Grib et al.* [1979]. It was on these 2 days, days 335 (3 hours) and 344 (12 hours), that the precipitous drop in energetic particle flux took place as described by *Smith et al.* [1978]. The proton dynamic (or convective) pressure is shown for the entire time interval, including the two intervals of particular interest, in Figure 3. The peak magnitudes ($3–5 \times 10^{-9}$ dyn cm^{-2}) indicate a tenfold increase over quiet values. This simulation then provides rather strong support for the suggestion made by those authors that large-scale compression of the Jovian magnetosphere, caused by the dynamic pressure of the two solar wind CIRs, produced a situation wherein Pioneer 10 temporarily found itself in the magnetosheath. That is, the tenfold dynamic pressure increases are sufficient to move the magnetopause from 100 R_J to well past the spacecraft at ~60 R_J, thus leaving the spacecraft outside the magnetosphere for a couple of days.

Figure 4 shows the same data as Figure 3, plotted on a semilogarithmic scale to give us a better look at the lower pressures between interaction regions. In addition to the pressure increases in the CIR's, several rarefactions stand out, trailing CIR's. Of special interest are the narrow rarefaction dips late on days 331 and 346, because they coincide with magnetopause crossings.

The timing of these crossings is visible in Figure 5, which shows the output of a trapped radiation detector superimposed on the same time scale as the simulated solar wind pressure. The detector is channel C1 of the UCSD Cerenkov counter, which responds to electrons of energy $E_e > 6$ Mev. The magnetopause crossings are marked on Figure 5 and listed in Table I, which reproduces information given by *Intriligator and Wolfe* [1976]. Because the magnetosheath was narrower than expected, *Wolfe et al.* [1974a] had speculated that the first inbound crossing, labeled 73MP1, occurred at a time of magnetospheric expansion. The results of our study make this suggestion all the more plausible, as a sudden drop in solar wind pressure was projected for just this time. If the magnetosphere responds to an increase in solar wind pressure by contracting, we can even state that it is obvious that it should respond to a decrease in solar wind pressure by ex-

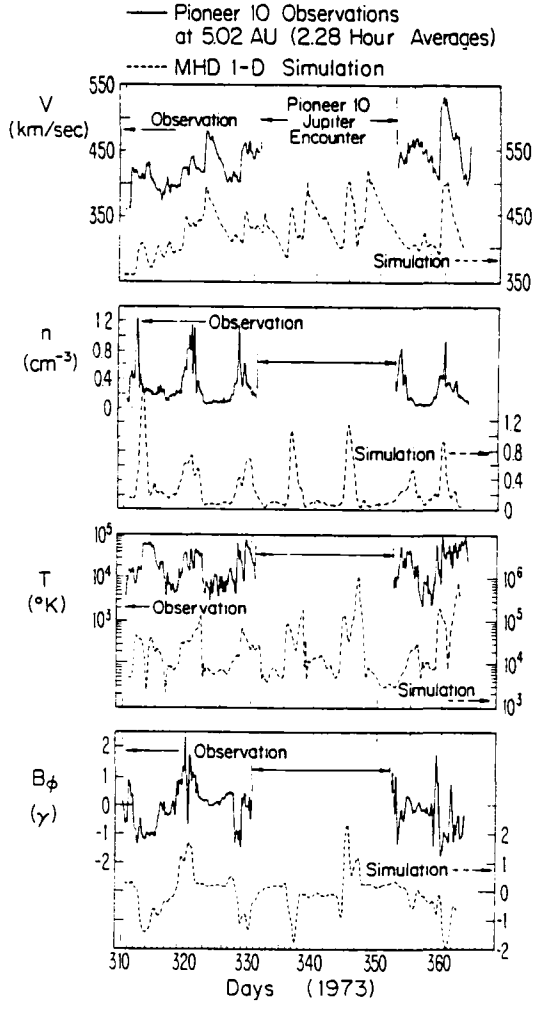

Fig. 2. Comparison of Pioneer 10 solar wind observations (before and after Jupiter encounter) with the MHD simulation on days 310–363, 1973.

TABLE 1. Jovian Magnetopause Crossings by Pioneer 10 (1973) and Pioneer 11 (1974)

Magnetopause Crossing	Day of Year	Distance From Jupiter, R_J	System 3 Longitude (1965), deg
73MP1	331.83	96.4	307
73MP2	335.11	54.3	276
73MP3	335.57	46.5	316
73MP4	344.50	97.9	238
73MP5	346.41	121.5	100
73MP6	346.42	121.7	109
73MP7	347.08	129.7	329
73MP8	348.78	150.1	11
74MP1	331.12	97.3	247
74MP2	331.33	94.5	72
74MP3	333.55	64.5	212
74MP4	340.34	56.6	318
74MP5	340.77	62.7	334
74MP6	342.03	80.0	348

From *Intriligator and Wolfe* [1976].

panding. However, this is the most direct evidence that this behavior occurs as expected.

The sequence of events on the Pioneer 10 outbound pass is particularly persuasive. Following the compression of the magnetosphere that occurred on day 343 and that pushed the magnetopause in past the spacecraft at 73MP4, the magnetosphere stayed compressed for about 2 days, until the CIR had passed. The subsequent solar wind rarefaction that occurred on day 346 frames magnetopause crossings 73MP5 and 73MP6. These two crossings are just 15 min apart, corresponding to a very brief reentry of the spacecraft into the magnetosphere and an immediate reexit. A spike of trapped electrons marks this reentry, although it is dwarfed by an earlier burst of magnetosheath electrons. The magnetosphere must have expanded rapidly to overtake the spacecraft at 73MP5; but owing to the narrowness of the rarefaction and the small solar wind pressure pulse that followed it, the expansion was brief, and the magnetopause was once again pushed in past the spacecraft at 73MP6. The spacecraft remained outside the magnetosphere until the small solar wind pressure pulse subsided; and for the last time the magnetopause expanded outward past the spacecraft at 73MP7.

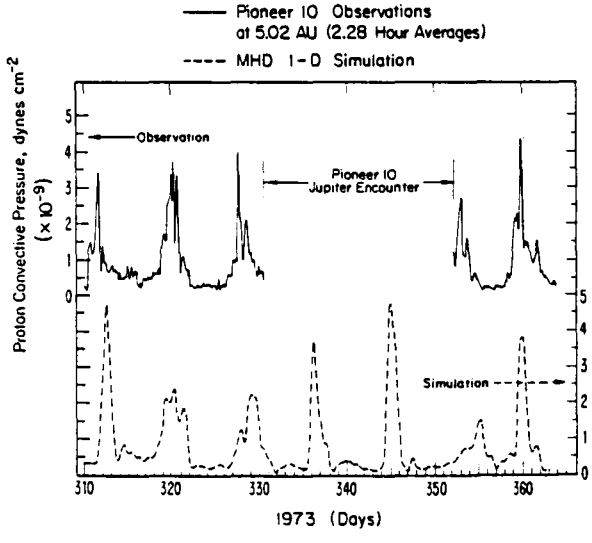

Fig. 3. Comparison of Pioneer 10 convective pressure observations (before and after Jupiter encounter) with the MHD simulation on days 310–363, 1973.

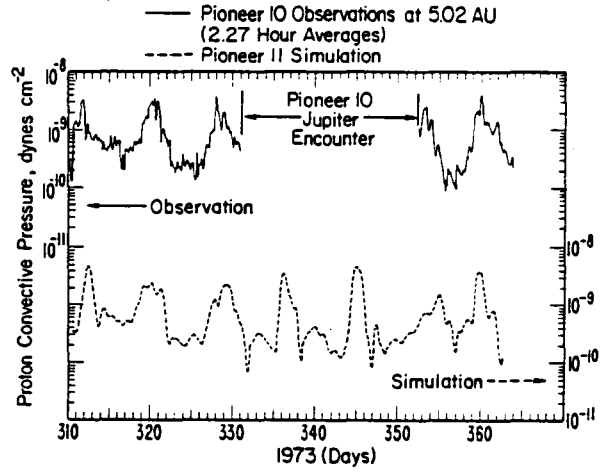

Fig. 4. Same as Figure 3 except that a semilog scale is used in order to emphasize the rarefaction regions of lower pressure between interaction regions.

The timing of the solar wind simulation is sometimes a bit late. For instance, the CIR on day 335 must have arrived a day earlier than shown in order to push the magnetopause in past the spacecraft at 73MP2. In spite of this timing error, there is no doubt that this CIR did indeed cause the compression event. Similarly, on the outbound pass the CIR on day 344 appears to be perhaps half a day late for magnetopause crossing 73MP4; and the trailing edge of the pulse on day 347 is about a day late for 73MP7. Nevertheless, the sequence of events in the magnetospheric data and the simulation dovetail so well that this breakdown in correlation is not serious.

It is interesting to speculate that another magnetospheric expansion must have occurred early on day 338. However, Pioneer 10 was close to periapsis at this time and too deep in the magnetosphere to observe its effect.

Results: 1974 Encounter. The observations (2.3 hour averages) of V, n, T_p, and B_ϕ before and after Pioneer 11's encounter with Jupiter in 1974 are shown in Figure 6. The encounter interval is marked by vertical bars in the figure. During this time, however, solar wind plasma data were also available be-

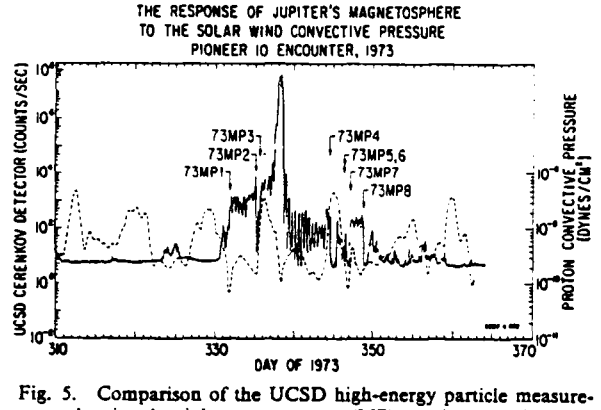

Fig. 5. Comparison of the UCSD high-energy particle measurements—showing the eight magnetopause (MP) crossings—and the observed convective pressure during the Pioneer 10 encounter in 1973.

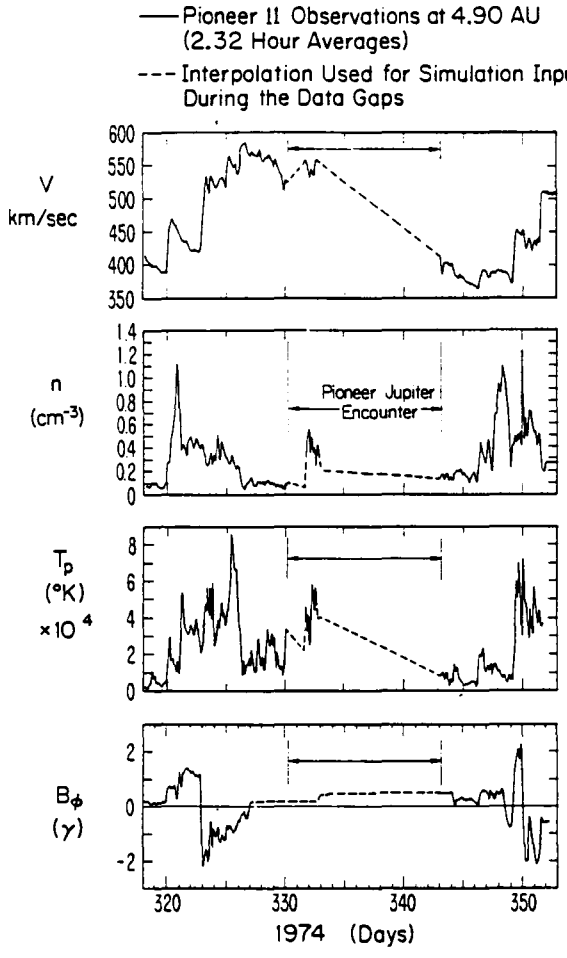

Fig. 6. Pioneer 11 solar wind observations (2.32 hour averages) before and after Jupiter encounter on days 318–353, 1974. The dashed lines for V, n, T_p, and B_ϕ (between the two vertical bars marked by the double arrow) indicate the values assumed for the solar wind in lieu of unavailable observed data for the input for the MHD model.

tween days 331.7 and 332.6. This cuts the Jupiter encounter interval into two data gaps. For input into the MHD simulation program, linear interpolations were used between the two data points bounding each of the two gaps. However, the two points bounding each gap were adjusted in such a way as to make the simulation obtained best fit the data downstream at 6.2 AU. These interpolations are shown by the dashed lines in Figure 6. As noted earlier, the simulation time scale was corrected for both the angular corotation delay and for the variations caused by spacecraft separation changes. In addition, two separate data points, whose density differed by more than a factor of 10 from the neighboring points, were removed.

It can be seen in Figure 6 that at least one large, complex CIR encountered Jupiter from day 320 to approximately day 330. Compression of the magnetosphere had undoubtedly taken place, followed prior to day 330 (~ 03h) by a brief expansion, during which a brief encounter with the bow shock took place for the first time at 97 R_J. This was followed by Pioneer 11 penetration of the magnetopause [see *Smith et al.*, 1978, Figure 3] until day 332 (~14 hours), when a second CIR arrived at Jupiter. This one was smaller in magnitude, but the pressure increase of a factor of 10 was sufficient to account for the magnetospheric compression to ~77 R_J. The third time interval associated with a precipitous drop-off of the energetic particle flux occurred at this time, as discussed by *Smith et al.* [1978], followed shortly thereafter on day 333 with reexpansion of the magnetosphere over the Pioneer 11 position. We then ask the following questions: (1) Were these two CIRs observed at Pioneer 10? (2) Was the complex CIR observed by Pioneer 11 after encounter on approximately days 346–352 also observed at Pioneer 10? (3) Is there any evidence at Pioneer 10 of a third CIR, following the second, that would account for the fourth interval of precipitous drop-off in energetic particle flux observed on day 340 by Pioneer 11?

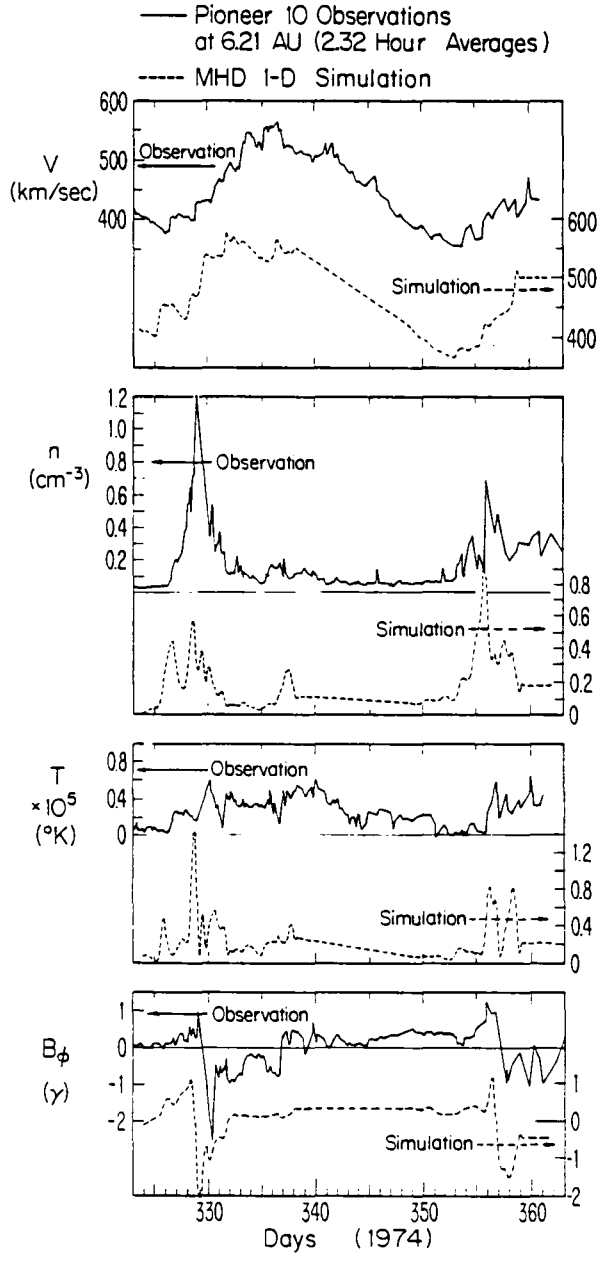

Fig. 7. Comparison of Pioneer 10 solar wind observations at 6.2 AU with the MHD simulation on days 323–363 (1974).

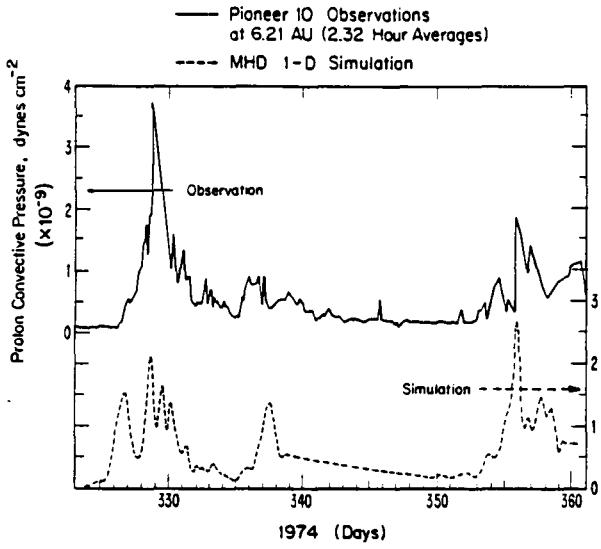

Fig. 8. Comparison of Pioneer 10 convective pressure observations at 6.2 AU with the MHD simulation on days 323–363 (1974).

The results of the numerical simulation, compared with the Pioneer 10 observations, are shown in Figures 7 and 8 in the same format discussed for the 1973 encounter for the basic parameters (V, n, T_p, and B_ϕ) and the proton convective pressure, respectively. The phasing and magnitudes are in reasonably good agreement, with the following exceptions: The simulated peak density of the first CIR was about one-half the observed one, and the simulated peak temperature was about 50% larger than the observed proton temperature. The latter deficiency has been explained [*Dryer et al.*, 1978*b*] by the fact that the present model is a one-fluid model which neglects thermal conduction within CIR's from protons to electrons. The latter particles rapidly conduct the thermal energy away from the protons because of their high thermal conductivity, thus lowering the proton temperature. This suggestion was confirmed by the two-fluid time-dependent model described by Metzler et al. (1979). It is, however, noteworthy that the present model predicted the variation of B_ϕ rather well.

Figure 8, in particular, shows that three CIRs were observed in both data and simulation at Pioneer 10. In proton convective pressure, the three asociated pressure pulses agree to within 24 hours in time. This agreement is not as good as that obtained for the 1973 case. In this case, however, the CIR's do not have the 'typical' form for which this model is best suited. The velocity remains high after the passage of the first CIR. Compare this to the first CIR of the 1973 case, for which the simulation also is off by 24 hours from the data. Thus questions (1) and (2) posed above are answered affirmatively.

Turning to question (3) concerning the interval on day 340 (1974) when Pioneer 11 found itself temporarily outside the magnetosphere (74MP4 to 74MP5 on Figure 10), we were unable to justify the assumption of a CIR at that time. That is, comparisons of the simulated and observed data in Figures 7 and 8 had no need for such a feature in the input forcing function that represented the solar wind at Jupiter. However, a full-fledged CIR may not have been necessary for the spacecraft to find itself outside the magnetosphere during this interval on the outbound pass. Referring to Figures 9–11, note that after the compression on day 331 the magnetosphere remained compressed for at least 2 days until the last inbound magnetopause crossing, 74MP3, on day 333. Indeed, from inspection of Figure 8, we may suppose that the solar wind pressure remained high for several days after 74MP3, delaying the reexpansion correspondingly. After all, the synthesized portion of our input forcing function was chosen for a satisfactory fit and simplicity, but there is room for an extended high pressure plateau before the start of the downward ramp. In any case, while the spacecraft was inside the magnetosphere, the solar wind evidently underwent a gradual decline in velocity, density, and pressure. It may be that the magnetosphere was still somewhat compressed at the first outbound magnetopause crossing, 74MP4; and at the second outbound crossing, 74MP5, it was merely reexpanding from the compression of the week before.

These two crossings do not appear anomalous when one analyzes the expected position as a function of solar wind pressure, allowing for the shape of the magnetopause. To illustrate this point, we have scaled the magnetopause distance to the subsolar point for each of the crossings listed in Table 1 and plotted this against the simultaneous solar wind convective pressure estimated from our MHD projections. When the magnetopause was thought to be in motion during a crossing, it appears in Figure 11 with an arrow pointing in the direction of the motion. In such cases the observed position is a limit only, and the arrow points in the direction of the equilibrium position. The work of *Engle and Beard* [1980] shows that the Jovian magnetosphere flares substantially in the dawn and dusk meridians and flattens somewhat at high latitudes. To normalize from the spacecraft trajectories to the subsolar point, we divided the distances to the Pioneer 10 and 11 outbound crossings by 1.33 and 0.84, respectively, and let the inbound distances stand as is.

These factors were scaled from the fifth-order inflated magnetopause model in Figure 6 of the paper by Engle and Beard. With the corrections for the idealized magnetopause shape, the projected solar wind pressure does a reasonably good job of ordering the magnetopause position. One can see that relative to the other data on Figure 11 the first two Pioneer 11 outbound crossings (74MP4 and 5) are not really out of place.

We have also plotted, on Figure 11, the three magnetopause crossings observed in the Voyager 1 Jupiter encounter data by *Bridge et al.* [1979]. They agree very well with the Pioneer data. The solid lines in Figure 11 represent a dependence of magnetopause location R upon pressure P in the form R is

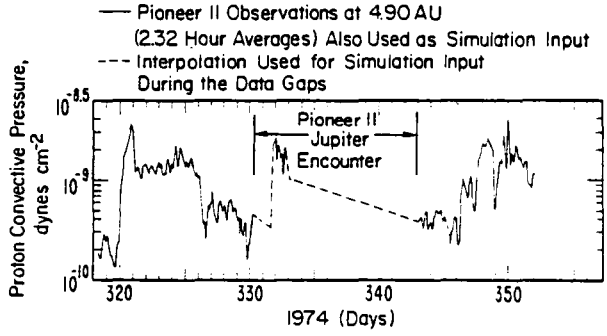

Fig. 9. Convective pressure observations by Pioneer 11 at Jupiter on days 318–352 (1974) and the interpolation used for the MHD simulation input.

proportional to $P^{-1/b}$ for $b = 3$ and $b = 4$. These values of b compare well with the dependence of the bow shock position upon solar wind pressure obtained by Voyager 1 and 2 [*Siscoe et al.*, 1980]. Using least squares fitting procedures, these authors obtained values for b from 2.6 to 4.3. A least squares fit to the Pioneer data gives a value of $b = 2.25 \pm 1.95$.

It is interesting to consider the functional dependence implied by this power law. If the magnetic field of the internal dipole alone had to stand off the solar wind, the expected dependence would be P proportional to $R^{-1/6}$. However, there is a substantial ring current in the outer Jovian magnetosphere, and the magnetic field magnitude falls off radially, not as R^{-3}, as it would for a dipole, but more like $R^{-1.5}$ to R^{-2}. Thus the magnetic field pressure inside the magnetosphere varies as R^{-3} to R^{-4}; i.e., with the same radial dependence exhibited by the data in Figure 11.

Attempts to refine this index must deal with errors that are nonstatistical in nature. For instance, there are likely to be differences between the Engle and Beard magnetopause, which is an equilibrium configuration, and the dynamic reality, which may not preserve its equilibrium shape when in motion (e.g., 73MP5 and 6). Also, it is more difficult to estimate the solar wind pressure in some cases than in others. The measured (or modeled) solar wind pressure is not the pressure required to maintain a steady state magnetopause at the location at which the measurement was made. Moreover, there are timing errors of up to a day in the simulated solar wind pressure; thus one must guess what is the correct instant to take a reading from the pressure graph. In many cases this is easy because a specific sharp feature in the solar wind data can be related to a magnetospheric event (e.g., 73MP1 and 2). In other cases this is harder: for instance, 73MP3 evidently occurred during a decline in solar wind pressure that lasted for a couple of days, and one can only guess at the timing error in this case. Because of these uncertainties, we feel that all values of the index b between 3 and 4 are acceptable, and further analyses of these data should be based on a dynamic magnetospheric model.

CONCLUSION

A single-fluid, time-dependent, 1-D MHD model was used together with a set of simultaneous plasma and magnetic field data to simulate the evolution of seven CIR's in 1973 and three CIR's in 1974 between the positions of Pioneer 11 and Pioneer 10. In the former case a portion of the solar wind data at the outermost spacecraft (Pioneer 10) was unavailable since it was (for the most part) within the Jovian magnetosphere. In the latter case, a portion of the solar wind data at the innermost spacecraft (Pioneer 11) was unavailable for the same reason, necessitating an assumption for a portion of the required solar wind input forcing function. Agreement of the simulation with the plasma and magnetic field data at the outermost spacecraft was satisfactory for both the 1973 and 1974 cases.

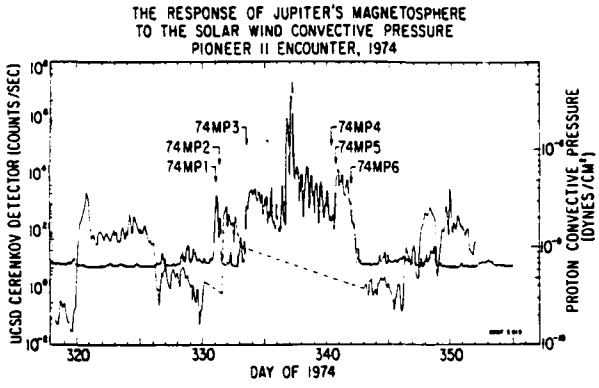

Fig. 10. Comparison of the UCSD high-energy particle measurements—showing the six magnetopause crossings—and the observed convective pressure during the Pioneer 11 encounter in 1974.

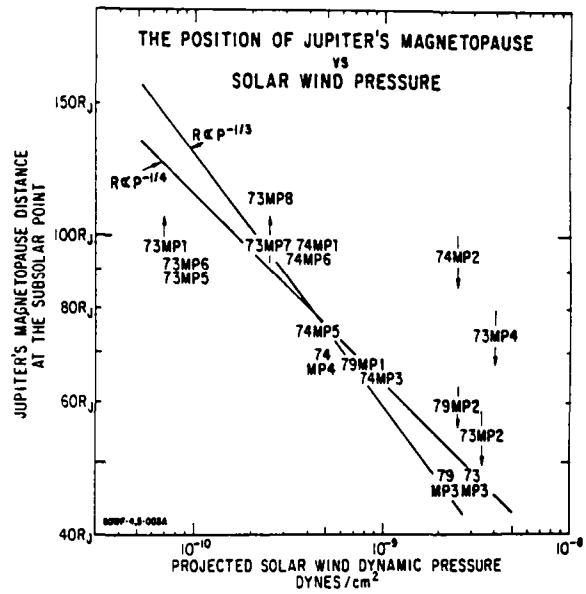

Fig. 11. Position of subsolar magnetosphere, as scaled [*Engle and Beard*, 1980] from Jovian magnetopause crossings, versus solar wind pressure for the Pioneer 1973 and 1974 encounters as well as for the Voyager 1979 encounter.

In the former case, two of the simulated CIR's appeared at Jupiter at the same times as precipitous drop-offs of energetic particle flux took place, thereby confirming the suggestion by *Smith et al.* [1978] that a large-scale compression of the magnetosphere had taken place in response to solar wind pressure pulses incident on the magnetosphere. In the latter case (1974), the pressure increase in the second observed CIR was sufficiently large for it to have been responsible for the third case of energetic particle flux drop-off. A third CIR was neither observed nor simulated, but it was shown that this does not necessarily imply that a different mechanism has to be invoked to explain the data observed at Jupiter.

Our MHD simulation, taken together with the Cerenkov counter observations, also strongly supports the idea that Jupiter's magnetosphere reacts—by expanding—to solar wind rarefactions that follow CIRs.

Acknowledgments. We wish to thank Elaine Parker of the Jet Propulsion Laboratory and J. D. Mihalov of the NASA Ames Research Laboratory for their valuable assistance in providing the magnetic and plasma data for our use. We are also grateful to D. Lewis and W. Ratallack of the NOAA Space Environment Laboratory for their indispensable aid in arranging for tape reading and computing assistance and to Ginger Caldwell of the NOAA Space Environment Laboratory for her valuable assistance in the error analysis. This report represents one aspect of research performed by JPL for NASA under contract NAS 7-100. The work carried out at UCSD was supported in part by NASA contract NAS 2-6552.

The Editor thanks J. W. Belcher and R. P. Lepping for their assistance in evaluating this paper.

REFERENCES

Bridge, H. S., J. W. Belcher, A. J. Lazarus, J. D. Sullivan, R. L. McNutt, F. Bagenal, J. D. Scudder, E. C. Sittler, G. L. Siscoe, V. M. Vasyliunas, C. K. Goertz, and C. M. Yeates, Plasma observations near Jupiter: Initial results from Voyager 1, *Science, 204*, 987, 1979.

Coroniti, F. V., and C. F. Kennel, Possible origins of time variability in Jupiter's outer magnetosphere, 1, Variations in solar wind dynamic pressure, *Geophys. Res. Lett., 4*, 211, 1977.

Dessler, A. J., and V. M. Vasyliunas, The magnetic anomaly model of the Jovian magnetosphere: Predictions for Voyager, *Geophys. Res. Lett., 6*, 37, 1979.

Dryer, M., Bow shock and its interaction with interplanetary shocks, *Radio Sci., 8*, 893, 1973.

Dryer, M., Interplanetary shock waves generated by solar flares, *Space Sci. Rev., 15*, 403, 1974.

Dryer, M., Interplanetary shock waves: Recent developments, *Space Sci. Rev., 17*, 277, 1975.

Dryer, M., and R. S. Steinolfson, MHD solution of interplanetary disturbances generated by simulated velocity perturbations, *J. Geophys. Res., 81*, 5413, 1976.

Dryer, M., C. Candelaria, Z. K. Smith, R. S. Steinolfson, E. J. Smith, J. H. Wolfe, J. D. Mihalov, and P. Rosenau, Dynamic MHD modeling of the solar wind disturbances during the August 1972 events, *J. Geophys. Res., 83*, 532, 1978*a*.

Dryer, M., Z. K. Smith, E. J. Smith, J. D. Mihalov, J. H. Wolfe, R. S. Steinolfson, and S. T. Wu, Dynamic MHD modeling of solar wind corotating stream interaction regions observed by Pioneer 10 and 11, *J. Geophys. Res., 83*, 4347, 1978*b*.

Engle, I. M., and D. B. Beard, Idealized Jovian magnetosphere shape and field, *J. Geophys. Res., 85*, 579, 1980.

Fillius, R. W., and C. E. McIlwain, Measurements of the Jovian radiation belts, *J. Geophys. Res., 79*, 3589, 1974.

Grib, S. A., B. E. Brunelli, M. Dryer, and W.-W. Shen, Interaction of interplanetary shock waves with the bow shock-magnetopause system, *J. Geophys. Res., 84*, 5907, 1979.

Hill, T. W., A. J. Dessler, and F. C. Michel, Configuration of the Jovian magnetosphere, *Geophys. Res. Lett., 1*, 3, 1974.

Intriligator, D. S., and J. H. Wolfe, Results of the plasma analyzer experiment on Pioneers 10 and 11, *Jupiter*, edited by T. Gehrels, pp. 848–869, University of Arizona Press, Tucson, Ariz., 1976.

Kennel, C. F., and F. V. Coroniti, Is Jupiter's magnetosphere like a pulsar's or Earth's?, *Space Sci. Rev., 17*, 857, 1975.

Metzler, N., S. Cuperman, M. Dryer, and P. Rosenau, A time-dependent two-fluid model with thermal conduction for the solar wind, *Astrophys. J., 231*, 960, 1979.

Michel, F. C., and P. A. Sturrock, Centrifugal instability of the Jovian magnetosphere and its interaction with the solar wind, *Planet. Space Sci., 22*, 1501, 1974.

Mihalov, J. D., H. R. Collard, D. D. McKibbin, J. H. Wolfe, and D. S. Intriligator, Pioneer 11 encounter: Preliminary results from Ames Research Center plasma analyzer experiment, *Science, 188*, 448, 1975.

Rosenau, P., Propagation of two-fluid interplanetary shock waves, *J. Geophys. Res., 84*, 5897, 1979.

Siscoe, G. L., N. Crooker, and J. W. Belcher, Sunward flow in Jupiter's magnetosheath, *Geophys. Res. Lett., 7*, 25, 1980.

Smith, E. J., and J. H. Wolfe, Observations of interaction regions and corotating shocks between 1 and 5 AU: Pioneers 10 and 11, *Geophys. Res. Lett., 3*, 137, 1976.

Smith, E. J., and J. H. Wolfe, Pioneer 10, 11 observations of evolving solar wind streams and shocks beyond 1 AU, *Study of Travelling Interplanetary Phenomena/1977*, edited by M. A. Shea, D. F. Smart, and S. T. Wu, p. 227, D. Reidel, Hingham, Mass., 1977.

Smith, E. J., L. Davis, Jr., D. E. Jones, D. S. Colburn, P. J. Coleman, Jr., P. Dyal, and C. P. Sonett, Magnetic field of Jupiter and its interaction with the solar wind, *Science, 183*, 305, 1974.

Smith, E. J., L. Davis, Jr., D. E. Jones, P. J. Coleman, Jr., D. S. Colburn, P. Dyal, and C. P. Sonett, Jupiter's magnetic field, magnetosphere and interaction with the solar wind: Pioneer 11, *Science, 188*, 451, 1975.

Smith, E. J., R. W. Fillius, and J. H. Wolfe, Compression of Jupiter's magnetosphere by the solar wind, *J. Geophys. Res., 83*, 4733, 1978.

Steinolfson, R. S., M. Dryer, and Y. Nakagawa, Numerical MHD simulation of interplanetary shock pairs, *J. Geophys. Res., 83*, 1576, 1975*a*.

Steinolfson, R. S., M. Dryer, and Y. Nakagawa, Interplanetary shock pair disturbances: Comparison of theory with space probe data, *J. Geophys. Res., 80*, 1989, 1975*b*.

Wallis, M., and M. Dryer, Sun and comets in an external flow, *Astrophys. J., 205*, 895, 1976.

Wolfe, J. H., H. R. Collard, J. D. Mihalov, and D. S. Intriligator, Preliminary Pioneer 10 encounter results from the Ames Research Center plasma analyzer experiment, *Science, 183*, 303, 1974*a*.

Wolfe, J. H., J. D. Mihalov, H. R. Collard, D. S. Intriligator, D. D. McKibbin, and L. A. Frank, Pioneer 10 observations of the solar wind interaction with Jupiter, *J. Geophys. Res., 79*, 3489, 1974*b*.

(Received December 24, 1980;
revised April 6, 1981;
accepted April 20, 1981.)

SATURN ENCOUNTER

Reprint Series
25 January 1980, Volume 207, pp. 425-431

SCIENCE

Trapped Radiation Belts of Saturn: First Look

W. Fillius, W. H. Ip, and C. E. McIlwain

Trapped Radiation Belts of Saturn: First Look

Abstract. *Pioneer 11 has made the first exploration of the magnetosphere and trapped radiation belts of Saturn. Saturn's magnetosphere is intermediate in size between Earth's and Jupiter's, with trapped particle intensities comparable to Earth's. The outer region of Saturn's magnetosphere contains lower energy radiation and is variable with time; the inner region contains higher energy particles. The pitch angle distributions show a remarkable variety of field-aligned and locally mirroring configurations. The moons and especially the rings of Saturn are effective absorbers of trapped particles; underneath the rings, the trapped radiation is completely absorbed. We confirm the discovery of a new ring, called the F ring, a new division, the Pioneer division, and a moon, called 1979 S 2. The latter has probably been seen from Earth. There may be evidence for more bodies like 1979 S 2, but at this stage the interpretation of the data is ambiguous. Using particle diffusion rates, we estimate that the cross-sectional area of the F ring is* $> 7 \times 10^{13}$ *square centimeters and that the opacity is* $> 10^{-5}$. *Cosmic-ray albedo neutron decay should be looked into as a source of energetic particles in the inner magnetosphere of Saturn.*

On its historic flight past Saturn, Pioneer 11 carried instrumentation for the measurement of magnetospheric particles and fields. One of these instruments was a trapped radiation detector package designed and built at the University of California, San Diego (UCSD) (Table 1). Data obtained with this package are providing (i) confirmation of the existence of a magnetosphere and trapped radiation belt at Saturn, (ii) greater understanding of that magnetosphere and measurements of trapped particle fluxes and energies, (iii) the opportunity to investigate particle acceleration processes under new conditions and to compare them with activity in other magnetospheres, and (iv) information about ring and satellite absorption effects, including the wake of what is probably a previously undiscovered object.

Traveling to Saturn by way of Earth and Jupiter, Pioneer 11 crossed three magnetospheres and, with its sister spacecraft Pioneer 10, gathered excellent material for comparative studies. Figure 1 shows the intensities and radial extents of particles in a common energy range at the three planets. Other comparative features that can be seen include the effects of moons and rings and the modulation of the radiation levels by planetary rotation.

Earth's moon is well outside the terrestrial magnetosphere and has no effect on it. However, many of the moons of Jupiter and Saturn are inside the zone of trapped radiation and interact strongly with the trapped particles. In Fig. 1, the arrows at the orbits of Io and Amalthea point to dips caused by absorption of the radiation. There are analogous absorption features at Saturn, too, but they are not shown distinctly in Fig. 1. The ring of Jupiter (*1*) produces an absorption dip like that of the moons (*2*), but the rings of Saturn produce the most dramatic effect of all. The trapped radiation is completely absorbed at the outer edge of the A ring and, on lines of force intercepted by the Saturn rings, cosmic rays fall to less than one fifth of their interplanetary level. Our counting rates here were the lowest recorded in the entire flight.

Modulation at the planetary rotation rate is visible only at Jupiter, where the gross intensity variations outside the orbit of Io carry the 10-hour period of Jupiter's rotation. Earth's magnetosphere could produce a 24-hour modulation if an observatory could be held stationary at a chosen location. However, the near-Earth data shown here span only 1 hour, so there is no chance of seeing such an effect. Like Jupiter, Saturn has a rotation period of 10 hours, but if modulation occurs at this frequency, it is not readily apparent. It is natural to attribute this uniqueness to the remarkable symmetry of Saturn's magnetic field, which has a dipole moment with near-zero values for both tilt and offset (*3*).

Figure 2, A to C, shows a time profile (*4*) of Saturn's magnetosphere as seen by several channels of the UCSD instrument. Refer to Fig. 3 for the encounter geometry and Table 1 for a description of the detectors.

The outer region of Saturn's magnetosphere extends from ~ 6 Saturn radii (R_S) (*5–7*) to the magnetopause. It is strongly influenced by the time-variable solar wind, and it contains particles of lower energy than the inner region. Pio-

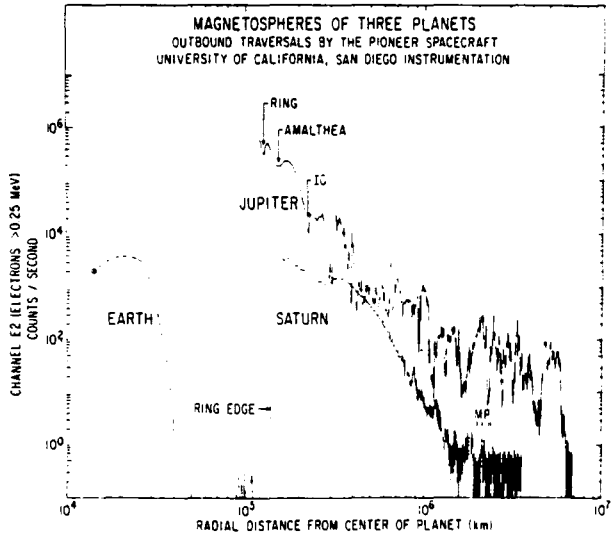

Fig. 1. Magnetospheres of three planets. These profiles of the radiation belts of Earth, Jupiter, and Saturn were made by University of California instrumentation on two Pioneer spacecraft. The profile of Earth's radiation belt was made in the dawn sector by Pioneer 10; those of Jupiter and Saturn were made by identical instrumentation on Pioneer 11 outbound in the noon and dawn sectors, respectively. The data shown are from an electron scatter detector with a geometric factor of 1.04 × 10^3 cm^2 sr^{-1} for electrons > 0.255 MeV. In the Jupiter magnetosphere inside Io, this detector responded mainly to omnidirectional electrons penetrating the shielding. For these particles the energy threshhold is 35 MeV and the geometric factor 0.038 cm^2. Note that the abscissa is in kilometers. To normalize to planetary radii, divide by 6371 km for Earth, 71,372 km for Jupiter, and 60,000 km for Saturn.

0036-8075/80/0125-0425$01.50/0

neer 11 entered this region inbound at 17.3 R_S (*8*) and, as seen at the extreme left of Fig. 2, A to C, the magnetopause crossing produced a jump of an order of magnitude in the counting rates of our low-energy channels. The outbound crossings are shown in Fig. 1: the intensity jumps outbound are much less prominent, since the trapped intensities were low and statistically irregular. Apparently, the reason for this difference lies not only in the local times of the inbound and outbound passes but also in a large temporal change in the magnetosphere during the Pioneer 11 flyby. As reported by Wolfe *et al.* (*8*), the spacecraft entered the magnetosphere at a time when it was compressed by a high-pressure solar wind stream. When it left, the solar wind pressure was lower, and presumably the magnetosphere was larger and the radiation less energetic.

The outer region contains several features that we tentatively attribute to temporal fluctuations. One such feature is the broad dip observed in low-energy electron intensities at about 0600 on day 244 (inbound near 10 R_S). Since this dip did not reoccur during the outbound pass, it does not seem to be a spatial phenomenon. It might be associated with the decompression of the magnetosphere and with growth of the diamagnetic ring current reported in this location by Smith *et al.* (*3*).

Another feature, observed at about 0900 on day 245 (~ 15 R_S outbound), occurred simultaneously with a large change in the magnetic field direction (*3*). The angular distributions of the low-energy particles underwent dramatic changes here also. It will take more analysis to describe the event fully; however, we are inclined to view this as a large temporal change, associated possibly with a magnetic tail and triggered by a change in interplanetary conditions.

The feature observed at about 1600 on day 245 (~ 20 R_S outbound) might be another temporal fluctuation, or it might be associated with Titan, since the spacecraft made its closest approach (~ 6 R_S) to Titan at this time and crossed its orbit shortly thereafter (*9*). The particle fluctuations were accompanied by a variation in the magnetic field (*3*). If this event is related to Titan, it implies that Titan itself is a source of energetic charged particles in Saturn's magnetosphere.

As Fig. 2C shows, during a large portion of the outbound pass the low-energy electron detector recorded a much higher flux when it faced parallel to the magnetic field than when it faced perpendicular. We think that this may be a manifestation of L-shell splitting (*10*) brought about by the change of the magnetic field geometry from highly compressed on the noon side to elongated at dawn. If this hypothesis is correct, quantitative modeling may tell us something about the field configuration in regions not sampled by the spacecraft.

Throughout the flyby, the pitch angle distributions underwent remarkable changes and, as shown by Trainor *et al.* (*11*), these changes varied with energy. Figure 4 shows the behavior of electrons in one energy range. If one ignores the noisy patches of data, one can see that the phase θ_2 tends to fall at either 0° or 90°, representing field-aligned (dumbbell) and perpendicular (pancake) angular distributions, respectively. These two patterns are familiar from both Earth and Jupiter, but are rarely seen to switch so

Table 1. Characteristics of the Pioneer 11 trapped radiation detector at Saturn encounter (September 1979). The detector has survived the Saturn radiation belt with no failures and no damage. However, because the radiation environment of Saturn is different from that of Jupiter or interplanetary space, some of our data channels count different types of particles than before. The main cause of these differences is the comparative absence of multi-MeV electrons at Saturn. The Cerenkov detector and channels M1 and M2 are most affected. Also, at Saturn there is little penetrating background on channels E and S. The ratios of their counting rates reveal that the three pulse height levels on detector M all responded to protons > 80 MeV (M1:M2:M3 = 3.3:1.4:1). By contrast, the signature of electrons at Jupiter was 1000:100:1. We could not measure the number of individual particles that were energetic enough to trigger the Cerenkov detector. However, inside 5 R_S the intensity of lower energy particles was sufficient to cause pileup; that is, several particles arriving closer together than the resolution time of the electronics add up to create a large pulse. The rate at which pileup events occur can be estimated by using the Poisson probability distribution function for an m-fold coincidence: $P_m = (\nu\tau)^m \exp(-\nu\tau)/m!$, where τ is the coincidence resolving time and ν is the primary rate of the single pulses (the rate when $\tau = 0$). The rate of n-fold coincidences ν_n is the product νP_{n-1} of the single rate and the probability that $n - 1$ pulses preceded any single pulse to create an n-fold coincidence. Then $\nu_n = \nu^n \tau^{n-1} \exp(-\nu\tau)/(n - 1)!$. By comparing the rates on the three pulse height channels and the total current on the CDC channel, we can tell that channels C1 and C2 count mostly pulses whose height is 13 photoelectrons and whose rate can be determined from the equation above. Then, from the known properties of the detector and the dimensions of the instrument housing, we deduce that these pulses are caused by electrons of energy > 2 MeV and that the instrument geometric factor is ≈ 20 cm² sr for these particles. The data from detector C are taken from the CDC channel to assure linearity, with a calibration constant of 2.8×10^{14} count sec^{-1} A^{-1} derived from the pileup analysis given above.

Detector name and description	Channel	Discrimination level	Particle selectivity	Geometric factor
Cerenkov counter:	C1	> 31 photoelectrons	Pileup of 2-MeV electrons	20 cm² sr
Water-methanol radiator (index	C2	> 65 photoelectrons	Pileup of 2-MeV electrons	20 cm² sr
of refraction, 4/3) monitored by	C3	> 135 photoelectrons		
a photomultiplier tube with pulse and current output	CDC	10^{-14} – 10^{-5} A	> 2-MeV electrons	7.3×10^{-14} A e^{-1} cm² sec sr
Electron scatter counter:	E1	> 0.089 MeV	> 0.16-MeV electrons	1.3×10^{-2} cm² sr
Silicon surface barrier diode	E2	> 0.19 MeV	> 0.255-MeV electrons	1.04×10^{-2} cm² sr
detector with a crooked aperture to admit scattered particles only	E3	> 0.40 MeV	> 0.460-MeV electrons	5.7×10^{-3} cm² sr
Minimum ionizing particle counter:	M1	> 0.40 MeV	> 80-MeV protons	0.038 cm²
Silicon surface barrier diode	M2	> 0.85 MeV	> 80-MeV protons	0.027 cm²
detector inside omnidirectional shielding (8 g cm^{-2})	M3	> 1.77 MeV	> 80-MeV protons	0.021 cm²
SP scintillator:	SPDC		> 100-keV protons	7.4×10^{-23} A eV^{-1} cm² sec sr (p)
Zn-S (Ag) phosphor (thickness, 1.5 mg cm^{-2}) monitored by a vacuum photodiode		10^{-14} – 10^{-5} A	> 10-keV electrons	7.4×10^{-23} A eV^{-1} cm² sec sr (e)
SE scintillator:	SEDC		> 100-keV protons	2.0×10^{-24} A eV^{-1} cm² sec sr (p$^+$)
Plastic scintillator (thickness, 1.5 mg cm^{-2}) monitored by a vacuum photodiode		10^{-14} – 10^{-5} A	> 10-keV electrons	1.4×10^{-23} A eV^{-1} cm² sec sr (e$^-$)

frequently or to have such large amplitudes. Information about this interesting behavior may ultimately be utilized in testing different physical mechanisms operating in Saturn's magnetosphere at the time of the encounter.

As the spacecraft approaches Saturn, the particle intensities increase, the spectrum hardens, and the higher energy channels are activated (this trend can be seen in Fig. 2). These are the characteristics of the usual pattern, in which particles are injected from the solar wind at the outer boundary and diffuse inward, breaking the third adiabatic invariant and conserving the first two (*12*).

However, at ~ 6 R_S there is an unexpected loss of low-energy particles (electrons and protons of < ~ 0.5 MeV). Because this feature occurs outbound as well as inbound, and because these particles appear to be permanently lost inside this distance, we believe that this is a spatial boundary rather than a temporal feature. We do not know the cause for the loss of these particles; possibilities include sweeping by the several known moons that orbit at and below this distance, absorption by a very tenuous material ring, and pitch angle scattering of the trapped radiation into the planetary loss cone by increased hydromagnetic wave activity. We note, however, that the electron pitch angle distribution turns from dumbbell-shaped to pancake-shaped where the losses begin (Fig. 4). Two of the suggested mechanisms, pitch angle scattering and absorption by a ring, would be expected to produce isotropy—not what is observed.

This low-energy particle cutoff is the boundary that we chose to separate the outer and inner regions of the magnetosphere. The inner region contains the higher energy particles that survive this hazard. These particles meet their fate at the outer edge of the visible ring system. As their bouncing motion causes the trapped particles to cross and recross the ring plane every few seconds, the optical depth of the ring material is multiplied by the number of particle bounces, and this product reaches unity before the trapped particles can diffuse past the obstacle. Only the two low-energy scintillators (the S detectors) recorded any substantial signal inside the outer edge of the A ring, but we believe that this signal was not caused directly by trapped radiation. The most likely explanation is that the thin cover foil was broken and the detectors responded to sunlight reflected by the rings and planet. Alternatively, they could have been sensing x- or ultraviolet radiation created by particle bombardment of the ring material.

A very strange feature, shown in Fig. 2, is a lack of symmetry in particle intensities between inbound and outbound passes. The intensities are significantly different and, equally remarkable, the

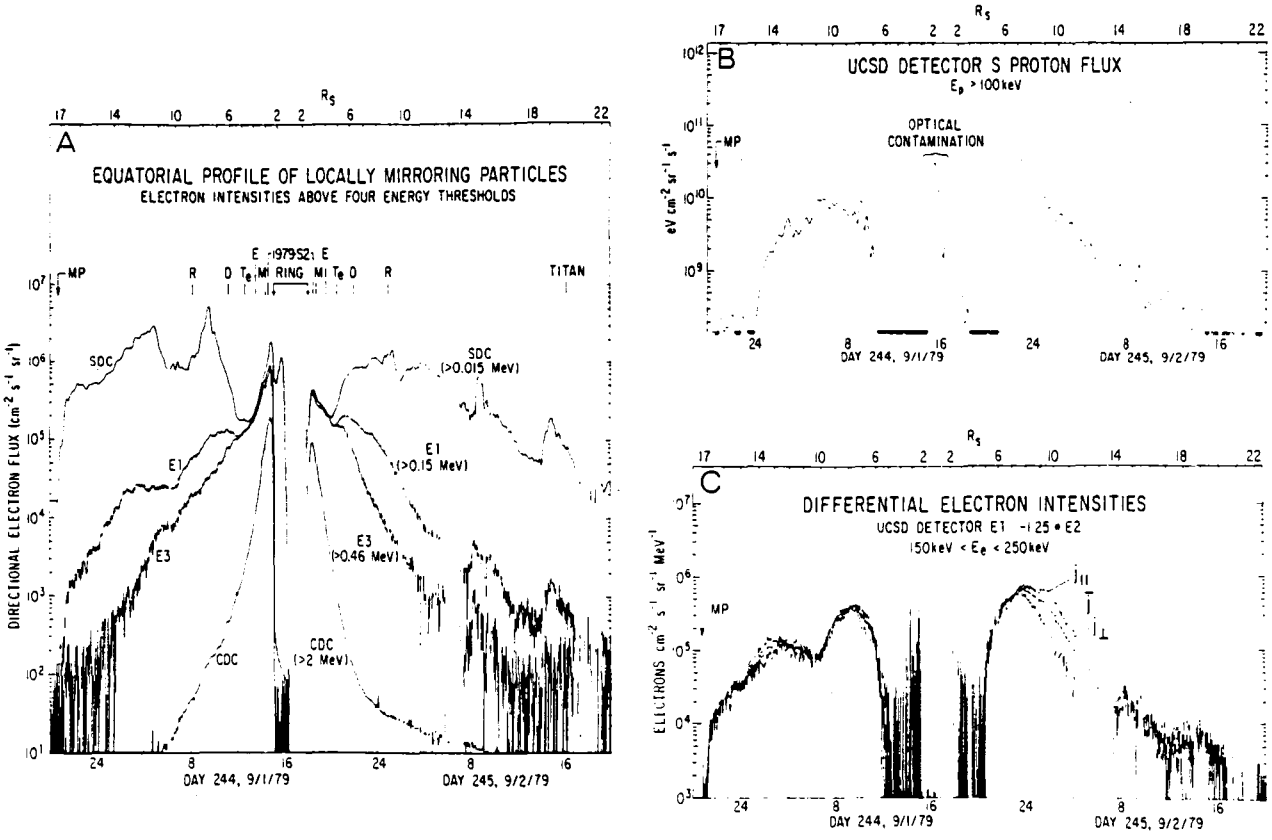

Fig. 2. Equatorial profiles of locally mirroring particles. The magnetopause crossing is marked *MP*. The orbits of Saturn's moons Rhea, Dione, Tethys, Enceladus, and Mimas are marked by *R*, *D*, T_e, *E*, and *M*, respectively. As the spacecraft spins and the viewing orientation of the trapped radiation detector is perpendicular to the spin axis, the detectors direct perpendicular to the magnetic field line twice during each spacecraft revolution. The intensity in this direction—that is, the directional flux of particles with 90° pitch angle, is shown here. (A) Electron intensities above four energy thresholds. The trace labeled *SDC* is a linear combinator of SPDC and SEDC outputs chosen to give the intensity of electrons only. As the detector is calibrated for energy flux (eV cm^{-2} sec^{-1} sr^{-1}), an average energy of 15 keV was used to convert to number flux (cm^{-2} sec^{-1} sr^{-1}). (B) Energy flux of protons above 100 keV. The trace is a linear combination of SPDC and SEDC outputs chosen to give the intensity of protons only. The detection threshold is approximately 2×10^9 eV cm^{-2} sec^{-1} sr^{-1}. (C) Electron intensity profiles at different pitch angles in the differential energy range $150 < E_e < 250$ keV. Also shown are the spin-averaged intensity and the intensity at the minimum pitch angle sampled. The differential energy band is a weighted difference between the outputs of two integral channels. For $L < 6\ R_S$ the difference is smaller than the statistical uncertainty in the integral channels, and the result is large amplitude random noise. These fluctuations are easily recognized and should be ignored.

asymmetry is different for different particles. For electrons from 0.5 to 2 MeV just outside the visible rings, the fluxes are higher inbound than outbound by a factor of about 2. For ~ 0.2-MeV electrons and ~ 150-keV protons at 6 R_S, the flux is higher outbound than inbound. However, for ~ 15-keV electrons at 6 R_S, the flux is higher inbound than outbound. Finally, although it is not shown in Fig. 2, the flux of 80-MeV protons just outside the rings is the same inbound and outbound. Since there are no magnetic field differences to account for these asymmetries (*3*), some combination of time variations in the radiation belts, large spatial electric fields, and electrostatic charge on the spacecraft (*13*) may explain these effects.

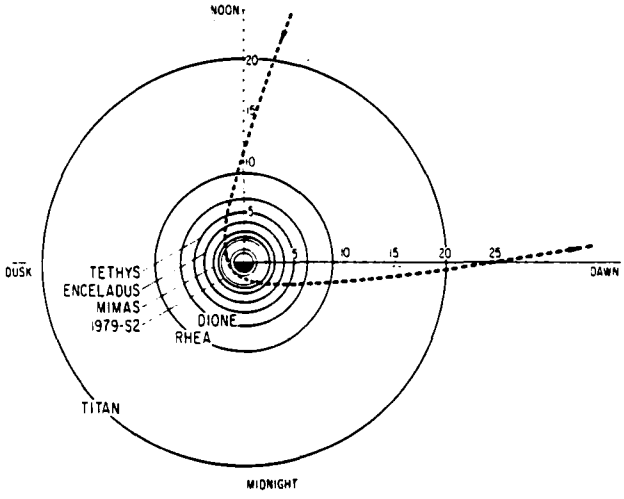

Fig. 3. Pioneer 11 encounter trajectory. The inclination of the trajectory was less than 6°, so this is essentially an equatorial profile.

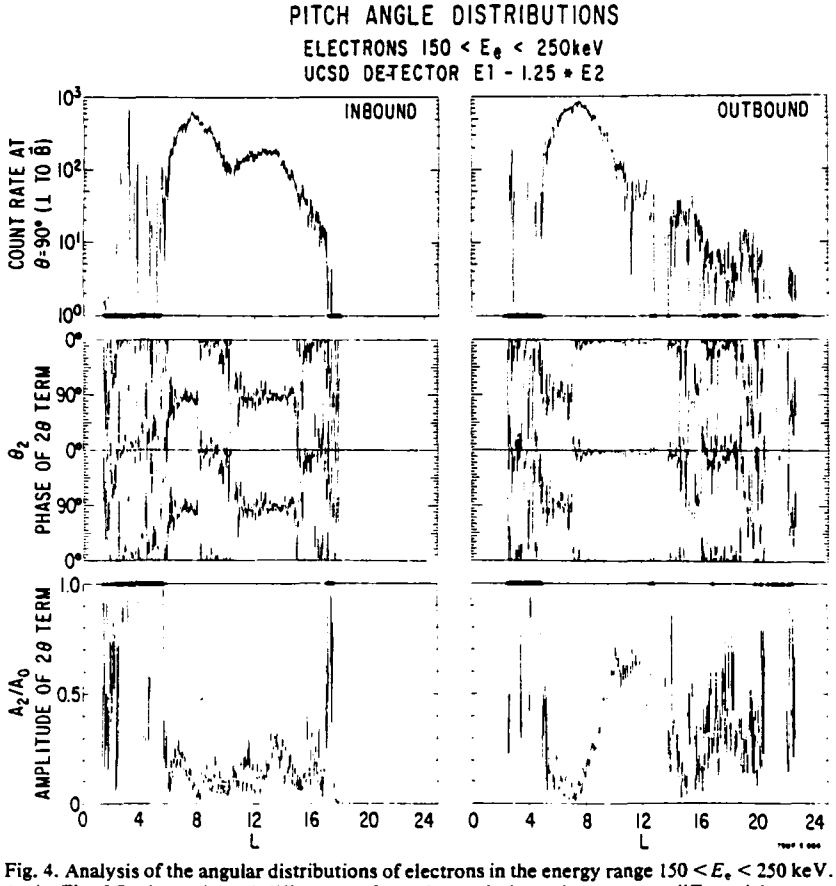

Fig. 4. Analysis of the angular distributions of electrons in the energy range $150 < E_e < 250$ keV. As in Fig. 2C, the weighted difference of two integral channels creates a differential energy passband centered at 200 keV. This technique reduces ambiguity when the angular distributions are energy-dependent. The data have been analyzed by a least-squares fit to the function $A(\theta) = A_0 + A_1 \cos(\theta - \theta_1) + A_2 \cos 2(\theta - \theta_2) + A_4 \cos 4(\theta - \theta_4)$, where θ is measured from the projection of the magnetic field vector onto the spin plane. The phase θ_2 ranges from −90° to 90° only, and the vertical scale wraps around at these limits to show the data twice and avoid cutting the pattern. We caution that A_2/A_0 and θ_2 tend to be random when A_0 is too small to be statistically significant. In some cases (for example, for $L < 5\ R_S$), A_0 fails this test because of statistical errors from the integral channels.

Figure 5 shows major features of Saturn's inner magnetosphere, constructed from data obtained during the Pioneer 11 inbound pass (a schematic of the trajectory is given in Fig. 6). The disappearance of trapped radiation at the outer edge of the rings has already been noted. However, the structure in this cutoff is a new and highly meaningful feature. The dip at 2.35 R_S confirms the discovery by the Pioneer 11 imaging photopolarimeter team (*4*) of a new ring, dubbed the F ring. The relative maximum to the left of this dip shows the profile of the interval between the A and F rings that was named the Pioneer division by Gehrels *et al.* (*14*). Broad absorption dips appear in the proton profile at the orbit of Mimas and at another position that is marked 1979 S 2. This latter evidently marks the orbit of one or more objects that may have been sighted previously, but whose orbital elements were too uncertain or inaccurate to permit positive identification (*15*).

There is a clear distinction between the profiles of the electron intensity ($E_e > 0.05$ MeV) and of the proton intensity ($E_p > 80$ MeV). The electrons seem to be enjoying the same advantage, against being swept up by these objects, that we observed previously at the orbit of Io in the Jupiter radiation belts (*16*). A combination of the corotational electric field and the curvature and gradient of the magnetic field gives them a drift velocity that is nearly synchronous with the Keplerian periods of the orbiting bodies. Thus they have a low probability of encountering the objects while radial diffusion carries them past their orbits. As the protons are carried in the opposite direction by the magnetic field curvature and gradient drifts, the probability of their having an encounter is enhanced. The sweeping of the protons appears to be complete at Mimas and 1979 S 2, whereas the reduction of the electron intensity appears negligible.

The spike marked 1979 S 2, one of the most remarkable events of the flyby, is shown in high time resolution in Fig. 7. For an interval of just 9 seconds, the counting rates of our detectors fell to ~ 1 percent of the neighboring values [simi-

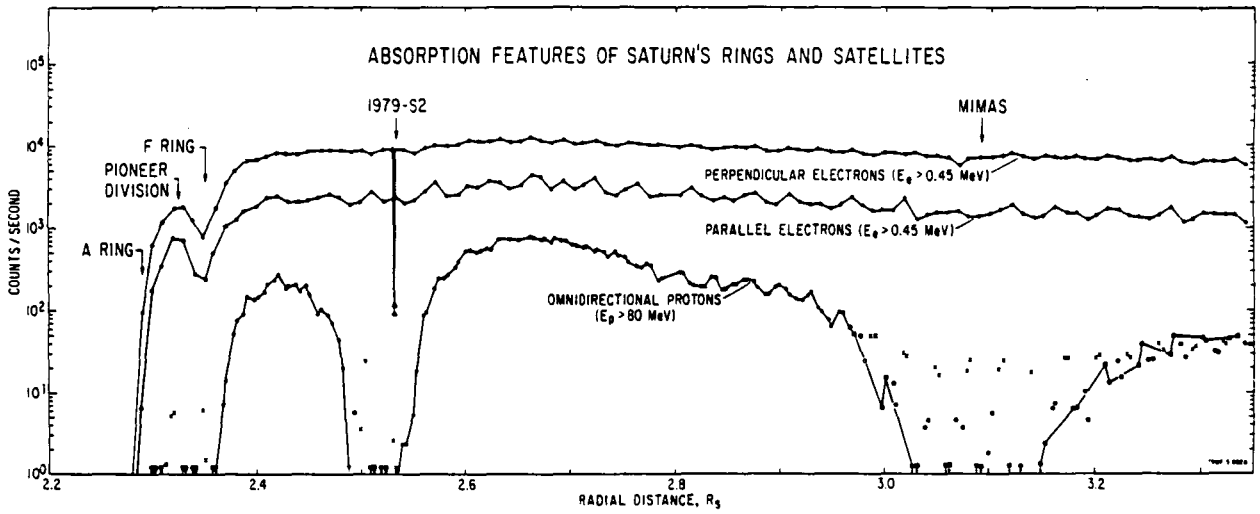

Fig. 5. Absorption features of Saturn's rings and satellites. This graph exhibits data from detectors E and M; all three channels of each are used to gain time resolution. To normalize them to channel E1, we multiplied the channel 3 counting rates by 2.8 and the E2 rates by 1.25, their relative efficiencies for electrons > 0.5 MeV. Detector E is directional, and the maximum and minimum readings from each electron sample have been plotted and labeled perpendicular and parallel, respectively. The bottom trace was made from normalized M detector data. Since the detector response is nearly isotropic, every reading is shown regardless of orientation. This detector responds to electrons > 10 MeV and protons > 80 MeV, the particles being identified by the three channels of pulse height information. The electron component contributes from 30 to 70 count sec^{-1} to channel M1. To show the proton profile below $L = 3$, electrons have been deducted from channel M1 by subtracting 0.0072 times the perpendicular E detector rate and from channel M2 by subtracting 0.0015 times the same rate (M3 needs no subtraction). After this correction, channels M2 and M3 were normalized to M1 by multiplying by 1.4 and 3.3, respectively, their relative efficiencies for protons. For $L > 3$, no subtraction was performed before scaling the channels. At the position of Mimas, a drop-off in the proton profile is shown by channel M3 (■—■). The flat electron profile is visible in channel M1 (x), and the pulse height signature of electrons can be seen during the proton drop-off. In the dip at 1979 S 2, electrons are subtracted and all the normalized data are connected by a line to emphasize the proton drop-off.

lar effects were registered by the other charged particle instruments as well (*17*)]. Outside the sharp minimum, the electron flux shows no sign of depletion and the proton flux is in the middle of a broad depression. The only explanation for such a sharp effect is that Pioneer 11 crossed through, or very close to, the flux tube connected to a large orbiting object. The object is being called 1979 S 2, even though it is probably identical to the object sighted shortly before by the Pioneer 11 imaging instrument (*14*, *15*). Since the planetocentric radial velocity of the spacecraft is 16.4 km/sec at this position, the diameter of 1979 S 2 can be taken to be at least 150 km. It could be larger if the electron drop-off is the cross section of a wake that had begun to fill in, or if Pioneer 11 went through the flux tube connecting to 1979 S 2 but missed the major diameter.

The orbit of 1979 S 2 may be eccentric, since the electron drop-off is noticeably not in the center of the proton absorption zone. Using $2ae$ for the sweeping width of an eccentric orbit, where a is the semimajor axis and e is the eccentricity, one can deduce that $a = 2.52 \pm 0.01\ R_S$ and $e = 0.010 \pm 0.002\ R_S$. These values could change if the magnetic field is shown to have a significant offset. However, this reasoning is confirmed at the Mimas orbit, where the width of the proton sweeping zone, $0.12 \pm 0.02\ R_S$, yields $e = 0.02 \pm 0.003\ R_S$, which agrees with tabulated values (*18*). On the other hand, if we restrict the orbit of the new satellite to perfect circularity, then more than one satellite may contribute to the sweeping of the 80-MeV protons in this region (*17*).

One can also make quantitative inferences about the F ring from trapped radiation measurements. In Fig. 5, the position and width can be read as $2.35 \pm 0.005\ R_S$ and $\leq 0.02\ R_S$, respectively. Bounds can be placed on the total cross-sectional area, mass, and opacity by comparing the sweeping rate of the ring with that of 1979 S 2 and Mimas. We use a statistical sweeping model in which loss rate $-dn/dt$ is proportional to particle density n times some probability p of absorption per unit of time t:

$$\frac{dn}{dt} = -np \qquad (1)$$

We picture the ring as an annulus of width W containing a randomly spaced collection of small objects whose cumulative cross-sectional area is given by A. Every time a trapped particle crosses the equator, its chance of hitting one of the objects is $A/(2\pi\ 2.35\ R_S\ W)$. Thus

$$p = \frac{2}{T_b}\ \frac{A}{2\pi\ 2.35\ R_S\ W} \qquad (2)$$

where T_b is the particle's bounce period. Equation 1 expresses the loss rate during the time it takes the particle to diffuse across the ring; that is, from $t = 0$ to $t = W/V$, where V is the particle's radial diffusion velocity. Integrating Eq. 1 between these limits and using Eq. 2, we obtain

$$A = -\ln\left(\frac{n}{n_0}\right)\ \frac{T_b}{2}\ 2\pi\ 2.35\ R_S\ V \qquad (3)$$

where n/n_0 is the fraction of particles that diffuse safely past the hazard.

All the parameters on the right-hand side of Eq. 3 are known except V, which we obtain by analysis of absorption at the moons. However, for moons the longitudinal distribution of absorbing material is not random: the particle and moon meet only when their relative azimuthal motion brings them past the same longitude. Hence

$$p = \frac{d_{eff}}{P\ L} \qquad (4)$$

(*2*, *19*) where d_{eff} is the sum of the moon's diameter d plus twice the particle's gyroradius r_g, P is the moon's period in the drift frame of the particles, and L is an arbitrary radial diffusion length $>> d_{eff}$.

Using Eq. 4 and integrating Eq. 1 as before from $t = 0$ to $t = L/V$, we obtain

$$V = \frac{-d_{eff}}{P\ \ln\ (n/n_0)} \qquad (5)$$

Table 2. Diffusion velocities past Mimas and 1979 S 2.

Parameter	Electrons (~ 1 MeV)		Protons (~ 80 MeV)	
	Mimas	1979 S 2	Mimas	1979 S 2
r_s (km)	6.4	3.5	1770	940
d (km)	400 ± 100	> 150	400 ± 100	> 150
d_{eff} (km)	410	> 160	3950	≤ 2040
P (hours)	100	300	0.2	0.25
n/n_0	> 19/20	> 19/20	< 1/400	< 1/1500
V (cm sec^{-1})	> 2.2×10^3	> 280	< 9.2×10^4	≤ 3.1×10^4
V (R_s year^{-1})	> 11	> 1.4	< 460	≤ 160

Note that L cancels out of the result. Because there appears to be complete transmission of electrons and complete absorption of protons, we can only give limits for the fraction of particles that survive, and we can only deduce limits on the radial diffusion velocities. Table 2 shows some of the parameters and results of Eq. 5 for 1-Mev electrons and 80-MeV protons at Mimas and 1979 S 2.

At the F ring there appears to be complete absorption of protons and ~ 90 percent absorption of electrons. Because the protons are diffusing immeasurably slowly, an infinitesimal amount of material might be enough to stop them; but the lower limit on the electron diffusion velocity tells us that at least enough material is present to absorb electrons that are diffusing into the ring at this rate. Thus Eq. 3 gives a lower limit for the cross-sectional area of the F ring. By using $n/n_0 = 10$ percent, $T_b = 2.5$ seconds, and the limit on V at 1979 S 2, we get, for the cross-sectional area of the F ring, $A > 7 \times 10^{13}$ cm^2. If the ring particles are uniform with radius h centimeters and density ρ grams per cubic centimeter, the total mass of the ring is at least $> 1 \times 10^{14}\ \rho\ h$ grams. The opacity depends on the radial width over which the ring material is distributed. Since the ring occupies the space $2\pi\ 2.35\ R_S\ W = 9 \times 10^{10}\ W$ cm^2, the opacity τ is bounded by $\tau > 10^3/W$, where W is in centimeters. By using the upper limit to W obtained from Fig. 5, we find a lower bound of $> 10^{-5}$ for τ.

In summary, then, our charged particle data give the following physical parameters for the new satellite 1979 S 2 and the F ring: for object 1979 S 2, the semimajor axis = 2.52 ± 0.01 R_S, eccentricity = 0.010 ± 0.002, and diameter ≥ 150 km; for the F ring, the semimajor axis = 2.35 R_S, width < 10^8 cm, area > 7×10^{13} cm^2, mass > $1 \times 10^{14}\ \rho\ h$ grams, and opacity > $10^3/W$.

There may be evidence for still more moons (*17, 20*). For instance, close inspection of the traces in Fig. 5 reveals a slight concavity in the proton contour at ~ 2.8 R_S—the position given for an earlier, unconfirmed, sighting of a moon tentatively called Janus. This feature is more prominent on the outbound pass, and could be due to sweeping by an orbiting object. However, the object must be tiny to produce such a small effect compared to those of Mimas and 1979 S 2, and it seems questionable that such an object would have been visible from Earth.

The apparent total absorption of 80-MeV protons by Mimas and 1979 S 2 presents an interesting paradox. If the protons of the inner magnetosphere come from the inward diffusion of solar wind particles, how do any get inside these totally absorbing barriers? Two possible explanations are: (i) the inner region is filled during times of higher particle mobility—such as magnetic storms—and (ii) the protons are created in place. The possibility that the particles come from the decay of albedo neutrons created by collisions of cosmic rays with the upper atmosphere and rings of Saturn should be investigated. Called CRAND for cosmic-ray albedo neutron decay, this mechanism is one of the first that was proposed to explain the high-energy component of Earth's radiation belt (*21*).

For CRAND to be an adequate source of protons, the injection rate must be equal to the loss rate. The loss rate is $(J_p/v)/T_p$, where T_p is the proton trapping lifetime, J_p is the trapped proton flux, and v is the proton's velocity. If absorption by the moons is the dominant loss mechanism, then $T_p = T_d$, the average time it takes to migrate to one of the sweeping channels. Treating the proton's radial motion as a random walk,

$$T_d = \frac{\langle \Delta L^2 \rangle}{2D} \qquad (6)$$

where $\langle \Delta L^2 \rangle$ is the mean squared displacement and D is the diffusion coefficient (*22*). The value for $\langle \Delta L^2 \rangle$ can be taken from the width of the region between Mimas and 1979 S 2, and we can use Fick's law (*23*) to obtain the diffusion coefficient

$$D = \frac{-V}{d(\ln n)/dL} \qquad (7)$$

By using 0.04 and 0.02 R_S for $[d(\ln n)/dL]^{-1}$ at Mimas and 1979 S 2, and taking V from Table 2, we get $D < 6 \times 10^{-7}$ and $D < 1 \times 10^{-7}\ R_S^2$ sec^{-1}, respectively. Then, for protons between Mimas and 1979 S 2, $T_d > 1$ day to 1 week.

The injection rate is $(J_n/v)/T_n$, where T_n is the neutron decay lifetime, J_n is the albedo neutron flux, and the neutron's velocity is the same as the proton's. Setting the injection rate equal to the loss

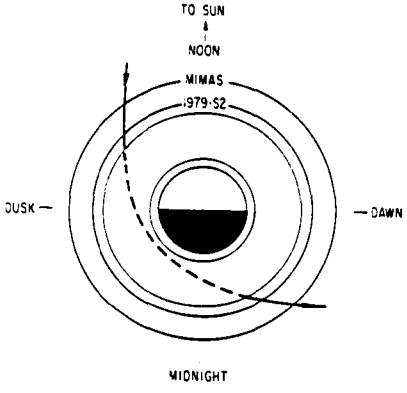

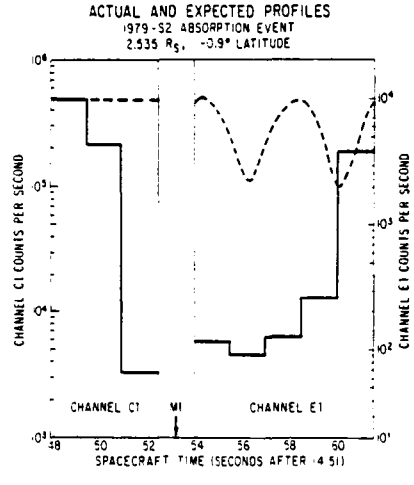

Fig. 6 (left). Trajectory of Pioneer 11 through the inner magnetosphere of saturn. Fig. 7 (right). Actual and expected profiles of the 1979 S 2 absorption event. Each reading from the UCSD instrument is shown for this interval, during which the internal commutator cycled through three channels—C1, M1, and E1. Each reading is a 1.5-second accumulation and is represented by the stepped bar graph. The M1 value was zero. The dashed line shows the counting rates expected on the basis of the neighboring readings. The expected profile of channel E1 reflects the spin modulation of the directional detector in a pancake angular distribution.

rate gives an expression for the proton-trapping lifetime that balances the CRAND source:

$$T_p = \frac{J_p}{J_n} T_n \quad (8)$$

At 2.7 R_S, the proton flux above 80 MeV is $\sim 2 \times 10^4$ cm^{-2} sec^{-1} and the neutron lifetime is 13 minutes. It is possible to calculate the neutron albedo flux at Saturn, but such an effort is beyond the scope of this report. To test the reasonability of our speculation, we merely write J_n as some factor F times the albedo neutron flux at Earth. The latter is ~ 0.1 cm^{-2} sec^{-1} for neutrons above 80 MeV (*24*), so we obtain, for the proton trapping lifetime that balances the CRAND source, $T = \sim 7.5/F$ years. If F is of the order of unity, this number is easily compatible with the diffusive loss time T_d. However, a more satisfying comparison must await a more extensive calculation.

W. FILLIUS
University of California, San Diego, La Jolla 92093

W. H. IP
Max-Planck-Institut für Aeronomie, Katlenburg-Lindau, West Germany

C. E. MCILWAIN
University of California, San Diego

References and Notes

1. B. A. Smith *et al.*, *Science* **204**, 951 (1979).
2. M. H. Acuña and N. F. Ness, *J. Geophys. Res.* **81**, 2917 (1976); W. Fillius, in *Jupiter*, T. Gehrels, Ed. (Univ. of Arizona Press, Tucson, 1976), pp. 896–927.
3. E. J. Smith, L. Davis, Jr., D. E. Jones, P. J. Coleman, Jr., D. S. Colburn, P. Dyal, C. P. Sonett, *Science* **207**, 407 (1980); M. H. Acuña and N. F. Ness, *ibid.*, p. 444.
4. All times given in this report are universal time at the spacecraft, which is obtained from ground-received universal time by deducting the one-way travel time of light (about 1 hour 26 minutes 20 seconds).
5. C. E. McIlwain, *J. Geophys. Res.* **66**, 3681 (1961).
6. In this report, L is the distance from the center of the planet to the equatorial crossing of the magnetic line of force through an observation point. It was computed by using a dipole field model with zero tilt and offset.
7. The unit of distance is the planetary radius, R_S, equal to 60,000 km.
8. J. H. Wolfe, J. D. Mihalov, H. R. Collard, D. D. McKibbin, L. A. Frank, D. S. Intriligator, *Science* **207**, 403 (1980).
9. J. W. Dyer, *ibid.*, p. 400.
10. E. C. Stone, *J. Geophys. Res.* **68**, 4157 (1963); J. G. Roederer, *Dynamics of Geomagnetically Trapped Radiaton* (Springer-Verlag, New York, 1970).
11. J. H. Trainor, F. B. McDonald, A. W. Schardt *Science* **207**, 421 (1980).
12. M. Schulz and L. J. Lanzerotti, *Particle Diffusion in the Radiation Belts* (Springer-Verlag, New York, 1974).
13. S. E. DeForest, *J. Geophys. Res.* **77**, 651 (1972).
14. T. Gehrels *et al.*, *Science* **207**, 434 (1980).
15. W. H. Blume *et al.*, in preparation.
16. R. W. Fillius and C. E. McIlwain, *J. Geophys. Res.* **79**, 3589 (1974); J. A. Simpson, D. C. Hamilton, R. B. McKibbin, A. Mogro-Campero, K. R. Pyle, A. J. Tuzzolino, *ibid.*, p. 3522.
17. J. A. Van Allen, M. F. Thomsen, B. A. Randall, R. L. Rairden, C. L. Grosskreutz, *Science* **207**, 415 (1980); J. A. Simpson *et al.* (*20*).
18. D. Morrison and D. P. Cruikshank, *Space Sci. Rev.* **15**, 641 (1974).
19. A. Mogro-Campero and W. Fillius, *J. Geophys. Res.* **81**, 1289 (1976).
20. J. A. Simpson, T. S. Bastian, D. L. Chenette, G. A. Lentz, R. B. McKibbin, K. R. Pyle, A. J. Tuzzolino, *Science* **207**, 411 (1980).
21. N. C. Christofilos, *J. Geophys. Res.* **64**, 869 (1959); P. B. Kellogg, *Nuovo Cimento* **11**, 48 (1959); S. F. Singer, *Phys. Rev. Lett.* **1**, 181 (1958); S. N. Vernov, special lecture to the Fifth General Assembly of the Comité Special de l'Année Geophysique Internationale, Moscow, 30 July to 9 August 1958.
22. F. Reif, *Fundamentals of Statistical and Thermal Physics* (McGraw-Hill, New York, 1974), pp. 486–488.
23. C. Kittell, *Elementary Statistical Physics* (Wiley, New York, 1958), p. 155.
24. R. E. Lingenfelter, in *Spallation Nuclear Reactions and Their Applications*, B. S. P. Shen and M. Merker, Eds. (Reidel, Dordrecht, Netherlands, 1976), pp. 193–205.
25. We are grateful to S. E. DeForest, E. Whipple, B. Johnson, J. Quinn, M. Greenspan, and C. Olson for assistance with the real-time data. C. Barnes, I. Goldman, and J. B. Blake made generous contributions to the detector calibrations, and E. Smith provided magnetometer data. Discussions with R. E. Lingenfelter were very helpful. The success of the Pioneer spacecraft reflects the superlative job done by the Pioneer Project Office under the leadership of C. F. Hall. This work was supported by NASA contract NAS 2-6552 and by NASA grant NGL-05-005-007.

3 December 1979

JOURNAL OF GEOPHYSICAL RESEARCH, VOL. 85, NO. A11, PAGES 5803–5811, NOVEMBER 1, 1980

Very Energetic Protons in Saturn's Radiation Belt

WALKER FILLIUS AND CARL MCILWAIN

Center for Astrophysics and Space Sciences, University of California at San Diego
La Jolla, California 92093

Very energetic protons are trapped in the inner Saturnian radiation belt. The University of California at San Diego instrument on Pioneer 11 has definitely identified protons of energy >80 MeV on channel M3 and has tentatively detected protons of energy >600 MeV on channel C3. The spatial distribution of the protons is distinct from that of the trapped electrons, the main difference being that the protons are strongly absorbed by the innermost moons and that the electrons are not. We have estimated the source strength for injecting protons by the decay of cosmic ray albedo neutrons generated in the rings of Saturn. The required proton lifetime is ~20 years.

INTRODUCTION

The first spacecraft encounter with Saturn was made in September 1979 by Pioneer 11. Preliminary scientific papers resulting from this flyby were written within 10 weeks and published together in the January 25, 1980, issue of *Science*. This collection provides an excellent overview of the discoveries made by Pioneer 11 and an introduction to further investigations.

One such investigation concerns the trapping of very energetic protons. We identified protons of energy greater than 80 MeV in the inner magnetosphere [*Fillius et al.*, 1980] and suggested that they may have originated with the decay of albedo neutrons formed in collisions between cosmic rays and the rings and upper atmosphere of Saturn. It is known that this mechanism, which bears the acronym Crand, operates on the polar atmospheres of earth to produce a high-energy proton belt in the inner magnetosphere [*White*, 1973; *Lingenfelter*, 1976]. The extrapolation of this mechanism to Saturn seems promising because the location of the rings and the large dimensions of the Saturnian magnetosphere are ideal for producing high trapping efficiencies. On the other hand, the large magnetic moment of Saturn [*Acuna and Ness*, 1980; *Smith et al.*, 1980] allows fewer cosmic rays to penetrate to the planet's surface than is the case at earth. The upper atmosphere probably contains relatively few intermediate Z nuclei, such as oxygen, which are favorable for neutron production. The planet itself may thus be only a weak source in comparison with the rings.

An alternate mechanism for producing these particles is by low-energy injection in the outer magnetosphere followed by inward radial diffusion and acceleration via breakdown of the third and conservation of the first and second adiabatic invariants [*Schulz and Lanzerotti*, 1974]. The problem with such an external source is that the high-energy proton belt appears to be separated from the outer magnetosphere by gaps at the orbits of moons 1979-S2, Mimas, and possibly Enceladus, Tethys, and the E ring as well. The absence of energetic protons in those gaps indicates that the moons patrol their orbits efficiently and sweep up protons which start to diffuse across. Hence the high-energy proton belt is isolated from its supposed source.

In order to fuel the debate over the source of these particles, this paper reexamines the evidence that high-energy protons are trapped in the inner magnetosphere. There are three lines of argument. In part one we compare different channels from our instrument and show that there are two distinctly different radial profiles which characterize electrons and protons separately. In part two we exhibit pulse height data from a solid state detector (detector M) which possesses particle identification capability. In part three we show differences between eastbound and westbound fluxes measured perpendicular to B by our directional Cerenkov detector. This east-west effect is caused by large spatial gradients in the distribution of particles with large gyroradii, i.e., high-energy protons. Of course, proving that high-energy protons are present does not identify their source, but a good description of the proton distribution is an essential first step. Finally, in part four, we estimate the Crand source rate and obtain a critical lifetime for the energetic protons if they do come from neutron decay. Knowledge of the proton lifetime could then decide their source. A solution to that question may come later.

RADIAL PROFILES

Figures 1*a* and 1*b* show radial profiles, inbound and outbound, from detector E and channels CDC and M3 of the University of California at San Diego (UCSD) trapped radiation detector. (Table 1 gives a brief summary of the characteristics. More descriptive information can be found in the paper by *Fillius and McIlwain* [1974].) A difference in character between channels is obvious. The profiles for detector E and channel CDC have an even, monotonic L dependence except where the radiation is absorbed by the A and F rings. The profile from channel M3 falls off more steeply with increasing L and has large dips at the orbital positions of 1979-S2 and Mimas, separated by intermediate maxima. There are two classes of particles: one which has very little interaction with the moons, and another which is swept clear of the moons' orbital paths. The detector design and response characteristics identify the former as electrons of about 1-MeV energy and the latter as protons of above 80-MeV energy.

The difference in profiles is explained by the relative sweeping probabilities of the two particle types. In general, sweeping probability is proportional to the difference between the particle's drift frequency $1/T_d$ and the moon's orbital frequency $1/T_K$; i.e., the relative frequency $1/T_{rel}$ with which their azimuthal motions carry them past each other. A particle's drift frequency is made up of two components: the drift motion caused by the gradient and curvature of the magnetic field, $1/T_m$, and the drift motion imposed by the corotational electric field, $1/T_r$. The magnetic field drift is in the prograde sense for protons and in the retrograde sense for electrons. By

Paper number 80A0936.
0148-0227/80/080A-0936$01.00

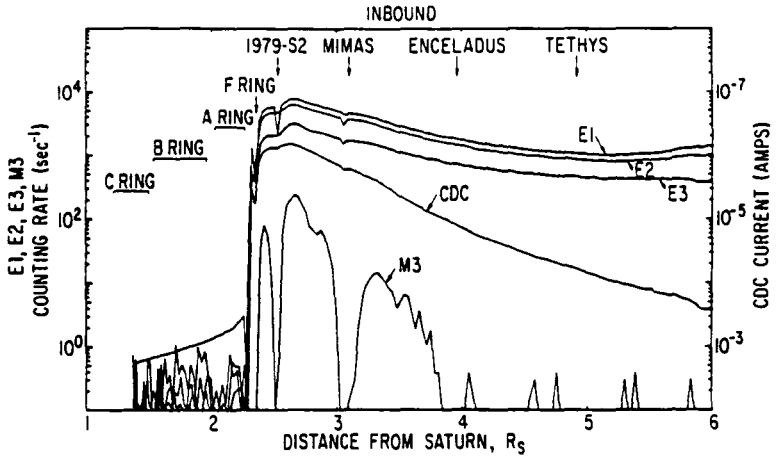

Fig. 1a

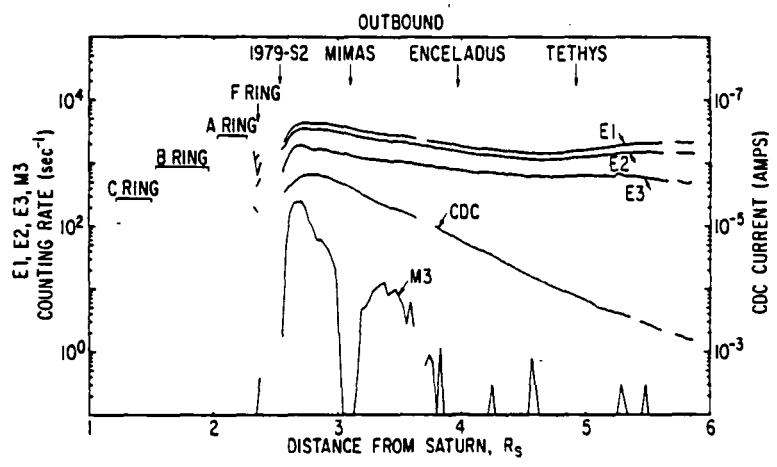

Fig. 1b

Fig. 1. Radial profiles for energetic electrons (channels E1, E2, E3, and CDC) and energetic protons (channel M3) in Saturn's inner magnetosphere. (*a*) Pioneer 11 inbound pass. (*b*) Pioneer 11 outbound pass.

representing prograde motion with a positive period and retrograde motion with a negative period one can write

$$1/T_{rel} = 1/T_d - 1/T_K = 1/T_e + 1/T_m - 1/T_K \qquad (1)$$

Taking 10 h 39.9 min for T_e [*Kaiser et al.*, 1980] and using a dipolar magnetic field to compute T_m, one obtains the relative periods shown in Table 2. For a radially diffusing particle to avoid being swept by a moon, it must move a radial distance equal to the moon's diameter plus two particle gyroradii in less time than the relative period T_{rel}. Thus the gyroradii of the particles add to the difference in their absorption rates. These quantities are also shown in Table 2.

Including both of these effects, the expected difference in absorption rates of 1-MeV electrons and 80-MeV protons is a factor of 10^4. This large difference evidently allows the electrons to fill the moons' orbits, but not the protons.

Radial profiles intermediate between the two types shown in Figure 1 are obtained by detector channels which are sensitive to both electrons and protons. Channels M1 and M2 of our instrument illustrate this type of profile (see Figure 2), as do several of the other detectors aboard Pioneer 11. Their outputs are simply linear combinations of the two types, with proportions depending upon their relative sensitivities to the different kinds of particles.

PARTICLE IDENTIFICATION BY PULSE HEIGHT SPECTRA

Figure 2 shows data from detector M. Besides illustrating the linear combination of electron and proton responses in the first two channels, it demonstrates the particle identification capability of the detector based upon pulse height information. Channels M1, M2, and M3 represent the count rates from three pulse height discriminators connected to a solid state detector buried inside 8 g cm^{-2} of omnidirectional shielding. Discriminator M1 is set just below the minimum ionizing threshold, so that it counts virtually all particles, electrons and protons, that can penetrate the shielding. The ratios of the discrimination levels, M1:M2:M3, are 1:2.12:4.5, which puts discriminator M3 above the maximum expected energy loss for an electron but not above that for a proton. Thus M3 is insensitive to electrons, but its efficiency for protons is a substantial fraction of that for channel M1.

The ratios of counting rates among these channels are an effective diagnostic of particle type. In Figure 2 the ratios M3/M1 and M2/M1 have binary distributions: that is, the ob-

TABLE 1. Characteristics of the UCSD Pioneer 11 Trapped Radiation Detector at Saturn Encounter, September 1979

Channel Name	Discrimination Level	Particle Selectivity	Geometric Factor
		*Cerenkov Counter**	
C1	>31 photoelectrons	pileup of ~2-MeV electrons	20 cm² sr
C2	>65 photoelectrons	pileup of ~2-MeV electrons	20 cm² sr
C3	>135 photoelectrons	$65 \gtrsim E_p \gtrsim 140$-MeV protons	0.002 cm²
		>600-MeV protons	1.5 cm² sr
CDC	10^{-4}–10^{-5} A	>~2-MeV electrons	7.3×10^{-14} A e^{-1} cm² s sr
		Electron Scatter Counter†	
E1	>0.089 MeV	>0.16-MeV electrons	1.3×10^{-2} cm² sr
E2	>0.19 MeV	>0.255-MeV electrons	1.04×10^{-2} cm² sr
E3	>0.40 MeV	>0.460-MeV electrons	5.7×10^{-3} cm² sr
		Minimum Ionizing Particle Counter‡	
M1	>0.40 MeV	>80-MeV protons	0.038 cm²
M2	>0.85 MeV	>80-MeV protons	0.027 cm²
M3	>1.77 MeV	>80-MeV protons	0.012 cm²
		SP Scintillator§	
SPDC	10^{-14}–10^{-5} A	>100-keV protons	7.4×10^{-23} A eV^{-1} cm² s sr (p)
		>10-keV electrons	7.4×10^{-23} A eV^{-1} cm² s sr (e)
		SE Scintillator¶	
SEDC	10^{-14}–10^{-5} A	>100-keV protons	2.0×10^{-24} A eV^{-1} cm² s sr (p$^+$)
		>10-keV electrons	1.4×10^{-23} A eV^{-1} cm² s sr (e$^-$)

*Uses a water-methanol radiator (index of refraction, $\frac{4}{3}$) monitored by a photomultiplier tube with pulse and current output.

†A silicon surface barrier diode detector with a crooked aperture to admit scattered particles only.

‡A silicon surface barrier diode detector buried inside 8-g m^{-2} omnidirectional shielding.

§A scintillator composed of Zn S (Ag) phosphor having a thickness of 1.5 mg cm^{-2} and being monitored by a vacuum photodiode.

¶A plastic scintillator having a thickness of 1.5 mg cm^{-2} and being monitored by a vacuum photodiode.

served values cluster near one or the other of two levels. The low values near the orbits of Mimas and 1979-S2 are characteristic of electrons, and the high values in between are characteristic of protons. It is evident in Figure 1 that there are electrons present between the moons' orbits also, but as the proton counting rate is much higher here, the ratio still indicates protons in these regions. Beyond 3.8 Saturn radii (R_S) the ratios become erratic because of poor counting statistics.

The ratios obtained here in the Saturnian radiation belt are the same as those obtained with an identical instrument in the proton beam of the synchrocyclotron at the Space Radiation Effects Laboratory in Newport News, Virginia, and the beam of the electron linac at Intelcom Radtek in San Diego, California. Thus the pulse height distributions completely verify the identification of radial profiles in the previous section.

EAST-WEST EFFECT

The third line of evidence for energetic protons in Saturn's inner magnetosphere is based upon east-west anisotropies detected by channel C3 of our Cerenkov detector. Right-left asymmetry is present in the channel C3 data below $L = \sim 3$. (Beyond 3 R_S the counting statistics are too poor to show it.) Figure 3 shows the spacecraft trajectory and the viewing geometry projected onto the magnetic equatorial surface, and Figures 4*a* and 4*b* exhibit the east-west anisotropy inbound and outbound.

First let us explain the viewing geometry. Detector C is mounted perpendicular to the spin axis of the spacecraft. The spin axis points to earth, for communications purposes, and since the earth happened to be near the Saturnian vernal equinox during encounter, the scan plane was almost perpendicular to Saturn's equator. Because Saturn's magnetic dipole axis nearly coincides with its spin axis, the scan plane was almost perpendicular to Saturn's magnetic equator as well. The instrument commutator monitors channel C3 continuously for 12 s, obtaining 8 accumulations of 1.5 s each, and then scans other channels for the next 96 s. Since the spacecraft spin period is 7.7 s, the angular distributions are as nearly instantaneous as possible. However, the angular resolution is poor, because the detector sweeps through 70° during each accumulation. (The intended spin period was 12 s. Pioneer 11 made its Saturn encounter at the higher spin rate owing to the failure of a despin thruster.)

Sample angular scans appear in Figures 4*a* and 4*b*. The distributions lean noticeably either to the left or to the right. This trend is verified by the profiles, which show the counting rate interpolated to 90° pitch angle in the east-looking and west-looking directions.

TABLE 2. Times and Distances Relevant to the Absorption of Particles by 1979-S2 and Mimas

Parameter	1979-S2 (2.52 R_S)		Mimas (3.10 R_S)	
	Protons (80 MeV)	Electrons (1 MeV)	Protons (80 MeV)	Electrons (1 MeV)
d, km	150	150	400	400
T_K, hour	16.8	16.8	22.6	22.6
T_m, hour	10.7	10.7	10.7	10.7
T_m, hour	0.24	−27.2	0.19	−22.2
T_d, hour	0.23	17.6	0.19	20.6
T_{rel}, hour	0.23	−386	0.19	228
ρ_g, km	940	3.5	1770	6.4
d_{eff}, km	2030	160	3940	410

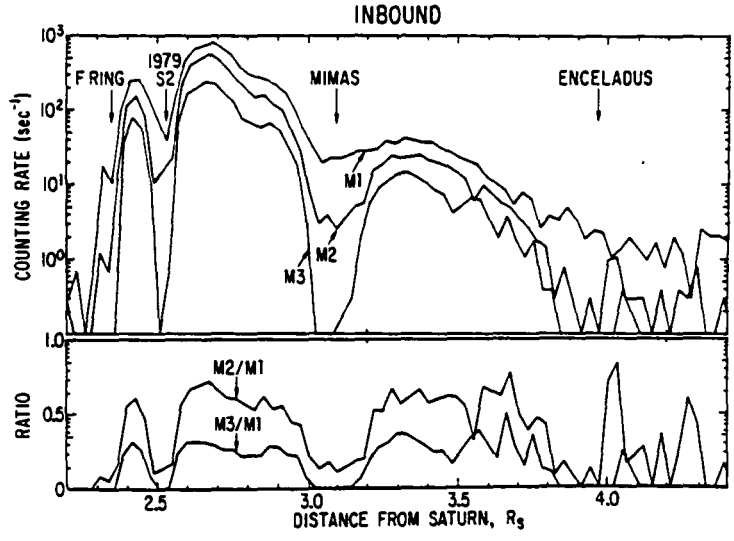

Fig. 2a

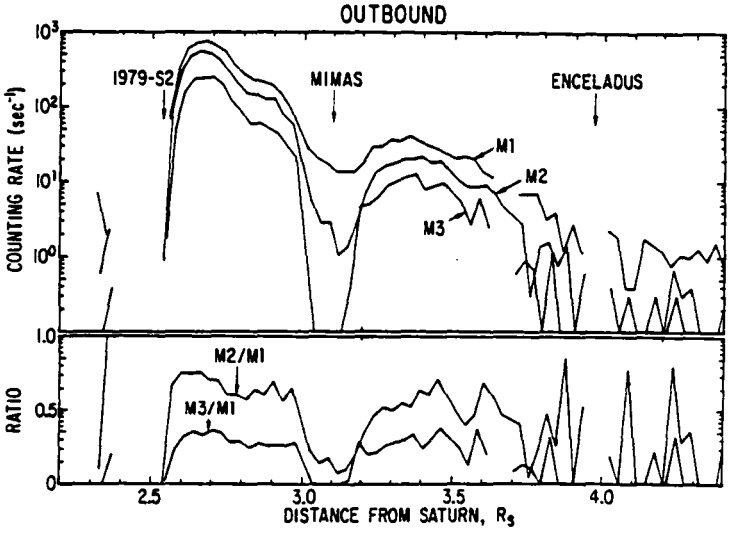

Fig. 2b

Fig. 2. Data from detector M. The top panel shows the counting rates from each channel, M1, M2, M3, and the bottom panel shows the ratios of the rates from the channels indicated. (*a*) Pioneer 11 inbound pass. (*b*) Pioneer 11 outbound pass.

The polarity of the east-west anisotropy follows a pattern with certain key features: (1) The dominant direction changes at or near the peak intensity. (2) The polarity reverses between inbound and outbound passes. (3) In features 1 and 2 mentioned above, the polarity is what one expects from positive particles. There is little likelihood that such a pattern came about by chance. Channel C3 is evidently counting high-rigidity positive particles. Because heavy nuclei would probably not have enough energy to penetrate the detector housing, we take these particles to be protons.

The quantitative evaluation of these features may be undertaken with reference to Figure 3. The magnified portions at $L = 2.75$ inbound and outbound emphasize the difference between the position of a proton's guiding center and its point of detection. If the guiding center density changes appreciably over the distance of a gyroradius, a directional sensor in a fixed position will measure different fluxes looking right and looking left, because the guiding centers are oppositely displaced from the point of observation. This anisotropy can be calculated by using the theory of *Northrop and Thomsen* [this issue]. Figure 4 illustrates an alternate approach. By applying Liouville's theorem to opposing points on a particle's gyrocircle, an observer with an ideal detector expects to measure the same flux looking right at position A and left at position B. Likewise, assuming longitudinal drift symmetry, he expects the same flux looking right at position C and left at position D. The ideal sensor would be sensitive to only one energy and would have a narrow acceptance cone, to sample an infinitesimal element of velocity space. Then the radial separation between right- and left-looking profiles should be equal to the particles' gyrodiameter multiplied by the cosine of θ, the angle between the spacecraft spin axis and the radial direction (see Figure 3). We have used this principle to try to evaluate the particles' energy.

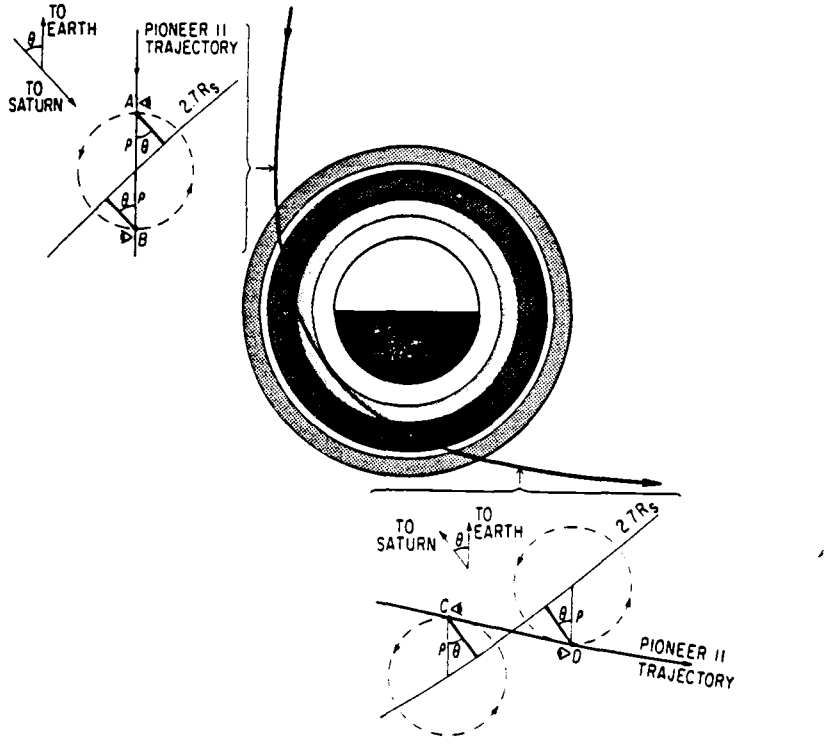

Fig. 3. The Pioneer 11 trajectory and the Cerenkov detector look directions. On the inbound leg, θ was 44°, and on the outbound leg 37.5°. The look directions, left and right, are defined as they appear in the figure; east and west are defined as used by geographers. Thus on the inbound leg, left is eastward and right is westward; on the outbound leg, left is westward and right is eastward.

Because of the sparsity of data the right-looking and left-looking intensities must be obtained by interpolating between data points. To perform the interpolation, we use the method of least squares to fit our data to a truncated harmonic series:

$$c(\chi) = b_1 t + b_2 t^2 + c_0 + c_1 \sin(\chi) + c_2 \cos(2\chi) + c_3 \sin(3\chi) + \cdots \quad (2)$$

where t is time and χ is the spacecraft roll angle measured from the projection of the magnetic field vector onto the scan plane. Cosine terms in odd harmonics and sine terms in even harmonics were deliberately omitted so that the function would be equal parallel and antiparallel to **B**; that is, we are assuming mirror symmetry about a plane perpendicular to **B**. The counting rate is interpolated to the left-looking direction by evaluating (2) at $\chi = 90°$ and to the right-looking direction by evaluating (2) at $\chi = 270°$. Thus $c(\text{left}) = b_1 t + b_2 t^2 + c_0 + c_1 - c_2 - c_3$, and $c(\text{right}) = b_1 t + b_2 t^2 + c_0 - c_1 - c_2 + c_3$. The east-west anisotropy appears in the odd harmonics; the even harmonics allow for flattening or elongation of the angular distribution along the magnetic field direction. Because of undersampling we must restrict the number of fitting parameters by truncating the series. This was also a consideration motivating our assumption of mirror symmetry. In addition to the undersampling difficulties, convolution of the particle distribution with the detector's angular response and accumulation interval results in a severe diminution of the higher harmonic coefficients of the series. In principle, the coefficients can be restored by dividing them by the following factors: $1\chi/0.9230$, $2\chi/0.7181$, $3\chi/0.4516$, $4\chi/0.1999$, $5\chi/0.0186$, and $6\chi/-0.0735$. In practice, terms higher than 3χ cannot be used because the measurement errors are amplified by the restoration process and can get out of hand.

The outcome of the analysis is problematical. We have tried fitting different numbers of data points with various numbers of time and angular coefficients. (Figure 4 was constructed by using 24 data points per fit and truncating the series after the linear time term and the 3χ harmonic.) Between different cases and within individual cases the separation between profiles varies, corresponding to proton energies from 20 to 300 MeV. The threshold for generating Cerenkov light is 480 MeV (at $\beta = \frac{1}{2}$), and the effective counting threshold for channel C3 is 600 MeV. Then there is a disagreement between the detector energy response and our anisotropy analysis. The analysis has been repeated at several points, using the method of Northrop and Thomsen, and the results are similar (T. G. Northrop, private communication, 1979). The latter analysis did not assume an ideal detector; this is not the source of discrepancy. We believe the underlying difficulty is that the angular distributions and radial (equivalent to time) profiles are undersampled and overconvolved. It is probable that the protons' energy is above the Cerenkov threshold; but we cannot rule out the possibility that the rigidity analysis is correct and that the detector responded to protons below the Cerenkov threshold.

It must be acknowledged that these measurements were made in a difficult environment. A high background of electrons (of energy $E_e \sim 2$ MeV) was bombarding the detector, causing pulse pileup in channels C1 and C2 and counting rates in channel C1 as high as 5×10^5 s^{-1}. These particles, however, do not explain the output of channel C3. In the first

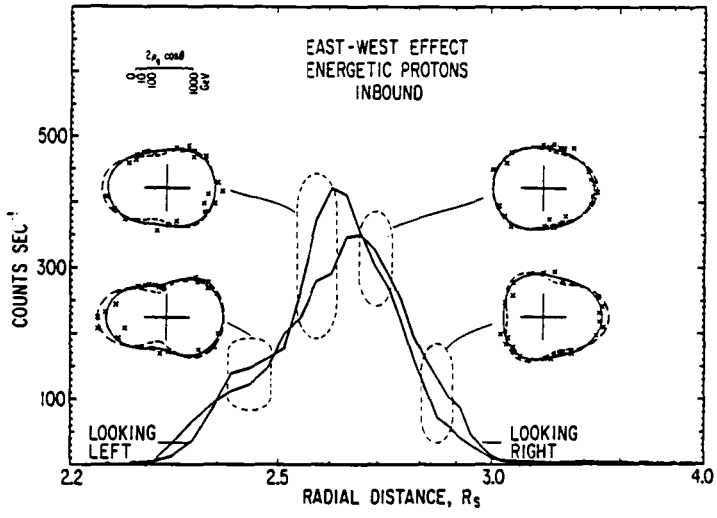

Fig. 4*a*

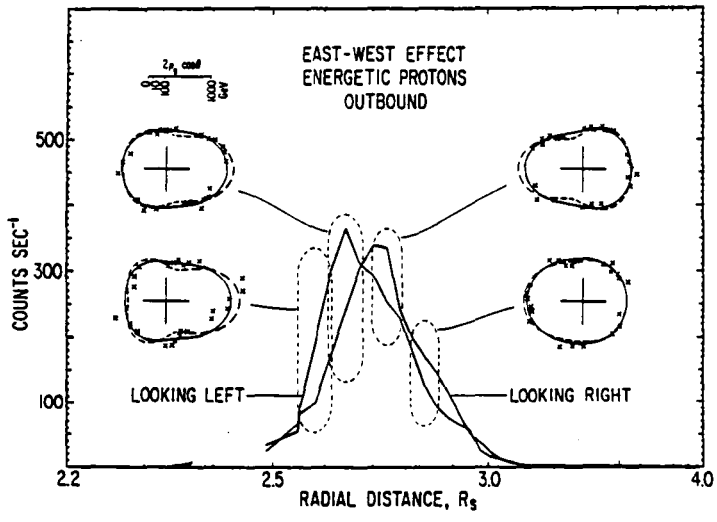

Fig. 4*b*

Fig. 4. Radial profiles from channel C3 of the Cerenkov detector. The radial distance scale is proportional to R^{-2}, so that the gyroradius of a given particle has the same length at all distances. The right-looking and left-looking directions are defined as they appear in Figure 3. The inserts show angular distributions based upon 3 scans of 8 readings each. The crosses are the 24 time-normalized data points; the solid line shows the harmonic fit to the data (equation (2)); and the dashed line shows the fit after deconvolution (see text). (*a*) Pioneer 11 inbound pass. (*b*) Pioneer 11 outbound pass.

place, the same pileup analysis that adequately fit the channel C1 and C2 rates [*Fillius et al.*, 1980] predicts $<10^{-2}$ c/s on channel C3. More empirically, the angular distributions for channel C3 are 90° out of phase with those recorded by channel CDC and the lower-threshold pulse channels that responded to pileup. It is a well understood feature of the detector that for radiation below the single-pulse threshold its cross section is peaked to the side, whereas for high-energy radiation it peaks in the forward direction. This argument puts an empirical upper limit on channel C3 pileup, at the rate recorded parallel to **B**, where the rate was maximum for the lower channels. Also, the radial profile of channel C3 resembles that of our proton channel, M3, rather than that of our electron channels (see Figure 1). Finally, because of both their small rigidity and the wrong polarity, electrons cannot account for the east-west anisotropy discussed above. Nevertheless, it is conceivable that the electron flux could alter the detector's response, for instance by adding randomly to the pulses left by the energetic protons or by disturbing the discrimination level baseline. Also, there could be enough of a high-energy tail to contribute some single pulses directly to the counting rate.

There is evidence for low to moderate contamination by electrons. In comparing Figures 1*a* and 1*b* note that the proton profiles match almost perfectly but that the electron profiles do not: inbound fluxes exceed outbound fluxes by a factor which starts at ~5 at $L = 2.5$ and decreases to unity beyond 3 R_S. This strange asymmetry was recorded by all of the electron detectors in our instrument and is seen in other instruments as well [*Simpson et al.*, 1980; *Van Allen et al.*, 1980]. The inbound and outbound channel C3 profiles in Figure 4*a* and 4*b* are almost identical except for an excess of

counts inside $L = 2.6$ inbound. As our other evidence indicates that protons are excluded from the sweeping corridor of 1979-S2 at $L = 2.52$ and as such an asymmetry is known for electrons, this excess is probably due to electrons.

Electron contamination at this level could be responsible for reducing the observable east-west anisotropy. In Figures 4*a* and 4*b* it is notable that the peaks show the largest horizontal separation—indicating higher-rigidity particles—and the flanks show less separation. The same difference in rigidity is obtained by the method of Northrop and Thomsen (T. G. Northrop, private communication, 1979). If electron background does reduce the observable anisotropy, the reduction should be greatest on the flanks, and the best measurements should be at the peaks. Then this evidence bolsters the argument for high-energy protons.

If we are to entertain all possibilities of abnormal detector response, scintillation in the optical materials is another concern. We calibrated an identical unit on the synchrocyclotron beam at the Space Radiation Effects Laboratory and determined that the scintillation response is very small. Allowing for a gain change in the Pioneer 11 detector at Jupiter encounter, we estimate the geometric factor at <0.002 cm^2 for protons from 65 to 140 MeV. As channel M3 is sensitive to particles in a comparable energy range, a simple comparison indicates that fewer than 16% of the channel C3 counts were from these particles.

ENERGY SPECTRUM

The energetic albedo neutron spectrum at earth can be represented by a power law:

$$J_n(>E) = J_{n0}E^{-0.8} \tag{3}$$

[*Preszler et al.*, 1976; *Merker*, 1972]. Expecting no major change in the nuclear processes, we adopt this spectrum also at Saturn. To relate the neutron spectrum to the proton spectrum, note that a decay proton retains essentially all the momentum of the neutron but that the decay rate is energy dependent owing to the relativistic time dilation factor γ in the neutron lifetime. Then the proton energy spectrum is expected to look like

$$J_p(>E) = J_{p0}E^{-0.8}/[1 + E/(mc^2)] \tag{4}$$

Subsequent radial diffusion may change it, but only by a limited amount, since the protons do not seem to cross the barriers at 2.5 and 3.1 R_S. The Crand theory can then predict the ratio between the counting rates in channels M3 and C3. With the geometric factors listed in Table 1, the predicted ratio of 0.76 closely matches the observation of ~0.7 between $L = 2.5$ and 3.1. Actually, neither the measurement nor the theory possesses the precision suggested by the agreement between these two numbers. Nevertheless, the high-energy interpretation of the channel C3 counting rate is evidently in good accord with Crand theory.

THE CRAND SOURCE STRENGTH

The Crand input to the Saturnian radiation belt can be estimated by comparing with the Crand input at earth.

First, the cosmic ray influx will be lower because the Stoermer cutoffs are higher. *Sauer* [1980] compared Stoermer's theory at Saturn and earth and pointed out a scaling law such that multiplying an earth-related rigidity by a factor of 6 produces the equivalent Saturn-related rigidity. His expression for the cutoff rigidity at Saturn in the vertical direction is

$$pc/e = 90 \cos^4 \lambda/R^2 \quad \text{GV} \tag{5}$$

where λ and R are the observer's latitude and distance in planetary radii from the center of the planet and pc/e is the particle's rigidity, in GV. The cutoff rigidities for particles moving in the eastbound and westbound directions can be obtained by multiplying the vertical rigidity by 4 and 0.69, respectively. The vertical cutoff at the outer edge of the A ring ($R = 2.29\ R_S$) is then 17.2 GV, at the outer edge of the B ring ($R = 1.95\ R_S$) it is 23.7 GV, and at the outer edge of the C ring ($R = 1.53\ R_S$) it is 33.5 GV. At the surface of Saturn on the equator it equals 90 GV, and at the surface of the earth on the equator it is 15 GV. In this energy range the integral cosmic ray intensity varies roughly as E^{-1} [*Meyer et al.*, 1974], and the radial gradient is very small [*Axford et al.*, 1976]. Therefore the integral cosmic ray intensities at the tops of the planets' atmospheres differ by about a factor of 6. However, the intensity incident on Saturn's rings is comparable to that on the earth's equatorial atmosphere.

The relative neutron production rates can now be estimated. The atmosphere of Saturn is expected to be unproductive because besides receiving a factor of 6 smaller influx of primaries it is composed mainly of hydrogen, from which neutrons are not easily made. However, the ring material is probably either water ice or rock, both of which contain major proportions of oxygen. (We have been told that ice is likely (J. Burns, private communication, 1979)). As oxygen and the similar nucleus, nitrogen, are the chief neutron producers in the earth's atmosphere, we will neglect Saturn's atmosphere henceforward and concentrate on the rings.

We can most easily scale neutron production in the rings to that at earth by comparing the rings to the earth's equatorial atmosphere. In so doing we will assume that the ring material is thick enough to allow a mature cosmic ray shower to develop from each primary. About 100–200 g cm^{-2} will do, and it may occur in clumps. In the absence of contradictory information about the ring mass this seems a reasonable assumption. The primary cosmic ray intensity at the rings is down by a small factor, between 15/17.2 and 15/33.5, from that on earth's equatorial atmosphere. However, we are likely to gain back a factor of ~2 from the capture of π^- mesons in the denser ring material. In a diffuse atmosphere most of these particles decay before capture, but in an iceball of a size of $>\sim 1$ m, most would be captured, generating more neutrons [see *Lingenfelter et al.*, 1972]. To relate neutron production in earth's equatorial atmosphere to the global average, we can refer to the values tabulated by *Lingenfelter* [1963, Table 1]. The ratio of equatorial to global production is 0.4. When we collect these factors, we find that the neutron production rate in the rings is about half of the global average rate in the earth's atmosphere.

The proportion of the neutrons that escape from the surface of the rings is dependent upon a model of the rings' structure. The earth's atmosphere, which is our basis for comparison, can be thought of as a semi-infinite slab. Applying this model to the rings has to be a worst case, because some of the neutrons ought to punch through. On the other hand, if the rings are really thin, a higher proportion will penetrate, but the production rate will decrease. Leaving these possibilities to offset each other, we will adopt the same ratio of escape flux to production rate as is obtained at earth.

Our final consideration is the neutron injection efficiency.

Lenchek and Singer [1962] and *Dragt et al.* [1966] took the point of view of a trapped particle and, proceeding backward in time, inquired into the efficiency with which its trajectory may be filled by decaying neutrons from the source. Following these authors, we define an injection coefficient η such that the proton source rate dJ_p/dt is given by

$$dJ_p/dt = \eta J_n/(\gamma T_n) \quad (6)$$

where J_n is the global average neutron albedo flux and γT_n is the dilated neutron lifetime. This agrees with the usage of Lenchek and Singer and differs by a factor of 2 from the definition used by Dragt et al. The latter authors used in the place of J_n the neutron escape current $\bar{J}_n$ defined by

$$\bar{J}_n = 1/(2\pi A) \int J_n \cos\phi \, dA \, d\omega \quad (7)$$

where ϕ is the zenith angle and the integral is taken over the surface of the earth and the upper hemisphere in velocity space. For a globally averaged, isotropic J_n, $\bar{J}_n = J_n/2$. Therefore their values for η are double those used here. Coefficient η reflects a dilution in phase space density which results from the difference between the velocity space occupied by the neutrons, which are confined to a cone defined by the source surface and the observation point, and that occupied by the protons, whose velocities are spread out by their gyromotion and bounce motion. It equals that fraction of a trapped particle's trajectory along which injection is possible, i.e., along which the instantaneous velocity vector of the gyrating proton lines up with that of a rectilinear neutron. Thus the eligible directions are those that scan the source surface. Defined in this way, η includes the inverse distance effect between the source and injection point because, as the distance increases, the solid angle occupied by the source surface decreases.

The rings have a very favorable injection geometry. The maximum possible value for η is 0.5 when the injection point is on the source surface itself. On the L shell at 2.7 R_S, η is about 0.3 for most mirror points. This is an order of magnitude higher than typical injection coefficients on the same L shell at earth.

We can now use (6) to estimate the proton injection rate at 2.7 R_S and from this the trapped proton lifetime T_p. At earth above a threshold of 80 MeV, $\bar{J}_n = 0.1$ cm^{-2} s^{-1} [*Preszler et al.*, 1976; *Merker*, 1972], and so $J_n = 0.2$ cm^{-2} s^{-1}. Then at Saturn, $J_n = \sim 0.1$ cm^{-2} s^{-1}. $T_n = 13$ min, $\eta = \sim 0.3$, $\gamma = \sim 1.1$, and so $dJ_p/dt = \sim 4 \times 10^{-5}$ cm^{-2} s^{-2}. We have measured the trapped proton flux at this point: $J_p = 2 \times 10^4$ cm^{-2} s^{-1}. Setting $dJ_p/dt = J_p/T_p$, we get $T_p = \sim 20$ years. This is the trapped proton lifetime compatible with a Crand source from the rings.

We do not know the lifetimes of protons at Saturn or the identity of the loss mechanism. In our preliminary paper [*Fillius et al.*, 1980] we addressed the diffusive radial motion of the protons and concluded that their lifetime against random excursions into one of the lunar sweeping corridors is greater than several days. Trapping lifetimes of protons in the earth's inner radiation belt are many decades [*Farley and Walt*, 1971]. In this light the value of 20 years at Saturn seems plausible.

CONCLUSIONS

1. Very energetic protons are trapped in the inner Saturnian radiation belt. Protons of energy >80 MeV have been definitely identified by channel M3 of the UCSD trapped radiation detector. These protons are concentrated mainly between Mimas's orbit and the rings and are strongly absorbed by Mimas and 1979-S2. This spatial distribution is distinctly different from that of the energetic electrons, which show very little absorption at the moons' orbits and extend to higher L values.

2. Protons of energy >600 MeV may have been detected by channel C3 of the UCSD instrument. Like the 80-MeV protons, these particles have a peak at $L \cong 2.65$ R_S and absorption features where swept by the adjacent moons. The energy spectrum is consistent with a Crand source.

3. Cosmic ray albedo neutrons are a possible source of energetic protons. Albedo from the rings is probably more effective than from the globe of Saturn. The Crand source strength is estimated to be $\sim 4 \times 10^{-5}$ cm^{-2} s^{-2} at $L = 2.7$ R_S, the peak of the energetic proton belt. This source strength requires a proton lifetime of ~20 years.

Acknowledgments. We have benefited from discussions with R. Lingenfelter, T. Northrop, and S. White. We gratefully acknowledge special help from personnel of the UCSD Computer Center and H. Fischer, the associate director. This paper would not have been written at this time but for the encouragement of A. Opp. This work was supported by NASA contract NAS2-6552 and grant NGL-05-005-007.

REFERENCES

Acuna, M. H., and N. F. Ness, The magnetic field of Saturn: Pioneer 11 observations, *Science, 207*, 444, 1980.

Axford, W. I., W. Fillius, L. J. Gleeson, and W.-H. Ip, Cosmic-ray gradients from Pioneer-10 and Pioneer-11, *Astrophys. J., 210*, 603, 1976.

Dragt, A. J., M. M. Austin, and R. S. White, Cosmic ray and solar proton albedo neutron decay injection, *J. Geophys. Res., 71*, 1293, 1966.

Farley, T. A., and M. Walt, Source and loss processes of protons of the inner radiation belt, *J. Geophys. Res., 76*, 8223, 1971.

Fillius, R. W., and C. E. McIlwain, Measurements of the Jovian radiation belts, *J. Geophys. Res., 79*, 3589, 1974.

Fillius, W., W.-H. Ip, and C. E. McIlwain, Trapped radiation belts of Saturn: First look, *Science, 207*, 425, 1980.

Kaiser, M. L., M. D. Desch, J. W. Warwick, and J. B. Pearce, Voyager detection of nonthermal radio emission from Saturn, *Science, 209*, 1238, 1980.

Lenchek, A. M., and S. F. Singer, Geomagnetically trapped protons from cosmic ray albedo neutrons, *J. Geophys. Res., 67*, 1263, 1962.

Lingenfelter, R. E., The cosmic ray neutron leakage flux, *J. Geophys. Res., 68*, 5633, 1963.

Lingenfelter, R. E., Cosmic ray produced neutrons and nuclides in the earth's atmosphere, in *Spallation Nuclear Reactions and Their Applications*, edited by B. S. P. Shen and M. Merker, pp. 193–205, D. Reidel, Hingham, Mass., 1976.

Lingenfelter, R. E., E. H. Canfield, and V. E. Hampel, The lunar neutron flux revisited, *Earth Planet. Sci. Lett., 16*, 355, 1972.

Merker, M., Energetic neutrons leaking from the top of the atmosphere, *Phys. Rev. Lett., 29*, 1531, 1972.

Meyer, P., R. Ramaty, and W. R. Webber, Cosmic rays—Astronomy with energetic particles, *Phys. Today, 27*, 23, 1974.

Northrop, T. G., and M. F. Thomsen, Theory of scan plane flux anisotropies, *J. Geophys. Res.*, this issue.

Preszler, A. M., S. Moon, and R. S. White, Atmospheric neutrons, *J. Geophys. Res., 81*, 4715, 1976.

Sauer, H. H., On Saturnian cosmic ray cutoff rigidities, *Geophys. Res. Lett., 7*, 215, 1980.

Schulz, M., and L. J. Lanzerotti, *Particle Diffusion in the Radiation Belts*, Springer, New York, 1974.

Simpson, J. A., T. S. Bastian, D. L. Chenette, G. A. Lentz, R. B. McKibben, K. R. Pyle, and A. J. Tuzzolino, Saturnian trapped radiation and its absorption by satellites and rings: The first results from Pioneer 11, *Science, 207*, 411, 1980.

Smith, E. J., L. Davis, D. E. Jones, P. J. Coleman, Jr., D. S. Colburn, P. Dyal, and C. P. Sonett, Saturn's magnetic field and magnetosphere, *Science*, *207*, 407, 1980.

Van Allen, J. A., M. F. Thomsen, B. A. Randall, R. L. Rairden, and C. L. Grosskreutz, Saturn's magnetosphere, rings, and inner satellites, *Science*, *207*, 415, 1980.

White, R. S., High-energy proton radiation belt, *Rev. Geophys. Space Phys.*, *11*, 595, 1973.

(Received June 20, 1980;
revised June 30, 1980;
accepted July 3, 1980.)

INTERPLANETARY

To be presented in Munich, W. Germany
Aug/75 - Cosmic Ray Conference

MEASUREMENTS OF COSMIC RAY ANISOTROPIES FROM PIONEERS 10 & 11

W. I. Axford,* W. Fillius, L. J. Gleeson,** W-H. Ip, and A. Mogro-Campero

University of California, San Diego
La Jolla, California 92037
USA

Cosmic ray anisotropy measurements are performed by the University of California, San Diego experiments on Pioneers 10 and 11. A directional Cerenkov counter sensitive to protons and α particles with kinetic energies $\geq$ 480 Mev/nucleon is used to determine east-west and north-south anisotropies (ξ_{EW} and ξ_{NS}). We find large variations in the anisotropies (e.g., $|\Delta\xi| \sim \langle\xi\rangle$), with a time scale of $\sim$ 60 days for the period April - November 1973 during which Pioneer 11 traversed the region of 1 - 3 AU. The total data set results in a well defined anisotropy, with $\xi_{EW} = 0.46 \pm 0.11\%$ and $\xi_{NS} = 0.03 \pm 0.11\%$. This result for ξ_{EW} is compatible with a large value of the ratio of the perpendicular to the parallel components of the diffusion coefficient ($\kappa_\perp/\kappa_\parallel \simeq 0.22 \pm 0.08$). This result is also consistent with the measurement on Pioneer 10 in November, 1973, at a distance of about 4.5 AU, just before its close encounter with Jupiter.

1. Introduction. This is a progress report on the cosmic ray anisotropy measurements of the UCSD experiment on board Pioneers 10 and 11. The Pioneer 11 results were obtained in the time interval between April and November, 1973, during which the spacecraft travelled from 1 to 2.8 AU. The Pioneer 10 results were obtained at 4.5 AU in November, 1973, just before its close encounter with Jupiter. Here we will report the results from the C1 channel of the Cerenkov detector. This counter detects nuclei with kinetic energy T $\geq$ 480 Mev/nucleon and electrons with T $\geq$ 6 Mev. The quiet time cosmic ray counting rates consist of about 84% protons, 12% α particles, and 2% each from heavy nuclei and electrons. A more detailed description of this instrument is presented elsewhere (Fillius and McIlwain, 1974; Axford et al., 1975). The spacecraft spin axis is always pointing towards the earth. Since the Cerenkov detector is mounted facing perpendicular to the spin axis, its look direction sweeps a circle in a plane perpendicular to the ecliptic plane, so that we can measure both the east-west and north-south components of the cosmic ray anisotropies.

* Max-Planck Institut für Aeronomie, Lindau/Harz, West Germany
** Monash University, Clayton, Victoria 3168, Australia

2. Instrumental response. To investigate the azimuthal streaming of the cosmic ray particles, we can express the angular distribution of the cosmic ray intensity I in the spacecraft equatorial plane as

$$I = I_o\left[1 + \sum_{n=1}^{N} \xi_n \cos\, n(\Psi - \Psi_n)\right] \tag{1}$$

where Ψ is the clock angle and Ψ_n is the direction of the n^{th} order term in the cosmic ray anisotropies. The first term ξ_1 is the resultant of the east-west and north-south anisotropies. With a unidirectional detector we can restrict ourselves to the first order term. Therefore Eq. (1) can be reduced to

$$I = I_o\left[1 + \xi_1 \cos(\Psi - \Psi_1)\right] \tag{2}$$

Since the spacecraft is rotating rapidly with a period of about 12 sec the detector will sweep a certain angular path δ within one data accumulation period. Such averaging effect will reduce the measured value of ξ_1 by a factor

$$f_1 = \sin(\delta/2)/(\delta/2) \tag{3}$$

In order to have a satisfactory angular resolution we only use the data with $\delta = 45^\circ$ and 90°. The reduction factor f_1 will consequently be 0.97 (45°) or 0.90 (90°). A similar reduction factor, namely, $f_2 = \sin(\pi/m)/(\pi/m)$, is also introduced due to our division of the angular distribution of the counting rates into m equal sectors. Here we have put $m = 8$, therefore $f_2 = 0.97$.

Another source of convolution of the experimental values is due to the finite width of the angular response of the C1 detector. It can be calculated that the corresponding reduction factor f_3 for protons is 0.81 (see Fig. 1 for the pattern of angular response). As for α particles, which make up $\sim$ 12% of the total counting rate, there is no experimental calibration. An approximation is made by assuming the ratio of response from the forward to that from the backward direction is 10:1. The resulting value of f_3 is estimated to be $\simeq$ 0.52. The total reduction factor due to instrumental effects is therefore equal to $f = f_1 f_2 f_3$. For both spacecrafts $f \simeq 0.63$. However, we must be careful in applying this result. For example, this method is not applicable for cases of angular distribution of cosmic ray intensity different from those defined in Eq. (2). Also, the derived value of ξ_1 is only the component tangential to the equatorial plane of the spacecraft and not necessarily the total value since here we are incapable of measuring a full 3-dimensional distribution.

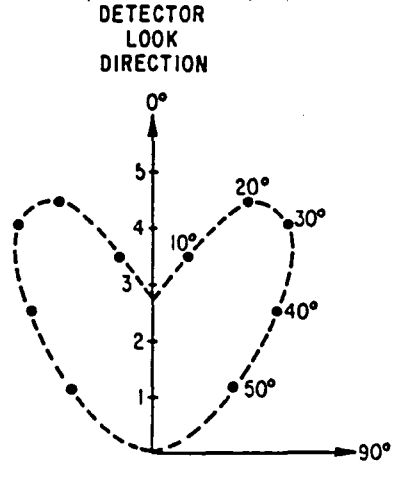

Fig. 1

3. Experimental results. We will first discuss the result from Pioneer 11. The counting rate of channel C1 from April to November, 1973, is shown in Fig. 2. At the end of April we observe a solar event followed by a Forbush decrease. In Fig. 3 we present the angular distribution of the counting rates during this event. To obtain the anisotropy pattern of the solar cosmic ray particles we have substrated the background counting rate due to the galactic cosmic ray particles from the data. It is evident that there exist large anisotropies on the order of 10% for the first six hours of the event. In this interval a peak value of ~ 50% has been observed with a finer time resolution. This azimuthal component of the solar cosmic ray streaming anisotropy persists for another day and then evolves into a sort of dumb-bell pattern at the later stage.

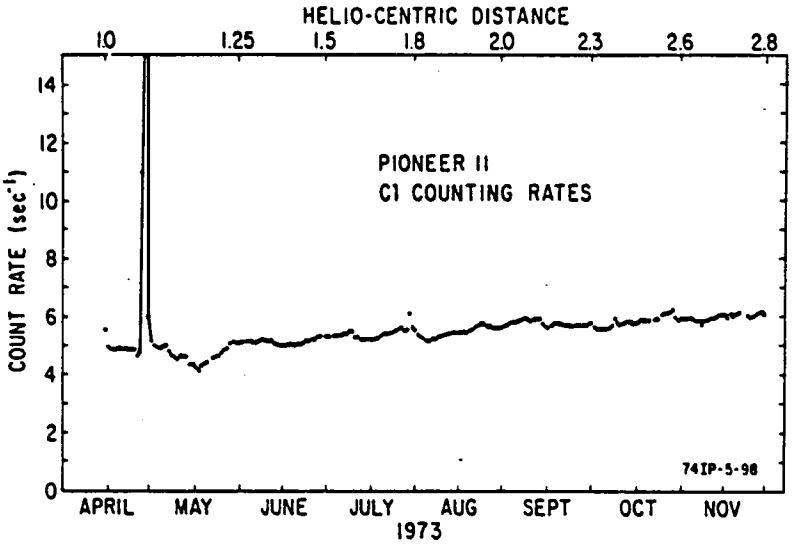

Fig. 2

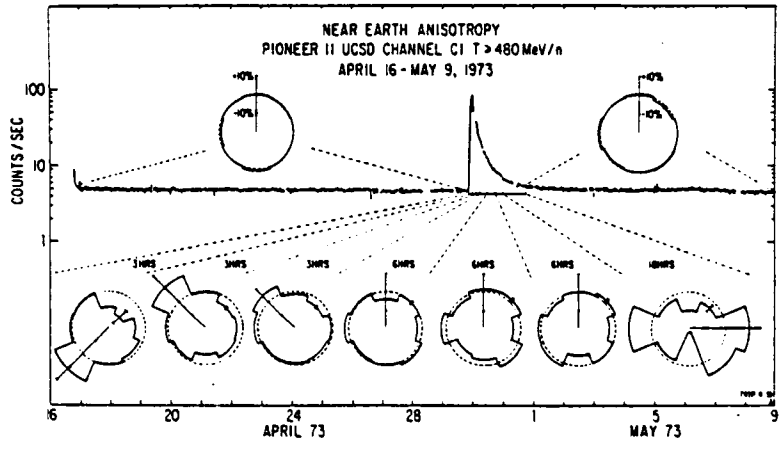

Fig. 3

The two-week averaged values of the east-west anisotropies ξ_{EW} have been computed. These are shown in Fig. 4a. Here the east-west anisotropies have an oscillatory pattern with a periodicity of about 59 ± 7 days. The ξ_{EW} value varies between -0.5% to +1%. Such a feature might be related to the conditions in interplanetary space, i.e. the sector structure of the interplanetary magnetic field, propagation of disturbances due to solar events, etc. Due to the lack of magnetic data at the present moment we are unable to pursue the correlation between the cosmic ray anisotropies and the interplanetary magnetic fields. As for mapping with solar events, there appears to be no direct correlation, at least, with the recurrence of the event in April which would lead to a periodicity of ~ 27 days. For the sake of comparison the two-week averaged values of the north-south anisotropies are plotted in Fig. 4b. It is clear that their magnitudes are much smaller than those of the east-west components. In fact, the average value for the whole period, with the solar event excluded, is (0.03 ± 0.11)% while the corresponding value of ξ_{EW} is (0.46 ± 0.11)%. The above values are obtained by adopting a reduction factor f = 0.63 in our calculation. We can apply the method of transormation as discussed in Sec. 2, since the angular distribution of cosmic rays for the total data set (Fig. 5) can be approximated by a sinusoidal variation as defined in Eq. (2). The maximum-minimum axis is found to be pointing in the east-west direction and the value of ξ_1 before adjustment for the instrumental effect is 0.29%

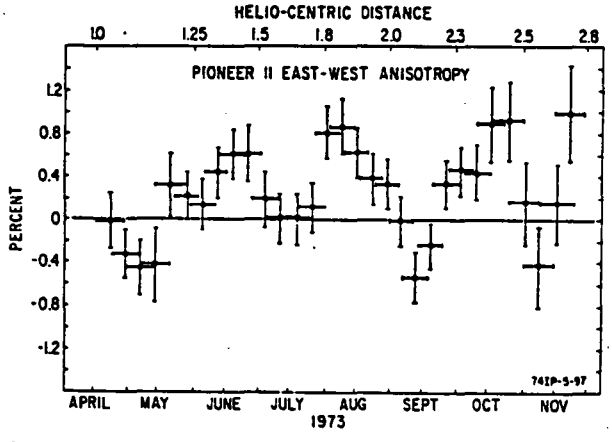

Fig. 4a

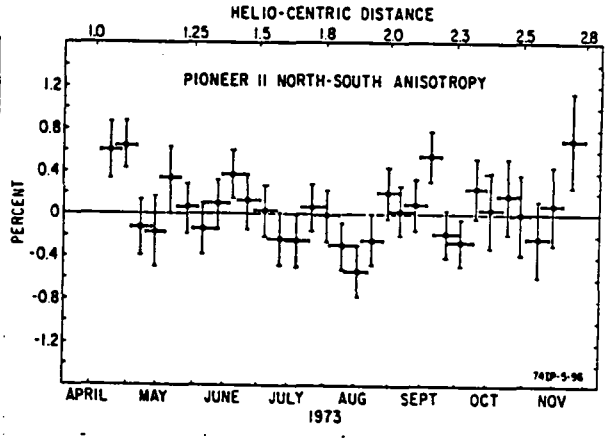

Fig. 4b

About a month before close encounter with Jupiter, Pioneer 10 was operated again in the favorable bit rate formats. In Fig. 6 is shown the C1 counting rates for Nov. 3 - Nov. 25, 1973, and the corresponding angular distribution of the cosmic ray anisotropies. We have divided the data set into several sections (A - G) according to the degree of Jovian electron contamination (Chenette et al., 1974; Teegarden et al., 1974). During the time intervals of

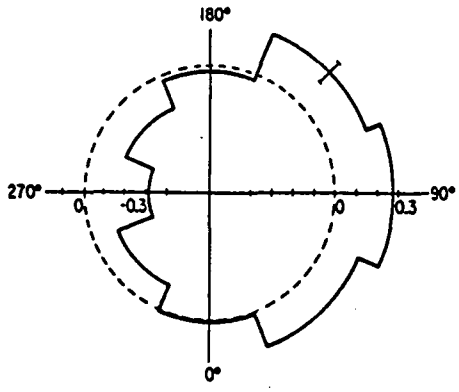

Fig. 5

Jovian electron events (sections B, D, and F), it is clear that the intensity in the hemisphere towards Jupiter is enhanced, indicating streaming of energetic electrons from Jupiter, with $\xi_1 \sim 2\%$ and $\psi_1 \sim 125^\circ$. On the other hand, the angular distributions of the cosmic ray intensity during 'quiet times' (sections A, C, E, and G) do not have a fixed pattern. The averaged value of ξ_1 for these time intervals combined together, has an east-west component $\simeq 0.6 \pm 0.4\%$ if the reduction factor f = 0.63. It is interesting to note that the results from both Pioneer spacecrafts point to a small value of ξ_{EW} throughout interplanetary space from 1 AU to ~ 5 AU, with measurements made at approximately the same time period. In the following section we will discuss briefly certain consequences of these results.

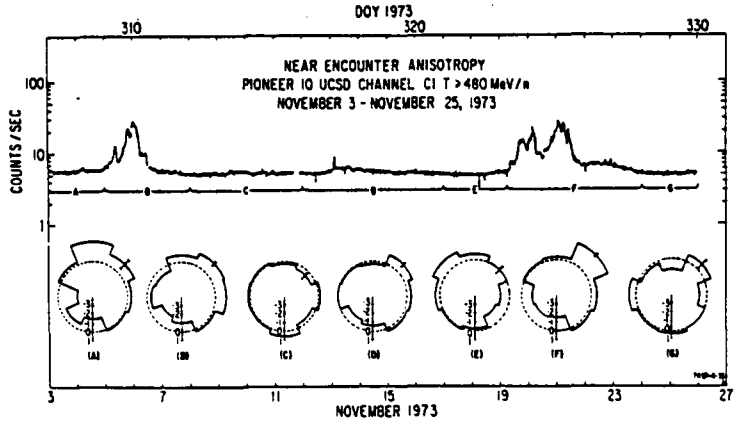

Fig. 6

4. Discussion. For the models of solar modulation of galactic cosmic rays, one of the unknown parameters is the ratio of the components of the diffusion coefficients, perpendicular ($\kappa_\perp$) and parallel ($\kappa_\parallel$) to the interplanetary magnetic field. Different values of this ratio would cause significant variation in the radial dependence of the corotation anisotropy, as suggested by Forman and Gleeson (1975). This relation is summarized in Fig. 7. Briefly speaking, the azimuthal anisotropy as a function of heliocentric distance has a maximum at $r = (\kappa_\parallel/\kappa_\perp)^{1/2}$, and larger values of $\kappa_\perp/\kappa_\parallel$ result in smaller values

of ξ_{EW}. Since this theoretical result is obtained by assuming steady state conditions and spherical symmetry, it may not be meaningful to compare it with the results in Fig. 4a, where large variations in ξ_{EW} are observed. However, for any model which assumes that the propagation of cosmic rays can be represented by steady state and spherical symmetry conditions in time scales $\geq$ the time for the solar wind to travel from the sun to a distance significantly larger than the radial positions of the spacecraft (e.g. 10 AU), it may still be appropriate to fit the observed average value of ξ_{EW} = (0.46 ± 0.11)% to a certain value of $\kappa_\perp/\kappa_\parallel$

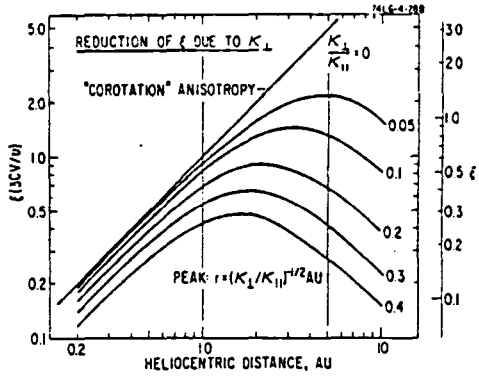

Fig. 7

within the range of 1 - 2.8 AU. After correcting for the small deviation of the plane in which the measurements are performed with respect to the E-W direction, and assuming that ξ_{EW} = 0.6 at 1 AU for $\kappa_\perp/\kappa_\parallel$ = 0 (as in Fig. 7), the resulting ratio is $\kappa_\perp/\kappa_\parallel \simeq 0.22 \pm 0.08$. This value is consistent with our Pioneer 10 result at 4.5 AU, and is higher than the value for this ratio deduced near 1 AU, where $\kappa_\perp/\kappa_\parallel \ll 1$ for E $\geq$ 1 Gev (e.g., see Rao, 1972).

5. Acknowledgment. This work was supported in part by NASA Grant NGR-05-009-081 and by Contract NAS 2-6552.

6. References.

Axford, W. I., Fillius, R. W., Gleeson, L. J. and Ip, W-H., submitted to Ap. J., 1975.

Chenette, D. L., Conlon, T. F. and Simpson, J. A., J. Geophys. Res., 79, 3551, 1974.

Fillius, R. W. and McIlwain, C. E., J. Geophys. Res. 79, 3589, 1974.

Forman, M. A. and Gleeson, L. J., Astrophys. & Space Sci. (in press), 1975.

Rao, U. R., Space Sci. Rev., 12, 719, 1972.

Teegarden, B. J., McDonald, F. B., Trainor, J. H., Webber, W. R., and Roelof, E. C., J. Geophys. Res., 79, 3615, 1974.

THE ASTROPHYSICAL JOURNAL, 210:603–613, 1976 December 1

COSMIC-RAY GRADIENTS FROM *PIONEER-10* AND *PIONEER-11*

W. I. AXFORD,* W. FILLIUS, L. J. GLEESON,† AND W.-H. IP
University of California, San Diego
Received 1974 October 28; revised 1976 April 19

ABSTRACT

The University of California at San Diego Cerenkov counters on the *Pioneer-10* and *Pioneer-11* spacecraft en route from Earth to Jupiter detect cosmic-ray protons and α-particles with kinetic energy $T > 480$ MeV per nucleon and cosmic-ray electrons with $T > 6$ MeV. Using simultaneous data from the two spacecraft, we have determined the cosmic-ray integral intensity gradient in the time interval 1973 April 16–August 31. During this period, *Pioneer-10* moved from 4.06 to 4.66 AU and *Pioneer-11* from 1.02 to 2.11 AU. We have used data in different channels to determine the counting rate from Jovian electrons and to subtract this from the cosmic-ray counting rate on *Pioneer-10*. During April and May there was a solar event followed by a Forbush decrease; we have examined the effect of this event on the measured gradient. It appears that disturbances of this kind can cause large changes in the gradient values. The radial gradient is found to be 0.15 ± 2.3 percent per AU, and we consider this value to be basically consistent with zero. We have calculated the theoretical gradient in this integral energy range using the force-field approximation and expect a value of about 8 percent per AU. Suggestions advanced to explain the discrepancy between theoretical and observed values include: (1) that the accepted diffusion coefficients are too low; (2) that spherically symmetric models are inadequate; (3) that temporal variations of the interplanetary medium are important; and (4) that another transport mechanism is required.

Subject heading: cosmic rays: general

I. INTRODUCTION

In this paper we report observations of the variation with heliocentric distance of the intensity of (mainly) cosmic-ray protons and α-particles having kinetic energy $T \gtrsim 480$ MeV per nucleon obtained between 1.02 and 4.66 AU in the period 1973 April–August.

These observations were made using the University of California at San Diego (UCSD) experiments on board *Pioneer-10* and *Pioneer-11* (*P10* and *P11*) as they traveled from Earth to Jupiter. They are of considerable interest currently in view of the fact that other observers are reporting gradients in the $T \sim 80$ MeV per nucleon range that are a few times less than those estimated in theoretical models using the best available prior estimates of the diffusion coefficients appropriate to cosmic rays in interplanetary space (see later references and discussion).

Pioneer-10 was launched on 1972 March 3 and encountered Jupiter in 1973 early December; *Pioneer-11* was launched on 1973 April 6. In this report we discuss the data between 1973 April 16 and August 31 (days 106–243). Positions of the two spacecraft, Earth, and Jupiter during this period are shown in Figure 1; *P11* moved from 1.02 to 2.11 AU, and *P10* from 4.06 to 4.66 AU.

* Max-Planck-Institut für Aeronomie, Lindau/Harz, West Germany.

† Monash University, Clayton, Victoria, 3168, Australia.

II. INSTRUMENTATION

The UCSD experiments on *P10* and *P11* each contain a Cerenkov counter designed to measure electron intensities in the magnetosphere of Jupiter. Since they respond to charged particles with $\beta > \frac{1}{2}$, they are well suited to count cosmic rays during the interplanetary cruise. The cosmic rays detected are protons, α-particles, and high-Z nuclei with $T > 480$ MeV per nucleon, and electrons with $T > 6$ MeV. The electron energy cutoffs are set by the particles' penetration depth through the housing and in the radiator. Three integral pulse-height discriminators, set for short, medium, and long path lengths in the radiator, provide a measure of the particles' range and angle of incidence. The highest discriminator requires a long range with favorable incidence along the detector axis toward the photodetector. Small pulses may be caused by short-range electrons that stop in the radiator, or by penetrating particles with unfavorable incidence angles. Since nuclei with velocities above the Cerenkov threshold all have ranges much greater than the dimensions of the detector, the three channels have essentially the same energy threshold for these particles and differ only in the sizes of their acceptance cones.

The different electron energy thresholds, the geometric factors for protons, and the counting rate composition are shown in Table 1. The proton geometric factors were derived from accelerator runs

TABLE 1

INTERPLANETARY RESPONSES OF THE CERENKOV COUNTERS

SATELLITE	PROTON GEOMETRIC FACTOR (cm² sr)	COUNTING RATE COMPOSITIONS (%)				ELECTRON ENERGY THRESHOLD (MeV)
		Protons	Alphas	High-Z Nuclei	Electrons	
P10:						
C1.....	15.5	81	15	2	2	6
C2.....	4.5	63	30	5	2	9
C3.....	0.47	23	59	17	1	13
P11:						
C1.....	17.8	82	14	2	3	5
C2.....	6.5	68	26	4	2	8
C3.....	0.93	34	52	13	1	12

using pions and from cosmic-ray muon calibrations, and the composition was deduced using the energy spectra and relative abundances of cosmic rays as measured in the vicinity of Earth (Webber 1973). These numbers had to be obtained indirectly, as particle beams are not available for direct calibration. The electron energy thresholds were determined experimentally (Fillius and McIlwain 1974), and the counting rate contribution from interplanetary cosmic-ray electrons was deduced from the spectrum of Caldwell *et al.* (1975). At launch approximately 1 percent of the counting rate was due to the Radioisotope Thermoelectric Generator (RTG) power source; this may increase by a factor of 2 by the time of the encounter with Jupiter. Our deduced responses predict the observed counting rates very well.

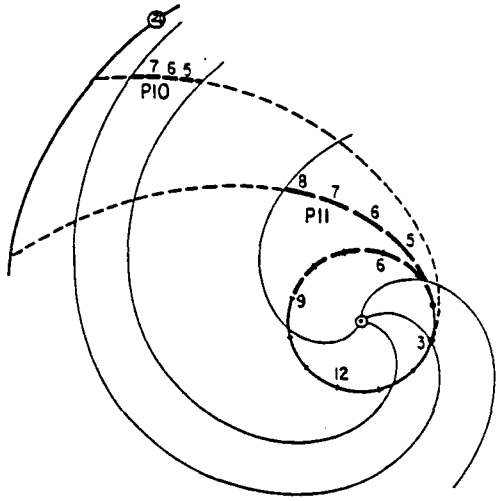

FIG. 1.—The trajectories of Earth, Jupiter, *Pioneer-10*, and *Pioneer-11* in the ecliptic plane, 1973 April 15–August 31. The heavy sections indicate the region traversed during the measurements reported in this paper. The mean interplanetary magnetic-field spirals are also shown.

A careful cross-calibration between the instrument on *P10* and that on *P11* was performed by comparing the prelaunch spectra induced by cosmic-ray muons at ground level. Using the counting rate of the high-energy neutron monitor at Kula, Hawaii, as reference and the appropriate corrections for atmospheric pressures and temperature with latitude (Carmichael, Bercovitch, and Steljes 1967; Bercovitch 1973), we confirmed that the muon fluxes at the times of our calibration runs were identical within 2 percent. Then, from the prelaunch muon calibration spectra, we determined that the discriminators on *P11* are lower than those on *P10* by a uniform factor of 0.83 ± 0.02. When we want to correct for this difference, we interpolate the observed *P11* pulse-height spectrum to the *P10* discrimination levels. A typical value for the correction factor is 0.75, with a systematic uncertainty of ± 0.03 arising from the determination of the relative discrimination levels.

Stability of the detectors is supported by laboratory tests of the prototype and flight instruments and by comparison with other sensors in flight. It was verified that the flight detectors and electronics experience no changes over the temperature range encountered. We did not have the flight instruments in the laboratory long enough to establish an aging baseline as long as the flight. However, an identical prototype detector was recalibrated after 3 years and showed no change.

The sensor used for comparison in flight is a silicon surface-barrier detector (channel M1) buried inside a passive omnidirectional shield. We have not used it for measuring gradients because we do not know *a priori* the relative geometric factors of *P10* and *P11*. Its energy response extends from ~85 MeV per nucleon to infinity. Since about 23 percent of the singly charged and 33 percent of the multiply charged particles in this range are below the Cerenkov threshold, different gradients for different energies and different species could cause these channels to differ somewhat. However, these are inherently stable sensors, and it is of interest to compare them with the Cerenkov counters. We have performed least-squares fits on the ratios of the M1 to the C1 counting rates versus time. Over the 140 day baseline, the time-dependent regression coefficient would allow decreases

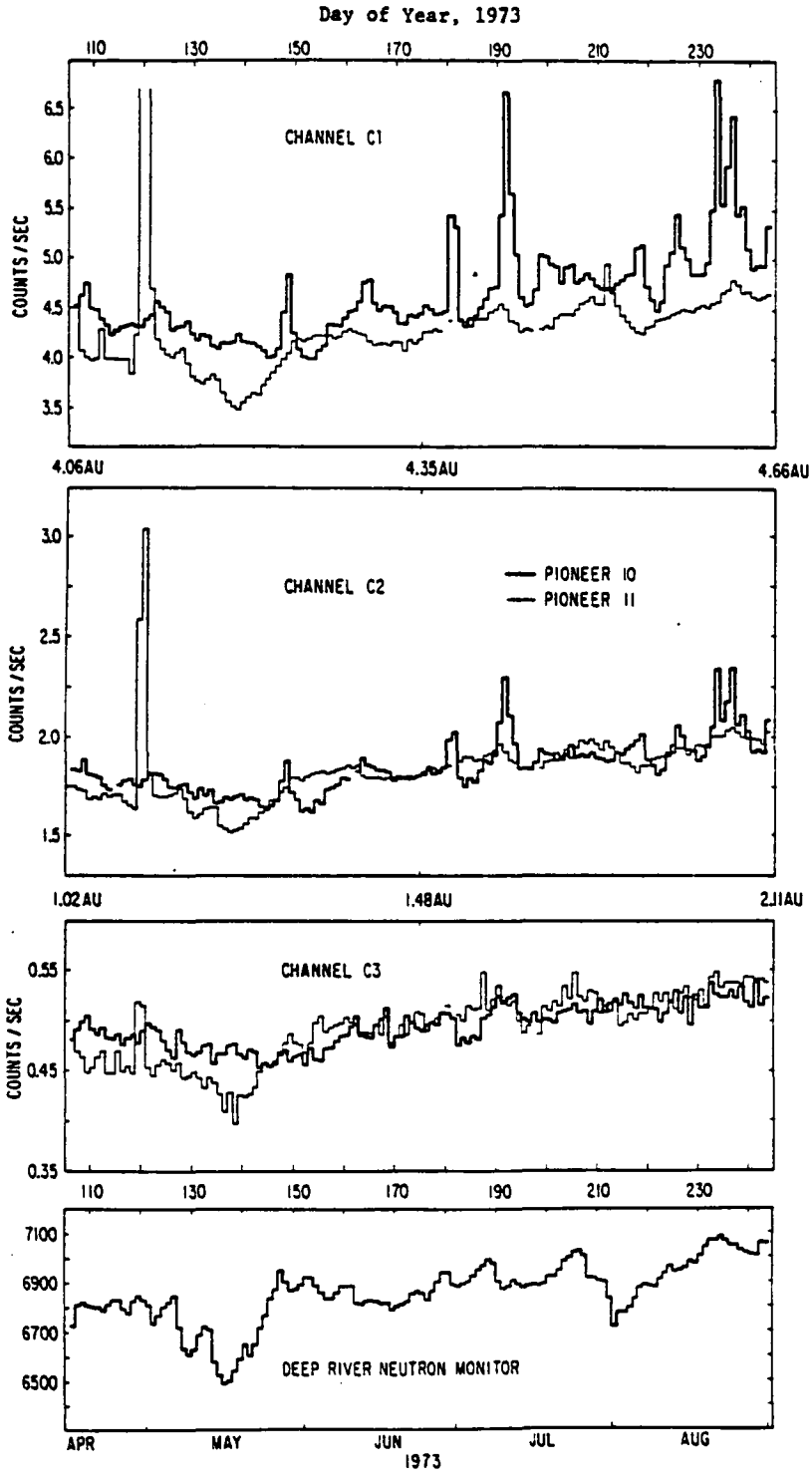

FIG. 2.—Counting rates of the three channels of the Cerenkov detectors on *Pioneer-10* and *Pioneer-11* in the time period between 1973 April 16 and August 31 (days of year 106–243). The *Pioneer-11* rates have been normalized to the *Pioneer-10* discrimination levels. Corresponding counting rates of the Deep River neutron monitor are also shown with arbitrary scale.

in the M1/C1 ratio of 5.4 ± 5.2 percent for *P10*, and 1.7 ± 1.4 percent for *P11*. These numbers are comparable with the day-to-day statistical fluctuations of the ratios (±4%), and they are compatible with zero. Thus the comparison supports the conclusion that both Cerenkov detectors are stable in flight.

Because of the time sharing of the electronic accumulator, each channel is in action for only one-ninth of the total time. With average counting rates of 5, 2, and 0.5 counts s^{-1}, we obtain approximately 4.8×10^4, 1.9×10^4, and 4.8×10^3 counts per day, and the error in the daily average counting rates due to statistical fluctuations is about 0.5, 0.7, and 1.4 percent.

III. OBSERVATIONS

The counting rates (daily average) observed on *P10* and *P11* during the period of analysis are shown in Figure 2. The Deep River neutron monitor daily average counting rate is also shown. This monitor has a magnetic vertical cutoff rigidity of ~1.0 GV (protons with $T > 480$ MeV; α-particles with $T > 120$ MeV per nucleon), which is similar to the threshold of our Cerenkov counter. However, because of the complexity of the magnetic cutoff and the effects of atmospheric absorption, the overall response is somewhat different from detector *C*. Therefore, we do not use the neutron monitor to compute a gradient; but the data do show interesting similarities.

The counting rates all rise steadily, except where they are modified by solar events, Forbush decreases, and Jovian electron events (Chenette, Conlon, and Simpson 1974; Teegarden *et al.* 1974). Solar events occurred on days 119 and 211, and the first one produced a large spike in the *Pioneer-11* detector. The Forbush decreases are most pronounced in the neutron monitor and *P11*. There is a systematic time shift in these features that seems to be the time taken for the solar wind to blow from the Earth to the spacecraft. Omitting disturbed periods, we have calculated correlation coefficients between the neutron monitor and the two spacecraft, using a time lag of $\Delta R/V$, where V is an assumed solar wind velocity. The correlations are optimum for a solar wind velocity of 400–500 km s^{-1}, values which compare favorably with those measured by the solar wind analyzer on board the spacecraft (Wolfe, private communication).

The Jovian electron events appear as spikes in the *P10* data. The electrons are most prominent in channel C1 and less so in channels C2 and C3 because of their higher electron energy thresholds.

IV. DETERMINING THE GRADIENT FROM THE DATA

If we define the gradient g by $g = \Phi^{-1} d\Phi/dr$ and suppose that the cosmic-ray intensity Φ is a separable function of time and radial distance r from the Sun, then we can represent the intensity by

$$\Phi(r, t) = T(t) \exp(gr) . \quad (1)$$

For a channel on *Pioneer-10* with geometric factor G_{10}, the average counting rate for a selected day, t_i, is then

$$C_{10}(t_i) = G_{10} T(t_i) \exp[g r_{10}(t_i)] , \quad (2)$$

where $r_{10}(t_i)$ represents the position of *Pioneer-10* as a function of time. The average counting rate for the corresponding channel on *Pioneer-11* is

$$C_{11}(t_i) = G_{11} T(t_i) \exp[g r_{11}(t_i)] . \quad (3)$$

When we normalize C_{11} for the small difference between *Pioneer-10* and *Pioneer-11* discrimination levels, we get

$$C_{11}'(t_i) = G_{10} T(t_i) \exp[g r_{11}(t_i)] . \quad (4)$$

G_{10} appears in equation (4) because C_{11}' is the rate that would have been recorded by the *Pioneer-10* detector at the same position. The adjustment factor $k_i \equiv C_{11}'(t_i)/C_{11}(t_i)$ is computed each day from the observed pulse-height spectrum and is typically about 0.75 (see § II).

Method 1.—The gradient can be obtained by dividing equation (2) by equation (4) and taking the logarithm. Representing $\ln [C_{10}(t_i)/C_{11}'(t_i)]$ by $X'(t_i)$ and $r_{10}(t_i) - r_{11}(t_i)$ by $\Delta r(t_i)$, we get

$$g_1(t_i) = X'(t_i)/\Delta r(t_i) . \quad (5)$$

We write g_1 to distinguish this method from another, explained below. Note that method 1 is an instantaneous measurement; we compute a new value each day from simultaneous intensity measurements on the two spacecraft.

The influence of the instrumental cross-calibration can be evaluated by writing

$$g_1(t_i) = [\ln C_{10}(t_i) - \ln k_i - \ln C_{11}(t_i)]/\Delta r(t_i) , \quad (6)$$

using the definitions of $X'(t_i)$ and k_i. An error Δk_i creates an error

$$\Delta g_1(t_i) = -\frac{1}{\Delta r(t_i)} \frac{\Delta k_i}{k_i} . \quad (7)$$

For the calibration accuracy quoted in § II, $\Delta g_1 \approx 1.5$ percent per AU.

Method 2.—The necessity for cross-calibration can be avoided by using a time-lapse method to evaluate the gradient. In this method, the intensities at different radial separations are measured by one instrument as it moves with respect to the other. The second instrument is used to separate out the time dependence, $T(t)$, of the cosmic radiation. Divide equation (2) by equation (3) and take the logarithm,

$$X(t_i) = \ln (G_{10}/G_{11}) + g\Delta r(t_i) , \quad (8)$$

where $X_i(t_i) = \ln [C_{10}(t_i)/C_{11}(t_i)]$. If the time period is long enough for Δr to change substantially, a linear regression analysis of X versus Δr yields a constant and a slope. The slope is the gradient, g_2, and, as it

TABLE 2

THE RADIAL GRADIENT $\Phi^{-1}d\Phi/dr$

PERCENT PER AU	METHOD 1* AVERAGE OF DAILY DETERMINATIONS (Electron Elimination Procedure)		METHOD 2† TIME-LAPSE DETERMINATION (Electron Elimination Procedure)	
	No Bursts	Subtraction Using Simultaneous Linear Equations	No Bursts	Subtraction Using Simultaneous Linear Equations
		Channel C1		
With FDI‡.....	+2.5 ± 1.7	+1.7 ± 1.5	+3.2 ± 3.9	+9.7 ± 2.6
Without FDI‡.....	+2.0 ± 1.7	+1.2 ± 1.3	−12.2 ± 4.7	−1.0 ± 2.8
		Channel C2		
With FDI‡.....	+0.3 ± 1.6	−0.3 ± 1.7	+12.0 ± 3.4	+14.5 ± 2.5
Without FDI‡.....	−0.4 ± 1.3	−1.0 ± 1.2	−7.4 ± 3.9	+0.9 ± 2.7
		Channel C3		
With FDI‡.....	+0.4 ± 1.7	0.0 ± 1.8	+19.3 ± 3.3	+18.8 ± 2.6
Without FDI‡.....	−0.5 ± 1.1	−0.8 ± 1.2	− 2.0 ± 3.0	+3.1 ± 2.5

* The error estimates quoted for method 1 represent the variance in the day-to-day determinations of g_1. An additional uncertainty of ~1.5 percent per AU arises from the cross-calibration of the detectors. The effect of counting statistics is negligible.

† The error estimates quoted for method 2 represent the uncertainty in determining the slope of eq. (8) by an rms fit. The effect of counting statistics is negligible, and there is no contribution from detector cross-calibrations.

‡ FDI = Forbush decrease interval.

represents data at different positions from the same instrument, it depends only on instrument autocalibrations (time stability). The cross-calibration between instruments appears in the constant term, which is not needed.

Determining the radial gradient of the cosmic radiation would be straightforward if the cosmic-ray intensity were accurately represented by equation (1) and there were no statistical errors or disturbances in the data. However, in our data set (Fig. 2), Forbush decreases disturb the galactic radiation, and, furthermore, solar particles and Jovian electrons are present part of the time. We find differences between the way these disturbances affect the results of method 1 and method 2, and we seek techniques by which these effects may be eliminated.

The solar particles are easily disposed of by omitting three days during the May event. For the Forbush decreases and Jovian electrons, we adopt a shotgun approach, and compare the results of different techniques and methods (Table 2). Two techniques for eliminating the Jovian electrons produce similar results, and we are satisfied that these particles do not contaminate our answers. The Forbush decrease effect is harder to eliminate, although method 1 gives more consistent results.

A rough and easy way to eliminate the effect of Jovian electrons is simply to omit periods when bursts are present. Excluding these days, we obtain the gradient values shown in Table 2 under the label "no bursts." However, this technique does not eliminate electrons that may be present between bursts.

To handle these quiet-time Jovian electrons, we use all three channels and take advantage of the fact that they have different relative geometric factors for Jovian electrons than for galactic nucleons. The counting rate of each channel is a sum of contributions from nucleons and electrons:

$$S_i = N_i + E_i \quad (i = 1\text{–}3), \tag{9}$$

where S_i is the total counting rate, N_i is the portion caused by nucleons, E_i is the portion triggered by electrons, and the subscript denotes channel C1, C2, or C3. By looking at data taken far from Jupiter when there is no electron activity, we can determine the ratios $\alpha_{ij} \equiv N_i/N_j$. Similarly, by taking data during electron bursts (and subtracting out a steady nucleonic component), we can determine the ratios $\beta_{ij} \equiv E_i/E_j$. With these ratios we can solve the simultaneous equations (9) for E_i and N_i:

$$E_i = \frac{\beta_{ij}(\alpha_{ij}S_j - S_i)}{\alpha_{ij} - \beta_{ij}},$$

$$N_i = \frac{\alpha_{ij}(S_i - \beta_{ij}S_j)}{\alpha_{ij} - \beta_{ij}}. \tag{10}$$

The main error in this solution arises from uncertainty

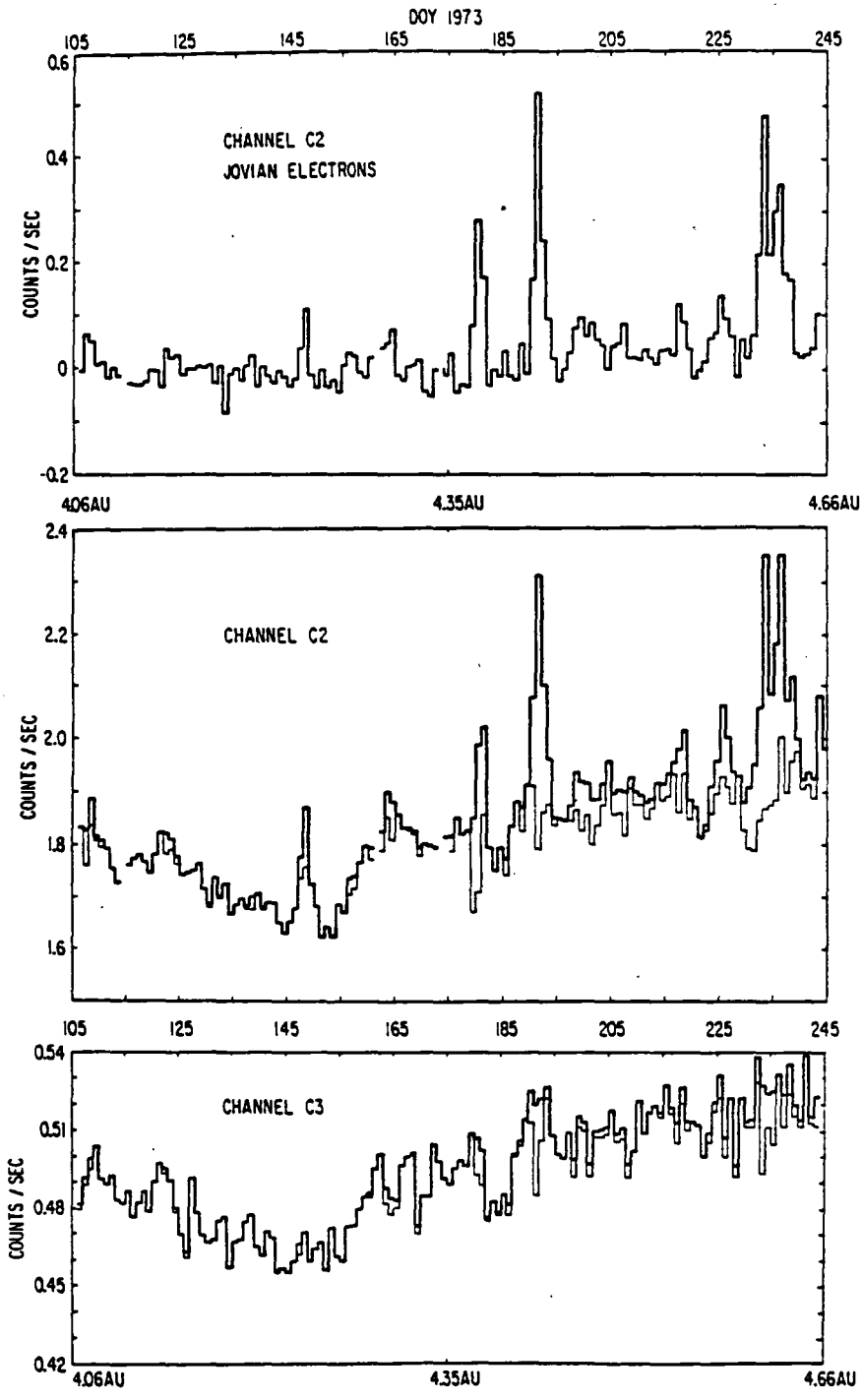

FIG. 3.—*Pioneer-10* counting rates decomposed into the separate contributions of nucleons and Jovian electrons. (*a*) The contribution of Jovian electrons to channel C2. (*b*) and (*c*) (*heavy line*) the total counting rate; (*thin line*) the nucleonic component alone.

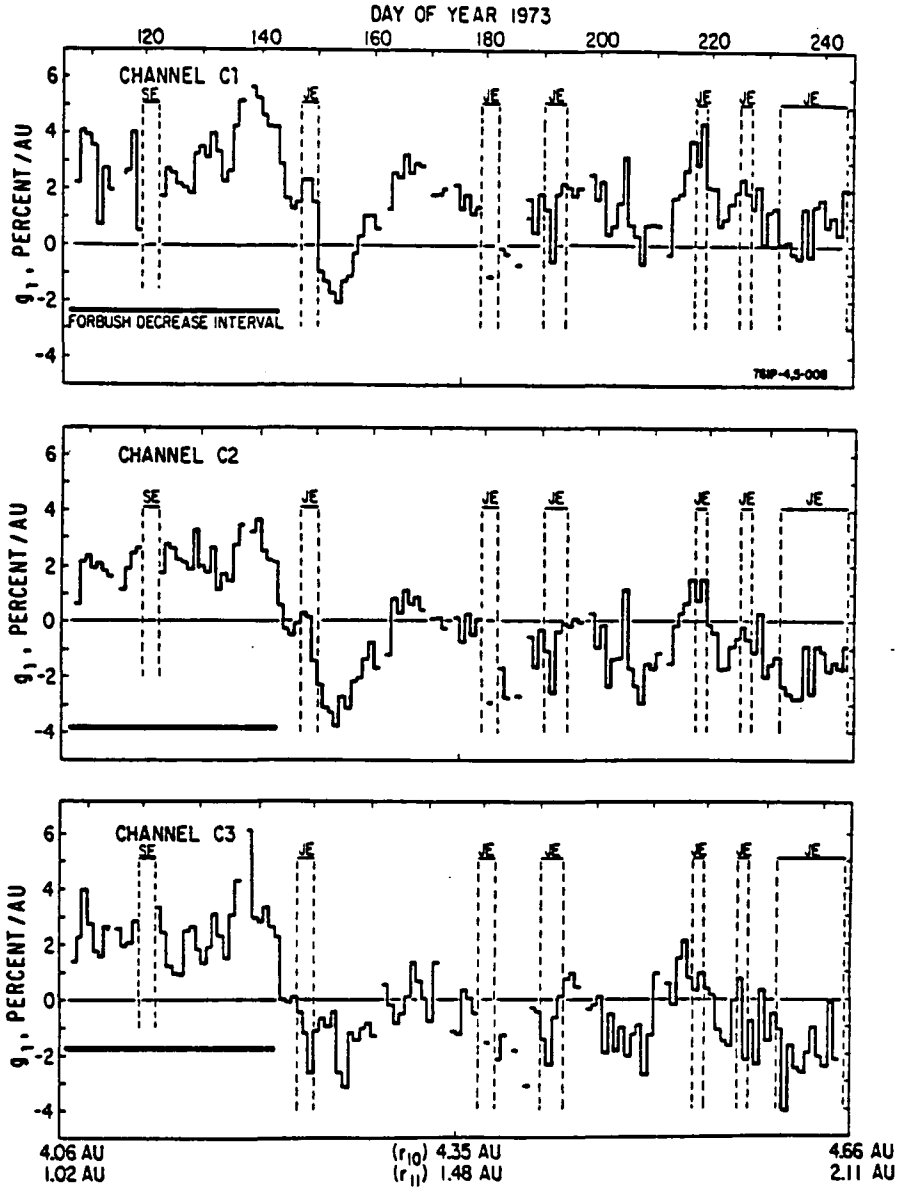

FIG. 4.—Radial gradient values calculated for each day using eq. (5). The times are indicated for the solar event (SE), Jovian electron bursts (JE), and Forbush decrease.

in the β_{1j} when there is a large fraction of electrons present:

$$\frac{\Delta N_1}{N_1} = \frac{1}{\alpha_{1j}/\beta_{1j} - 1}\left[\frac{E_j}{N_j}\frac{\Delta\beta_{1j}}{\beta_{1j}} - \frac{\Delta\alpha_{1j}}{\alpha_{1j}}\right], \qquad (11)$$

where $\alpha_{12}/\beta_{12} = 0.57$, $\Delta\beta_{12}/\beta_{12} = 0.18$, $\Delta\alpha_{12}/\alpha_{12} = 0.01$, $\alpha_{13}/\beta_{13} = 0.14$, $\Delta\beta_{13}/\beta_{13} = 0.63$, and $\Delta\alpha_{13}/\alpha_{13} = 0.01$.

Figure 3 presents the result. Figure 3*a* shows the channel C2 counting rate caused by Jovian electrons. The rise of the baseline indicates that there is a small residue of electrons present between bursts. For the most part this result agrees well with the electron counting rates for the same period of time given by Teegarden *et al.* (1974) and by Chenette, Conlon, and Simpson (1974). In Figures 3*b* and 3*c* we show the counting rates of channels C2 and C3 with and without Jovian electron subtraction. The correction for the C2 counting rates is sometimes substantial; that for channel C3 is not.

After the correction for Jovian electrons, we can

proceed to calculate the radial gradients of the undisturbed cosmic rays. Figure 4 shows the daily values of g_1 for channels C1, C2, and C3. The times are indicated when electron bursts were present. These intervals were omitted before, but by using the electron subtraction procedure, we can include them without introducing any apparent bias to the results.

Gradients calculated by this procedure are listed in Table 2 under the heading "Electron Elimination Procedure: Subtraction Using Simultaneous Linear Equations." Under both methods 1 and 2, there is no large departure from the gradient values calculated by omitting the times of the electron bursts. Figures 3 and 4 show that the electrons are accounted for, and the evidence is that Jovian electrons do not significantly contaminate our results.

There remains the question of what effect the Forbush decreases have on our results. There is a 27 day cycle apparent in Figure 4 that arises from the large Forbush decrease after the solar event of day 119 and the following recurrent decreases visible in Figure 2. In addition, there seems to be a time variation between the positive values of g_1 before the initial Forbush decrease and the negative values thereafter. We have computed gradient values for the entire time interval (days 106–245) and, to exclude the initial Forbush decrease, once again just for the interval between days 143 and 243. Table 2 compares the results. It is evident that method 2 is highly dependent on the time interval chosen, but the average of method 1 values is not. The susceptibility of method 2 is illustrated in Figure 5, where we have plotted ln (C_{10}/C_{11}) versus Δr. The straight lines show the minimum variance fits to equation (8) for the time intervals. It is clear just from looking at the data that the slopes will be different for the two cases. It is noteworthy that Forbush decreases do not satisfy the separation of time and spatial parameters assumed in equation (1). Because of the radial propagation lag, these decreases arrive at *Pioneer-10* later than at *Pioneer-11*, and the ratio C_{10}/C_{11} goes first up and then down, like a differentiated pulse. Such a differentiated pulse will perturb the slope of ln (C_{10}/C_{11}) versus Δr, but not the average value ln (C_{10}/C_{11}).

Time changes in the propagation conditions must also be considered in weighing these results. If the gradient g is a function of time, one would expect to see the time dependence mapped out by method 1. Method 2, on the other hand, should be either modified or segmented in such a way as to match the changes, or else averaged over a larger sample in which several changes tend to balance one another. The primary uncertainty in determining the gradient from our data set arises not from counting rate statistics, not from instrument calibrations, and not from extraneous electron and solar proton events. One can bracket these uncertainties by selecting different time periods for analysis. The primary uncertainty arises from time changes in the data. These time changes appear to be real; they limit the precision with which we can determine a value for the gradient.

In consideration of this uncertainty, we prefer to quote values determined by method 1. The best technique for eliminating Jovian electrons is subtraction using simultaneous linear equations. Combining statistics, calibrations, and time fluctuations into one error term, and averaging the results from the three channels, we get a gradient of 0.15 ± 2.3 percent per AU. Because of the relatively large error, we could consider the measured gradient as consistent with zero.

V. THE EXPECTED GRADIENTS

Calculations of the differential gradient to be expected in spherically symmetric models have been given by Urch and Gleeson (1972) for protons and α-particles of kinetic energies above 10 MeV per nucleon. They provide a guide but cannot be used directly, as the present observations are integral and consist of a mixture of two species. To provide the integral gradients and a background for discussion, we give the following analysis.

We omit the electron and high-Z nucleon contributions and consider the counts as composed of protons and α-particles. The gradients expected are a function of the cosmic-ray modulation and hence of solar activity. The solar activity was at a minimum and the cosmic-ray flux maximum in 1965; the solar activity was at a maximum and the cosmic-ray flux minimum about 1969; and, according to the cosmic-ray monitors (J. Humble, private communication), in 1973 conditions were again approaching those of the 1965 solar-activity minimum. Consequently, we use solar-minimum spectra for our conditions and take those given in the review of Webber (1973).

At the energies of the UCSD experiment ($T \gtrsim 480$ MeV per nucleon), the differential gradient $\gamma(r, T)$ at radius r and kinetic energy T is given closely by the force-field approximation,

$$\gamma(r, T) = C(r, T)V(r)/\kappa(r, t)\,, \qquad (12)$$

with $C(r, T)$ the Compton-Getting factor (depending on spectral slope), V the solar wind speed, and $\kappa(r, T)$ the (energy-dependent) diffusion coefficient (Gleeson and Axford 1968; Gleeson and Urch 1973). Different values of C and κ, and hence of γ, apply for each species. The differential gradient expected with an instrument counting two species is

$$\gamma = f_p\gamma_p + f_\alpha\gamma_\alpha\,; \qquad (13)$$

the subscripts p, α refer to protons and α-particles, and f_p, f_α to the fraction of the counts due to each species. The cosmic-ray intensity spectra for protons and α-particles at $T \gtrsim 480$ MeV per nucleon have substantially the same form (e.g., Gloeckler and Jokipii 1967).

The integral gradient of a species is

$$g(r, T) = \int_T^\infty \gamma(r, T')j(r, T')dT' \Big/ \int_T^\infty j(r, T')dT'\,, \qquad (14)$$

with $j(r, T)$ the differential intensity. For a composite

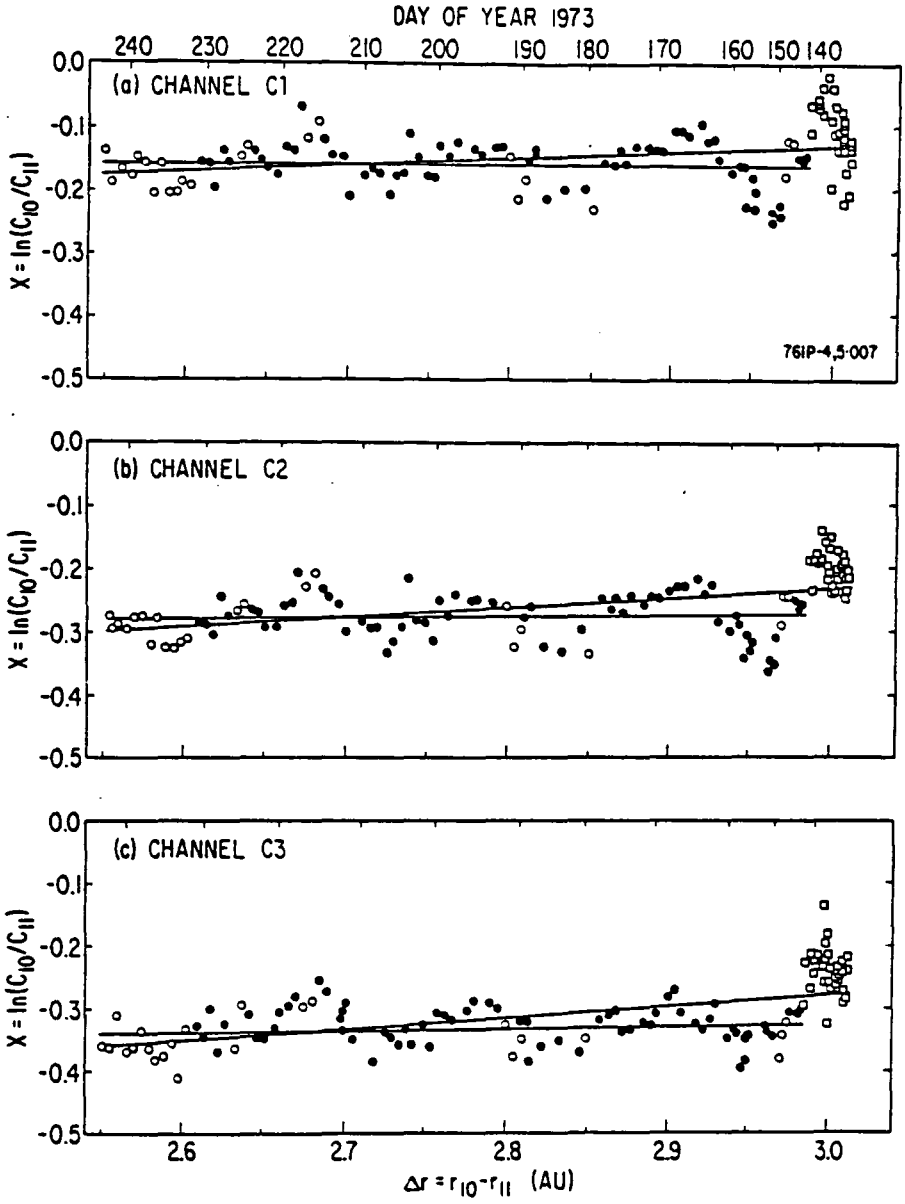

FIG. 5.—The ratios of *Pioneer-10* to *Pioneer-11* counting rates plotted as a function of their radial separation. Time goes from right to left because *Pioneer-11* was moving faster than *Pioneer-10*. Data during the Forbush decrease are plotted with the open squares; the days of Jovian electron events are plotted with open circles. The lines represent least-squares linear fits, one to the entire data set, and the other excluding the time of the Forbush decrease.

measurement such as reported here, the expected integral gradient is

$$g = f_p g_p + f_\alpha g_\alpha ; \qquad (15)$$

this formula is dependent on the differential spectra having (approximately) the same form.

The usual value of V is about 350 km s^{-1}; values of C range from about 0.6 to 1.6 for the present particles. At these energies, the diffusion coefficients used in numerical studies which reproduce the observed modulation and consistent with magnetic-field data have been of the form $\kappa = \kappa_0 P\beta$ with P the particle rigidity and β = (particle speed)/(speed of light) (Urch and Gleeson 1972). This form of κ gives $\gamma = CV/\kappa_0 P\beta$ with $\gamma_\alpha = \frac{1}{2}\gamma_p$ at the same kinetic energy per nucleon. It also follows that, with similar

differential intensity spectra, $g_\alpha \approx \frac{1}{2} g_p$. Hence, for our conditions of measurement,

$$g = (f_p + 0.5 f_\alpha) g_p . \quad (16)$$

Urch and Gleeson (1972), based on the magnetic-field power spectrum work of Jokipii and Coleman (1968), used $\kappa = 2.2 \times 10^{21}$ cm^2 s^{-1} for protons at $P = 1$ GV and hence $\kappa_0 = 3 \times 10^{21}$ cm^2 s^{-1} (GV)$^{-1}$ for 1965 (solar-minimum) interplanetary conditions.

Using these values, $V = 380$ km s^{-1}, and the solar-minimum spectra in Figure 12 of Webber (1973), we find that the corresponding differential gradients at kinetic energies of 500, 1000, and 4000 MeV per nucleon are 22.0, 16.9, and 5.9 percent per AU, respectively, for protons (γ_p) and about half these values for α-particles (γ_α). The integral gradients for $T \geqslant 480$ MeV per nucleon calculated from (5), and assuming these diffusion coefficients and spectra, are

$$g_p = 10.0\% \text{ per AU}, \qquad g_\alpha = 6.5\% \text{ per AU}. \quad (17)$$

The corresponding composite integral gradient expected for the UCSD instrument is thus

$$g = 9.3\% \text{ per AU for channel C1},$$
$$g = 8.7\% \text{ per AU for channel C2},$$
and
$$g = 7.3\% \text{ per AU for channel C3} \quad (18)$$

in the vicinity of the orbit of Earth.

For completeness, and later reference, the values of C, γ, and g, at several kinetic energies, are given in Table 3 for solar-minimum conditions (as above) and also for solar-maximum conditions (maximum modulation). The spectra of Figure 12 in Webber (1973) have been used. Note that the decreases in gradients here are entirely due to spectrum changes, κ_0 having been kept at 3.0×10^{21} cm^2 s^{-1} GV^{-1}.

VI. DISCUSSION AND CONCLUSIONS

The observed gradients are an order of magnitude below the expected values. The possible error in this order of magnitude is very large. First, the observational error is large, permitting a maximum of ~2.5 percent per AU; second, the diffusion coefficient of Jokipii and Coleman (1968) used here was given to be accurate within a factor of ~2. Taking extreme values, then, the discrepancy may only be a factor 2 or 3. We regard this as unlikely, however, and proceed with the discussion on the basis that there is a significant discrepancy.

There are several possibilities for removing this discrepancy between observation and model prediction, as follows:

1. The magnitude of the diffusion coefficient is too small. An increase in κ by a factor 5–8 would bring (cf. eq. [12]) good agreement between observation and theory. If this is the explanation, then it follows that the relationship between κ and the observed interplanetary magnetic-field power spectrum must be inadequate on either the observational side or the theoretical side. The latter may be the case, since there is controversy above the adequacy of the theories that have been accepted since 1967 (Roelof 1966; Jokipii 1966); the difficulties are discussed and references given in Fisk *et al.* (1973).

An erroneous magnitude of κ would be an attractive solution, since its adoption does not change the bulk of the work on cosmic-ray modulation and models. Spherically symmetric models could still be used and the same modulation achieved, provided the modulation parameter between the observation point at r_0, say, and the outer boundary of the modulation region at R,

$$\varphi(r_0, R) = \frac{1}{3} \int_{r_0}^{R} \frac{V(r)}{\kappa_0(r)} \, dr , \quad (19)$$

were maintained (see the discussion in Urch and Gleeson 1972). This simply requires an extension of the modulation region over that presently assumed, or a distant shell of high modulation.

2. The spherically symmetric model may be inadequate. It may be necessary to use a two-dimensional model in heliocentric distance r and heliocentric latitude λ in which there may be major changes in modulation with latitude and significant cross-latitude transport of particles. Studies have been begun along these lines (Fisk 1975; Moraal and Gleeson 1975; Cecchini and Quenby 1975).

3. There may be further transport processes not included in the equation of transport currently used.

TABLE 3

PREDICTED DIFFERENTIAL AND INTEGRAL GRADIENTS (force-field)
($\kappa = 3.0 \times 10^{21} P(\text{GV}) \beta$ cm^2 s^{-1}; units % per AU)

T (MeV/n)	Solar Maximum						Solar Minimum					
	Protons			Helium			Protons			Helium		
	C	γ_p	g_p	C	γ_α	g_α	C	γ_p	g_p	C	γ_α	g_α
400	0.53	14.9	6.4	0.67	9.3	4.8	0.83	23.2	10.3	1.18	16.5	6.9
600	0.71	14.0	6.2	0.82	8.9	4.7	1.05	20.7	9.6	1.35	13.3	6.0
800	0.83	12.9	5.9	1.14	8.7	4.5	1.27	19.6	8.8	1.42	11.0	5.2
1000	0.97	12.5	5.6	1.32	8.5	4.2	1.32	16.9	7.8	1.45	9.3	4.5
2000	1.21	8.7	4.5	1.43	5.2	2.9	1.38	9.9	5.2	1.43	5.2	2.9
4000	1.40	5.6	3.1	1.54	3.1	1.8	1.48	5.9	3.3	1.54	3.1	1.8
10000	1.50	2.6	1.5	1.64	1.4	0.9	1.50	2.6	1.5	1.64	1.4	0.9
100000	1.56	0.3	0.2	1.56	0.1	0.1	1.56	0.3	0.2	1.56	0.1	0.1

One such is the cross-field drift put forward by Bercovitch and Barnden (AGU Spring Meeting, 1974) and currently being investigated by them (private communication).

4. The temporal effect involved in the transition from solar minimum to solar maximum might be important.

Other experimenters on *P10* and *P11* have also reported values of cosmic-ray gradients. The University of Iowa (Thomsen and Van Allen 1976) reported $g = 0 \pm 2$ percent per AU for galactic cosmic rays with $E > 80$ MeV over the range 0.99–5.26 AU. In a more recent study (Van Allen 1976) using data out to 9 AU, they obtained a value of 2.0 ± 0.5 percent per AU. The University of Chicago group (McKibben *et al.* 1975) report small but nonzero gradients in several ranges. In an integral energy range, $E \geq 70$ MeV per nucleon, they report 2.8 ± 1.3 percent per AU during the *Pioneer-11* transit from 1 to 2.9 AU, and 4.4 ± 0.4 percent per AU during the *Pioneer-10* transit. In two differential energy windows, combining results from both spacecraft, they found 4.4 ± 7.1 percent per AU for protons and 10.0 ± 4.4 percent per AU for helium in the window $10 \leq E \leq 19$ MeV per nucleon, and 4.2 ± 2.6 percent per AU for protons and 8.3 ± 2.8 percent per AU for helium in the window $29 \leq E \leq 67$ MeV per nucleon. The group from the Goddard Space Flight Center and the University of New Hampshire (GSFC and UNH) (McDonald *et al.* 1975) retracted the small but positive values they had reported earlier (Teegarden *et al.* 1973) and announced 0 ± 3 percent per AU for helium in four differential energy ranges between 110 and 526 MeV per nucleon. The experiments of the University of Chicago and the GSFC/UNH groups were specifically designed for interplanetary cosmic-ray studies and must be given more weight than the others.

Our experimental result is compatible with the University of Iowa and the GSFC/UNH results. It is also within reach of the University of Chicago, if we point out that the proper comparison is to the *P11* integral result and blame time variations for the difference between this and the other values. However, we cannot reconcile with all groups at once without being inconsistent. The largest disagreement is between the University of Chicago and the groups reporting zero. This may not be a serious disagreement if allowance is made for the different expectations at different rigidities, or if the results can be pushed slightly beyond their quoted errors. Certainly the experimental inconsistency is small compared with the discrepancy between experiment and theory.

Finally, we comment on the reports which give zero for their result. In our remarks, we have tacitly assumed that gradients are positive, but small and nonzero. One can question whether this is sustained by the observations. Our data are consistent with, and suggest that, $g = 0$, and we feel that we cannot exclude the possibility of gradients which are essentially zero.

We are grateful to L. Barnden for providing the Deep River neutron monitor data, and to S. Duggal, M. Pomerantz, and particularly M. Bercovitch, for discussions on the muon background calibration prior to launch. We also thank A. Mogro-Campero for comments and discussions. This work was supported in part by NASA grant NGR 05-009-081 and contract NAS 2-6552.

REFERENCES

Bercovitch, M. 1973, private communication.
Caldwell, J., Evenson, P., Jordan, S., and Meyer, P. 1975, *Proc. 14th Internat. Cosmic Ray Conf.* (Munich), 3, 1000.
Carmichael, A., Bercovitch, M., and Steljes, J. F. 1967, *Tellus*, 14, 1.
Cecchini, S., and Quenby, J. J. 1975, *Proc. 14th Internat. Cosmic Ray Conf.* (Munich), 3, 911.
Chenette, D. L., Conlon, T. F., and Simpson, J. A. 1974, *J. Geophys. Res.*, 79, 3551.
Fillius, W., and McIlwain, C. E. 1974, *J. Geophys. Res.*, 79, 3589.
Fisk, L. A. 1975, *Proc. 14th Internat. Cosmic Ray Conf.* (Munich), 3, 905.
Fisk, L. A., Goldstein, M. L., Klimos, A. J., and Sandri, G. 1973, Goddard Space Flight Center (Greenbelt, MD), Reprint X-666-73-320.
Gleeson, L. J., and Axford, W. I. 1968, *Canadian J. Phys.*, 46, S937.
Gleeson, L. J., and Urch, I. H. 1973, *Ap. and Space Sci.*, 25, 387.
Gloeckler, G., and Jokipii, J. R. 1967, *Ap. J. (Letters)*, 148, L41.
Jokipii, J. R. 1966, *Ap. J.*, 149, 480.
Jokipii, J. R., and Coleman, P. J., Jr. 1968, *J. Geophys. Res.*, 73, 5495.
McDonald, F. B., Lal, N., Teegarden, B. J., Trainor, J. H., and Webber, W. R. 1975, *Proc. 14th Internat. Cosmic Ray Conf.* (Munich), 4, 1511.
McKibben, R. B., Pyle, K. R., Simpson, J. A., Tuzzolino, A. J., and O'Gallagher, J. J. 1975, *Proc. 14th Internat. Cosmic Ray Conf.* (Munich), 4, 1512.
Moraal, H., and Gleeson, L. J. 1975, *Proc. 14th Internat. Cosmic Ray Conf.* (Munich), 6, 910.
Roelof, E. C. 1966, unpublished Ph.D. thesis, University of California, Berkeley.
Teegarden, B. J., McDonald, F. B., Trainor, J. H., Roelof, E. C., and Webber, W. R. 1973, *Ap. J. (Letters)*, 185, L155.
Teegarden, B. J., McDonald, F. S., Trainor, J. H., Webber, W. R., and Roelof, E. C. 1974, *J. Geophys. Res.*, 79, 3615.
Thomsen, M. E., and Van Allen, J. A. 1976, *Ap. J.*, 206, 599.
Urch, I. H., and Gleeson, L. J. 1972, *Ap. and Space Sci.*, 17, 426.
Van Allen, J. A. 1976, *Trans. Am. Geophys. Union*, 57, 304.
Webber, W. R. 1973, *Proc. 13th Internat. Cosmic Ray Conf.* (University of Denver), 5, 3568.

W. Ian Axford: Max-Planck-Institut für Aeronomie, Institut für Stratospharen-Physik, 3411 Lindau/Harz, Germany

Walker Fillius: Department of Physics M/S B-019, University of California, San Diego, La Jolla, CA 92093

Leo Gleeson: Science, Monash University, Clayton, Victoria 3168, Australia

Wing-Huen Ip: Department of Applied Physics and Information Science M/S C-014, University of California, San Diego, La Jolla, CA 92093

VOL. 83, NO. A4 JOURNAL OF GEOPHYSICAL RESEARCH APRIL 1, 1978

Quiet Time Interplanetary Cosmic Ray Anisotropies Observed From Pioneer 10 and 11

W.-H. IP,[1] W. FILLIUS, AND A. MOGRO-CAMPERO[2]

University of California at San Diego, La Jolla, California 92093

L. J. GLEESON

Monash University, Clayton, Victoria 3168, Australia

W. I. AXFORD

Max-Planck-Institut für Aeronomie, D-3411 Katlenburg/Lindau 3, Federal Republic of Germany

The University of California at San Diego Cerenkov counters on the Pioneer 10 and Pioneer 11 spacecraft are capable of detecting protons and alpha particles with kinetic energy $T \geq 480$ MeV/nucleon and electrons with $T \geq 6$ MeV. With these instruments we have made measurements of cosmic ray anisotropies in interplanetary space, using the Pioneer 11 detector between April 17 and November 31, 1973 (during which interval the spacecraft moved from 1.1 to 2.7 AU), and the Pioneer 10 detector between March 1 and November 31, 1974 (during which interval the spacecraft moved from 6.0 AU to 6.8 AU). From the Pioneer 11 data the east-west anisotropy has been determined to be $\xi_\phi^* \approx 0.41 \pm 0.11\%$, and the north-south anisotropy $\xi_\theta^* \approx 0$. The ratio of the perpendicular and parallel components of the diffusion coefficient ($\kappa_\perp/\kappa_\parallel$) is on this basis estimated to be $\approx 0.26 \pm 0.08\%$. From the Pioneer 10 data, $\xi_\phi^* \approx 0.59 \pm 0.18\%$, $\xi_\theta^* \approx 0.25 \pm 0.08\%$, and we estimate that $\kappa_\perp/\kappa_\parallel \approx 0.13 \pm 0.04$. The large value of ξ_θ^* obtained from Pioneer 10 suggests that there was a substantial component of cosmic ray streaming from north to south. A comparison of the anisotropy and magnetic field data suggests that such a north-south anisotropy could be due at least in part to the gradient drift effect and perhaps in part to an additional streaming independent of the magnetic field polarity. To produce the observed value of ξ_θ^* from the gradient drift effect the radial gradient at this distance should have a value of $\approx 0.3 \pm 0.3\%$/AU, which is not incompatible with the radial gradients obtained from direct measurements.

1. INTRODUCTION

Until recently, most galactic cosmic ray measurements have been carried out by using either ground-based instruments or detectors carried on spacecraft near the earth's orbit. Consequently, relatively little is known about the behavior of galactic cosmic rays in the interplanetary medium beyond 1 AU, especially the variations of the radial intensities and anisotropies as functions of heliocentric distance. Following the launches of the spacecraft Pioneer 10 in 1972 and Pioneer 11 in 1973 the situation has greatly changed. Measurements of radial gradients at heliocentric distances up to 9 AU have been reported by several groups [*McDonald et al.*, 1975; *McKibben et al.*, 1975; *Van Allen*, 1976; *Axford et al.*, 1976] (see the review by *McKibben* [1975]). In general, the radial gradients are found to be about a factor of 5 smaller than the values predicted earlier on theoretical grounds. In addition, measurements of the anisotropies of high-energy galactic and solar cosmic rays have been made for the first time at large heliocentric distances. (See *Dyer et al.* [1974] for a near-earth measurement made on board the Heos 1 spacecraft.) A preliminary account of the Pioneer results has been given by *Axford et al.* [1975], and a more detailed description is presented here.

According to two-dimensional models [see *Parker*, 1964; *Axford*, 1965; *Forman and Gleeson*, 1975], the cosmic ray particles should exhibit an azimuthal (east-west) anisotropy in the solar equatorial plane associated with the corotation of the interplanetary magnetic field line (IMF) structure with the sun. Furthermore, because of the $\mathbf{B} \times \nabla U$ drift perpendicular to the IMF there should also be a north-south anisotropy (see discussion in section 4). Since *Pomerantz and Duggal* [1974] have produced a comprehensive review of this subject, we will not discuss detailed theoretical questions and previous experimental observations here; instead we simply emphasize that within the framework of current solar modulation theory the ratio of the perpendicular and parallel components of the diffusion coefficients can in principle be derived from the magnitude of the azimuthal anisotropy. In turn, information concerning the manner in which cosmic ray particles diffuse in interplanetary space can be deduced. It is therefore very desirable to have such anisotropy observations in addition to radial gradient measurements. Because of the requirement for narrow angular resolution and high count rate, among the detectors on board Pioneer 10 and 11, only the Cerenkov detector in the University of California at San Diego (UCSD) instrument package is capable of performing such anisotropy measurements satisfactorily.

In this paper we will report results of the cosmic ray anisotropy measurements of the UCSD experiment on board both Pioneer 10 and Pioneer 11. In addition to the Pioneer 11 results obtained for the time interval between April and November 1973, in which the spacecraft traveled from 1 to 2.8 AU [see *Axford et al.*, 1975], postencounter data from Pioneer 10 are included. The Pioneer 10 interplanetary measurements of quiet time anisotropies were made between November 1974 and March 1975 at a Jovicentric distance $r_J > 1.7$ AU and a

[1] Now at Max-Planck-Institut für Aeronomie, D-3411 Katlenburg/Lindau 3, Federal Republic of Germany.

[2] Now at General Electric Research and Development Center, Schenectady, New York 12301.

Paper number 7A1057.
0148-0227/78/047A-1057$03.00

heliocentric distance $r \approx 6$–7 AU. In the following section the instrumentation and data analysis are discussed. The observations are described in section 3, and finally, the results are interpreted and summarized in section 4.

2. INSTRUMENTATION

The C1 channel of the Cerenkov detector used in the measurement detects nuclei with kinetic energy $T \geq 480$ MeV/nucleon and electrons with $T \geq 6$ MeV. The quiet time counting rates due to galactic cosmic rays comprise approximately 84% protons, 12% α particles, and 2% each heavy nuclei and electrons. More detailed descriptions of this instrument have been presented elsewhere [*Fillius and McIlwain*, 1974; *Axford et al.*, 1976]. The spacecraft spin axis points always toward the earth, and the Cerenkov detector is mounted facing perpendicular to the spin axis, so that its look direction sweeps a circle in a plane perpendicular to the ecliptic plane.

We express the angular distribution of the cosmic ray intensity Φ in the spacecraft equatorial plane as

$$\Phi = \Phi_0\left[1 + \sum_{n=1}^{N} \xi_n \cos n(\psi - \psi_n)\right] \quad (1)$$

where ψ is the clock angle and ψ_n is the reference direction of the nth-order term of the expansion. The first-order term ξ_1 can be measured only by a unidirectional counter. Since unidirectionality is an inherent feature of the Cerenkov detector, we can measure the east-west and north-south components of the cosmic ray intensity contained in this term. During quiet times the anisotropy is small, and only the first-order term is important. Thus (1) can be reduced to

$$\Phi = \Phi_0[1 + \xi_1 \cos(\psi - \psi_1)] \quad (2)$$

According to the geometry we adopted, with the spin vector pointing toward the earth and the detector scanning in a plane perpendicular to the ecliptic plane, $\psi = 0$ when the detector is pointing downward, and $\psi = 90°$ when the detector is pointing eastward in the ecliptic plane. The east-west component of the anisotropy is consequently given by $\xi_\phi = \xi_1 \sin \psi_1$, with $\xi_\phi > 0$ for cosmic ray particles streaming along the spiral interplanetary magnetic field lines into the inner solar system (i.e., east to west) and $\xi_\phi < 0$ for particles streaming away from the sun (west to east). Similarly, the north-south component of the anisotropy is given by $\xi_\theta = -\xi_1 \cos \psi_1$, wherein $\xi_\theta > 0$ for particles streaming from north to south and $\xi_\theta < 0$ for particles streaming from south to north.

In addition to analyzing the data by fitting to (2) we have also evaluated the east-west and north-south anisotropies directly by defining them as the ratio of the difference to the sum of the counting rates in opposite sectors. Denoting these by $\tilde{\xi}_\phi$ and $\tilde{\xi}_\theta$ and the sector counting rates as $C_1(\psi)$, we can express the east-west anisotropy as

$$\tilde{\xi}_\phi = [C_1(\psi_A) - C_1(\psi_B)]/[C_1(\psi_A) + C_1(\psi_B)] \quad (3)$$

where $\psi_A = 90°$ and $\psi_B = 270°$. For the north-south anisotropy ξ_θ, $\psi_A = 180°$, and $\psi_B = 0°$. When the statistical certainty of the measurement is good, $\xi_\phi \approx \xi_1 \sin \psi_1$ and $\xi_\theta \approx -\xi_1 \cos \psi_1$. This correspondence holds true for the longest time intervals over which we have averaged the data (e.g., Figures 4 and 7), but it is sometimes masked by statistical fluctuations in the shorter-term averages. This is because, with an average counting rate of $\sim 5\ s^{-1}$ and a duty cycle of 1/9, our detector yields about 5×10^4 counts per day, and it takes several days of data at least to gain adequate statistical resolution. Therefore care must be taken in the interpretation of short-term variations of the cosmic ray anisotropies.

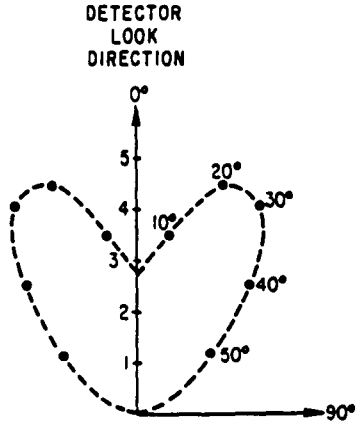

Fig. 1. Directional response of the UCSD C1 channel Cerenkov detector for protons with $T > 480$ MeV.

Several convolution factors must be evaluated to determine the anisotropies. Since the spacecraft rotates with a period of about 12 s, the detector sweeps a certain angular path δ within one data accumulation period. The resultant averaging effect will reduce the measured value of ξ_1 by a factor

$$f_1 = [\sin(\delta/2)]/(\delta/2) \quad (4)$$

The value of δ scales according to the spacecraft telemetry rate and data format. There are three values that give adequate directional resolution for anisotropy measurements, namely, $\delta = 45°$, 90°, and 180°. The reduction factor f_1 is consequently 0.97 (45°), 0.90 (90°) and 0.64 (180°).

A similar convolution factor is introduced by our method of data analysis. For simplicity we have sorted the data into bins which correspond to equal sectors of the detector look direction evaluated at the midpoint of the accumulation period. This boxcar averaging procedure produces a second reduction

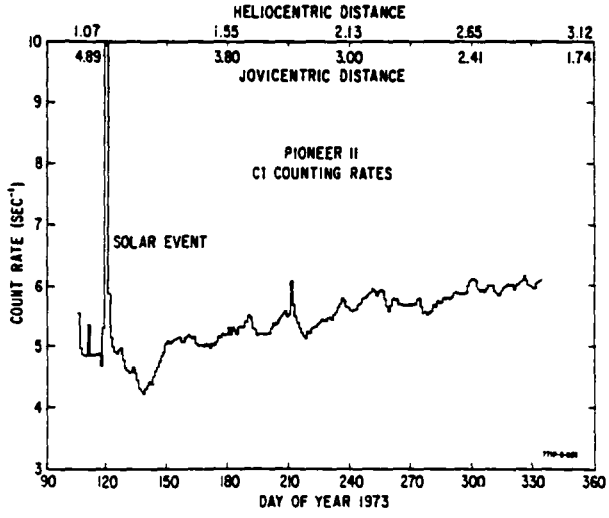

Fig. 2. Counting rate of the C1 Cerenkov detector on Pioneer 11 in the interval between April 17 and November 31, 1973, during which the spacecraft traveled in heliocentric distance from 1 AU to 2.8 AU and in Jovicentric distance from 4.9 AU to 2.2 AU.

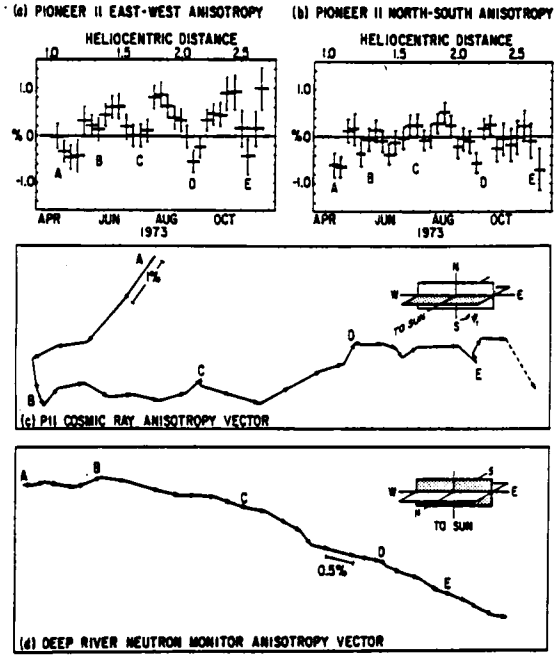

Fig. 3. (*a*) Anisotropies ξ_ϕ evaluated from 2-week averages of the counting rates in the east and west sectors. The anisotropy varies from −0.5% to +1% over a cycle of 59 ± 7 days. (*b*) Anisotropies ξ_θ evaluated from 2-week averages of the counting rates in the north and south sectors. The magnitude and variation are smaller for ξ_θ than for ξ_ϕ. (*c*) Sequential representation of the anisotropy vector ξ_1 obtained by fitting the 2-week-averaged Pioneer 11 counting rates to (2). In the insert the ecliptic plane is shaded, and the NS-EW plane represents the plane of the figure. The arrowheads point in the detector look direction (opposite the direction of cosmic ray streaming). (*d*) Sequential representation of the anisotropy vector obtained from the Deep River neutron monitor and projected on the ecliptic plane. The values are averaged over the same time intervals as those in part *c*. In the insert the ecliptic plane is shaded and represents the plane of the figure.

factor $f_2 = [\sin(\pi/m)]/(\pi/m)$, where we have used $m = 8$ so that $f_2 = 0.97$.

Another source of convolution of the experimental values is associated with the finite width of the angular response of the C1 detector. We have calculated that the corresponding reduction factor f_3 for protons is 0.81 (see Figure 1 for the pattern of angular response). For α particles, which make up ~12% of the total counting rate, no experimental calibration has been made, but by assuming the ratio of the response from the forward direction to that from the backward direction to be 10:1 the resulting value of f_3 for α particles is estimated to be $\simeq 0.52$. The net value of f_3 is weighted appropriately according to the average count rates observed for each species.

The total reduction factor due to convolution effects is therefore equal to $f = f_1 f_2 f_3$. In other words, if ξ_1 is the value of the anisotropy obtained directly from the data, the actual value of the cosmic ray anisotropy due to azimuthal streaming would be $\xi_1^* = \xi_1/f$. However, one must be careful in applying this result, since, for example, the method is not applicable for cases of angular distribution of cosmic ray intensity different from those defined by (2). Furthermore, the derived value of ξ_1^* is only the component in the equatorial plane of the spacecraft and not necessarily the total value, since here we are not able to make a full three-dimensional measurement of the distribution function.

3. OBSERVATIONS

The operational data format of Pioneer 10 allowed anisotropy measurements only shortly before Jupiter encounter. On the other hand, the data format of Pioneer 11 was favorable for the determination of the cosmic ray anisotropies between 1 and 2.8 AU. Hence since both ground-based and satellite measurements have concentrated in the past on the study of cosmic ray streaming at $r \sim 1$ AU, it seems appropriate here to present the Pioneer 11 data first, even though Pioneer 10 was launched before Pioneer 11.

a. Pioneer 11 Interplanetary Quiet Time Data (April 17 to November 31, 1973, $r \approx 1.0$–2.8 AU)

The counting rate of channel C1 from April to November 1973 is shown in Figure 2. At the end of April we observe a solar event followed by a Forbush decrease. The time evolution of the anisotropy pattern of the solar cosmic ray particles has been reported by *Axford et al.* [1975]. Here we limit our discussion to the anisotropies for the period of quiet interplanetary conditions only.

Figure 3 shows cosmic ray anisotropy measurements during this time period. Figures 3*a* and 3*b* show the east-west and north-south anisotropies ξ_ϕ and ξ_θ plotted versus time; Figure 3*c* shows the evolution of the anisotropy vector given by (2); and Figure 3*d* shows for comparison the anisotropy vector computed from Deep River neutron monitor data at 1 AU. The data points and vectors are spaced at 1-week intervals, but each represents an average of 2 weeks of data (for better statistical resolution). Occasionally, there are small differences between the vector components in Figure 3*c* and Figures 3*a* and 3*b*. These enter through the difference between (2) and (3) and indicate the presence of higher harmonics in the anisotropy expansion (1), but because of the limitations of statistical resolution they do not have any significance. In longer-term averages these harmonics vanish. We retain the dual

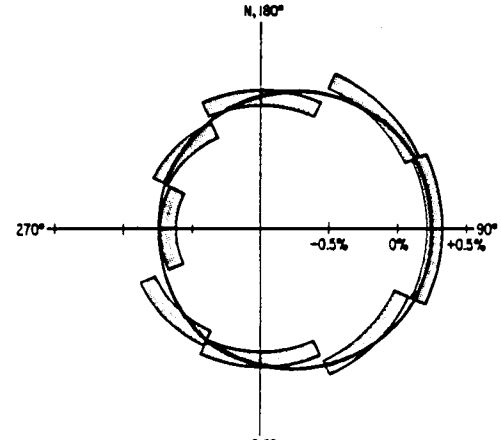

Fig. 4. Angular distribution calculated by averaging the channel C1 counting rate in eight angular bins and normalizing to the spin average. The shaded strips represent the probable error in the measurement ($\Delta\xi_1 \approx 0.07\%$). The heavy line is the anisotropy pattern obtained by fitting the eight-sector distribution to (2). With $f = 0.63$ we obtain $\xi_1^* = 0.41 \pm 0.11\%$ and $\psi_1 = 89°$. Note that the radial scale has been expanded (the origin corresponds to −1%) in order to make the small effect visible. The Pioneer 11 data shown here ($T > 480$ MeV/nucleon, $1.0 < r < 2.8$ AU) cover the period from April 17 to November 31, 1973, excluding the solar event on April 29–30.

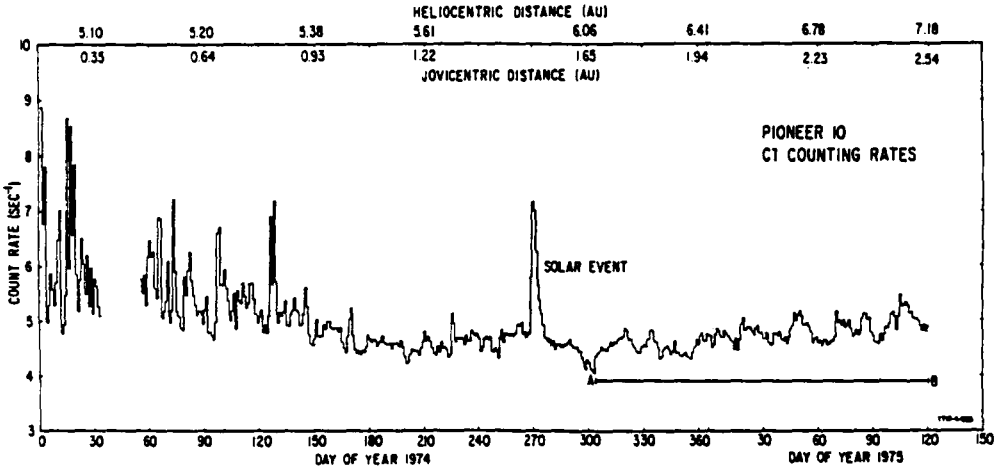

Fig. 5. Counting rates of the C1 channel on Pioneer 10 in the interval between January 1, 1974, and March 31, 1975, during which the spacecraft traveled in heliocentric distance from 5.1 to 7.2 AU and in Jovicentric distance from <0.35 to 2.5 AU. The quiet time anisotropies are derived from the data between day 305, 1974, and day 90, 1975 ($A \rightarrow B$).

representation of the anisotropy in order to illuminate the data from different perspectives.

From Figures 3*a*, 3*b*, and 3*c* it is readily apparent that the east-west anisotropy is much greater than the north-south component. In fact, the average value of $\bar{\xi}_\theta$ for the whole period, excluding the solar event, is (0.02 ± 0.07)%, while the corresponding value of $\bar{\xi}_\phi$ is (0.29 ± 0.07)%. In the interval covering the solar event and the subsequent Forbush decrease ($A \rightarrow B$) the streaming of particles away from the sun along the interplanetary magnetic field is evident from the behavior of the ξ_1 vectors, which have $\psi_1 \sim 270°$–$360°$. The south-to-north streaming of the cosmic rays during this interval might be related to the north-south asymmetry frequently observed following oblique interplanetary shocks [*Duggal and Pomerantz*, 1976]. Later the value of ψ_1 returns to ≈90°, which indicates that the galactic cosmic rays are streaming along the inter-

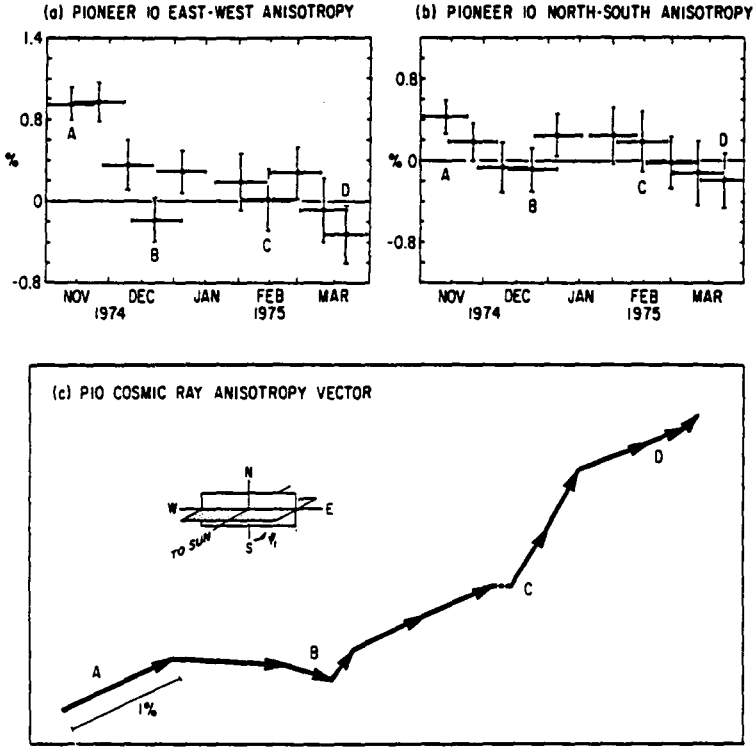

Fig. 6. (*a*) Anisotropies $\bar{\xi}_\phi$ evaluated from 26-day averages of the counting rates in the east and west sectors. (*b*) Anisotropies $\bar{\xi}_\theta$ evaluated from 26-day averages of the counting rates in the north and south sectors. (*c*) Sequential representation of the anisotropy vector ξ_1 obtained by fitting the 26-day-averaged Pioneer 10 counting rates to (2). In the insert the ecliptic plane is shaded, and the NS-EW plane represents the plane of the figure. The arrowheads point in the detector look direction (opposite the direction of cosmic ray streaming).

planetary magnetic field toward the sun (i.e., from east to west consistent with the rotation of the sun). In Figure 3*a* the east-west anisotropy appears to have a cyclic pattern of periodicity 59 ± 7 days and amplitude varying between −0.5% and +1%. This pattern is not so obvious in Figure 3*c*, but it can be seen that the anisotropy vector becomes very small at the points marked *C*, *D*, and *E* and resumes an appreciable magnitude between these points.

The anisotropy vector obtained from the Deep River neutron monitor (Figure 3*d*) depicts the projection onto the ecliptic plane of the anisotropy of particles with cutoff rigidity of ≈1 GV and average rigidity of ≈10 GV. Perhaps because of better statistics the Deep River anisotropy ξ_{DR} has a steadier pattern than that measured by the Cerenkov detector, and it is always pointing to the right, indicating persistent streaming of cosmic ray particles in the direction of solar rotation. However, during the interval $A \rightarrow B$, when the Cerenkov counter sees particles streaming away from the sun, the values of ξ_{DR} are rather small (≈0.2% compared to ≈0.5% after point *B*). It is possible that the Deep River anisotropy responds to some extent to the particles observed by the Cerenkov detector, and thus there is some consistency in the dynamical response of the two anisotropy vectors to the state of the interplanetary medium. The remaining differences are caused presumably by the difference in the particle rigidities concerned (average rigidity of ≈10 GV for Deep River neutron monitor and ≈5 GV for the C1 detector) and possibly by the difference in their heliocentric longitudes.

As we have mentioned before, because of the large uncertainty involved in fitting the angular distribution of the 2-week-averaged counting rates to a sinusoidal anisotropic pattern, caution must be taken in the interpretation of the short-term behavior presented in Figure 3*c*. On the other hand, more confidence can be given to the long-term behavior of the cosmic ray anisotropy. The angular distribution of cosmic rays for the total data set excluding the solar event is shown in Figure 4, and it is evident that the data can be approximated very well by a sinusoidal variation as defined by (2). The maximum-minimum axis is found to point in the east-west direction with $\psi_1 = 89°$ and $\xi_1 = 0.26 \pm 0.07\%$. Adopting the calculated reduction factor $f \approx 0.63$, we find that $\xi_1^* = 0.41 \pm 0.11\%$ in the region between 1.0 and 2.8 AU for the period of this observation.

b. Pioneer 10 Interplanetary Quiet Time Data (November 1, 1974 to March 31, 1975, $r \approx 6$–7 AU and $r_J \approx 1.7$–2.5 AU)

For several months after Jupiter encounter a series of Jovian electron events were detected up to a Jovicentric distance $r_J \approx 0.9$ AU. The prevalence of the Jovian electrons in this period can be seen in Figure 5, which depicts the variation of the C1 counting rates with time. Because of the large fluctuation in the counting rates it is rather doubtful that any segment of this data with $r_J < 1$ AU can be considered to be representative of quiet time interplanetary conditions at all. To determine the quiet time interplanetary cosmic ray anisotropy, it is preferable to analyze data as far away from Jupiter as possible. In this section we therefore present only results obtained for the region $r_J \approx 1.7$–2.5 AU and r between 6 and 6.8 AU from processed data available to us at the present time.

Between points *A* and *B* in Figure 5, no large fluctuation due to solar or Jovian particle events is apparent. There is, however, a long-term variation with an amplitude of ≈5–10%, presumably due to the 26-day cycle of solar rotation. We suggest that this set of data can be considered to be representative of the quiet time interplanetary condition, even though we cannot rule out residual contamination by Jovian electrons and the possibility that systematic effects associated with the 26-day modulation might introduce some confusion.

Following the procedure described previously, the values of the 26-day averaged peak-to-peak anisotropies are given in Figures 6*a* and 6*b* to facilitate the observation of temporal variations of the cosmic ray streaming. The maximum value of ξ_ϕ is ≈1%, which is comparable to the largest values observed in $r \sim 1$–2.8 AU (see Figure 3*a*). On the other hand, the values of ξ_θ shown in Figure 6*b* are significantly increased in comparison with the corresponding values shown in Figure 3*b*. Indeed, the value of ξ_θ averaged over the whole period of data is estimated to be ≈0.17 ± 0.14%, while an average value of ξ_ϕ is ≈0.41 ± 0.14%. That is, the north-south anisotropy is about one third the value of the east-west anisotropy for the period and range of heliocentric distance under consideration. One should of course note that the statistical uncertainty of the estimate for ξ_θ is relatively large.

In Figure 6*c* we present the variation of the anisotropy vectors ξ_1 obtained by fitting the same set of 26-day-averaged C1 counting rates to (2). The presence of a component of the cosmic ray anisotropy perpendicular to the ecliptic plane shows up rather conspicuously. Also the switching of ξ_ϕ to negative values in Figure 6*a* is seen to occur when the absolute value of ξ_1 is small. The angular distribution of the C1 counting rates for the whole data set is shown in Figure 7, and from these results it is found that $\xi_1 \approx 0.44 \pm 0.14\%$ and $\psi_1 = 113°$. With the reduction factor $f \approx 0.69$ appropriate to the operational format of Pioneer 10 during this period we find that between 6 and 7 AU, $\xi_1^* \approx 0.64 \pm 0.20\%$.

4. DISCUSSION

The two-dimensional streaming of galactic cosmic rays along the spiral magnetic field lines in the interplanetary me-

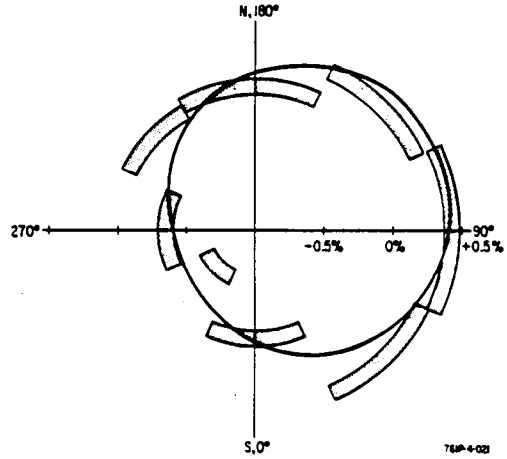

Fig. 7. Angular distribution calculated by averaging the channel C1 counting rate in eight angular bins and normalizing to the spin average. The shaded strips represent the probable error in the measurement ($\Delta\xi_1 \approx 0.12\%$). The heavy line is the anisotropy pattern obtained by fitting the eight-sector distribution to (2). With $f = 0.69$ we obtain $\xi_1^* = 0.64 \pm 0.20$ and $\psi_1 = 113°$. Note that the radial scale has been expanded (the origin corresponds to −1%) in order to make the small effect visible. The Pioneer 10 data shown here ($T > 480$ MeV/nucleon, $6.1 < r < 7.0$ AU) cover the period between November 1, 1974, and March 31, 1975.

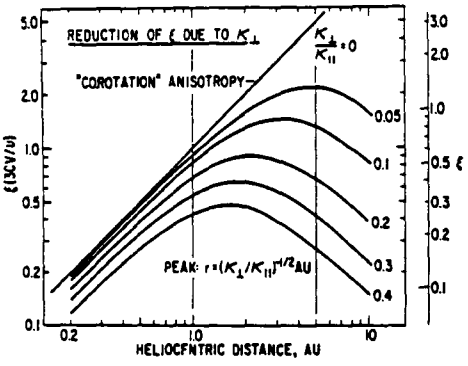

Fig. 8. Radial variation of the east-west anisotropy for different ratios of $\kappa_\perp/\kappa_\parallel$ according to the two-dimensional theory.

dium has been studied by *Forman and Gleeson* [1975], with the effects of spatial diffusion taken into account. In simple terms, it is expected that there will be an azimuthal streaming due to the corotation of the IMF and a streaming perpendicular to the ecliptic plane due to the gradient drift $\nabla U \times \mathbf{B}$, in which ∇U is the radial gradient of the galactic cosmic rays and $\mathbf{B}$ the magnetic field vector. Expressing the streaming in terms of cosmic ray anisotropies, we have (see, for example, *Pomerantz and Duggal* [1974])

$$\xi_\phi^* = \xi_1^* \sin\psi_1 = \frac{3V_sC}{v}\frac{(\kappa_\parallel - \kappa_\perp)\sin\chi\cos\chi}{\kappa_\parallel\cos^2\chi + \kappa_\perp\sin^2\chi} \quad (5)$$

as the azimuthal component (i.e., in the east-west direction) and

$$\xi_\theta^* = \xi_1^*\cos\psi_1 = \frac{\rho C V_s \sin\chi}{\kappa_\parallel\cos^2\chi + \kappa_\perp\sin^2\chi} \quad (6)$$

as the component perpendicular to the ecliptic plane (i.e., in the north-south direction). In (5) and (6), V_s is the solar wind velocity, C the Compton-Getting factor [*Gleeson and Axford*, 1968], v the velocity of the cosmic ray particles, χ the angle between the average magnetic field direction and the radial direction, ρ the gyroradius of the particles, and $\kappa_\parallel$ and $\kappa_\perp$ the components of the diffusion tensor parallel and perpendicular to the mean magnetic field direction, respectively.

If $\kappa_\perp \ll \kappa_\parallel$, one finds that $\xi_\phi^* = (3\,CV_s/v)\tan\chi$, and since $\tan\chi \propto r$, it might be expected that ξ_ϕ^* increases more or less linearly as r increases. However, since $\xi_\phi^* \approx 0.6\%$ at 1 AU, the average value of ξ_ϕ^* derived from Pioneer 11 for r between 1 and 3 AU should then be $\approx 1\%$, and the corresponding value from Pioneer 10 for r between 6 and 7 AU should be $\approx 4\%$. Since the values observed do not exceed 0.6%, it seems that $\kappa_\perp$ is not negligibly small, as is usually assumed (see, for example, *Rao* [1972]). The variation of the azimuthal anisotropy as a function of r for various values of $\kappa_\perp/\kappa_\parallel$ is shown in Figure 8. This shows that for nonzero ratio of the diffusion coefficients the ξ_ϕ^* value will reach a peak value at $r \approx (\kappa_\parallel/\kappa_\perp)^{1/2}$, assuming of course that the ratio remains constant. Since this result is obtained by assuming steady state conditions and spherical symmetry, it may not be meaningful to compare it with the results shown in Figures 3 and 6, where large variations in ξ_ϕ are observed. However, assuming that it is appropriate to fit the observed average (quiet time) value $\xi_\phi^*(\text{P11}) = (0.41 \pm 0.11)\%$ to a certain value of $\kappa_\perp/\kappa_\parallel$ within the range 1–2.8 AU, we find, after correcting for the small deviation of the plane in which the measurements are performed with respect to the east-west direction and assuming that $\xi_\phi^* = 0.6\%$ at 1 AU for $\kappa_\perp/\kappa_\parallel = 0$, that the resulting ratio is $\kappa_\perp/\kappa_\parallel \simeq 0.26 \pm 0.08$. Similarly, the quiet time value $\xi_\phi^*(\text{P10}) = 0.64 \pm 0.20$ yields $\kappa_\perp/\kappa_\parallel \approx 0.13 \pm 0.04$ for r between 6 and 6.8 AU.

These results are summarized in Table 1, where two outstanding features can be noticed. First, besides being larger than the values usually assumed in model calculations, the nominal value of $\kappa_\perp/\kappa_\parallel$ decreases by a factor of 2 as the radial distance increases from 1–3 AU to 6–7 AU. Second, the ratio of ξ_θ^* to ξ_ϕ^* increases from 0 to 0.42, indicating that at large distances there is a strong component of cosmic ray streaming from north to south with a magnitude comparable to that of the azimuthal streaming. In fact, such a variation of the ξ_θ^*/ξ_ϕ^* ratio is not unexpected, since this ratio varies as $1/\cos\chi$ and $\cos\chi \to 0$ at large distances from the sun. What is more interesting here is that following the usual formulation of solar modulation theory we can derive the radial gradient from the observed value of ξ_θ^*, since the north-south anisotropy is given approximately by

$$\xi_\theta^* \approx \rho \cdot g_r \sin\chi \quad (7)$$

where $\xi_\theta^* > 0$ for IMF pointing outward from the sun (positive magnetic sector) and $\xi_\theta^* < 0$ for IMF pointing inward (negative sector). Hence given ξ_θ^*, ρ, and $\sin\chi$, we can derive a value of g_r from (7). Since $B \approx 0.5\ \gamma$ at 6–7 AU, the average value of the gyroradius $\bar{\rho}$ for the Cl channel is ≈ 0.24 AU (for an average kinetic energy $\bar{T} \approx 4.5$ GeV), and $\sin\chi \approx 1$. Setting $\xi_\theta^* \approx 0.25\% \pm 0.08$, we obtain $g_r \approx 1.0 \pm 0.3\%/\text{AU}$, which is comparable to the integral gradient $0.15 \pm 2.3\%/\text{AU}$ estimated for $r < 5$ AU by *Axford et al.* [1976] and the integral gradient $T > 80$ MeV of 2%/AU between 1 and 9 AU recently reported by *Van Allen* [1976].

The situation is actually more complex, because in the above discussion we have assumed the polarity of the magnetic field to be the same over the whole time interval of interest, whereas the IMF near the ecliptic plane at 1 AU is divided into roughly equal sectors of opposite magnetic field polarities. (See *Smith et al.* [1977] for a recent view of the sector structure throughout the heliosphere.) The anisotropy due to gradient drifts should be such that $\xi_\theta^* > 0$ in positive sectors and $\xi_\theta^* < 0$ in negative sectors. The observed ξ_θ^* value when averaged over

TABLE 1. Comparison of the Pioneer 10 and Pioneer 11 Anisotropy Data

Spacecraft	Time Interval, Day of Year	Solar Distance, AU	Jovicentric Distance, AU	Reduction Factor f	ξ_1, %	ψ_1, deg	ξ_1^*, %	ξ_ϕ^*, %	ξ_θ^*, %	ξ_θ^*/ξ_ϕ^*	$\kappa_\perp/\kappa_\parallel$
Pioneer 11	107, 1973 to 334, 1973	1.1–2.8	4.9–2.0	0.63	0.26 ± 0.7	89	0.41 ± 0.11	0.41 ± 0.11	~0	0	0.26 ± 0.08
Pioneer 10	305, 1974 to 90, 1975	6–6.8	1.7–2.5	0.69	0.44 ± 0.14	113	0.64 ± 0.20	0.59 ± 0.18	0.25 ± 0.08	0.42	0.13 ± 0.04

TABLE 2. Comparison of the Pioneer 10 Anisotropy and Magnetic Field Data

Magnetic Field Polarity	Time Intervals, Day of Year 1974	Total Number of Days	ξ_t*, %	ψ_t, deg	ξ_ϕ*, %	ξ_θ*, %	g_r, %/AU
Positive	312–329 337–356	38	0.38 ± 0.26	116	0.34 ± 0.23	0.17 ± 0.11	0.7 ± 0.5
Negative	307–311 330–336 357–361	17	0.58 ± 0.36	86	0.58 ± 0.36	−0.04 ± 0.03	0.2 ± 0.1

one solar rotation or longer time interval would depend on the net polarity of the IMF, among other things. For example, if the sector structure has equal proportions of positive and negative polarities, the averaged value should be ≈0; and if the positive sectors combined occupy twice as much area as that occupied by the negative sectors, the observed anisotropy will be only one third the value measured within the individual sector.

To examine the variation of ξ_θ* in regions of different magnetic polarities and also the effect of the $\nabla U \times \mathbf{B}$ drift, we have calculated the cosmic ray anisotropies corresponding to different magnetic field polarities according to magnetic field data provided for us by E. J. Smith (private communication, 1976). Of the 55 days (307–361, 1974) covered by the magnetic field data we find that there are 38 days with positive polarity and 17 days with negative polarity. The results for the anisotropies and radial gradients derived for these two intervals are presented in Table 2, where one sees that even though the experimental uncertainty is large, the variation of the sense of the north-south anisotropy is suggestive of the presence of the gradient drift. It is, however, interesting to note that the north-south anisotropy in positive sectors is quite appreciable (ξ_θ* ≈ 0.17 ± 0.11%). while the corresponding value in the negative sectors is close to zero (ξ_θ* ≈ −0.04 ± 0.03%). This is not consistent with the simple $\nabla U \times \mathbf{B}$ drift effect, which should yield similar magnitudes in the two cases. It is possible that the observed north-south anisotropy is a combination of two types of streaming: one due to the drift effect described, which gives a value of ξ_θ* = ξ_D* in positive sectors and ξ_θ* = −ξ_D* in negative sectors, and one with a cosmic ray streaming which will produce ξ_θ* = ξ_A* across the ecliptic plane regardless of the sign of the magnetic field. In this case the observed north-south anisotropies are given by $\xi_{\theta+}$* = ξ_D* + ξ_A* and $\xi_{\theta-}$* = ξ_D* − ξ_A*. Putting $\xi_{\theta+}$* ≈ 0.17% and $\xi_{\theta-}$* ≈ −0.04%, we obtain ξ_D* ≈ 0.07% ± 0.06% and ξ_A* ≈ 0.11% ± 0.06%, and the radial gradient g_r from this value of ξ_D* is ≈0.3 ± 0.3%/AU, which is consistent with the value 0.15 ± 2.5%/AU determined directly from our experiment [*Axford et al.*, 1976] and compatible with the values derived by other groups [*McDonald et al.*, 1975; *McKibben et al.*, 1975; *Teegarden et al.*, 1973; *Van Allen*, 1976].

With due allowance for the simplicity of the models we have used, it appears that the observed anisotropies and radial gradients close to the ecliptic plane are reconcilable with the two-dimensional solar modulation model provided $\kappa_\perp/\kappa_\parallel$ lies in the appropriate range 0.13–0.26, and the parallel diffusion coefficient $\kappa_\parallel$ is perhaps a factor of 10 larger than the usually accepted value of 3×10^{21} cm^2 s^{-1} GV^{-1} [see *Jokipii and Coleman*, 1968; *Birmingham and Jones*, 1975; *Axford et al.*, 1976]. The presence of an additional north-south streaming of the cosmic ray particles is, however, required. As has been pointed by M. A. Forman (private communication, 1977), a north to south gradient perpendicular to the ecliptic plane with $g_\perp$ ≈ 4%/AU could produce a north-south anisotropy with the observed ξ_A ≈ 0.11%. It is also possible that the observed values can be explained by a three-dimensional model with latitude-dependent modulation [e.g., *Fisk*, 1976; *Moraal and Gleeson*, 1975], using different sets of parameters; and in this case the north-south streaming with ξ_A* ≈ 0.11% may be the result of an asymmetry in the latitude dependence of the modulation. Another alternative is that the 26-day modulation effect (which causes a variation of the mean intensity of ~5–10% in our detector) produces anisotropies which do not average out to zero. These fluctuations occur with time scales of the order of 5–10 days, corresponding to radial gradients of ≈5%/AU (i.e., much larger than the measured average gradient). The positive and negative gradients are not necessarily equal, and furthermore, owing to the behavior of the fast solar streams and interplanetary magnetic field sector structure associated with these fluctuations, it is entirely possible that systematic effects can occur which lead to a nonzero average north-south anisotropy. Obviously, more detailed study of the correlation between the cosmic ray anisotropies and the magnetic field data, and especially measurements at larger distances and out of the ecliptic plane, would be extremely useful in providing answers to these questions.

Acknowledgments. We thank M. Berkovitch for Deep River neutron monitor data and E. J. Smith for unpublished Pioneer 10 magnetic field data. We also thank M. Forman for helpful criticism. This work was supported by NASA through contract NAS 2-6552 and grant NGR 05-009-081.

The Editor thanks S. P. Duggal for his assistance in evaluating this paper.

REFERENCES

Axford, W. I., The modulation of galactic cosmic rays in the interplanetary medium, *Planet. Space Sci., 13*, 115–130, 1965.

Axford, W. I., W. Fillius, L. J. Gleeson, W. H. Ip, and A. Mogro-Campero, Measurements of cosmic ray anisotropies from Pioneer 10 and 11, *Proc. Int. Conf. Cosmic Rays 14th, 4*, 1519–1524, 1975.

Axford, W. I., W. Fillius, L. J. Gleeson, and W. H. Ip, Cosmic-ray gradients from Pioneer 10 and Pioneer 11, *Astrophys J., 210*, 610–613, 1976.

Birmingham, T. J., and F. C. Jones, Cosmic ray diffusion—Report of the Workshop in Cosmic Ray Diffusion Theory, *NASA Tech. Note TN D-7873*, 1975.

Duggal, S. P., and M. A. Pomerantz, Origin of transient north-south anisotropy of cosmic rays, *J. Geophys. Res., 81*, 5032, 1976.

Dyer, C. S., A. R. Engel, J. J. Quenby, and S. Webb, Observation and explanation of a 0.3% sunward radial streaming of 1 to 5 GV cosmic radiation, *Solar Phys., 39*, 243–259, 1974.

Fillius, R. W., and C. E. McIlwain, Measurements of the Jovian radiation belts, *J. Geophys. Res., 79*, 3589–3599, 1974.

Fisk, L. A., Solar modulation of galactic cosmic rays, 4, Latitude dependent modulation, *J. Geophys. Res., 81*, 4646–4650, 1976.

Forman, M. A., and L. J. Gleeson, Cosmic-ray streaming and anisotropies, *Astrophys. Space Sci., 32*, 77–94, 1975.

Gleeson, L. J., and W. I. Axford, The Compton-Getting effect, *Astrophys. Space Sci., 2*, 431–437, 1968.

Jokipii, J. R., and P. J. Coleman, Jr., Cosmic ray diffusion tensor and its variation observed with Mariner 4, *J. Geophys. Res.*, *73*, 5495, 1968.

McDonald, F. B., N. Lal, B. J. Teegarden, J. H. Trainor, and W. R. Webber, The radial gradient of galactic cosmic rays, *Proc. Int. Conf. Cosmic Rays 14th*, *4*, 1511, 1975.

McKibben, R. B., Cosmic ray intensity gradients in the solar system, *Rev. Geophys. Space Phys.*, *13*, 1088–1099, 1975.

McKibben, R. B., K. R. Pyle, J. A. Simpson, A. J. Tuzzolino, and J. J. O'Gallagher, Cosmic ray radial intensity gradients measured by Pioneer 10 and Pioneer 11, *Proc. Int. Conf. Cosmic Rays 14th*, *4*, 1512, 1975.

Moraal, H., and L. J. Gleeson, Three-dimensional models of the galactic cosmic-ray modulation, *Proc. Int. Conf. Cosmic Rays 14th*, *3*, 910, 1975.

Parker, E. N., Theory of streaming of cosmic rays and the diurnal variation, *Planet. Space Sci.*, *12*, 735–749, 1964.

Pomerantz, M. A., and S. P. Duggal, The sun and cosmic rays, *Rev. Geophys. Space Phys.*, *12*, 343–361, 1974.

Rao, A. R., Solar modulation of galactic cosmic radiation, *Space Sci. Rev.*, *12*, 719–809, 1972.

Smith, E. J., B. T. Tsurutani, and R. L. Rosenberg, Observations of the interplanetary sector structure up to heliographic latitudes of 16°: Pioneer 11 (abstract), *Eos Trans. AGU*, *58*, 484, 1977.

Teegarden, B. J., F. B. McDonald, J. H. Trainor, E. C. Roelof, and W. R. Webber, Pioneer-10 measurements of the differential and integral cosmic ray gradient between 1 and 3 astronomical units, *Astrophys. J.*, *185*, L155, 1973.

Van Allen, J. A., Galactic cosmic ray intensity from 1 to 9 AU, *Geophys. Res. Lett.*, *3*, 425–428, 1976.

(Received August 16, 1977;
accepted November 14, 1977.)

1. Report No.	2. Government Accession No.	3. Recipient's Catalog No.
NASA CR-166360		

4. Title and Subtitle	5. Report Date
Pioneer 10/11 Data Analysis of the Trapped Radiation Experiment	January 1982
	6. Performing Organization Code

7. Author(s)	8. Performing Organization Report No.
Walker Fillius	
	10. Work Unit No.

9. Performing Organization Name and Address	11. Contract or Grant No.
Center for Astrophysics and Space Science University of California San Diego, California	NAS2-6552
	13. Type of Report and Period Covered

12. Sponsoring Agency Name and Address	13. Type of Report and Period Covered
National Aeronautics and Space Administration Washington, DC 20546	Contractor Report - Final
	14. Sponsoring Agency Code

15. Supplementary Notes

Technical Monitor: Christopher A. Leidich, Mail Stop 244-8, NASA Ames Research Center, Moffett Field, CA 94035
(415) 965-5692, FTS 448-5692

16. Abstract

Contract NAS2-6552 was undertaken by the National Aeronautics and Space Administration (NASA) and the University of California, San Diego (UCSD) to accomplish the reduction, analysis, dissemination, and publication of data from the UCSD Trapped Radiation Experiment on the NASA Pioneer 10 and 11 spacecraft. This report gives a brief outline of the data handling operations and the data base which has been produced by this experiment. The balance of the report consists of reprints of technical publications which record the discoveries and analyses based on this experiment to date. These papers chronicle the first in situ measurements of trapped radiation at both Jupiter and Saturn, the extension of cosmic ray observations to the outer heliosphere, the presence of Jovian electrons in interplanetary space, analyses of the interaction between planetary satellites and the trapped radiation that engulfs them, and further investigations of the radiation environments of both planets.

17. Key Words (Suggested by Author(s))	18. Distribution Statement
Pioneer 10 and 11 Planetary Magnetospheres Jupiter's Radiation Belts Saturn's Radiation Belts Cosmic Rays	Unclassified - Unlimited STAR Category - 12

19. Security Classif. (of this report)	20. Security Classif. (of this page)	21. No. of Pages	22. Price*
Unclassified	Unclassified	214	

*For sale by the National Technical Information Service, Springfield, Virginia 22161

End of Document